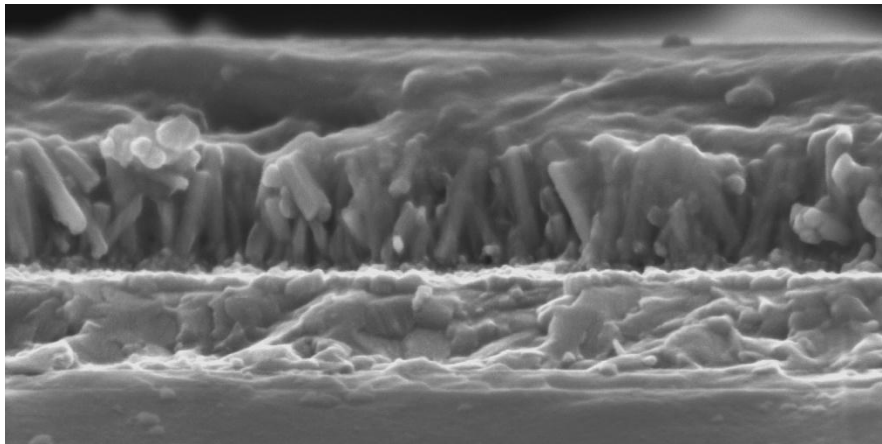


# **Metal oxide layer in organic solar cells**



**Doctoral Thesis**

vorgelegt von

**Haiyan Sun**

angefertigt in der Arbeitsgruppe  
Hybrid Nanostructures  
Prof. Dr. Lukas Schmidt-Mende

Fakultät für Physik  
Ludwig-Maximilians-Universität München  
Juni 19, 2012

Erstgutachter: Prof. Dr. Lukas Schmidt-Mende  
Zweitgutachter: Prof. Dr. Alexander Högele  
Datum der mündlichen Prüfung: 09.08.2012

# Contents

Abstract .....	v
List of Abbreviations.....	ix
1 Introduction.....	1
1.1 Solar cells working principles.....	3
1.1.1 Organic photovoltaic materials .....	3
1.1.2 Donor-acceptor concept .....	4
1.1.3 Charge generation .....	5
1.1.4 Morphology in organic solar cells.....	8
1.1.5 Recombination mechanisms.....	11
1.2 The performance of OPVs.....	13
1.2.1 Efficiencies of devices .....	14
1.2.2 Stability of the devices .....	15
1.2.3 To improve the performance of devices .....	17
1.3 Organic photovoltaic devices.....	19
1.3.1 Organic solar cells.....	19
1.3.2 Dye-sensitized solar cells .....	20
1.3.3 Hybrid solar cells .....	22
1.4 Metal oxides in hybrid solar cells .....	24
1.4.1 TiO <sub>2</sub> and ZnO metal oxides.....	25
1.4.2 Applications in hybrid solar cells.....	26
1.4.3 Nanostructures of metal oxides .....	27
2 Experimental Methods .....	30
2.1 Solar cell architecture.....	30
2.1.1 Solar cell design .....	30
2.1.2 Non-inverted solar cells .....	31
2.1.3 Inverted solar cells .....	32
2.1.4 Inverted-inverted solar cells architecture .....	33
2.1.5 Flexible devices architecture.....	34
2.1.6 Transparent devices architecture .....	35
2.2 Materials and fabrication methods .....	36
2.2.1 Photoactive materials and blend layer.....	36

2.2.2 Syntheses of the TiO <sub>2</sub> blocking layers.....	37
2.2.3 Syntheses of the ZnO blocking layer .....	41
2.2.4 Fabrication of buffer layers .....	43
2.2.5 Deposition of electrodes.....	44
2.3 Characterization .....	45
2.3.1 I-V Characterization.....	45
2.3.2 EQE characterization .....	48
2.3.3 Absorption measurement.....	49
2.3.4 Microscopy techniques.....	50
2.3.5 XRD measurements .....	50
2.3.6 Van der Pauw method and Hall Effect measurement .....	51
2.3.7 Intensity dependence measurement.....	53
2.3.8 Impedance spectroscopy measurement .....	54
2.3.9 Photo-CELIV method .....	55
3. Device Optimization .....	57
3.1 Blocking layers improvement .....	57
3.1.1 TiO <sub>2</sub> Surface Cleaning.....	57
3.1.2 N-Doped TiO <sub>2</sub> to increase the absorption .....	61
3.1.3 Mg-doped ZnO to enhance the V <sub>OC</sub> .....	66
3.1.4 TiO <sub>2</sub> -ZnO co-blocking layer .....	69
3.2 P3HT:PCBM layer improvement .....	71
3.2.1 P3HT:PCBM blend solutions.....	72
3.2.2 P3HT:PCBM ratios .....	74
3.2.3 P3HT:PCBM layer thickness .....	76
3.2.4 Post-deposition treatment process on blend layer .....	78
3.3 Spray-deposited PEDOT: PSS for air stable inverted organic solar cells .....	81
3.3.1 Background.....	81
3.3.2 PEDOT:PSS layer deposition.....	83
3.3.3 Device performance .....	83
3.3.4 Time evolution of the V <sub>OC</sub> .....	87
3.3.5 Summary .....	88
3.4 Conclusion .....	89
4 Effect of Blocking Layer.....	91
4.1 Introduction.....	91
4.2 Device structure and experimental.....	92
4.3 Properties of TiO <sub>2</sub> and ZnO layers .....	93
4.3.1 Crystallinity.....	93

---

4.3.2 Conductivity and mobility.....	94
4.3.3 Surface morphology .....	95
4.3.4 Absorption.....	97
4.3.5 Summary .....	99
4.4 Performances of inverted devices based on TiO <sub>2</sub> and ZnO.....	99
4.4.1 EQE characterization of TiO <sub>2</sub> and ZnO devices.....	100
4.4.2 I-V characterization of TiO <sub>2</sub> and ZnO devices .....	101
4.4.3 Charge carrier mobility of TiO <sub>2</sub> and ZnO devices.....	104
4.4.4 Charge recombination of TiO <sub>2</sub> and ZnO devices .....	105
4.5 Effects of trap states in blocking layers.....	109
4.5.1 Trap filling of photoinduced TiO <sub>2</sub> and ZnO .....	109
4.5.2 Filter effect of TiO <sub>2</sub> and ZnO .....	111
4.6 Stability of the inverted devices based on TiO <sub>2</sub> and ZnO .....	113
4.6.1 Illumination stability .....	113
4.6.2 Air stability.....	115
4.7 Conclusion .....	116
5 ZnO Nanowires Electrodes .....	119
5.1 Introduction.....	120
5.2 Device fabrication and optimization .....	122
5.2.1 Devices fabrication.....	122
5.2.1 Hydrothermal method .....	123
5.2.2 ZnO seed layers optimization.....	125
5.3 Morphology of ZnO NW .....	127
5.3.1 Influence of ZnO seed layer on morphology.....	127
5.3.2 Influence of HT solution on morphology.....	129
5.3.3 Influence of temperature on morphology.....	130
5.3.4 Influence of time on morphology.....	132
5.3.5 Summary .....	134
5.4 P3HT:PCBM solar cells based on ZnO NW .....	134
5.4.1 Dependence of solar cell performance on the ZnO NW length .....	134
5.4.2 P3HT:PCBM ratio vs different ZnO NW lengths .....	144
5.5 ZnO NW surface modified by AALD N-doped ZnO.....	146
5.5.1 Solar cells preparation.....	147
5.5.2 Stability of ZnO NW .....	148
5.5.3 Absorption measurements .....	149
5.5.4 EQE measurements .....	151
5.5.6 I-V measurements .....	153

5.5.7 Light intensity measurements.....	155
5.5.8 Improvement of the performance.....	156
5.6 Conclusion .....	156
6 Conclusion and Outlook.....	158
Bibliography .....	163
Appendix: Publications and Presentations .....	175
Curriculum Vitae.....	176
Acknowledgment .....	178

## Abstract

Organic photovoltaic devices have drawn a lot of attention as means for the renewable energy conversion due to the remarkable combination prospective low cost of manufacturing and rapid improvement of performance approaching the traditional silicon solar cells. By introducing metal oxides in organic photovoltaics, the hybrid solar cells show great potential in terms of device performance with the high exciton dissociation, the favorable charge transport ability and the air stability. In this thesis, the  $\text{TiO}_2$  and  $\text{ZnO}$  are investigated as charge selective layers in hybrid solar cells, focusing on their impacts on the device performance.

Initially, the fabrication process of solar cells is optimized by several important steps summarized as follows: the  $\text{TiO}_2$  and  $\text{ZnO}$  are cleaned on the surface and modified by doping. The blend layer is influenced by the solution, layer thickness and the post treatment process implemented. A proper interface layer of PEDOT:PSS is spray deposited between the organic layer and silver top contact to extract holes selectively. All these processes can significantly influence the device performance.

Additionally,  $\text{TiO}_2$  and  $\text{ZnO}$  in hybrid solar cells are investigated for their influences on the device performances. Despite of the advantages on surface area, transparency and mobility,  $\text{ZnO}$ -based devices perform lower than the  $\text{TiO}_2$ -based devices, as a result of the higher recombination. Moreover, these two types of devices present, due to their different light absorption characteristics, a different behavior in terms of filtering effect, trap filling effect, and illumination stability.

Furthermore, ordered  $\text{ZnO}$  nanowires (NW) obtained via a hydrothermal method were used in hybrid solar cells to provide pathways for charge collection. Compared to the flat  $\text{ZnO}$ -based device,  $\text{ZnO}$  NW solar cells show exceptional high efficiency with a value improved from 1.91% up to 2.23%, due to the enhanced absorption and the reduced recombination. Charge recombination is further reduced by coating a thin layer of N-doped  $\text{ZnO}$  on NW. With efficiency increase two fold in comparison to the uncoated device, this type of device offers an opportunity towards the promising photovoltaic performance.

## Zusammenfassung

Während der letzten Jahre rücken organische Solarzellen mehr und mehr in den Fokus des Forschungsinteresses, vor allem, nachdem sich die erzielten Wirkungsgrade immer mehr denen klassischer Siliziumsolarzellen annähern. Ein großer Vorteil organische Solarzellen gegenüber klassischer Photovoltaik sind außerdem die vergleichsweise niedrigen Produktionskosten. Die zusätzliche Verwendung von Metalloxiden in sogenannten Hybridsolarzellen stellt eine vielversprechende Möglichkeit dar, um den Wirkungsgrad organischer Solarzellen weiter zu erhöhen, da Exzitonen effizienter getrennt und Ladungsträger besser transportiert werden können. Die vorliegende Arbeit behandelt  $\text{TiO}_2$  und  $\text{ZnO}$  als elektronenselektive Kontakte in derartigen Hybridsolarzellen.

Zunächst wird die Optimierung des Herstellungsprozesses von Hybridsolarzellen diskutiert. Ansätze wie Oberflächenbehandlung und Dotierung von  $\text{TiO}_2$  und  $\text{ZnO}$ , Einfluss des Lösungsmittels auf die photoaktive Schicht sowie die Verwendung von PEDOT:PSS als lochselektive Beschichtung unter dem Silberrückseitenkontakt werden beschrieben. Nur für ein ausbalanciertes Zusammenspiel dieser verschiedenen Prozessierungsschritte können hohe Wirkungsgrade und gut funktionierende Solarzellen hergestellt werden.

Die Arbeit beschäftigt sich außerdem mit einem direkten Vergleich von  $\text{ZnO}$  und  $\text{TiO}_2$  als elektronenselektiver Kontakt in Hybridsolarzellen. Trotz vorteilhafter Oberflächenbeschaffenheit, höherer Elektronenmobilität und besserer Transparenz für sichtbares Licht sind Solarzellen mit  $\text{ZnO}$ -Schichten denen mit optimierten  $\text{TiO}_2$ -Schichten unterlegen, da Ladungsträgerrekombination durch letztere nachhaltiger unterdrückt werden kann. Interessante Unterschiede ergeben sich auch im Bereich von Lichtabsorption und -filterung, Effekten durch Elektronen-Fallenzustände und für die Lebensdauer von Solarzellen unter Beleuchtung.

Der letzte Teil der Arbeit beschreibt Hybridsolarzellen, in denen  $\text{ZnO}$  Nanodrähte zum Einsatz kommen. Diese Nanodrähte können durch hydrothermales Wachstum hergestellt werden und ermöglichen einen gerichteten Transport von Ladungsträgern. Der Wirkungsgrad von Hybridsolarzellen kann von 1.91% auf 2.23% gesteigert werden, wenn nanostrukturiertes



ZnO anstelle von flachen ZnO-Schichten verwendet wird. Zusätzlich wird gezeigt, dass Ladungsträgerrekombination durch Aufbringen einer dünnen Schicht von stickstoffdotiertem ZnO auf die Nanowires verringert werden kann. Somit kann ein Effizienzgewinn um einen Faktor 2 erreicht werden, was das große Potential dieser Materialkombination unterstreicht.



## List of Abbreviations

AALD	Atmospheric atomic layer deposition
$\eta$ & PCE	Power conversion efficiency
AFM	Atomic force microscopy
Ag	Silver
Al	Aluminium
Au	Gold
CBZ	Chlorobenzene
CF	Chloroform
$\epsilon_0$	Permittivity of free space
$\epsilon$	Dielectric constant
$E_g$	Bandgap energy
EtOH	Ethanol
EQE	External quantum efficiency
FF	Fill factor
H <sub>2</sub> O	Water
HOMO	Highest occupied molecular orbital
HMT	Hexamethylenetetramine
HT	Hydrothermal
IQE	Internal quantum efficiency
IS	Impedance spectroscopy
$I_{sc}$	Short circuit current
ITO	Indium tin oxide
I-V	Photocurrent-voltage
$k_B$	Boltzmann's constant
$L_D$	Exciton diffusion length
LiF	Lithium fluoride
LUMO	Lowest unoccupied molecular orbital
MPP	Maximum power point
N <sub>2</sub>	Nitrogen

NW	Nanowires
O <sub>2</sub>	Oxygen
OPV	Organic photovoltaic device
P3HT	Poly (3-hexylthiophene)
PCBM	[6,6]-phenyl-C61-butyric acid methyl ester
PEDOT:PSS	Photoluminescence
PL	Poly(3,4-ethylene-dioxythiophene) poly (styrenesulfonate)
SEM	Scanning electron microscopy
R	Recombination rate
R <sub>S</sub>	Series resistance
R <sub>Sh</sub>	Shunt resistance
t <sub>del</sub>	Delay time
T <sub>g</sub>	Glass transition temperature
TiO <sub>2</sub>	Titanium dioxide
V <sub>oc</sub>	Open circuit voltage
WO <sub>3</sub>	Tungsten oxide
XPS	X-ray photoelectron spectroscopy
XRD	X-ray diffraction
ZnO	Zinc oxide
Zn(NO <sub>3</sub> ) <sub>2</sub>	Zinc nitrate hexahydrate

---

# 1 Introduction

Today, the increasing energy consumption and the fossil resources shortage of in the world are forcing to look for sustainable and renewable power sources. Solar radiation with the abundant magnitude of usable energy ( $\sim 10^{15}$  J) on the Earth [1], is considered to be one of the most promising alternatives to the traditional energy. An analysis recently conducted by the German Advisory Council on Global Change (WBGU) points that a major contribution (about 70%) of the global energy needs to the year 2100 will be provided by the solar thermal and photovoltaic means [2].

A lot of researches have been conducted on the investigation of photovoltaic technologies, with the aim to converse the energy from solar light to electricity. However, comparing with the traditional energy sources, the high costs of photovoltaic devices still limit their wide applications. The organic photovoltaic devices (OPVs) have drawn an increasing interest of the considering the great potential of low production costs. An OPV is a photovoltaic solar cell that uses organic electronics—a branch of electronics that deals with conductive organic polymers or small organic molecules for light absorption and charge transport [3]. The deposition of organics by techniques such as screen printing, doctor blading, inkjet printing, spray deposition, and thermal evaporation, lends itself to incorporation in high-throughput roll-to-roll coating systems [4], which can efficiently reduce the cost of the application.

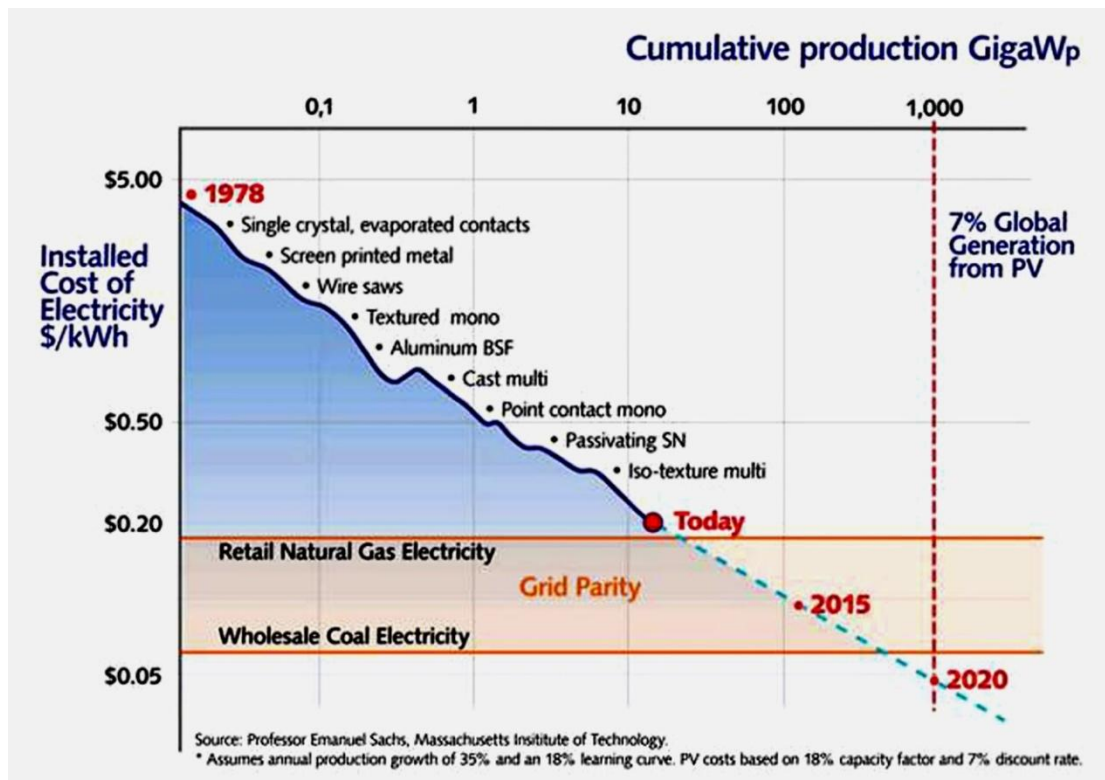


Figure 1.1: The forecast for the cost of electricity provide by photovoltaic device [5]. By the year of 2020, electricity provide by photovoltaic device will lower than the other type of energy source.

Besides the low-cost, OPVs have many other attractive features listed as below [6]:

1. feasible for large area deposition,
2. easy integration in different devices,
3. potential to be flexible and semitransparent,
4. potential to be manufactured in a continuous printing process,
5. environmental friendly and economic advantages.

All of these advantages make OPVs to be a competitive power supply for commercial use, and possible to realize a technologically worldwide application in the future.

## 1.1 Solar cells working principles

### 1.1.1 Organic photovoltaic materials

Organic photovoltaic materials generally exhibit an alternating single bond–double bond structure (conjugated structure) based on  $sp^2$ -hybridized carbon atoms. The  $\pi$ - $\pi^*$  transitions between the bonding and anti-bonding  $p_z$  orbitals provide two energy states for the electrons to reside. These orbitals are commonly referred to as the highest occupied molecular orbital (HOMO) and the lowest unoccupied molecular orbital (LUMO) respectively, corresponding in semiconductors to valence and conduction bands. The position and separation of them can be tuned by altering the molecular structure of the organic semiconductor.

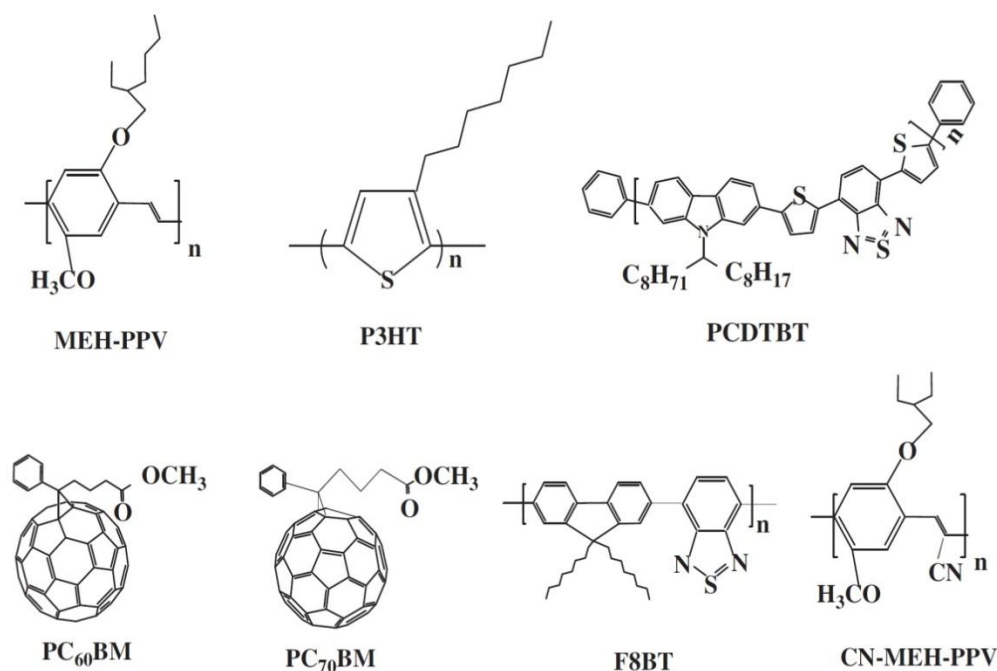


**Figure 1.2: Several representatives of organic photovoltaic materials [6].**

MEH-PPV: poly[2-methoxy-5-(2'-ethyl-hexyloxy)-1,4-phenylene vinylene]; P3HT: poly(3-hexylthiophene)

PCDTBT: poly[N-9'-hepta-decanyl-2,7-carbazole-alt-5,5-(4',7'-di-thienyl-2',3'-b3nzothiadiazole)

PC<sub>60</sub>BM: 6,6-phenyl-C61-butyric acid methyl ester; PC<sub>70</sub>BM: 6,6-phenyl-C71-butyric acid methyl ester

F8BT: poly(9,9'-dioctylfluorene-co-bis-N,N'-(4-butylphenyl)-bis-N,N'-phenyl-1,4-phenylenediamine

CN-MEH-PPV: poly-[2-methoxy-5,2'-ethylhexyloxy]-1,4-(1-cyano vinylene)-phenylene

The energy difference between the HOMO and LUMO is referred as  $E_g$ , which is corresponding to the bandgap of inorganic semiconductors. As electrons in these orbitals become delocalized, it enables both absorption within the visible light region and electrical charge transport—two requirements that need to be met by semiconductors for power generation in solar cells [7]. The optical energy differences of most conjugated polymers are around 2 eV, which limit the optical absorption of the solar spectrum below 650 nm. On the other hand the silicon bandgap is fairly small ( $\sim 1.1$  eV) and it can utilize the portion of spectrum up to 1100 nm.

New organic conjugation materials with small energy difference between the HOMO and LUMO are required in the future to extend the absorption spectra. On the other hand, the absorption coefficients are comparatively high ( $\sim 10^5$  cm<sup>-1</sup>) and allow for efficient absorption in very thin active layers [7]. This can not only reduce the cost of manufacturing, but also provide a possibility for ultra-light production beneficial for customer usage.

### 1.1.2 Donor-acceptor concept

A typical OPVs architecture is an organic material sandwiched between a transparent electrode and a reflecting metallic electrode. Since the light absorption, exciton separation and charge transport all occur in the organic layer, this type of devices commonly exhibit very low efficiency, due to the poor exciton dissociation.

To improve this architecture, a second organic or inorganic material is added in the original material to dissociate the excitons. In this so-called heterojunction, an electron donor material and an electron acceptor material are brought together, with HOMO and LUMO energy levels offset matching each other. As shown in Figure 1.3, after excitons are dissociated into a geminate charge pair on the interface, electron transfer from the donor to the acceptor and hole transfer from the acceptor to the donor, respectively. In the year 1992, Sariciftci et al. found that ultrafast electron transfer takes place from a conjugated polymer to C<sub>60</sub> fullerene, showing the great potential of fullerenes as acceptor materials [8]. Besides the efficient charge transport, this type of device can also be beneficial regarding the broadened absorption spectra by using two materials absorbing different parts of the solar spectrum.



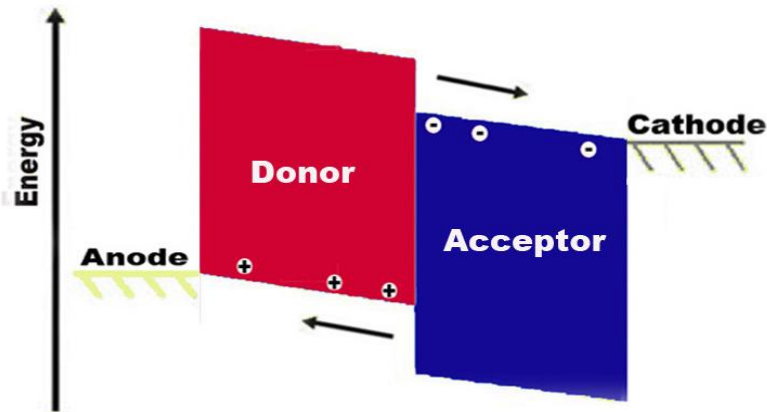


**Figure 1.3:** Schematic representation of the device with electron donor and acceptor materials under operating conditions. After charge separation, the electron and hole are transported through the respective materials and collected by the electrodes.

### 1.1.3 Charge generation

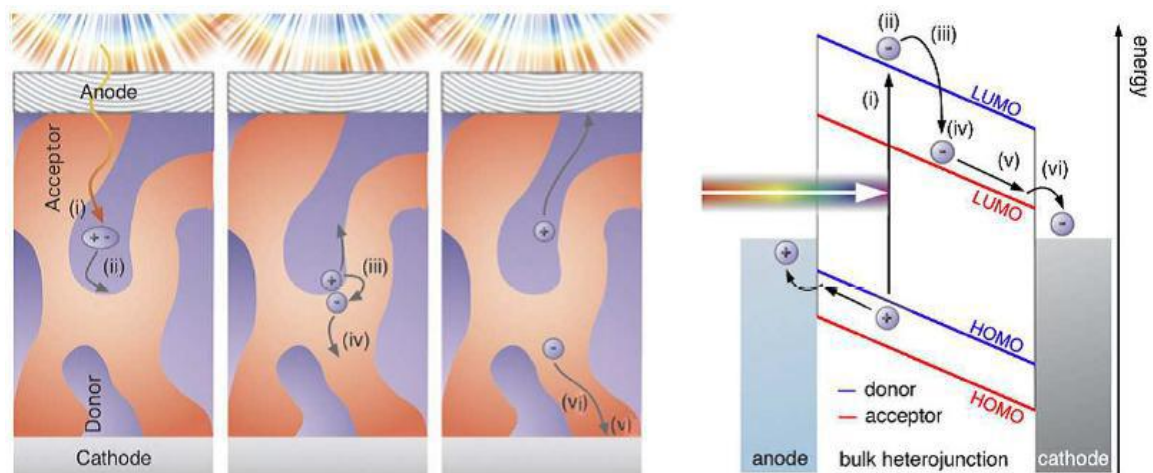


**Figure 1.4:** The schematic of Photocurrent generation mechanism in bulk heterojunction devices [9].

(i) Exciton generation arising from the absorption of a photon. (ii) Exciton diffusion to a donor-acceptor interface. (iii) The separation of the charge pair. (iv) Charge transport to the respective electrodes. (v) Charge collection. These processes are illustrated according to (left) the spatial location at which they occur and (right) on a simplified energy diagram.

The process of charge separation in solar cells, shown in Figure 1.4, generally consists of the following steps: (i) an exciton (electron-hole pair) is generated due to photon absorption in the donor. (ii) It diffuses through the organic material to the donor-acceptor interface within its lifetime. (iii) The bound electron-hole pair separates into free charge carriers. (iv) Electron and hole transfer through the organic materials to the contacts interface. (v) Finally, photocurrent is generated when the charge carriers reach the outer contacts.

### Photon absorption

The Air Mass 1.5 Global ( $1000 \text{ W m}^{-2}$ , AM1.5G) solar spectrum is used as the terrestrial reference spectra for photovoltaic performance evaluation. It can be easily converted to spectral photon flux density (in units of  $\text{photons m}^{-2} \text{ s}^{-1} \text{ nm}^{-1}$ ), as shown in Figure 1.5.

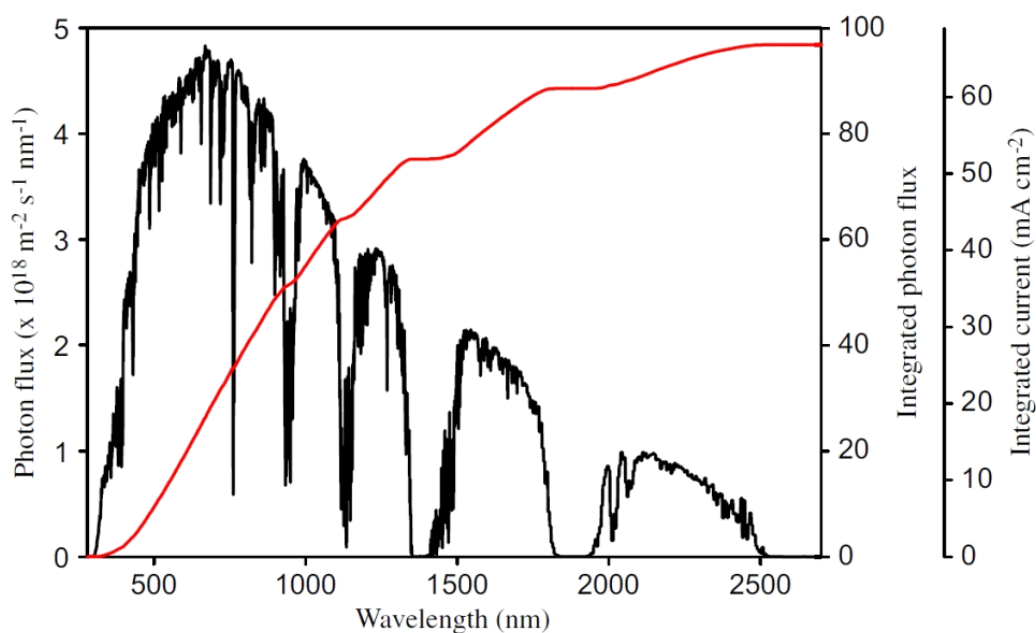


**Figure 1.5: Photon flux from the sun at the earth's surface ( $1000 \text{ W m}^{-2}$ , AM1.5G) as a function of wavelength.** The integral of the curve is shown on the right y-axis as a percentage of the total number of photons and as the obtainable short circuit current density for an absorber material with a step function absorbance at that wavelength [10].

Light absorption is a critical step for the efficiency of solar cell. Organics are attractive because of their high absorption coefficients, with a maximum value around  $\sim 2 \times 10^5/\text{cm}$  depending on the synthesis and materials. Since the absorption is not complete when the peak absorbs less than 90% of the light, organic solar cells could ideally be engineered to absorb nearly all light, as efficient as inorganic solar cells. The light absorption of an OPV can be increased by increasing the thickness of the organic film, as well as by broadening the spectrum. Future work should also evolve to minimize by light trapping, anti-reflective coatings, or surface texturing method [10].

Another obvious route to maximize the light absorption is the materials design to extend the conjugation and minimize bond-length [11]. This can lower the bandgap to more effectively cover the solar spectrum and to increase the maximum photocurrent [12]. The excellent design and synthesis of low bandgap organic materials have been reported recently, showing the absorption wavelength as low as 1000 nm [13].

### **Exciton diffusion and separation**

The absorbed photon can excite electron from the HOMO to the LUMO in the solar cells, thus exciton is generated in the organic conjugation materials. These photo generated excitons must transport to the donor-acceptor interface within its lifetime with a scale of nanoseconds, [14] which is usually described as diffusion process. Excitons are driven by progressively lower energy to travel along a conjugated chain segment for a certain distance before it recombined. This so called exciton diffusion length is defined for the exciton migration as:

$$L_D = \sqrt{D \times \tau} \quad (1.1)$$

Where  $D$  is the exciton diffusivity and  $\tau$  is the natural lifetime of the exciton. The exciton diffusion length ( $L_D$ ) is commonly much lower than the optical absorption length of organic materials  $1/\alpha$  [15]. For example, the reported diffusion length in P3HT is around 20 nm [16], while it is used as a photoactive material in polymer solar cells usually with a thickness around 100 nm for only 60% light intensity absorption [17]. In order to maximize the efficiency of exciton diffusion, bulk heterojunctions with a large interfacial area are commonly used to reduce the distance for the exciton to travel [18].

In order to separate the exciton into free charge carriers, excess energy is required to overcome the Coulombic attraction, which is typically large in organic semiconductors due to their low dielectric constants [19]. Therefore the exciton with a strong binding energy ( $\sim 0.1-1.0$  eV) can usually not be dissociated by the thermal activation energy at room temperature ( $k_B T \sim 0.025$  eV) alone [20]. At the heterojunction in the organic materials, there is a potential drop that compensates for the binding energy of the bound state, and it allows for separation of the exciton.

### **Charge carrier transport**

Following separation of an exciton into free charge carriers, the resulting holes and electrons have to travel along the conducting organic materials to the external contacts of the device. The charge transport efficiency is typically quantified by the material mobility  $\mu$ , which is defined as the average particle velocity in response to an electric force per unit electric field (E) [21].

Due to the lack of long-range order in organic materials, charges must move between localized states on neighboring molecules, referred as hopping transport. Therefore a continuous pathway is required in each conducting material to transport the separated charge to the contacts. The relationship between  $\mu$ , E and the charge-carrier transport length  $L_{e,h}$  is defined as:

$$L_{e,h} = \mu_{e,h} \tau_{e,h} E \quad (1.2)$$

Where  $\tau_{e,h}$  is the carrier lifetime. The values of  $L_h = 90$  nm in P3HT is reported from experimental measurements for P3HT:PCBM solar cells. It could be the main limitation for the active layer thickness [22], which is typically around 100 nm observed for the optimized devices.

#### **1.1.4 Morphology in organic solar cells**

The performance of organic solar cells is not only determined by the electrical properties of the pristine organic compounds but also significantly depends on the microscopic morphology of the active layer [23]. Due to the short diffusion lengths in organic semiconductors, excitons generated beyond this distance from the organic heterojunction will recombine before travel-

ing to the interface, instead of being separated into free charge carrier. On the other hand, a commonly used organic layer thickness is in the range of hundreds of nanometers, in order to achieve substantial light harvesting. Therefore, the interface optimization of the heterojunction in devices can determine the mechanisms of exciton separation and charge carrier transport, and benefit the performance of device.

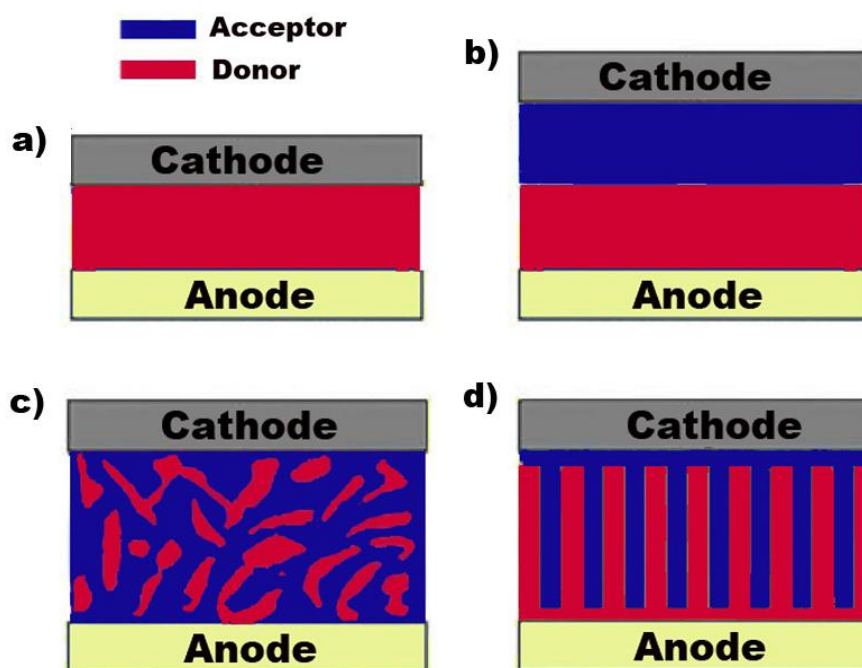


**Figure 1.6: Architectures of typical organic solar cells:** a) Monolayer device, b) Planar heterojunction device, c) Bulk heterojunction device, and d) Ordered bulk heterojunction device.

### Monolayer devices

The first generation of OPVs were based on single organic layers sandwiched between two metal electrodes of different work functions [24]. The rectifying behavior of single layer devices was attributed to the asymmetry in the electron and hole injection into the molecular  $\pi^*$  and  $\pi$ -orbitals, respectively, and to the formation of a Schottky-barrier between the p-type (hole conducting) organic layer and the metal with the lower work function [25]. This type of devices commonly exhibited generally poor performance due to the low exciton dissociation.

### **Planar heterojunction devices**

Compared to the single layer devices, the performance of planar heterojunction devices is significantly improved [26]. This type of device was first reported by Tang, who used two different materials stacked in layers [27]. By adding another layer of organic material into the system as an acceptor, it can efficiently enhance the dissociation of the excitons, however this improvement on the device performance is still low. The primary reason for this is low exciton harvesting, since excitons typically migrate distances of only 3–8 nm before decaying [28]. Most of the excitons generated away from the interface beyond this distance recombine before they reach the interface and dissociate. Thus only less than half of the incident photons are absorbed and ultimately converted to free electrons and holes. These devices have attained quantum efficiencies as high as 60% [18] and power conversion efficiencies of over 3% [16].

### **Bulk heterojunction devices**

By blending donor and acceptor materials on a nanometer scale (about 10 nm), their interface is significantly enlarged and well distributed throughout the device, which can ensure the quantitative dissociation of the photogenerated excitons. This so called bulk heterojunction in organic solar cells commonly uses a mixture of polymer and fullerene as donor and acceptor molecules, respectively. Due to the ease of electron transfer and the efficient exciton separation, a remarkable value over 5% has been reported for the power conversion efficiencies (PCE) of this type of device, using bulk heterojunction of poly-3-hexyl-thiophene (P3HT) and [6,6]-phenyl-C60-butyric acid methyl ester (PCBM) [29]. However, this configuration still suffers from poor charge collection efficiency, resulting from the inherently random interpenetrating network morphology and the segregation of the donor and acceptor type phases. It leads to non-continuous pathways for the electron transport that can effectively trap the charge carriers [30]. Additionally, the poor collection efficiency also limits light harvesting by placing constraints on the thickness of the active layer.

### **Ordered bulk heterojunction devices**

In the ordered heterojunction, the ideally interdigitated interfaces on a nanometer scale donor and acceptor materials are well separated and directly contact to their respective electrodes.

This morphology can dramatically enhance the exciton separation rate due to the large interfaces with a space close to the diffusion length. It also provides a fast pathway for the separated electrons and holes to travel along appropriate conducting materials to the respective electrodes. Therefore, in ideal case photon absorption and exciton generation will become decoupled and the charge separation bottleneck can be overcome. However, this ordered heterojunction is still limited by the poor hole mobility in the polymer, leading to recombination of holes with electrons in the inorganic semiconductor. Since the typical range of exciton diffusion lengths in organic materials is below 20 nm, the spacing between the nanostructures is typically chosen to that value to promote charge separation. At this scale, it is commonly not easy to fill the organic materials completely into the mesoporous structure. Therefore the performance of device will be significantly influenced by the inadequate infiltration.

### 1.1.5 Recombination mechanisms

There are two main charge recombination mechanisms, the space charge and the bimolecular recombination. They present in organic photovoltaic devices that can limit the performance as good as those seen in inorganic solar cells. [31]

#### Space charge recombination

Space charge is induced by the mismatch in carrier mobilities. It leads to a redistribution of the electric field and hinders the electron-hole dissociation and the charge collection. The space-charge limited photocurrent for a bulk heterojunction is given by [31]:

$$J_{\text{SCLPC}} = e (9\epsilon_0 \epsilon \mu_{\text{low}}/8e)^{1/4} G^{3/4} V^{1/2} \quad (1.3)$$

Where  $\mu_{\text{low}}$  is the lower of the two carrier mobilities,  $\epsilon_0$  is the permittivity of free space,  $\epsilon$  is the dielectric constant of the medium,  $G$  is the generation rate of charge pairs,  $e$  is the electron charge, and  $V$  is the internal voltage of the cell. It is reported for polymer:PCBM devices that the space-charge limited photocurrent in blends with a mismatch in mobilities as high as 2–3 orders of magnitude difference [32]. The photocurrent of many polymer/PCBM cells linearly depends on light intensity at strong reverse bias the saturation regime [33]. As a result, the efficiency is limited by space charge recombination. Therefore, it is important to balance the

mobilities in the device to prevent the generation of space charge.

For the planar heterojunction, since the charge separation occurs on the interface of the two layers, the net charge stays on either side of the junction. Without diffusion, the photocurrent limited by space-charge should simply follow Child's law [31]:

$$J_{SCLC} = 9/8 \epsilon \epsilon_0 \mu_{low} V^2 L_{low}^{-3} \quad (1.4)$$

Where  $\mu_{low}$  and  $L_{low}$  are the mobility and the layer thickness of the low mobility material, respectively. In this case, space charge can become a problem even if the mobilities are matched.

### **Bimolecular recombination**

For the bulk heterojunction with matched mobilities and the planar heterojunctions with mobilities high enough, the charge carriers can be lost through bimolecular recombination. It involves non-geminate electrons that recombine with holes as the carriers travelling through the device to their respective electrodes. Usually in organics with electron density ( $n$ ) and hole density ( $p$ ), the recombination rate ( $R$ ) is given by [31]:

$$R = -\beta n p \quad (1.5)$$

Where  $\beta$  is the fitting parameter. Since the effects of space charge are the main limitation of organic bulk heterojunctions, the bimolecular recombination seems to be less important in this type of architectures. However, as these devices have more efficient geminate separation by choosing materials of high and matched mobilities, it is very useful to understand role of morphology and geometry of bulk heterojunctions on recombination. The bimolecular recombination in most organic cells appears to follow Langevin-like kinetics [34]. In this case,  $\beta$  is given as:

$$\beta = (\mu_h + \mu_e)/e \epsilon_0 \epsilon \quad (1.6)$$

Langevin recombination rate is limited by the rate an electron and hole meet. Recently, a deviation from Langevin kinetics in bulk heterojunction cells was reported [35] and explained that the recombination rate is limited by the slowest carrier, rather than the fastest as above,



because the carriers are confined to their own phases—electrons in fullerene and holes in polymer.

## 1.2 The performance of OPVs

As shown in Figure 1.7, a critical triangle of all requirements, the efficiency, stability and costs, for photovoltaic devices have to fulfill simultaneously, otherwise they will be limited to a niche market[6, 36]. Although efficiencies of these OPVs have not yet reached those of their inorganic counterparts (20%), the perspective of cheap production drives the development of organic photovoltaic devices further in a dynamic way. In the last decade, it has attracted more scientific and economic interest triggered by a rapid increase in power conversion efficiencies [25].

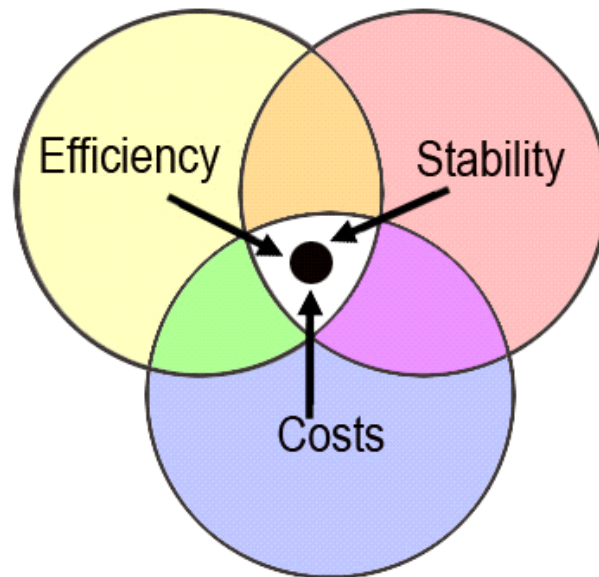


Figure 1.7: The critical triangle for OPVs to fulfill: stability, efficiency, and costs [37].

### 1.2.1 Efficiencies of devices

The efficiencies of a photovoltaic device can be referred as the internal quantum efficiency (IQE), external quantum efficiency (EQE) and power conversion efficiency (PCE). They are defined as different concepts given as follows :

Internal Quantum Efficiency (IQE) is the ratio of the number of charge carriers collected by the solar cell to the number of photons of a given energy that impinge on the solar cell from outside and are absorbed by the cell.

External Quantum Efficiency (EQE) is the ratio of the number of charge carriers collected by the solar cell to the number of photons of a given energy impinging on the solar cell from outside (i.e. incident photons).

Power Conversion Efficiency (PCE) is a portion in percent of solar power that is converted to electricity by a solar cell with an active surface area.

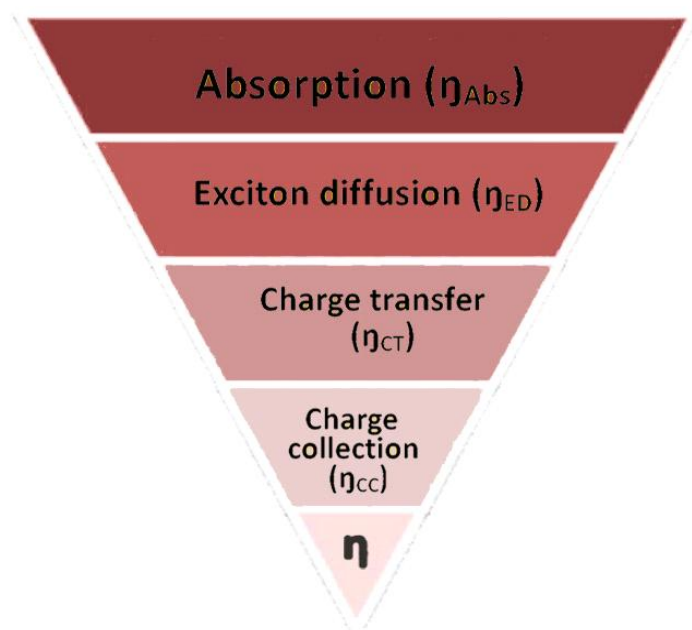


Figure 1.8: The energy conversion process of organic photovoltaic device [38].

PCE is the most important parameter for the determination of a solar cell performance, also known as energy conversion efficiency ( $\eta$ ). A high IQE or EQE does not guarantee good

photovoltaic energy conversion, but it is a prerequisite. To determine the limits to the PCE or  $\eta$  of organic solar cells, the optical-to-electrical conversion process is exhibited in details in Figure 1.8. It is the product of four efficiencies, each corresponding to a step in the charge generation process [38]:

$$\eta_{\text{EQE}} = \eta_{\text{Abs}} \cdot \eta_{\text{ED}} \cdot \eta_{\text{CT}} \cdot \eta_{\text{CC}} \quad (1.7)$$

where  $\eta_{\text{Abs}}$  is the absorption efficiency of light within the active region of the solar cell;  $\eta_{\text{ED}}$  is the exciton diffusion efficiency to a dissociation site;  $\eta_{\text{CT}}$  is the charge transfer efficiency, which is the efficiency for dissociation of an exciton into a free electron and hole pair at that site; and  $\eta_{\text{CC}}$  is the charge collection efficiency. The efficiencies of exciton diffusion and charge collection are the factors that lead to a dependence of photocurrent, whereas absorption and charge transfer are considered to be voltage-independent [39].

For an OPV, the thickness of device is about the average optical absorption length  $L_{\text{Abs}}$ , in order to obtain an absorption efficiency approximately  $\eta_{\text{Abs}} > 50\%$ . On the other hand, the exciton diffusion length is typically an order of magnitude smaller than the  $L_{\text{Abs}}$ . Therefore the majority of photogenerated excitons in single layer devices are lost before separation, resulting in a low  $\eta_{\text{ED}}$  and low power conversion efficiency [40]. Therefore large interface for the majority of excitons dissociation is required to maintain a high  $\eta_{\text{ED}}$ .

However, the electron mobilities of many conjugated polymers are extremely low, typically below  $10^{-4} \text{ cm}^2 \text{ V}^{-1} \text{ s}^{-1}$  [41]. The low charge carrier mobilities can limit the  $\eta_{\text{CT}}$  because the slow movement of charges transport towards the electrodes will enhance the current losses caused by recombination [42]. Therefore, OPVs rely on the introduction of inorganic material, such as high density nanowire arrays, to improve charge conduction.

### 1.2.2 Stability of the devices

Since OPVs have shown great potential for the low-cost manufacture, the other important aspect of device performance identified as the power conversion efficiency is the stability; however, this area has been given relatively little consideration. This section mainly presents the degradation processes occurring in the OPVs, and the methods to enhance the stability are also discussed.

The chemical degradation of OPVs is mainly caused by the oxygen, water and electrode material reacting with the organic materials. During the Nitrogen-free fabrication process of OPVs, it is difficult to avoid introduction of some oxygen and water and their absorption in the different layers. Furthermore, oxygen and water moisture can also diffuse into the device in even greater amounts while the finished OPV is exposed in air [37]. By using  $^{18}\text{O}_2$  and  $\text{H}_2^{18}\text{O}$  to map the reaction products into OPV devices, oxygen/water diffusion process can be detected [43]. It was found that oxygen and water diffuse through the outer electrode (counter electrode to ITO) more than through the sides of the device [44]. It was also reported that ITO can etch the active layers indirectly by observing indium diffusion into the OPV device [45]

Therefore, to use air stable conjugated polymers in the OPVs can limit the chemical degradation by reducing the influences of oxygen and water diffusion. P3HT is one of the examined polymers with superior stability, presumably due to the lack of easily oxidizable vinylene groups. The reaction of P3HT with oxygen has not been investigated clearly yet, however, it was found that as a consequence the carrier mobility and conductance of P3HT films increased dramatically with the oxygen concentration. The formation of charge transfer complexes between oxygen and P3HT is reversible but does not in itself lead to degradation of the polymer [37].

The degradation of the electrode is induced by the reactions between the ITO or unstable metal and oxygen or water respectively. For example, it is well known that aluminum (Al) as a top contact can react with oxygen to form  $\text{Al}_2\text{O}_3$  within several minutes explored in air. The moisture and impurities within the polymer can further enhance ionic conduction and hence accelerate corrosion [46]. This problem can be solved by using a noble metal with a high work-function as top contact, while a metal oxide is introduced in the hybrid solar cells as a charge carrier selective layer and deposited on the other unstable electrode made of ITO.

For the hybrid solar cells using inorganic semiconductor oxides such as titanium dioxide ( $\text{TiO}_2$ ), Zinc oxide ( $\text{ZnO}$ ),  $\text{SnO}_2$ ,  $\text{Nb}_2\text{O}_5$ , and  $\text{CeO}_2$ , the lifetime of devices depends on the presence of oxygen and UV-irradiation in a complicated way. For example, the photocatalytic properties of  $\text{TiO}_2$  can lead to the oxidation of organic materials adsorbed to the surface. Therefore the  $\text{TiO}_2$ -based hybrid solar cells exhibit a competition between the extraction of the charge carriers and the reaction with oxygen and degradation of the organic components, with the presence of oxygen and illumination by sunlight [37]. In addition,  $\text{TiO}_2$  can be excited by UV illumination to photogenerate electron-hole pairs. The electron is very efficiently transferred to bound oxygen ( $\text{O}_2$ ) to generate the superoxide radical anion  $\text{O}^{-2}$ ,

which can deacidize many organic compounds including polymers; the photogenerated holes can react with surface hydroxyl groups to produce  $\text{TiOH}^+$  that again can react and degrade adsorbed organic compounds [37]. As a result of all the effects given above, the hybrid solar cells based on  $\text{TiO}_2$  are often observed device degradation under illumination [47-49]. Since the irradiation with UV-light results in degradation of organic materials, a UV-filter with a cut-off at 400nm improves the stability in hybrid solar cells. A slower decay was observed on the degradation of the polymer due to the usage of a UV-filter for the device based on MDMO-PPV and zinc oxide nanoparticles [50]. Another possible way to improve the stability of  $\text{TiO}_2$ -based OPVs is to use poly(3-carboxythiophene-co-thiophene) (P3CT) as an interface layer between the  $\text{TiO}_2$  electrode and P3HT in a hybrid cell. This P3CT polymer was used to prepare very stable solar cells with a lifetime in excess of 10,000 h under AM1.5G illumination [51], high temperature and with exclusion of oxygen and moisture [45].

As discussed above, oxygen was found to be critical to the performance of the solar cells. On the other hand, the presence of air can significantly influence the photocurrent of hybrid devices using oxides  $\text{TiO}_2$ ,  $\text{Nb}_2\text{O}_5$  or  $\text{ZnO}$  in a bilayer structure with the organic polymer MEH-PPV [52]. A significant short-circuit current ( $I_{\text{SC}}$ ) showed only in the presence of air, and a rapid decrease in  $I_{\text{SC}}$  when the devices were tested in an argon atmosphere or in vacuum. If oxygen was then admitted, partial recovery of solar cell performance was observed [37]. This is corresponding to a later study, using isotopic labeling  $^{18}\text{O}_2$  in hybrid solar cells. It showed that oxygen can diffuse throughout the device and is incorporated in the semiconductor oxide layer ( $\text{Nb}_2\text{O}_5$ ) under illumination [53].

However, the interaction of oxygen in hybrid solar cells is still not clear at present. Taking the  $\text{ZnO}$ -based hybrid cells for example, some results were reported that annealing step in air led to a better device performance [54], while other study achieve the best cell performance operating in the absence of oxygen [55].

### 1.2.3 To improve the performance of devices

In order to improve the performance of organic photovoltaic, the following areas need more attention [56]: (i) low bandgap materials to harvest more of the red and infrared portions of the solar spectrum; (ii) controlled morphology to generate optimal interfacial area for exciton dissociation while maintaining a bicontinuous structure allowing percolation of the separated charges to the collecting electrodes; (iii) new materials with higher charge mobilities; (iv)

ability to tailor the absolute HOMO and LUMO levels to match the donor with acceptor to maximize device efficiencies; and (v) a better understanding of device architecture to optimize light harvesting, electron or hole blocking, and optical spacer layers and minimize device fabrication costs.

To expand the spectral range of absorption, the narrower bandgap materials such as CdSe, PbS and PbSe nanoparticle are used in OPVs as absorber and an electron transporter [57]. These devices achieved high efficiency of 2.6%, almost twice higher than those inorganic components with large energy difference between HOMO and LUMO [58].

The nanostructured ZnO with controllable morphology can be synthesized by a hydrothermal method on conducting glass or plastic substrates, resulting in an enlarged surface area about 10 times of a flat film [59]. As the majority of the exciton dissociation takes place at the P3HT:PCBM interface, the large surface of inorganic phase can favor extra charge carriers separation, which can contribute to the device  $I_{SC}$ .

The materials with high mobilities, such as single-crystalline nanostructured ZnO and InP, are recently used in OPVs to speed the charge transport [60]. With films of P3HT:PCBM, ZnO nanowires device demonstrated higher efficiencies corresponding to longer nanowires, which suggests that the ZnO behaves as a better charge conductor than the PCBM, rather than an interface for charge separation [54].

Since the  $V_{OC}$  of devices depends strongly upon the heterojunction offset, the new materials design is needed to achieve a major improvement upon current systems for enlarging the bandgap which currently limits the  $V_{OC}$  to 0.6 V or less for  $TiO_2$ /P3HT, P3HT/PCBM, and CuPc/ $C_{60}$  systems [40].

Furthermore, OPVs are designed with novel structures to increase the efficiency. For example, the tandem device with double layers of photoactive layer in series can significantly increase the PCE of device nearly twice as much as that of the OPVs with typical structure. By using light trapping and antireflection coatings, EQEs can be increased over the entire absorption range of the organic materials to above 90% [61].  $TiO_2$  layer used as optical spacer can shift the absorption spectra to the maximum energy range, leading to an approximately 50% enhancement in short-circuit [62].

The usage of metal oxides in OPVs seems to be a promising way to improve the charge separation of device by the high conducting properties of the nanowires. It may be the ideal

route to produce the stable, efficient and low-cost OPVs.

### 1.3 Organic photovoltaic devices

Various concepts and device architectures of OPVs have been developed during the last three decades [25]. The first donor-acceptor junction cell was reported in 1986 with power conversion efficiency (PCE) of 1 % [27], while recently laboratory polymer: fullerene bulk hetero-junction devices with efficiency over 8% have been realized. A predicted efficiency beyond 15 % for these novel techniques offers the OPVs potential to compete with inorganic photovoltaic [63], opening up completely new commercial applications for photovoltaics.

#### 1.3.1 Organic solar cells

Organic solar cells are constructed by applying two photoactive organic materials as the electron donor and acceptor respectively, for the photocurrent generation and power conversion process in thin film photovoltaic devices [25]. The well matched energy band offsets of these two photoactive components allow to separate charge efficiently and to convert solar light into electrical energy.

With the advantages of low temperatures fabrication and roll-to-roll printing techniques, this type of solar cells can drive the cost of OPVs down to compete with current grid electricity. Additionally, the low temperature deposition techniques allow the flexible devices to be fabricated on plastic substrates and to offer a decrease in the price of PV panels by reducing installation costs due to the ultra-light weight and large-scale manufacture [64].

As shown in Figure 1.9, the organic photoactive layer is usually sandwiched between a transparent conducting oxide (TCO), e.g. indium tin oxide (ITO) and a metal top contact, e.g. Al for charge carrier collection. When illuminated with sun light, exciton is generated in the photoactive layer and then separated into free charge carriers of electron and hole pair. The electrons and holes are driven by the work function difference of the two electrodes, to transfer through the acceptor and through the donor respectively. Subsequently, photocurrent is generated when the charge carriers reach the electrodes.

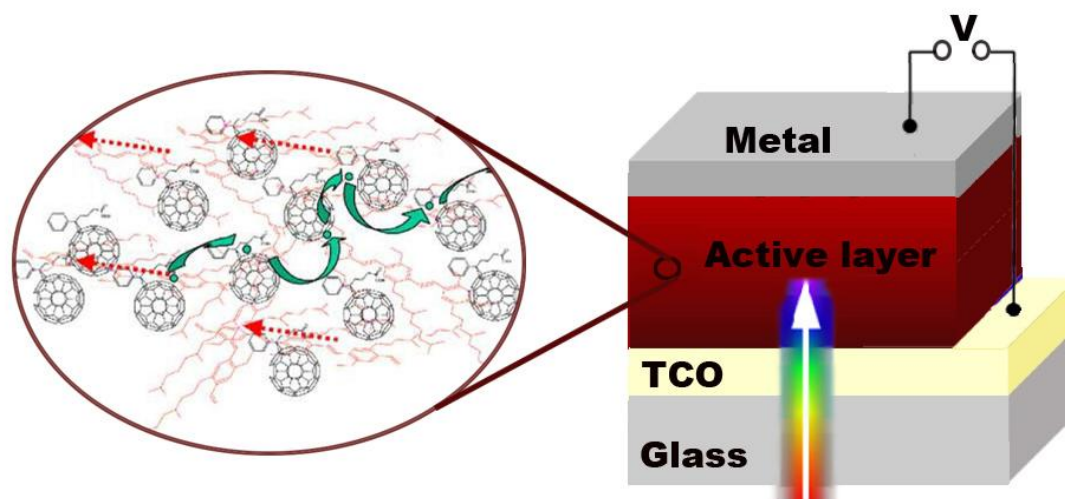


**Figure 1.9: Structure and working principles of an organic solar cell.** (Organic material structures are from [6]) Exciton is generated in photoactive layer when illuminated with sun light, and then it is separated into free charge carriers on the interface of donor and acceptor. When the separated carriers reach the electrodes, photocurrent is generated.

### 1.3.2 Dye-sensitized solar cells

Dye-sensitized solar cell (DSSC) was first reported by Michael Grätzel in the early 1990s using an organic dye as strong absorber in combination with a wide bandgap semiconductor of nanocrystalline morphology to generate free charge carriers under illumination [65]. The schematic of a typical dye-sensitized solar cell, as shown in Figure 1.10, is mainly consisted by the electrolyte, a mesoporous layer of  $\text{TiO}_2$  nanoparticles and a monolayer of dye which is attached to the metal oxide. The dye-sensitized  $\text{TiO}_2$  is in contact with a transparent electrode, commonly using a glass substrate coated with a TCO like fluorine-doped tin oxide (FTO).

The ideal sensitizer should absorb all light below the wavelength of 920 nm and must carry attachment groups such as carboxylate or phosphonate to firmly graft it to the semiconductor oxide surface. Under illumination, the photo-excited dye should inject electrons into the solid with a quantum yield of unity. The energy level of the excited state should be well matched to the lower bound of the conduction band of the  $\text{TiO}_2$  to minimize energetic losses during the electron transfer reaction. After the electron injection into the conduction band of the  $\text{TiO}_2$ , it will be collected at the electrode. Then the dye is regenerated by the surrounding redox electrolyte, which itself is regenerated at the electrode opposing to the  $\text{TiO}_2$  when elec-



trons passed through the load [66]. Accordingly, a photocurrent is generated and a potential between the two electrodes is built.

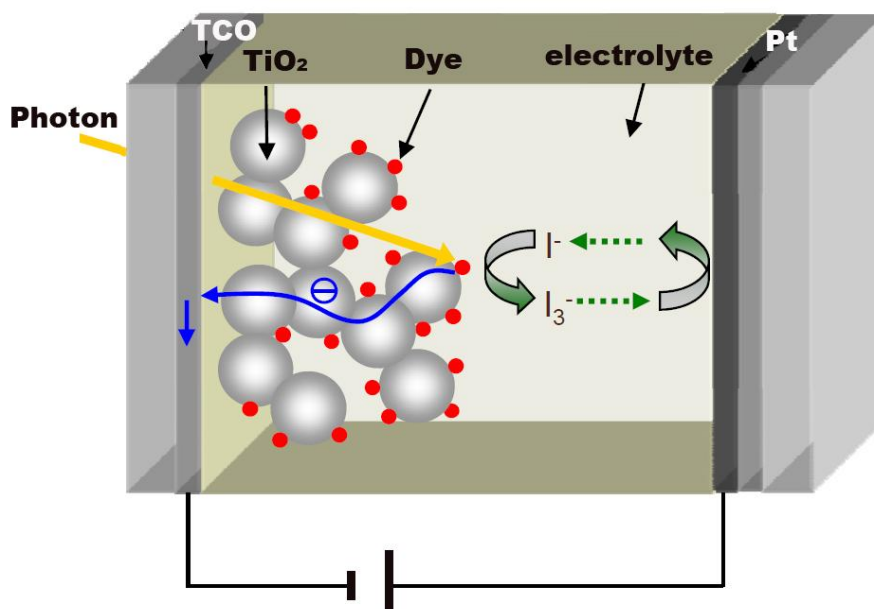


**Figure 1.10: Structure and working principles of a dye-sensitized solar cell (Images courtesy of Dr. F. Fabregat-Santiago).** Monolayers of dye are attached to the surface of mesoporous  $\text{TiO}_2$  layer with strong light absorption. Under illumination, the dye is excited and electrons are transferred to the  $\text{TiO}_2$ , followed by the regeneration of dye caused by the surrounding electrolyte of iodide, which transports electrons from the Pt electrode to the dye.

Further efficiency optimization has been slow down since the dramatic improvement of performance over 10% reported in 2001 [67]. Besides of that, the liquid electrolyte may be the main problem for the application of DSSCs, because it can limit the stability of device due to its evaporation when the cell is imperfectly sealed. Additionally, the diffusion and reaction of water or oxygen molecules can reduce cell performance, and the fabrication process of DSSCs also makes the manufacturing of large scale modules difficult [68]. Meanwhile both the required encapsulation of device and the need for recycling of liquids containing toxic iodine and other additives will worsen the inherent economics of manufacturing and may lead to less widespread customer usage. As a solution of the electrolyte problem, solid-state dye sensitized solar cells have been developed to replace the liquid iodine by solid organic mate-

rials as a hole-conductor [69]. In this way, a solid-state heterojunction of very large contact area can be formed. Furthermore, an approach for the device performance optimization is to substitute the mesoporous  $\text{TiO}_2$  layer by ordered metal oxide nanostructures that allow higher electron mobilities and directed charge transport [70]. However, the efficiencies of these solid-state devices still can't compete with the liquid electrolyte cells at present [71].

### 1.3.3 Hybrid solar cells

A typical hybrid solar cell is consisted by an inorganic material with large surface area and an organic conducting absorber, which can be an organic hole conducting material or a blend of organic electron and hole conductors [72].

Two techniques are used to interface inorganic with organic photovoltaic materials. The first method deposits a suspension of stabilized inorganic nanoparticles or nanorods, in polymer solution (see Figure 1.11a); the second method deposits porous inorganic architectures, subsequently intercalating organic materials [56]. Although the inorganic nanoparticles used in the first method, can be formed in a large range of shapes, sizes and materials [73], which is beneficial to the photovoltaic application because of size-dependent properties resulting from the quantum confinement effects, this type of devices are still limited by the discontinuous charge transport process via hopping of electrons between the nanoparticles [56]. Therefore the nanostructured morphology is required that can provide pathways to transport charge carrier to the electrodes without recombination.

Thus, the metal oxides such as  $\text{ZnO}$  or  $\text{TiO}_2$  with a distinct advantage of controllable nanostructure are commonly used in the hybrid solar cells produced by the second technique [42, 74] (see Figure 1.11b). In this type of solar cells, nanostructured metal oxides are first fabricated via various methods, and then filtered with organic materials [75-77]. Since the mobilities of metal oxides are significantly higher than the organic materials [78], it offers an ultrafast pathway for the charge carrier transport. The charge transport dynamics of devices is further improved by modifying the surface of metal oxides to reduce the charge carrier recombination as well as by controlling the spacing of nanostructures close to the exciton diffusion length [79].

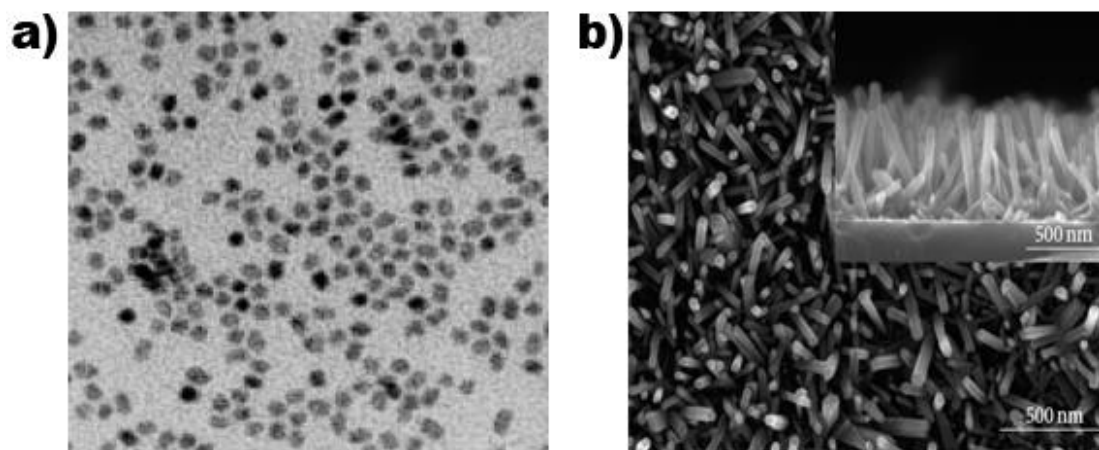


Figure 1.11: Two typical inorganic materials used in hybrid solar cells: a)  $\text{TiO}_2$  nanoparticles [42]; b)  $\text{ZnO}$  nanowires [74].

### Advantage of the hybrid solar cells

The metal oxides are beneficial to hybrid solar cells not only because of its high mobility for a better charge transport, but also due to its various nanostructures applied for the ordered heterojunction, which can efficiently improve the exciton dissociation. Therefore the performance of device can be improved significantly with the application of metal oxides.

As the solar cells have to fulfill all the requirements of a niche market, such as lifetime, efficiency and costs, the hybrid solar cells present remarkable advantages both on the potential of stability and low cost. By using the metal oxides as bottom electrodes, it is possible to use noble metals as top electrodes and to avoid the performance losses caused by oxidation of top contact [80], therefore the air stability of devices can be improved.

Since there is oxygen involved in the fabrication process, and the metal electrode is air stable, nitrogen glove box is not necessary for preparation of the hybrid solar cells. This can dramatically reduce the cost for the large scale manufacture. Additionally, the usage of cheap metal oxides instead of expensive organic conducting materials, can further lower down the price of production.

### **Limitation of hybrid organic solar cells**

The current efficiencies of hybrid solar cells are still not satisfactory, with a highest value of 0.74% reported for ZnO-P3HT bi-layer device [81] and 3-4% for the blend-TiO<sub>2</sub> template device [30]. One reason for the low efficiency is possibly caused by the degradation of the organic components due to the presence of oxygen. It has been reported that UV illumination of TiO<sub>2</sub> powder results in photogeneration of an electron-hole pair with highly oxidizing hole, which can effectively oxidize many organic compounds including polymers. To this end the photogenerated holes can react with surface hydroxyl groups to produce TiOH<sup>+</sup> that again can react and degrade adsorbed organic compounds [82].

Another limitation is attributed to the high temperature condition during the fabrication process, since it is necessary for the metal oxides to be crystalline. As for the TiO<sub>2</sub> film fabrication, a commonly used temperature is 450 °C, which will certainly limit its application on flexible substrates.

### **1.4 Metal oxides in hybrid solar cells**

The low cost of manufacturing is not enough for the OPVs to compete with the traditional devices, and more attention should be paid to the device low efficiencies and poor stability. These two problems can be solved by introducing metal oxides into OPVs, with the expectation to improve both of the performance and the life time of devices. Besides the usage of WO<sub>3</sub>, MoO, V<sub>2</sub>O<sub>5</sub>, etc. as an electron buffer layer to improve the device performance [83], and the insertion of a TiO<sub>x</sub> layer as an optical spacer [62], metal oxides also show attractive potential in DSSC, reaching a measured efficiencies as high as 12.3% [84].

In addition, wide bandgap inorganic semiconductor materials such as TiO<sub>2</sub>, ZnO are commonly applied in hybrid solar cells. In this type of devices, light absorption and exciton generation take place in the organic materials, while the metal oxides are used as an acceptor for electron transport. These hybrid solar cells can benefit both from the high absorption coefficient of polymer in the visible range, and the higher charge carrier mobility of electrons transport of inorganic materials.

### 1.4.1 TiO<sub>2</sub> and ZnO metal oxides

#### TiO<sub>2</sub>

As an attractive n-type semiconductor, TiO<sub>2</sub> shows fundamental and practical advantages [85], and is widely applied in the industry, such as photocatalysts, gas sensors, pigments, cosmetics and solar cell [65, 86, 87]. One dimensional titania nanostructures are even broaden the applications due to their novel properties depending on its crystalline phase state, dimensions and morphology [88].

#### ZnO

ZnO is a remarkable technological material with many attractive properties such as strong piezoelectric and pyroelectric properties, antibacterial property and its bactericidal efficacy [89]. Due to the reduction in size, the one-dimensional ZnO shows novel electrical, mechanical, chemical and optical properties, which are beneficial to be the application of surface acoustic wave filters, photodetectors, light emitting diodes, gas sensors, optical modulator waveguides, and solar cells [90].

Both of TiO<sub>2</sub> and ZnO are used in OPVs because of their similar optical and electrical properties. These two metal oxides are transparent to visible light, due to their respective wide bandgaps of 3.2 eV and 3.37 eV, only absorbing in UV range of solar light. Their high electron affinity, which stems from the position of their conduction bands, allows them to match with the LUMO of almost all organic semiconductors [91]. This high exciton binding energy in TiO<sub>2</sub>/ZnO-organic photovoltaic device allows efficient exciton emission at room temperature.

In additional, the mobility of TiO<sub>2</sub> presents with a range of 20 to 10<sup>-6</sup> cm<sup>2</sup>V<sup>-1</sup>s<sup>-1</sup>, highly depending on its structure [92], and an even higher value of mobility can be obtained by doping ZnO with Al [93]. Since the mobility of metal oxides is much higher than of the organic semiconductor, it provides an ultra-fast pathway for electron transfer and generally improves the charge transport in the devices.

### 1.4.2 Applications in hybrid solar cells

Various approaches have been explored to apply these structured metal oxides in hybrid solar cells with expectation of increasing the efficiencies of devices. The vertically aligned nanostructured oxide has both the advantages of increasing the donor–acceptor interfacial area and creating electron transport pathways toward the negative electrode that possess very high electron mobility [54]. Depending on the architectures of the device, the combination of metal oxides and organic semiconductor can be distinguished as:

- (a) planar structure with active layer coating on metal oxides;
- (b) blending nanoparticles, nanorods, or nanobelts with organic materials;
- (c) infiltrating active layer into nanostructured metal oxides.

As the planar structure of hybrid solar cells are limited by the small interface between the organic and inorganic materials. This can be solved by using an organic donor-acceptor blend coating on flat metal oxides layer. However, the same problem appears in the second structure of hybrid solar cell, which is blending metal nanoparticles with organic materials. It is caused by the random mixture and the non-continuous conducting pathways, which significantly limits the performance of devices. Therefore, a highly ordered nanostructure metal oxides can significantly improve device efficiencies.

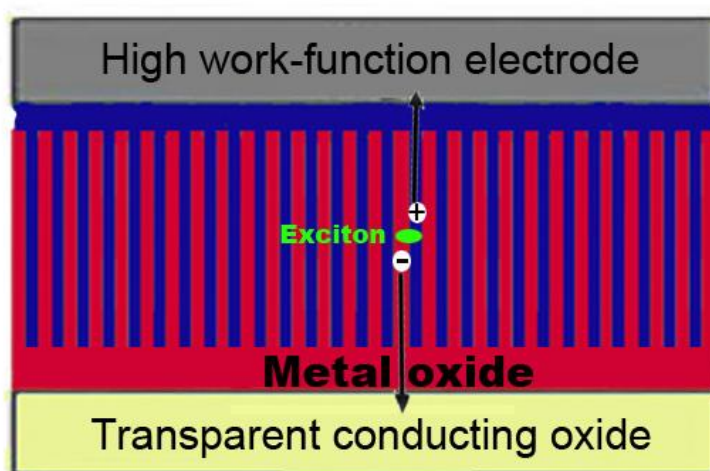
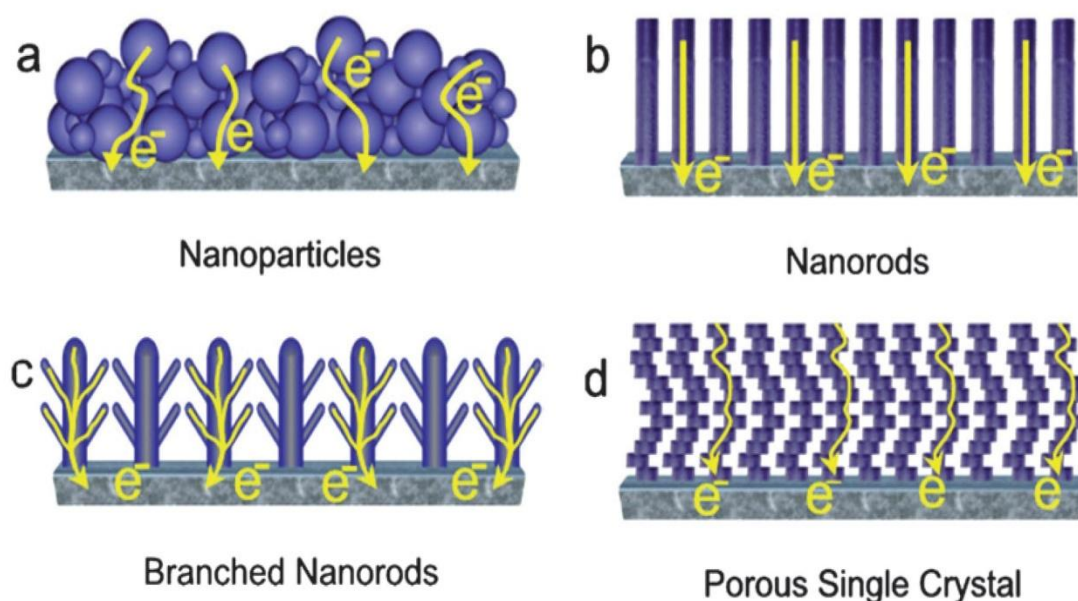


Figure 1.12: Schematic diagram of an ideal nanostructured oxide/conjugated polymer photovoltaic device.

As shown in Figure 1.12, in an ideal nanostructured oxide/conjugated OPV, excitons can diffuse to the donor-acceptor interface within their lifetime, since the size of the inorganic nanostructures is below the exciton diffusion length. Additionally, the separated charge carriers may travel along direct pathways provided by ordered metal oxide, resulting in an efficient charge collection.

### 1.4.3 Nanostructures of metal oxides

There have been numerous reports on the nanostructure design of both  $\text{TiO}_2$  and  $\text{ZnO}$ . Different structures, for example, nanoparticles, nanostructured  $\text{TiO}_2$  templates (nanowire, nanotube and mesoporous substrates) and one-dimensional  $\text{ZnO}$  (nanowires, nanorods, and nanobelts) have been successfully synthesized. With different nanostructures, metal oxides can provide various pathways for electron transport in OPVs, as shown in Figure 1.13.



**Figure 1.13:** Schematic representation of the possible electron path taking place on different nanostructured metal oxides electrodes made with (a) nanoparticles, (b) nanorods, (c) branched nanorods and (d) porous single crystal. Image from [94].

Some of the commonly used synthesis methods for different nanostructures fabrication are listed as follows:

## **TiO<sub>2</sub> nanostructures and synthesis methods**

For the nanostructured TiO<sub>2</sub> fabrication, one of the most widely used methods is template synthesis, which can be classified as Chemical-template assisted synthesis and AAO-template assisted synthesis.

The Chemical- template assisted synthesis, also known as the soft template method, is carried out by controlling the condensation of TiO<sub>2</sub> with the self-assembled template molecules, then selective removal of the templating agent by calcination. It is generally used for the nanorods fabrication, of which different sizes, shapes and aspect ratios can be synthesized with the aid of surfactant [95].

The AAO-template assisted synthesis, also known as the hard template method, is widely used for the high ordered TiO<sub>2</sub> nanowires and nanotubes fabrication. The ordered TiO<sub>2</sub> nanowire arrays can be obtained by electrophoretic deposition of TiO<sub>2</sub> colloidal suspensions into the long pores of an AAO. In a typical procedure, a TiO<sub>2</sub> precursor sol is prepared before the reaction. Platinum is used as the anode, and an AAO with an Au substrate attached to Cu foil is used as the cathode. The TiO<sub>2</sub> sol is deposited into the pores of the AAO under a voltage and annealed. Isolated TiO<sub>2</sub> nanowires can be obtained by dissolving the AAO template in NaOH solution [96].

The internal surface of cylindrical pores of anodic alumina is used for the deposition of TiO<sub>2</sub> thin films from various precursors [88]. The AAO templates were immersed in NaOH solution to broaden the pores. The AAO substrate is infiltrated with a TiO<sub>2</sub> sol-gel precursor solution. After drying at room temperature, the sample was heated in air in order to complete the conversion to crystalline titania. Isolated TiO<sub>2</sub> nanotube arrays were finally obtained after removing the alumina template by etching in NaOH solution [97].

Besides the template synthesis, there are many other methods, such as hydrothermal method and sol-gel method are used for TiO<sub>2</sub> fabrication [85]. Those synthesis processes can not only control the nanostructure of TiO<sub>2</sub>, but also obtain the phase depending on the application requirement.



### **ZnO nanostructures and synthesis methods**

The ZnO nanostructures can be obtained via various synthesis methods, which in general can be classified as gas phase synthesis methods and solution phase synthesis methods.

The gas phase synthesis uses gaseous environment in closed chambers. Normally the synthesis is carried out at high temperatures from 500 °C to 1500 °C. Some of the gas phase methods are commonly used for ZnO nanowire fabrication, such as physical vapor deposition [98], chemical vapor deposition [99], and metal organic chemical vapor deposition (MOCVD) [100].

During the solution phase synthesis, the growth process is carried out in a liquid, below the boiling temperature of this liquid. Normally aqueous solutions are used and the process is then referred to as hydrothermal growth process [101]. This type of synthesis is usually used for ZnO nanorods growth, for example, using sol-gel method driven by zinc acetate hydrate (ZAH) [102], and using spray pyrolysis to obtain ZnO thin films [103]. The most attractive synthesis is ZnO nanowire grown by hydrothermal method due to its non-toxic, low-temperature and easy-controlled properties. This method has been used for the ZnO-based hybrid solar cells and it can provide highly ordered ZnO nanowires that can dramatically enhance the device efficiencies [81]. By controlling the growing process different morphology of ZnO nanowires can be obtained [101].

---

## 2 Experimental Methods

This chapter provides an overview to the experimental methods used for solar cells and material production, as well as the device characterizations and evaluation.

### 2.1 Solar cell architecture

#### 2.1.1 Solar cell design

Organic solar cells are fabricated on ITO coated glass substrates with a size of  $14 \times 14 \text{ mm}^2$  bought from Kintec Technologies GmbH. A 3 mm thin strip of ITO is etched off from one side of the substrates, using a cotton Q-tip with 32% hydrochloric acid solution and Zinc powder. During most of the measurements, solar cells are loaded in a self-designed holder with contact-pins contacting to the individual photoactive pixels. To avoid the short circuits, the strip of ITO in the contact area has to be removed.

ITO substrates are cleaned using a series of ultrasonication treatments: in detergent saturated water, acetone and subsequently isopropyl alcohol baths for 15 minutes each. This is followed by an Oxygen ( $\text{O}_2$ ) plasma cleaning step carried out in a Diener Femto plasma cleaner for 7 min, in order to avoid contamination caused by remaining carbon residues on the surface and to increase the hydrophilicity of the substrates for the organic materials deposition. The active layer are deposited via solution spin coating, followed by the deposition of the metal top contacts via sputter coating or vacuum evaporation. In order to provide direct contact to the

ITO with the bottom contact, the organic layer is removed on the opposing side of the removed ITO side. Additional layers like  $\text{TiO}_2$ , Poly(3,4-ethylene-dioxythiophene) poly(styrenesulfonate) (PEDOT:PSS) or Lithium fluoride (LiF) can be introduced underneath or on top of the organic layer as selective blocking layers or to modify the effective work functions of the contacts.

The cell design is shown in Figure 2.1 as a schematic representation of resulting devices with a top view (a) and a side view (b). Three pixels of solar cell are assembled on the same ITO substrates by the top contact deposition through a patterned shadow mask. Dashed squares mark the active areas with a value of  $0.125\text{cm}^2$  that defined by the shadow mask under illumination for all photoelectrical characterization experiments. The three photoactive pixels are referenced as: Pixel L (left), Pixel M (middle) and Pixel R (right). For solar cell measurements, top and bottom contacts are contacted via gold pins.

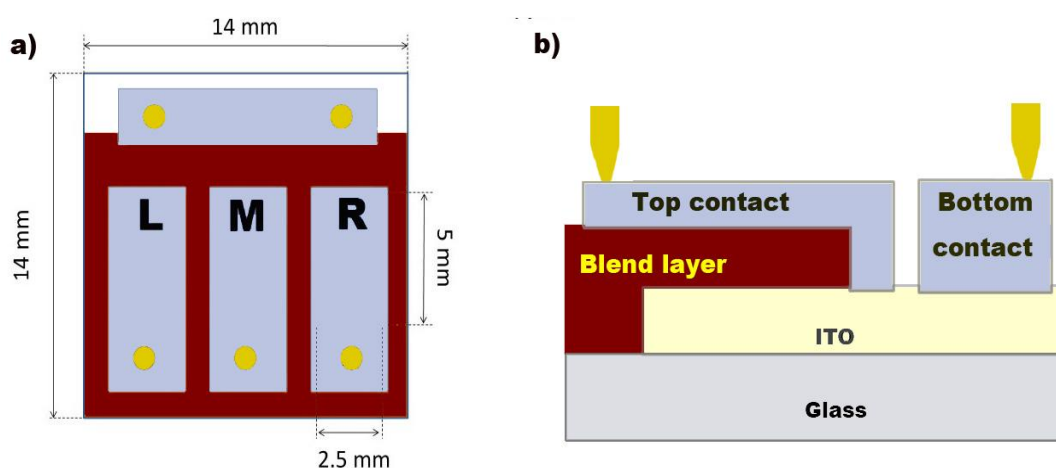


**Figure 2.1: Schematic of the used solar cell design (Images courtesy of J. Weickert).** a) Top view of a solar cell; b) Side view of a solar cell;

### 2.1.2 Non-inverted solar cells

The typical non-inverted solar cell features the following layers:

**ITO/ PEDOT: PSS/ P3HT:PCBM/ LiF/ Al**

The cleaned ITO substrates are coated with a PEDOT:PSS layer, followed by a P3HT:PCBM blend layer deposition by spin coating process. The organic layer is carefully removed from

one side and annealed at 105 °C for 5 min. Then LiF interface layer and Al top contact are deposited via thermal evaporation. All layer fabrication processes will describe in detail in the following sections.

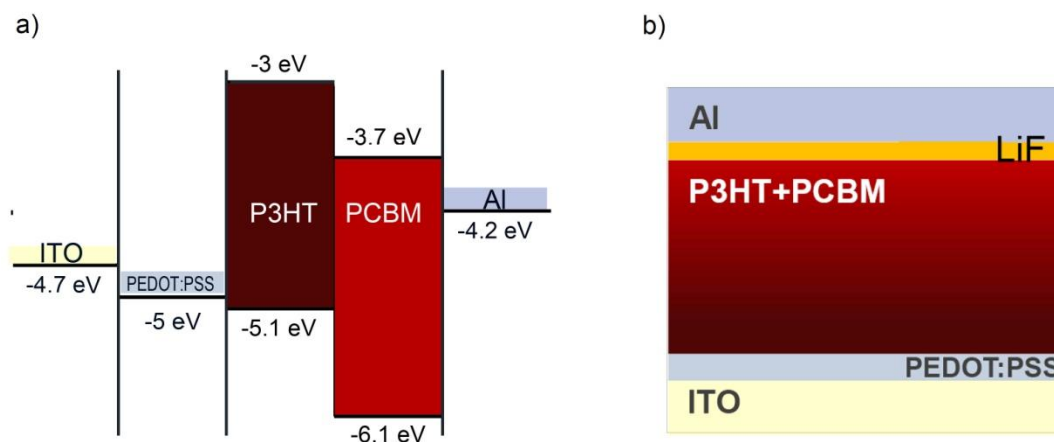


**Figure 2.2: Energy levels and cell geometry for non-inverted P3HT:PCBM cells.** a) Energy level diagram for non-inverted P3HT:PCBM cell [16]. b) Schematic of the geometry of a non-inverted P3HT:PCBM cell.

### 2.1.3 Inverted solar cells

The inverted solar cells are built with a following structure:

**ITO/ Blocking layer/ P3HT:PCBM/ Buffer layer/ Ag,**

A metal oxide film is deposited on cleaned ITO as charge carrier selective blocking layers via different fabrication methods (see section 2.2), such as spray pyrolysis, sol-gel, sputtering and atmospheric atomic layer deposition (AALD). A P3HT:PCBM blend layer is then spin-coated on top of the metal oxide. It is followed by the deposition of a buffer layer via evaporation of  $\text{WO}_3$  or spray coating of PEDOT:PSS layer. Then, a 100 nm Ag layer is deposited as the top contact. The deposition processes of those layers will be described in section 2.2.4 and 2.2.5.

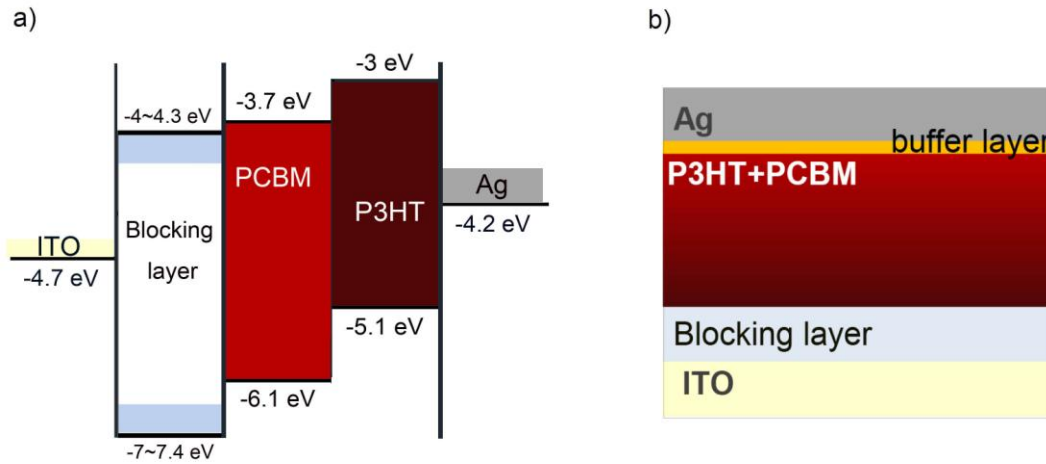


**Figure 2.3: Energy levels and cell geometry for inverted P3HT:PCBM cells.** a) Energy level diagram for inverted P3HT:PCBM cell [104]. b) Schematic of the geometry of an inverted P3HT:PCBM cell.

#### 2.1.4 Inverted-inverted solar cells architecture

The inverted-inverted solar cells are produced with a structure of:

**ITO/ PEDOT: PSS/ P3HT:PCBM/ Blocking layer/ Al**

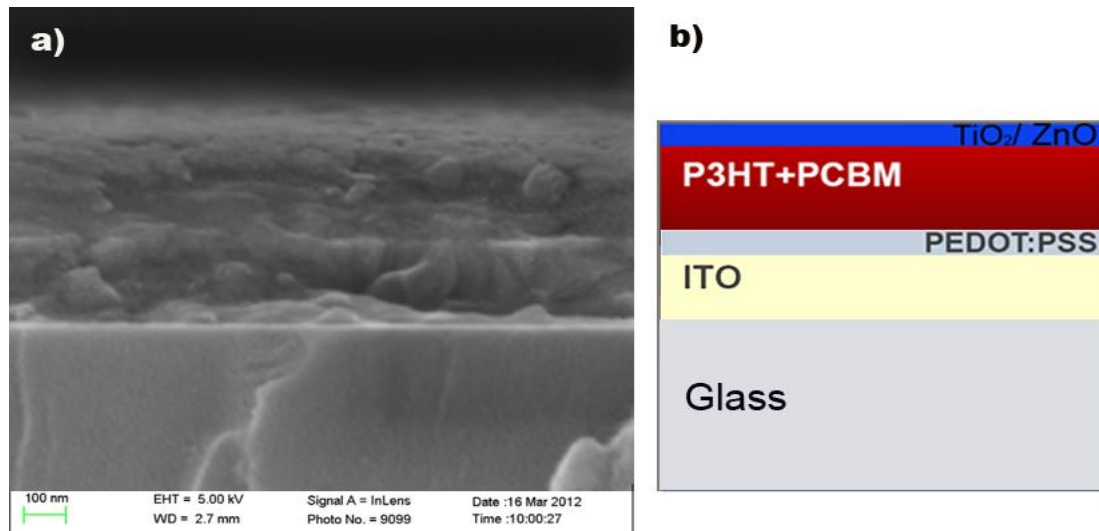


**Figure 2.4: SEM image and structure of inverted-inverted P3HT:PCBM cells.** a) SEM cross-section image of an inverted-inverted P3HT:PCBM device without Al layer. b) Schematic of the structure of an inverted-inverted P3HT:PCBM device without Al layer.

As AALD methods are carried out at low temperature, it allows a thin film of crystallized  $\text{TiO}_2$  or  $\text{ZnO}$  deposited on top of organic film (see section 2.2.2.5 and section 2.2.3.4). This inorganic semiconductor film working as blocking layer is located at the opposite position of the typical inverted device, thus the term of inverted-inverted solar cell. The PEDOT:PSS layer and blend organic layer are deposited with the same process for non-inverted solar cells. After the organic and blocking layers have been removed from one side, a 100 nm Al is evaporated at moderate rates of 1.0-2.5  $\text{\AA}/\text{s}$ . Figure 2.4 shows the side image and the schematic of structure of inverted-inverted P3HT:PCBM device. To present the morphology of  $\text{TiO}_2$  blocking layer, SEM cross-section image is obtained without Al top contact deposition. It can be clearly observed that the blocking layer completely covers the organic layer underneath. Initial results have shown that this type of solar cell exhibits a PCE of around 0.3%. Further experiments are required to optimize the deposition of both blocking layers and organic layers for a better device performance.

### **2.1.5 Flexible devices architecture**

The flexible solar cells are demonstrated with both non-inverted and inverted structures. For such solar cells, additional attention must be paid to the temperature of the fabrication processes, due to the low glass transition temperature ( $T_g$ ) of the plastic substrates. However the inverted device fabricated on flexible ITO is the most attractive design, because this could enable roll-to-roll preparation of solar cells in air, with the expectation of the significant improvement on the device lifetime and the reduced production cost.

The fabrication is similar to the conventional architecture, only with an additional step required for the spin coating process, since the shape of ITO films could change when loaded on the spin coater fixed by vacuum underneath. An additional rigid substrate is necessary to hold the flexible ITO film during spin coating. A polydimethylsiloxane (PDMS) film is used as such a connection between the two layers, which can not only strongly bond the ITO film to the rigid substrate without damaging it, but also be easily removed afterward.

The AALD deposition of  $\text{TiO}_2$  or  $\text{ZnO}$  can be produced at a temperature as low as 100  $^\circ\text{C}$ , which is lower than the  $T_g$  of flexible ITO substrates with a value of 145  $^\circ\text{C}$ . This allows a flexible inverted solar cell fabricated as:  $\text{TiO}_2$  or  $\text{ZnO}$  films deposited via AALD method (see section 2.2.2.2 and section 2.2.3.3) on flexible ITO, followed by a P3HT:PCBM blend layer spin coated on top. Then Ag top contact is evaporated through a shadow mask. Photo image

of device is shown in Figure 2.5b. The initial result of device performance shows a PCE closed to 0.5%, which is promising but still limited by the conductivity of flexible ITO. This type of device can be further improved with better quality ITO substrates and optimized fabrication parameters in the further research.

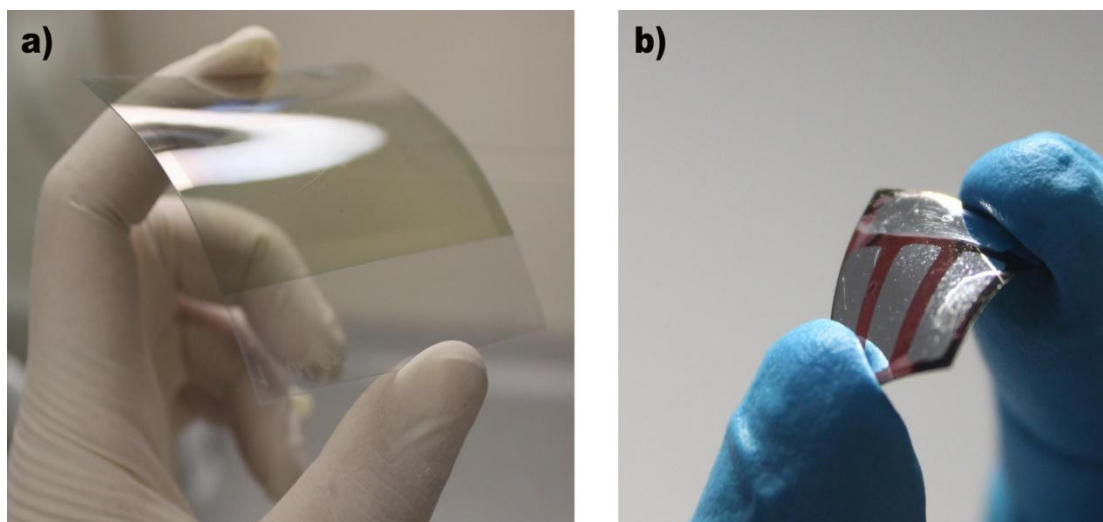


**Figure 2.5: P3HT:PCBM solar cells fabricate on flexible ITO.** Photo images of: a) a flexible ITO coated with  $\text{TiO}_2$  layer; b) a flexible inverted device with a structure of ITO/  $\text{TiO}_2$ / P3HT:PCBM/PEDOT:PSS/Ag.

### 2.1.6 Transparent devices architecture

The transparent solar cells are produced with two transparent electrodes, which are ITO substrates coated with different charge carrier selective layers in this case. Instead of layer by layer deposition for typical organic solar cells, imprinting process is carried out to combine the two substrates together (see Figure 2.6a).

One of the cleaned ITO substrate is used for the bottom contact, with a thin PEDOT:PSS layer and a thick P3HT:PCBM layer spin coated on top. The deposition of PEDOT:PSS and blend layers are the same as the non-inverted solar cell architecture. A strip of organic material is removed to allow a direct contact between the ITO electrode and the measurement electrode. The other cleaned ITO substrate is coated with a nanostructured metal oxide as a hole blocking layer, such as  $\text{TiO}_2$  film by spray pyrolysis (see section 2.2.2.1) or ZnO nanowires grown by hydrothermal method as (see Chapter 5). A strip of ITO is covered during the deposition of the blocking layer to allow electrical contact to the ITO electrode in the finished device.

Then, the second substrate coated with nanostructured  $\text{TiO}_2$  or  $\text{ZnO}$  is imprinted on the first ITO covered with organic materials at  $140\text{ }^\circ\text{C}$  with a pressure of 2 Pa. The imprinting process and the resulting devices are shown in Figure 2.6. During the initial performance test, this transparent device shows a PCE of 1.1%, which is relatively high considering the transmission loss through the device. Further investigation on the light response is limited by the stability of devices. This could be possibly improved by an interface layer deposition between the organic layer and the structured blocking layer.

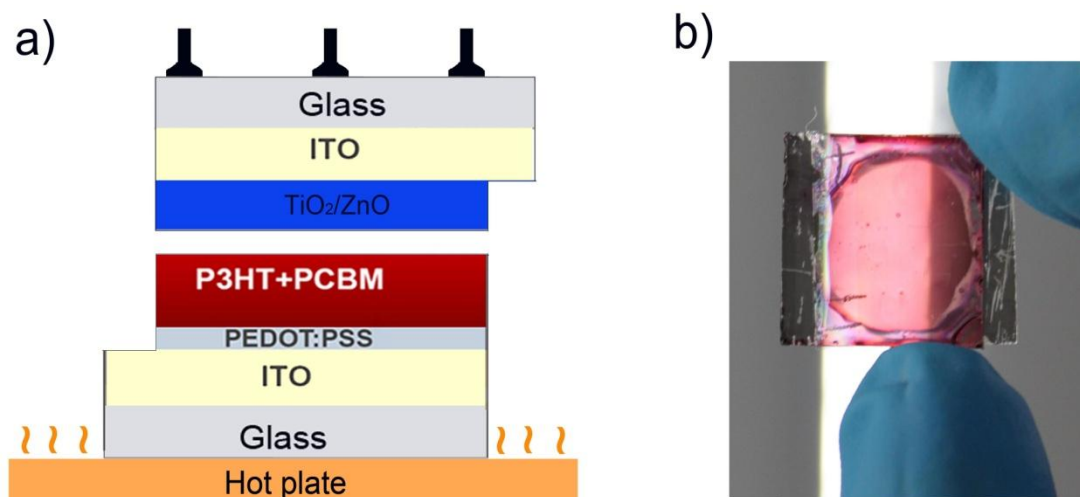


**Figure 2.6: Transparent solar cells fabricated on two ITO substrates.** a) Schematic of the imprinting process for devices fabrication; b) a transparent device with a structure of ITO/  $\text{TiO}_2$ / P3HT:PCBM/ PEDOT:PSS/ ITO.

## 2.2 Materials and fabrication methods

### 2.2.1 Photoactive materials and blend layer

P3HT and PCBM are purchased from Merck and Nano-C, respectively. The blend solution preparation is investigated in details for the influences on device performance in Chapter 3. The process can be briefly described as follows: P3HT and PCBM are dissolved in chlorobenzene (CBZ) with concentrations of 30 mg/ml and 24 mg/ml, respectively; after mixing the two solutions with a volume ratio of 1:1, the blend solution is stirred in the dark for 12 hours; then blend layers are spin coated on substrates at a slow spin speed of 600 rpm for 1 min; followed



by a slow dry process after taking out samples of spin coater, they are covered with petri dish for 30 min; a pre-annealing process at 105 °C for 5 min and a post-annealing process at 140 °C for 10 min are carried out via heating the samples on a hotplate before and after the deposition of top contact respectively.

### 2.2.2 Syntheses of the TiO<sub>2</sub> blocking layers

Previous reports present organic solar cells incorporating TiO<sub>2</sub> hole-blocking layers deposited via different methods, such as sol-gel[105], sputtering [106], atomic layer deposition (ALD) [107], pulsed laser deposition (PLD) [108], spray-pyrolysis [109], hydrothermal synthesis[110], and chemical vapor deposition (CVD) [111]. The deposition method of TiO<sub>2</sub> layer must be appropriately selected for a given device type. In this section, different fabrication methods for TiO<sub>2</sub> films used in this thesis are described in details, and the structures of devices are given as well.

#### 2.2.2.1 TiO<sub>2</sub> layer deposited by spray pyrolysis

The titanium source is obtained from the organic solution of di-isopropoxytitanium bis(acetylacetonate) (TAA, Sigma Aldrich). This precursor is a mixture of 0.1 M of titanium tetra-isopropoxide (Sigma-Aldrich, 99.99) and 1.2 M acetylacetonate (AcAc, Fluka, 99.9).

Initially, the precursor is diluted in ethanol with a ratio of 1:10, and then the mixed solution is filled in a chromatographic atomizer and sprayed on cleaned ITO substrate via layer-by-layer deposition. The ITO substrates are placed in a group of six on a hot plate with the edges of every sample covered by a self-designed mask, in order to protect a strip of ITO from TiO<sub>2</sub> deposition and to leave for a direct bottom contact (see section 2.1).

Each 10 times portion of the precursor is sprayed with a pause of 10 seconds, to complete the pyrolysis of the previous layer and to restore the initial substrate temperature. Meanwhile, the ITO substrates are turned by 90°, so that the precursor is distributed evenly on every single sample.

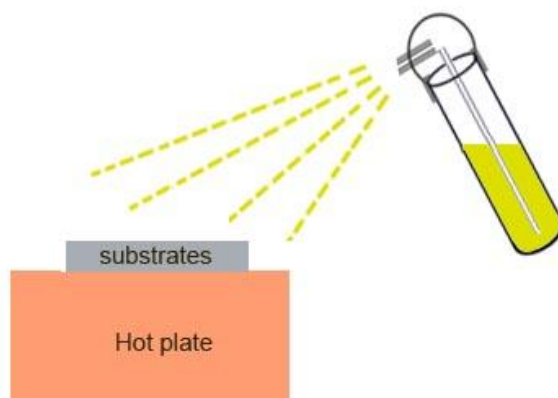


**Figure 2.7 Schematic of spray pyrolysis deposition:** Precursor filled in the chromatographic atomizer and sprayed deposited on cleaned ITO substrate

The ideal temperature at which the  $\text{TiO}_2$  crystallizes is  $450\text{ }^\circ\text{C}$ , to complete the crystallization of  $\text{TiO}_2$  nanoparticles and to remove the remaining organic traces [112]. The annealing is done at  $450\text{ }^\circ\text{C}$  with a ramp of  $15\text{ min}$  ( $30\text{ }^\circ\text{C min}^{-1}$ ) with a dwell time of  $15\text{ min}$ , and then the heating plate is switched off to cool the substrates down to the room temperature at a rate of approximately  $2\text{-}3\text{ }^\circ\text{C min}^{-1}$ .

The secondary reaction products must be desorbed out of the surface and then ventilated by the chemical fume hood. Depending on how many times the precursor is sprayed on top of the heated ITO glass, the thickness of  $\text{TiO}_2$  film can be controlled. The ideal thickness of  $\text{TiO}_2$  film is also investigated later in section 4.2.1.

#### 2.2.2.2 $\text{TiO}_2$ thin film deposited by AALD

In this thesis, AALD method is used for blocking layer deposited on organic materials and flexible ITO benefited with the low temperature condition. These projects are carried out in collaboration with Dr. David Muñoz-Rojas from Prof. Judith Driscoll's group in the University of Cambridge.

The AALD method has many advantages compared to the conventional ALD, such as low-temperature conformal deposition of high quality films with precisely controlling over the film thickness, but without the high vacuum, gas filling, or purging steps. One of the novel approaches has been designed by Kodak is carried out in the following processes: different

precursors are piped and kept apart by an inert gas flow, through a head onto the surface of substrates to be coated. The device is reminiscent of ink jet printers and the precursors are separated in space rather than mixed together in the sequence of pulse-purge steps in conventional ALD [113].

Figure 2.8 shows a scheme of the AALD system. Nitrogen flows are bubbled through a volatile metal-organic precursor and water, and then are sent to the head that are distributed along parallel channels, kept apart by a  $N_2$  flow. And the sample scans while the flows are coming out of the head, the conventional ALD pulse sequence is replicated. This novel system is much faster than the conventional ALD, since no purge step is needed, and easily scalable making it promising for large scale fabrication.

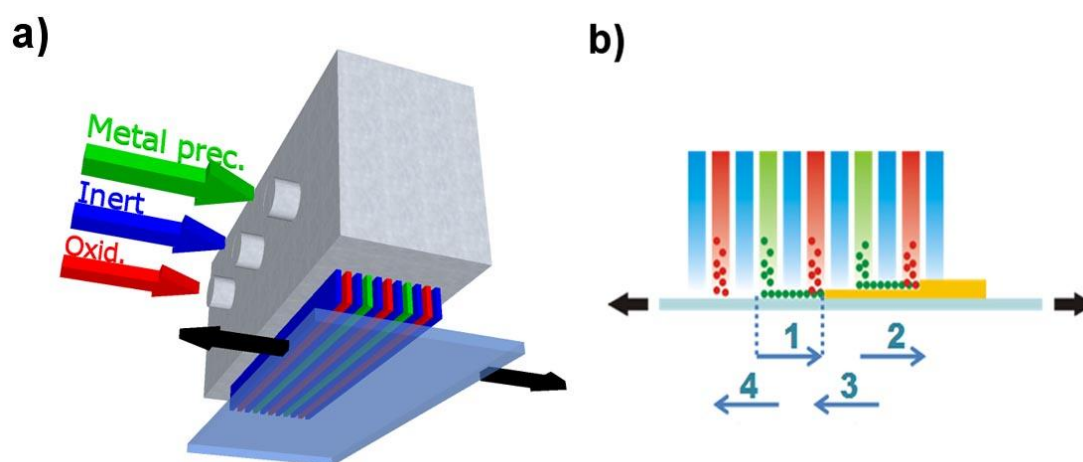


**Figure 2.8: Schematic of the atmospheric atomic layer deposition (AALD) system, Images courtesy of Dr D. Muñoz-Rojas. a) 3D scheme of the head in the AALD system.** The carrier gasses containing the metal precursor (green) and oxidizer (red),  $TiCl_4$  and  $H_2O$  in this case, are distributed in parallel flows over the substrate to be coated, and are kept apart by inner ( $N_2$ ) gas flows (blue); **b) side-view representation of the AALD coating process.** As the sample scans back and forth under the head, it encounters 2 flows carrying the metal precursors. Thus, each AALD cycle (back and forth oscillation of the sample), 4 conventional ALD cycles are achieved, as labeled in the scheme.

For the AALD depositions, films are grown using  $TiCl_4$  (Sigma-Aldrich) as the metal oxide precursors and  $H_2O$  and oxidizing precursors. Inert gasses carrier flow is used to bubble through  $TiCl_4$  and  $H_2O$  with rates of 50 ml/min and 25 ml/min, respectively. The sample is scanned under the head at  $50 \text{ mm s}^{-1}$  and the depositions are carried out at  $100 \text{ }^\circ\text{C}$ .

### 2.2.2.3 TiO<sub>2</sub> layer deposited by sputtering

The sputtering method as a promising way to produce trap-free TiO<sub>2</sub> films is carried out with a Surrey NanoSystems Gamma 1000 C sputter system. Before the sputtering process, the ITO substrates are further cleaned under vacuum using a heat lamp operated at 200 °C. The sputtering process is implemented at 100 W and Ar pressure of  $6-7 \times 10^{-3}$  mbar at room temperature using a TiO<sub>2</sub> target (99.99% purity) from Testbourne materials. The TiO<sub>2</sub> thickness can be controlled by the sputtering time. Subsequently, the substrates are then removed from the sputtering chamber and are heated at 450 °C for 1 hour in air to improve the crystallinity of the film. This heat treatment has a rise and fall time of 1 hour and 10 hours respectively.

### 2.2.2.4 TiO<sub>2</sub> layer produced by sol-gel method

TiO<sub>2</sub> sol-gel is prepared using of Titanium(IV) ethoxide (Ti(OEt)<sub>4</sub>) (Sigma Aldrich) and HCl (37%) as starting materials. 0.745 ml (9.07 mmol) of HCl is added dropwise into 1.05 ml (5.06 mmol) of Ti(OEt)<sub>4</sub> to obtain a slightly viscous yellow solution. The mixed solution is stirred for about 10 mins to cool as it is a highly exothermic reaction. After adding this to 14 ml of THF (Tetrahydrofuran), 100 µl of the resulting solution is carefully pipetted on top of the clean FTO glass followed by a spin coating process set at 4000 rpm for 30 sec. The coated FTO glass is put in an oven at 60 °C for 60 min then on a ramp for 11 hours to 450 °C ( $0.6 \text{ °C min}^{-1}$ ) with a dwell time of 30 min.

Films deposited by the sol-gel method can efficiently cover the substrates underneath with rough surface, due to its reformed process during decomposition at high temperature. The sol-gel method for TiO<sub>2</sub> fabrication is used to cover mecoporous ITO as blocking layer, and then it is used to enhance the conductivity of TiO<sub>2</sub> films by doping with Nb. This project is carried out in collaboration with Dr. Yujing Liu from the Prof. Bein group in chemistry department of LMU.

### 2.2.2.5 TiO<sub>2</sub> nanoparticles synthesis at low temperature

This low-temperature fabrication method is used to synthesis crystallined TiO<sub>2</sub> nanoparticles as blocking layer coated on top of P3HT:PCBM blend layer. This allows to use the

nanostructured reflection layers underneath organic materials, or to use the TiO<sub>2</sub> nanoparticles as an optical spacer. Titanium(IV) isopropoxide (Ti[OCH(CH<sub>3</sub>)<sub>2</sub>]<sub>4</sub>, Aldrich, 99.999 %, 10 mL) is prepared as a precursor by mixing 2-methoxyethanol (Aldrich, 99.9+ %, 50 mL) and ethanolamine (Sigma Aldrich, 99+ %, 5 mL) with a weight ratio of 96:4. The mixed solution is filled in a three-necked flask equipped with a condenser, a thermometer, and an argon-gas inlet/outlet and heated to 80 °C for 2 h in a silicon-oil bath under magnetic stirring, followed by a heating process at 120 °C for 1 h. The two-step heating (80 and 120 °C) is then repeated. The typical TiO<sub>2</sub> precursor solution is prepared in isopropyl alcohol with a volume ratio of 1:5. Then the desolated precursor is spin coated in air on organic photoactive films, depending on whether it is to be used as a blocking layer or an optical spacer. During this process, the precursor is converted to TiO<sub>2</sub> by hydrolysis.

### 2.2.3 Syntheses of the ZnO blocking layer

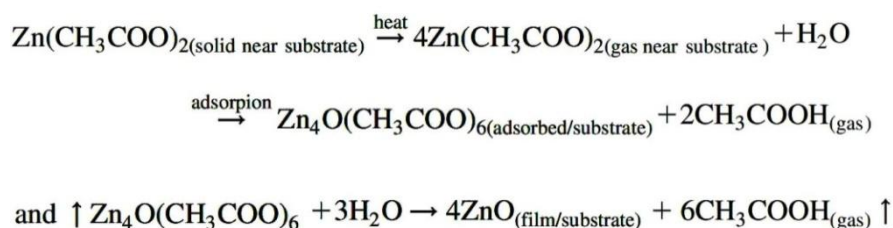
Zinc oxide films as an alternative blocking layer is widely used in solar cells due to its high chemical stability against reducing environments, textured surface, high transparency in the visible region and high conductivity [114]. The deposition of high quality ZnO thin films is reported using a wide variety of techniques [115-118], such as reactive evaporation, sputtering, AALD deposition, chemical vapor deposition, spray pyrolysis, sol-gel method and electrochemical deposition. While these techniques result in different production of coatings, their application in solar cells fabrication are required by the device architectures. Four different producing methods of ZnO films are given in details in this section.

#### 2.2.3.1 ZnO by spray pyrolysis

Spray pyrolysis has been proven to be a simple and inexpensive method, particularly useful for large area applications [119]. Initially, Zinc acetate dihydrate (Zn(CH<sub>3</sub>COO)<sub>2</sub>•2H<sub>2</sub>O, Sigma Aldrich) is dissolved in distilled water. Then the solution is mixed with ethonal (Sigma Aldrich, 99.99) at a ratio of 1:3, and the concentration of the mixed solution of zinc acetate is kept at 0.1 M. To enhance the film growth rate, acetic acid is added to adjust the solution pH (~4).

Additionally, the zinc acetate solution is filled in the chromatographic atomizer and the carrier gas pressure is controlled by hand, using the same setup as shown in Figure 2.7. Then the solution is sprayed layer-by-layer deposited on cleaned ITO. Six ITO substrates are loaded into a self-designed mask that attached to the heater. The solution of precursor is sprayed 25 times for a portion consecutively. A following 10 seconds pause allows to complete the pyrolysis of the previous layer, to remove the water of crystallization, and to restore the initial substrate temperature [120]. Meanwhile, the samples are rotated by 90° and this process is repeated. The deposition from four different directions promotes uniform film growth.

When the Zinc acetate solution droplets arrive close to the heated substrate, a pyrolytic process is produced and a highly adherent film of ZnO develops according to the following steps [119]:



The main product of this set of reactions is a ZnO film deposited on the cleaned ITO substrate. Other reaction products must be desorbed out of the surface and then ventilated by the chemical fume hood. The thickness of the ZnO film can be controlled by the total spraying time, for example, it has to spray for 100 times to obtain a 50 nm thick ZnO film. The ideal thickness of the film will be investigated in Chapter 4.

### 2.2.3.2 ZnO by sol-gel method

ZnO sol-gel is prepared using  $\text{Zn}(\text{CH}_3\text{COO})\cdot 2\text{H}_2\text{O}$ , 2-methoxyethanol and ethanolamine (all from Sigma Aldrich) as the starting material, solvent and stabilizer, respectively. Initially,  $\text{Zn}(\text{CH}_3\text{COO})\cdot 2\text{H}_2\text{O}$  is dissolved in 2-methoxyethanol with a concentration of 0.5 mol/L at room temperature. Then, the mixture is ultrasonic dispersed for 5 min, followed by adding droplets of ethanolamin in the suspension solution until it turns clear. The mixed solution of 2-methoxyethanol and ethanolamin should have a weight ratio of 96:4. The resultant solution is stirred at 60 °C for the duration of 15 min to yield a clear and homogeneous solution. The

gel films are fabricated by spin coating the solution coated on ITO substrates at speed of 1500 rpm. The films are then directly put onto the hot plate and heated at 375 °C for 10 min. After passively cooling the films down to room temperature, ZnO seed layers are obtained.

### **2.2.3.3 ZnO thin film by AALD**

For the AALD depositions of ZnO films, the process and equipment are the same as for TiO<sub>2</sub> AALD fabrication (see section 2.2.2.2). This method is used to coating two thin layers of ZnO (with and without N-doping) on top of ZnO nanowires to modify the surface as investigated in Chapter 5.

Normal ZnO (without doping) films use diethyl zinc (Sigma Aldrich) and H<sub>2</sub>O as the metal oxide and oxidizing precursors, respectively, while the N-doped ZnO layer is produced by adding approximately 30% ammonia to the oxidizing water. Both of the ZnO films are controlled with a thickness of 10 nm via 20 cycles scanning deposition.

### **2.2.3.4 ZnO nanowires by hydrothermal method**

The description of hydrothermal (HT) method for ZnO nanowires (NW) growth will be given in details in Chapter 5. Briefly, a flat dense ZnO film fabricated by sol-gel method, zinc nitrate hexahydrate (Zn(NO<sub>3</sub>)<sub>2</sub>) and hexamethylenetetramine (HMT) from Sigma-Aldrich are used as a seed layer, Zn<sup>2+</sup> source and growing template respectively. The ZnO seed film is dipped into the aqueous solution composed of equal molar Zn(NO<sub>3</sub>)<sub>2</sub> and HMT, with a concentration of 0.025 M. Growing at a temperature of 95 °C for 10 min to 60 min, a set of ZnO NW with controllable length from 50 nm to 250 nm could be obtained.

## **2.2.4 Fabrication of buffer layers**

### **PEDOT:PSS layers**

PEDOT:PSS or poly(ethylenedioxythiophene) poly(styrene sulfonic acid) (H.C. Starck 1.2-1.4 % in H<sub>2</sub>O) is used as a hole transporting layer between the ITO electrode and active

layer in non-inverted solar cells, as shown in Figure 2.2 for the device structure. This deposition process of PEDOT:PSS is carried out by the following steps: a PEDOT:PSS solution is ultrasonic dispersed for 10 min and subsequently filtered using a 0.45  $\mu\text{m}$  pore diameter filter, then spin coated at 5000 rpm and annealed at 145  $^{\circ}\text{C}$  for 10 min in ambient air.

For the inverted solar cells, PEDOT:PSS used as an interface layer between the organic layer and the top contact (see Figure 2.3), in order to avoid contact recombination caused by the injection of metal during thermal deposition. The deposition process and its influence on the device performance will be discussed in details in section 3.3. A brief description is given as follows: the PEDOT:PSS solution is dissolved in 2-propanol with a ratio of 1:10. This solution is sprayed onto the sample mounted on a spin coater using a glass nozzle. Immediately after wetting the sample is spin-coated at 600 rpm to yield a homogenous layer of PEDOT:PSS. The thickness of the PEDOT:PSS can be easily varied using different spin speeds.

### **LiF layer**

LiF has been widely used as a contact interface material in non-inverted organic solar cells. Extremely thin layers of LiF around 0.7 nm typically cannot completely cover the organic layer surface, but induce changes in the work function of adjacent top contact materials, due to doping ejects of lithium reacting with organic material [121]. In addition, LiF films can also limit oxygen diffusion into the organic layers [122]. A 0.7 nm thick LiF is evaporated in glove box at a rate of 0.1  $\text{\AA}/\text{s}$  and with a start pressure of  $3 \times 10^{-6}$  mbar.

### **Tungsten oxide layer**

A  $\text{WO}_3$  layer is deposited on the organic layer as a charge selective and buffer layer in inverted devices. Due to its high work function of 4.8 eV the blocking layer can be used to extract holes but suppress electron during exciton migration through the organic-metal interface in inverted solar cells [123]. The  $\text{WO}_3$  layer is deposited by thermally evaporation for a thickness of 10 nm at a rate of 0.1  $\text{\AA}/\text{s}$  below  $3 \times 10^{-6}$  mbar.

## **2.2.5 Deposition of electrodes**

The electrodes of solar cells are selected depending on the work functions of the other layers in devices as described in section 1.2.



### **Al layer**

Al is commonly used as the cathode in non-inverted solar cells, and it is deposited by thermal evaporation in glove box at 0.2-2.0 Å/s and below  $3 \times 10^{-6}$  mbar.

### **Ag layer**

For the inverted devices presented in this thesis are all deposited with 100nm Ag. It is deposited via sputter deposition using a table top sputter deposition system (Emitech K575X ), at 10 mA and an Ar pressure of  $1 \times 10^{-2}$  mbar, with a deposition rate of 0.1-2.0 Å/s

## **2.3 Characterization**

Various methods have been employed to characterize the properties of prepared metal oxide layers and the performances of devices based on them. The main focus of this section is the description of these different characterization techniques.

### **2.3.1 I-V Characterization**

Current-voltage characterization or I-V curve is a widely used and important method to measure the power conversion efficiency of a solar cell. By recording the current flow through the device at a certain bias voltage measure, the maximum power point could be determined.

The light-curve of solar cell is analyzed under illumination of AM1.5G spectrum, which is a standard illumination spectrum provided by the National Renewable Energy Laboratory . It is provided by a solar simulator (L.O.T. Oriel) using 150W Xe-lamp and AM1.5G filters with approximately  $100 \text{ mW/cm}^2$ . The dark I-V-curve is recorded while testing device without illumination. A bias voltage is swept typically from -0.5 V to +1 V with a step of 10 mV, the current through the device is monitored by a Keithley 2400 source meter unit using a self-made LabView program.

Figure 2.9 shows the commonly used equivalent circuit of organic solar cell for the

description of device performance. It includes the following elements: a current source known as photocurrent, a diode with reverse saturation current is representing the charge carrier on the interface, a shunt resistor where the current can leak across and a series resistor as the sum of series resistances of all the layers in devices.

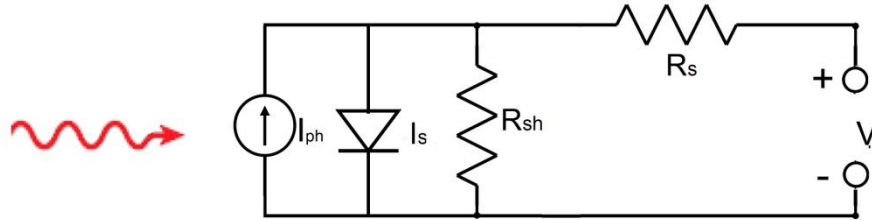


**Figure 2.9: A typical equivalent circuit for organic solar cell.** The model contains series and shunt resistances,  $R_s$  and  $R_{sh}$ , an applied bias  $V$ , a diode with reverse saturation current  $I_s$  and a current source known as the photogenerated current ( $I_{ph}$ ).

The I-V characterization of device using this equivalent circuit can then be described by the Generalized Shockley Equation:

$$I = \frac{R_{sh}}{R_{sh} + R_s} \left\{ I_s \left[ \exp \left( \frac{q(V - IR_s)}{nk_B T} \right) - 1 \right] + \frac{V}{R_{sh}} - I_{ph}(V) \right\} \quad (2.1)$$

with the  $I_s$  representing the reverse saturation current,  $n$  the diode ideality factor,  $k_B$  Boltzmann's constant,  $T$  is the temperature,  $I_{ph}$  is the photo-generated current, and  $R_s$  and  $R_{sh}$  are the series and shunt resistance, respectively.

This equation could be applied to simulate I-V characteristic, as shown in Figure 2.10 for a typical I-V curve. Then the parameters of solar cell performance can be calculated by different working regimes under illumination:

- (1) To short circuit the top and bottom electrodes, the photocurrent defined as short circuit current ( $I_{SC}$ ) is obtained;
- (2) At a certain forward bias  $V_{MPP}$  and current  $I_{MPP}$ , the cell is generating a maximum energy output:  $P_{max} = V_{MPP} \times I_{MPP}$ .

- (3) The open circuit voltage ( $V_{OC}$ ) compensates for the internal built-in field, showing where the current decrease to zero.
- (4) Series ( $R_s$ ) and shunt resistance ( $R_{sh}$ ) can be estimated from the slope at large forward bias and small reverse bias voltage, respectively.
- (5) The Fill Factor (FF) represents a measure of the quality of the shape of the I-V characteristic. It is defined as:

$$FF = \frac{I_{MPP} \times V_{MPP}}{I_{SC} \times V_{OC}} \quad (2.2) \quad (2.2)$$

- (6) The power conversion efficiency ( $\eta$ ) represents the fraction of incident power that is converted into electrical power:

$$\eta = P_{out}/P_{in} = (FF \cdot V_{OC} \cdot I_{SC})/P_{in} \quad (2.3)$$

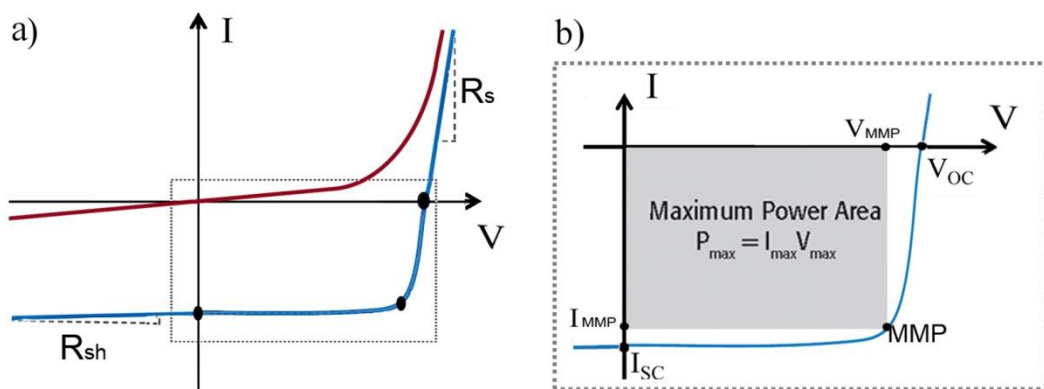


**Figure 2.10: I-V curves of a photovoltaic device.** a) I-V Characterization in the dark (blue) and under illumination (red). b) I-V characteristics under illumination, parameters of the device:  $V_{OC}$ ,  $I_{SC}$ ,  $P_{max}$ ,  $V_{MPP}$ ,  $I_{MPP}$  and FF can be calculated.

The dark current, on the other hand, is defined as the current that would flow through the device under a bias in the dark in the opposite direction as the photocurrent. This current can

be dominated by injection from the contacts, transport of the fastest carrier, recombination at the electrodes, or recombination in the bulk of the device. In inorganic p–n junction cells, this current is most often written as [31]:

$$J_{\text{dark}} = J_0 \exp(V - V_{\text{bi}}) / n k_B T \quad (2.4)$$

where  $J_0$  is the reverse saturation current and can be related to the intrinsic carrier density and their mobilities,  $V_{\text{bi}}$  is the built-in potential, and  $n$  is the “ideality factor” which can vary between 1 and 2 depending on whether recombination in the depletion region or minority carrier diffusion to/from junction dominates the current [124].

### 2.3.2 EQE characterization

The external quantum efficiency (EQE) gives insight to the spectral response of a photovoltaic device. It is defined as the number of electrons delivered to an external circuit divided by the number of incident photons at a specific wavelength:

$$\text{EQE}(\lambda) = \frac{I(\lambda)}{q P_0(\lambda)} \frac{hc}{\lambda} \quad (2.5)$$

Where  $I(\lambda)$  is the current density,  $q$  the electronic charge,  $P_0(\lambda)$  the incident power,  $h$  Planck’s constant,  $c$  the speed of light in a vacuum.

$$I_{\text{SC}} = \int \lambda \text{EQE}(\lambda) P(\lambda) d(\lambda) \quad (2.6)$$

The theoretical short circuit current  $I_{\text{SC}}$  can be obtained from the measured EQE, which is convolved with the AM 1.5G solar spectrum and integrated over all wavelengths. The  $I_{\text{SC}}$  can be calculated as:

EQE characterization is obtained by recording the photocurrent responding to illumination with monochromatic light at different wavelengths. A 150 W Xe lamp is focused onto a LOT-Oriel Omni 150 monochromator. The illumination wavelength is swept from 280 nm to

800 nm in steps of 2 nm. Curves are recorded using a Keithley 2400 Source-Meter controlled by a self-made LabView program. Devices are kept in an opaque metal box during the measurements. The light intensity at different wavelengths is calibrated with a Fraunhofer Institute certified silicon reference solar cell equipped with a KG5 filter.

### 2.3.3 Absorption measurement

Absorption spectra shown in this thesis are recorded with an Agilent 8453 UV-vis spectrometer from thin films in transmission mode. Thin films are prepared on ITO, which is used as a blank sample. Absorption results of blocking layers and organic layers are obtained by subtracting the blank spectra from the substrates coated with these two films. Absorption of the typical organic layers can be modeled using macroscopic optical quantities, which is commonly using Lambert-Beers law to correlate the layer thickness with the wavelength dependent light intensity:

$$I(\lambda) = I_0 \exp^{-\alpha(\lambda)d} \quad (2.7) \quad (2.7)$$

where  $I_0$  is the light intensity before injection,  $\alpha$  is the absorption constant,  $d$  is the thickness of the absorber.

It has to point out that the interference effect could considerably influence the absorption spectra of samples, especially for the thin semiconductor films with low absorptivity. Therefore, it should avoid using the UV-vis analysis directly for quantitative comparison and those two effects has to be considered for the characterization. For the influences of these two effects on the results of absorption could be referred from their respective definitions.

The Interference is constructive when the optical path difference is equal to an integer multiple of the wavelength of light, showing a relation of:

$$2nd \cos(\theta) = m\lambda \quad (2.8) \quad (2.8)$$

As the angle of incidence of the original wave on the film is commonly set at  $90^\circ$ , it indicates that the responding wavelength ( $\lambda$ ) on absorption spectra is determined by the refractive index of the film ( $n$ ) and the film thickness ( $d$ ).

### **2.3.4 Microscopy techniques**

#### **Scanning electron microscopy (SEM)**

SEM from Zeiss Ultra is used in this thesis to image the morphology of ZnO nanowires, especially their lengths, size and orientation. Characterization is performed at 2-5 kV acceleration voltage with a working distance of 1-10 mm. For SEM side views, the investigated samples are scratched at the backside with a diamond pen, cooled in liquid Nitrogen and cracked. Together with the samples for top views, they are stick onto a SEM stub with carbon tape to discharge it from the electron beam, and sputter with a 2 nm Au films to reduce charging effects during the SEM measurements.

#### **Atomic Force Microscopy (AFM)**

AFM measurements are implemented on a Veeco instruments Inova in a tapping mode. In this tapping mode, the cantilever of atomic force microscopy oscillates at its resonant frequency, and the slightly motion of cantilever is tracked by a laser focused on it. While the tip scans the sample, the interaction of cantilever tip and the reflection of the laser changes depending on the topography. Therefore the morphology of surface could be recorded. Data are analyzed using Gwyddion, a scanning probe microscopy analysis program.

### **2.3.5 XRD measurements**

X-ray diffraction (XRD) is used to study the materials phase composition and crystal structure by utilization of electromagnetic radiation with the wavelength of only a few angstroms [125]. The process of XRD is based on the diffraction effect interacting between X-rays and the

matter, using the Bragg condition defined as:

$$n\lambda = 2d \sin \theta \quad (2.9)$$

The value  $n$  gives the order of the diffraction,  $\theta$  is the angle of incidence,  $\lambda$  is the X-ray wavelength,  $d$  is the plane-to-plane distance. Bragg's equation describes the relationship between diffraction and plane-to-plane distance  $d$ . It means that the diffraction position corresponds to the characteristic information of the related crystal structure. Furthermore, the relative intensity of diffraction peaks depends on the type and arrangement of the atoms in the crystals. By analyzing the diffraction pattern, one can have insights into the phase composition and crystal structure of the studied materials.

XRD patterns presented in this thesis are recorded with a standard X-ray powder diffractometer (CuK $\alpha$ ,  $\lambda = 0.1542$  nm) in the range of 5–65 ° with a 0.0258 sampling step.

### 2.3.6 Van der Pauw method and Hall Effect measurement

Electrical properties of semiconductor blocking layers are characterized via Van der Pauw method and Hall measurement. The conductivity, charge carrier density and charge mobility of TiO<sub>2</sub> and ZnO films are presented in Chapter 4 as an important evidence for the working mechanism of the inverted devices. The Hall measurement is carried out using an Ecopia system of HMS3000.

Conductivity, also known as inherent conductance, is identified as the ability of material to conduct an electrical current. It can be calculated from the characterized resistance the sample with a known shape (geometrical parameters of the sample such as its length and the cross-sectional area):

$$\sigma = 1/\rho = l/(R \cdot A) \quad (2.10)$$

Where:  $\sigma$  is the dc conductivity (S/m),  $\rho$  is the resistivity ( $\Omega \cdot m$ ),  $R$  is the resistance ( $\Omega$ ),  $l$  is the length or thickness of the sample (m),  $A$  is the cross-sectional area ( $m^2$ ).

$$R = \frac{V}{I} \quad (2.11)$$

According to Ohm's law, the resistance  $R$  can be obtained by applying a voltage ( $V$ , volt) and recording the current flowing ( $I$ , amperes) through the sample. According to this basis, the Van der Pauw method is used to measure the resistance of two-dimensional samples with four Ohmic contacts placed on the boundary of the sample.

To determine the sheet resistance  $R_S$ , two characteristic resistances  $R_A$  and  $R_B$  are required, which are calculated from a series of resistances measured among the four Ohmic contacts by applying a voltage on one edge of the sample and recording the current crossing the opposite edge. Their relation with sheet resistance  $R_S$  is given via the Van der Pauw equation:

$$\exp\left(-\pi \frac{R_A}{R_S}\right) + \exp\left(-\pi \frac{R_B}{R_S}\right) = 1 \quad (2.12)$$

The bulk electrical resistivity of the sample can be calculated from the sheet resistance and sample thickness ( $d$ ), and then the conductivity can be obtained.

$$\rho = R_S \times d \quad (2.13)$$

The conductivity is produced by charge carrier density ( $n_c$ ,  $m^{-3}$ ) and charge mobility ( $\mu$ ,  $m^2V^{-1}s^{-1}$ ), thus, in order to extract the charge mobility, the charge carrier density is required. By Hall Effect measurement the  $n_c$  can be approached by applying a magnetic field which is perpendicular to the current flow in the sample. Then the induced Lorentz force will result in a Hall voltage  $V_H$  perpendicular to the applied electric field and magnetic field.  $V_H$  is measured through appliance of positive and negative magnetic field, while changing the injected current direction. With the presence of elemental charge  $q$ , the charge carrier density and charge mobility can be calculated from the following equations:

$$n_c = \frac{I \times B}{q \times V_H} \quad (2.14)$$

$$\mu = \frac{\sigma}{q \times V_H} \quad (2.15)$$



### 2.3.7 Intensity dependence measurement

Light intensity characterization is presented in Chapter 5 to investigate the recombination mechanisms in the devices. Intensity dependent I-V is carried out with the solar light radiation filtered by a combination of two six-position filter-wheels, which are set by a series of different ND filters. The filter combination can present 36 different light intensities and can be automatically controlled by a Lab view program.

The recombination mechanism governs the extent to which the incident light intensity modulates the open-circuit voltage. When a polymer solar cell is under illumination at open circuit conditions, where the current is zero; all photogenerated carriers recombine within the cell. Thus, recombination studies near open circuit are particularly sensitive to the details of the recombination mechanism [126].

Under open circuit, the applied voltage equals the difference between the quasi-Fermi levels within the donor and acceptor phase separated domains, following the expression of:

$$V_{OC} = \frac{E_{gap}}{q} - \frac{kT}{q} \ln\left(\frac{n_e n_h}{N_c^2}\right) \quad (2.16)$$

where the  $E_{gap}$  is denoted as the energy difference between the HOMO and LUMO levels,  $n_e$  and  $n_h$  are the electron and hole densities at open circuit, and  $N_c$  is the density of conduction states at the band edge.

When the bimolecular recombination is dominant, it results in  $V_{OC} = (k_B T/e) \ln I + \text{constant}$ , where  $I$  is the incident light intensity. The slope is equal to  $k_B T/e$ . This universality highlights the generality of bimolecular recombination kinetics at open circuit solar cells.

If the monomolecular recombination is the dominant mechanism over the full range of applied voltages from short circuit to open circuit, the  $n_e$  and  $n_h$  at open circuit will each be proportional to the intensity, and the slope of  $V_{OC}$  vs  $\ln I$  should be  $2k_B T/e$ .

If the slope is between 1 and 2, it suggests that recombination at open circuit is a combination of monomolecular and bimolecular processes.

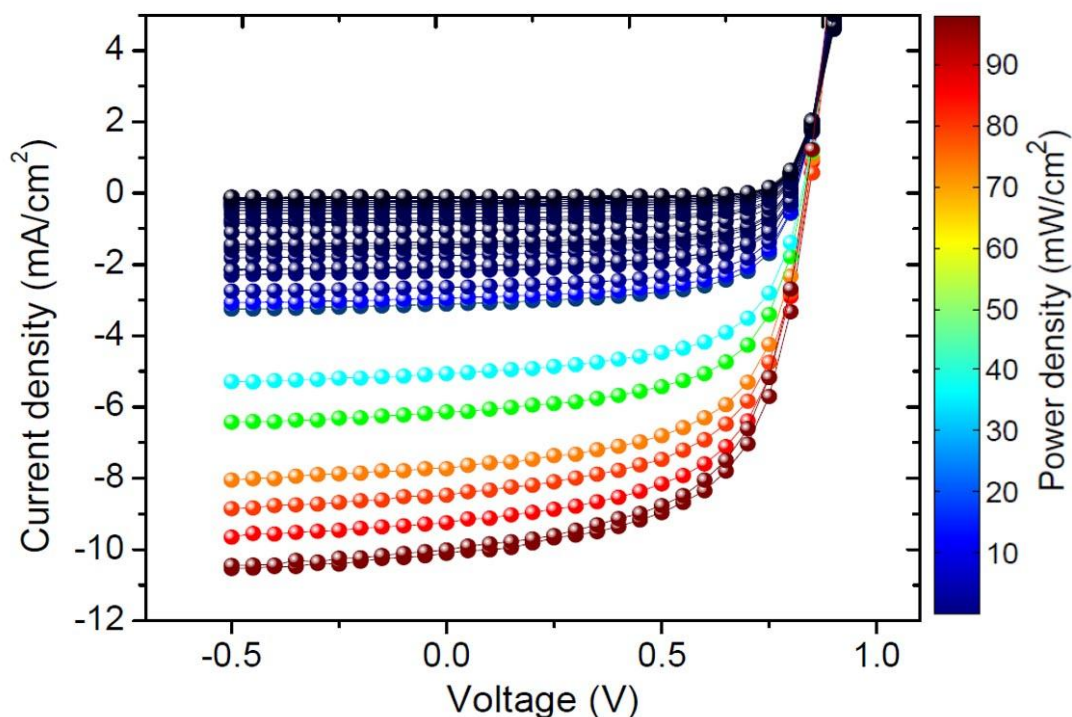


**Figure 2.11:** The I-V characteristics of PCDTBT:PC<sub>71</sub>BM solar cells as a function of incident light intensity. It shows that the open-circuit voltage varies logarithmically with light intensity [126].

### 2.3.8 Impedance spectroscopy measurement

The measurement of impedance spectroscopy (IS) is considered as a useful method to distinguish the physical processes of charge carrier transfer in OPVs. In the IS measurement, the applied alternating voltage  $V(t)$  is response with a polarization and/or an alternating current  $I(t)$ . The polarization is induced by either the typical reasons such as atomic, ionic, and orientation polarization, or a multitude of physical processes, e.g. the charge transfer at the interfaces, grain boundaries and impurities in the materials. Different polarizations are responding at a characteristic time constant (certain frequency) by a relaxation behavior, leading to a phase shift between the  $I(t)$  and the  $V(t)$  and to a certain current-amplitude. The ratio between both quantities is the time-dependent impedance.

$$Z(t) = \frac{V(t)}{I(t)} \quad (2.17)$$

For the IS measurement, a Metrohm Autolab PGSTAT 302N is used with two electrodes respectively connecting to the top and bottom contacts of samples, respectively. Devices are kept in an opaque metal box during the measurements to reduce electronic perturbations from

outside and to provide a sufficient dark condition. An offset voltage a range of 21 steps between 0.5 V and -0.5 V, 100 frequencies in a range from 1MHz to 30 Hz and an amplitude of the perturbation voltage of 20mV are applied on the devices. The fitting process to simulate the obtained IS data is implemented with the software Nova 1.6.

### 2.3.9 Photo-CELIV method

Photo-CELIV method is a charge extraction technique used to investigate charge carrier mobility and recombination kinetics of the device [127]. It could be briefly described as the devices are exposed to a short laser pulse, followed by a voltage sweep for the photogenerated charges collection [128].

The experimental setup consists three main parts listed as follows: a waveform generator to apply a compensation voltage that prevents charges from exiting the device via the external contacts. A pulsed laser to generate free charge carriers in the device may either recombine or become extracted through the subsequent voltage sweep. And a digital storage oscilloscope with a termination resistance of 50  $\Omega$  is used to exhibit and record the data.

As reported by Mozer et al., upon application of a reverse bias triangular-shaped voltage pulse with a voltage rise speed  $A=dU/dt$ , the typical electrical response is a rectangular-shaped current transient with a plateau value corresponding to the capacitive displacement current  $j(0)=A \times \epsilon \epsilon_0/d$ , where  $\epsilon$  and  $\epsilon_0$  are the dielectric constants of the material and vacuum, respectively, and  $d$  is the thickness of the dielectric. When a strongly absorbed laser flash hits the sample, charge carriers are photogenerated throughout the layer. The photogenerated charge carriers either undergo recombination or exit the device through the external circuit under the influence of the built-in electric field (short circuit condition). The external photocurrent ( $\Delta j$ ) upon photoexcitation can be minimized by the application of a dc offset bias ( $U_{\text{offset}}$ ) forcing the charge carriers to remain in the device and to recombine. The remaining charge carriers can be extracted after an adjustable delay time ( $t_{\text{del}}$ ). By selecting the proper voltage rise speed  $A$ , the extraction current reaches a maximum value  $j$  as shown by the dashed line in Figure 2.12. From the time to reach the current maximum ( $t_{\text{max}}$ ), if  $\Delta j \leq j(0)$ , the mobility can be calculated according to:

$$\mu = \frac{2d^2}{3At_{max}^2 \left[ 1 + 0.36 \frac{\Delta j}{j(0)} \right]} \quad (2.18)$$

Equation 2.18 has been derived by solving the continuity, current, and Poisson equations. The expression  $1 + 0.36j / j(0)$  in the denominator has been introduced to compensate for the redistribution of the electric field during charge extraction, and it is valid for moderately conductive samples [129].

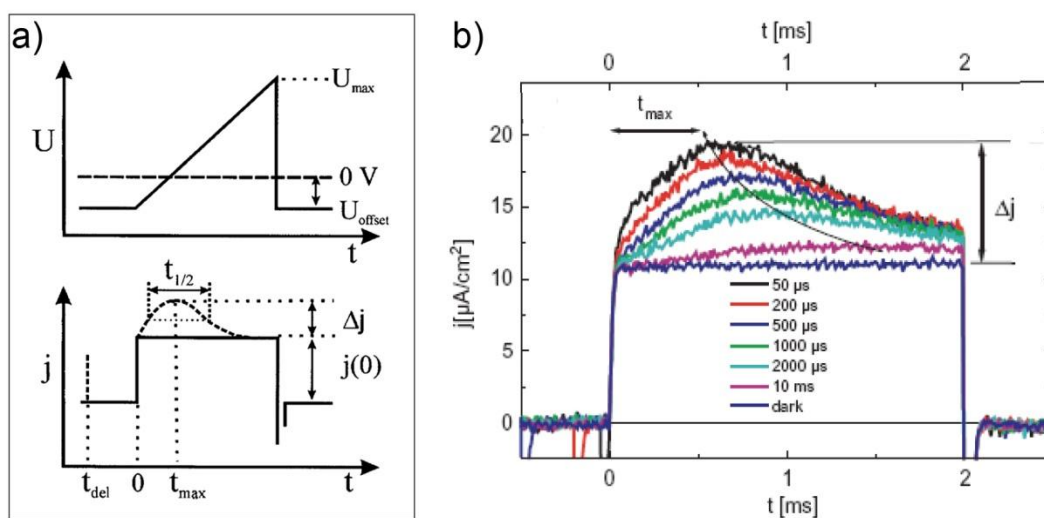


**Figure 2.12:** a) Schematic illustration of the photo-CELIV method.  $U$  is the applied voltage to the sample;  $j$  is the corresponding current transient. b) Photocurrent transients of photo-CELIV at different delay time of pulse of light [129].

## 3. Device Optimization

In this chapter, several important processes of the device preparation are optimized for metal oxides-organic hybrid device geometry, and their impacts on device performance are described. The TiO<sub>2</sub> and ZnO hole blocking layers are modified by doping with N and Mg respectively. A co-blocking layer of TiO<sub>2</sub>-ZnO is used in the hybrid device. The morphology of blend layer is influenced by the solution concentration and processing for the organic photoactive materials and the post treatment process implemented, while its layer thickness determines the light absorption. A proper interface layer of PEDOT:PSS has been deposited between the organic layer and Ag top contact to extract selectively holes. All of the above fabrication processes can significantly influence the performance of solar cells.

### 3.1 Blocking layers improvement

#### 3.1.1 TiO<sub>2</sub> Surface Cleaning

One of the most attractive advantages of organic solar cells is the low cost production process, mainly attributed to the ultra-thin films that could allow roll-to-roll processing to be applied and the cheaper materials synthesis matters to reduce the cost of devices production [16]. On the other hand, this is a challenge for the device architecture because thin film design will increase the chance of short circuits induced by the defects in the thin film or on its surface. In this case, a smooth and dense blocking layer is necessary for the inverted blend solar cells. As described

in the fabrication process of spray pyrolysis (see section 2.2.2.1),  $\text{TiO}_2$  film is obtained by the pyrolysis of organic precursor at  $450\text{ }^\circ\text{C}$  in open air, with the substrates placed in a chemical fume hood. The whole process takes about 2 hours. During the fabrication process explored in air, defects on the  $\text{TiO}_2$  surface forms due to the incomplete decomposition of the  $\text{TiO}_2$  precursor, as well as the dust particles in the environment falling down to the film. The existence of defects is confirmed in Chapter 4, which can significantly influence the device performance. The particles attached on the  $\text{TiO}_2$  film surface can increase the chance of short circuits in the device during characterizations. Therefore a proper cleaning process on the  $\text{TiO}_2$  film is necessary for a working device.

### Mechanical Cleaning

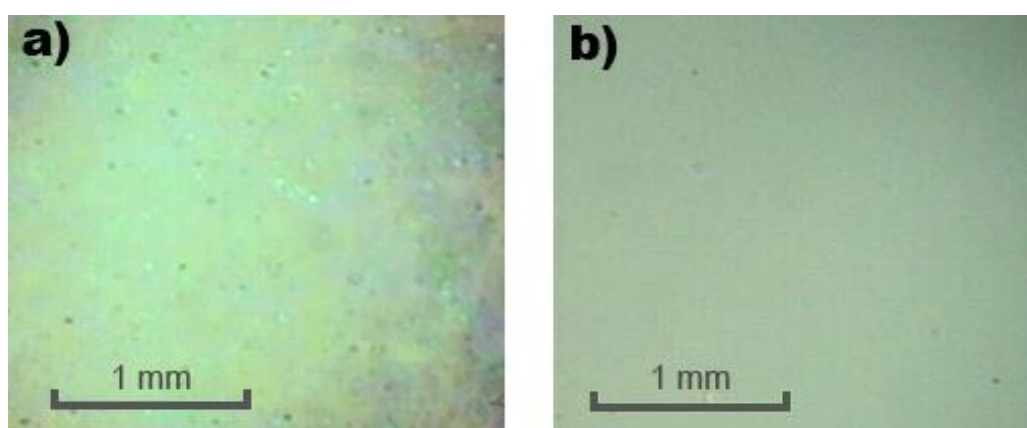


**Figure 3.1**  $\text{TiO}_2$  films magnified image before (a) and after (b) mechanical cleaning

Initially,  $\text{TiO}_2$  films are cleaned by a mechanical method after fabrication. The process is described as follows: the surface of the  $\text{TiO}_2$  films is wiped using a cotton Q-tip, keeping the sample in a petri dish filled with ethanol. Photographic images of  $\text{TiO}_2$  films surface are shown in Figure 3.1. It is obvious that the mechanical cleaning can efficiently remove the particles on the film to obtain a macroscopically clean and smooth surface.

### Ultrasonic Cleaning

The next step of cleaning process is carried out on the  $\text{TiO}_2$  films via ultrasonication. The

substrates are placed in a beaker filled with ethanol and ultrasonic cleaned for 2 min. Then blend solar cells are produced on  $\text{TiO}_2$  films. The I-V characterizations of samples cleaned by three different cleaning processes: no cleaning, mechanical cleaning and mechanical cleaning followed by ultrasonic cleaning, are shown in figure 3.2. The I-V curves exhibit that the performance of devices are influenced by the different cleaning steps. A significant increasing of PCE is observed from the I-V curves of  $\text{TiO}_2$  solar cells after cleaning. After the first mechanical cleaning step, PEC of device enhance from 1.53% to 1.72%, while a further improvement to 1.96% after the second step of ultrasonic cleaning. As a result, a nearly 30% increasing is observed for the device built on the  $\text{TiO}_2$  been cleaned by both mechanical cleaning and ultrasonic cleaning.

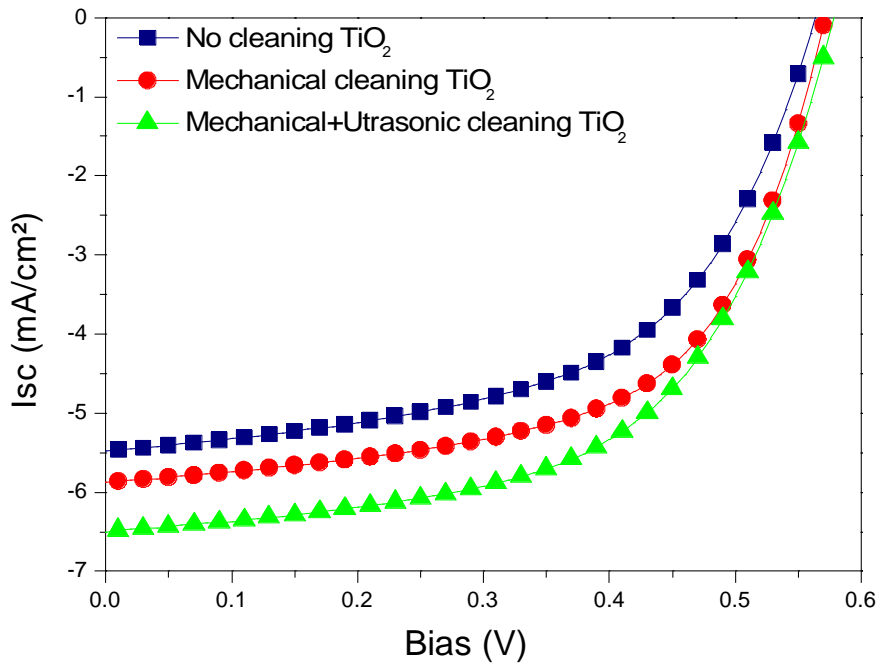


**Figure 3.2:** I-V curves of ITO/  $\text{TiO}_2$ / P3HT:PCBM/ Ag devices treated by different cleaning methods on the  $\text{TiO}_2$  surface. No cleaning (black squares), Mechanical cleaning (red circles) and Mechanical-ultrasonic cleaning (green triangles). Samples are characterized under illumination with simulated AM 1.5G solar light ( $100 \text{ mW/cm}^2$ ).

### Plasma Cleaning

Plasma cleaning is widely accepted as an efficient method to modify the surface of ITO [129-131], in order to clean the organic impurities formed during production or the other

processing steps, and to improve the hydrophilic property for a better coating of polymer layer. The plasma cleaning is assumed to be favorable for  $\text{TiO}_2$  surface, with expectation of removing the organic compounds remained from the decomposition of precursor and the organic cleaning solution. Therefore blend solar cells are fabricated after a plasma cleaning process has been applied to the  $\text{TiO}_2$  blocking layer, and I-V measurements are recorded for the devices performance.

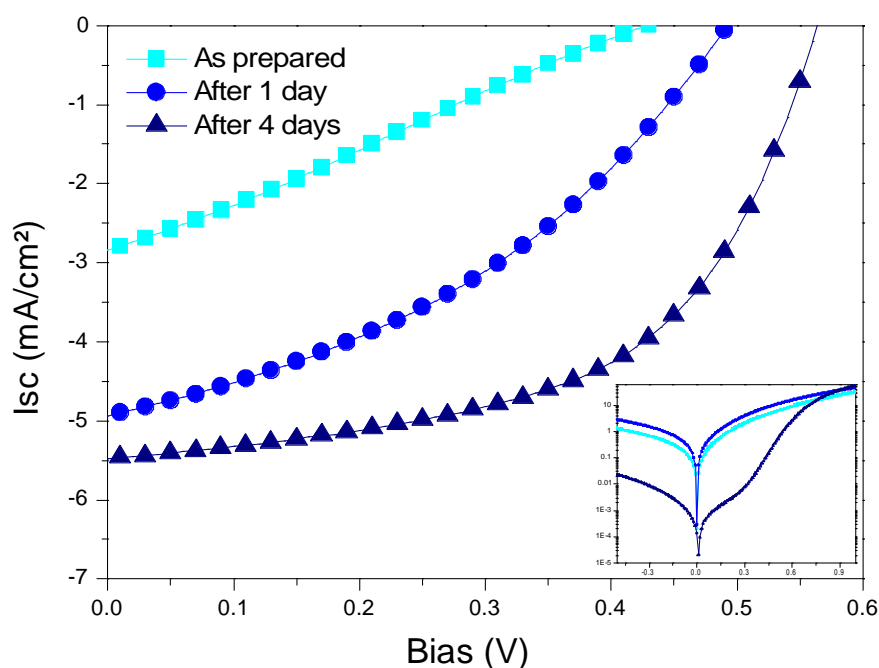


**Figure 3.3** I-V curves of device with  $\text{TiO}_2$  surface cleaned by  $\text{O}_2$  plasma. Characterization implement on samples as prepared and after storing in dark for 1 and 4 days Samples are characterized under illumination with simulated AM 1.5G solar light ( $100 \text{ mW/cm}^2$ ).

As shown in Figure 3.3, an unexpected degradation is observed for the plasma cleaned  $\text{TiO}_2$  film. With the apparent S shape shown in the I-V curve, the performance of device is significantly reduced attributed to the low  $I_{\text{SC}}$ ,  $V_{\text{OC}}$ , and FF (below 25%). When stored in dark for 1 day, obviously this sample recovers in terms of devices performance, and this improvement increases with increasing aging time. Four days after being produced, the devices perform remarkably well with an enhanced efficiency by a factor of 3 compared to those freshly prepared.



It is interesting to observe this reduced performance caused by plasma cleaning on TiO<sub>2</sub> surface, although this is not a helpful optimization for its fabrication process. The reason need to be further investigated fundamentally, however many previous research confirmed that plasma surface treatment could change the oxygen binding state [130, 131]. Therefore it is reasonable assumed that extra oxygen band generated by oxygen plasma can attach to the TiO<sub>2</sub> surface. As a direct result, the work function is changed and the charge transport will be influenced, which is represented by the S-shape of I-V curve. Additionally, the O<sup>-</sup> rich surface is more active under UV light illumination, resulting in photogeneration of electron-hole pairs. Electrons are very efficiently transferred to bound oxygen to generate the superoxide radical anion O<sup>-2</sup>, which in turn can deacidize many organic compounds including polymers. The photogenerated holes can react with surface hydroxyl groups to produce TiOH<sup>+</sup> that again can react and degrade adsorbed organic compounds [49, 132], and reduce the device performance. On the other hand, since the solar cells do recover after a few days, it suggests that the Ti-O binding state induced by plasma is not stable, and the scission of this chemical bond takes place in the low-oxygen environment [133]. More evidences are required to support the assumption given above, such as XPS measurement which is responsible for electrochemical characteristics of the TiO<sub>2</sub> film surface. Limited by the measurement equipment, further research of oxygen plasma working mechanics has not implemented. Since the initial results demonstrate that plasma on TiO<sub>2</sub> film causes negative effect on their performance, therefore this step will not be included in the cleaning process for device fabrication.

### 3.1.2 N-Doped TiO<sub>2</sub> to increase the absorption

Among the semiconductor materials being applied for solar cell as blocking layer, TiO<sub>2</sub> remains the most promising one because of its high efficiency, low cost, chemical inertness, and photostability [134-136]. However, the widespread technological use of TiO<sub>2</sub> is impaired by its wide bandgap (3.2 eV), which limits the absorption in UV light. N doped TiO<sub>2</sub> could extended its absorption to the longer wavelengths, and it has been investigated extensively regarding the photocatalyst yield [137, 138]. Substitution doping of nitrogen was found to be most effective because its p states contribute to the bandgap narrowing by mixing with O 2p states [139].

Since the normal photoactive materials, such as P3HT and PCBM can mainly harvest the light with wavelength from 500 nm to 650 nm, the IPCE of organic device is relatively low near UV range [140]. By N-doping TiO<sub>2</sub> as blocking layer in solar cells, it can effectively broaden the

light response to the visible range, which results in the energy levels shift of TiO<sub>2</sub> layer. As the HOMO level of TiO<sub>2</sub> is -4.3 eV, it is far below that of PCBM with a value of -3.7 eV. Therefore, a slight increase of bandgap should not influence on the exciton separation, but the improvement of the V<sub>OC</sub> of devices can be expected.

In addition, usually oxygen deficiency is contained in the crystal structure of pure TiO<sub>2</sub> [137, 141, 142]. It is known that oxygen deficiency can create electron-hole pairs and that the oxidizing holes can react with the polymer and cause the degradation of device performance [143], therefore the lifetime of the organic solar cell will be shortened. With the illumination of UV light, this degradation process can be even stronger [49]. In this respect, to enhance the UV absorption of TiO<sub>2</sub> layer by N-doping is also a very promising strategy to improve the stability of these solar cells by reducing the UV light reaching the organic materials.

### **Synthesis methods**

It is important to have a proper nitrogen source in the synthetic procedure to dope the TiO<sub>2</sub> films. The nitrogen is introduced in various ways through bubbling nitrogen into the precursor solution, using pressurized nitrogen to spray the precursor instead of air, and adding Urea to the precursor solution. Initially the standard cells have to be presented without nitrogen doping, in order to compare the effects of the three different methods. The fabrication techniques of standard TiO<sub>2</sub> films are described in section 2.2.1. It is carried out by spraying TiO<sub>2</sub> precursor on ITO glass substrates heated to 450 °C.

#### 1. Spray pyrolysis with pressurized N<sub>2</sub>

Instead of using pressurized air as for the standard spray pyrolysis, pressurized nitrogen is used to spray the precursor on to the substrate.

#### 2. Nitrogen bubbling of the Precursor Solution

Nitrogen gas is bubbling through the precursor solution for about 30 minutes prior to spraying.

#### 3. Adding Urea in the Precursor Solution

1ml Urea aqueous solution with a concentration of 30 mg ml<sup>-1</sup> (0.5 mmol) is mixed in 10 ml

TiO<sub>2</sub> precursor (See section 3.2.2.1). To make a fair comparison with the mixture precursor, 1ml di-water is added in the standard TiO<sub>2</sub> precursor. Apparently differences are shown on the color of the two solutions in Figure 3.4.



**Figure 3.4: TiO<sub>2</sub> Precursor Solutions. a) TiO<sub>2</sub> standard precursor (left), b) TiO<sub>2</sub> precursor mixed with Urea (right).**

## Results and Discussion

After the fabrication of N-doped TiO<sub>2</sub> films by these three different doping techniques, the absorption measurements are carried out to determine whether the films had been successfully doped in comparison with a standard TiO<sub>2</sub> film without doping. Then solar cells are built by coating P3HT:PCBM blend layer on top of the substrates, followed by the evaporation of WO<sub>3</sub> and Ag top contact. Devices performances are recorded with I-V measurements, which are extracted for the six individual pixels of each cell set and the respective standard deviations are calculated.

To remove the influence of TiO<sub>2</sub> film thicknesses, the absorption results are normalized as shown in Figure 3.5. Comparing to the standard TiO<sub>2</sub>, a slight red-shift is observed for the TiO<sub>2</sub> films doped by sprayed and bubbled method. This could be an evidence for the N-doping, of which mainly results in a reduced bandgap for a broaden absorption [144].

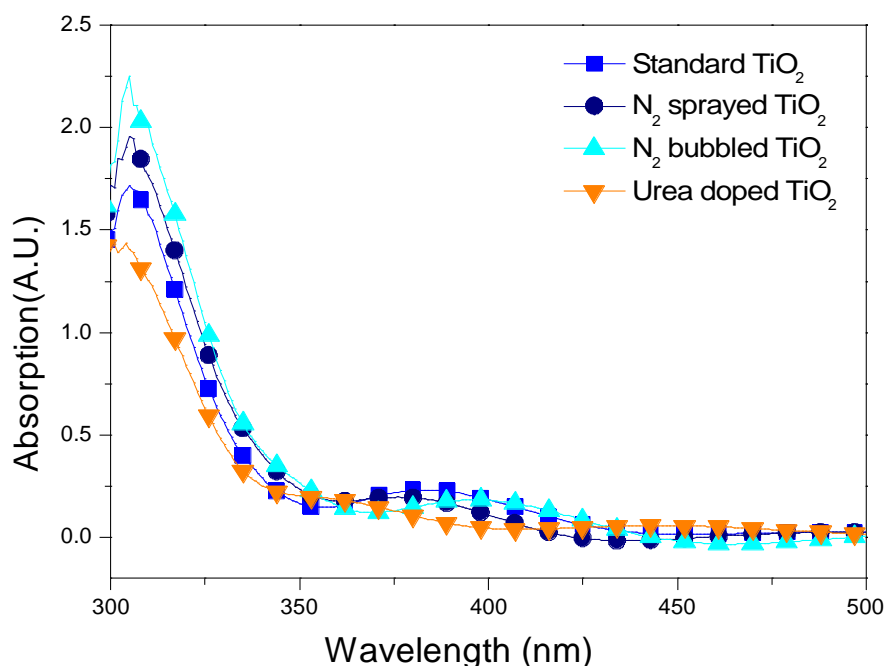


**Figure 3.5 Absorption of four types of TiO<sub>2</sub> films.** Standard TiO<sub>2</sub>, without doping (blue squares), N-doped TiO<sub>2</sub> via different N source: spraying with pressurized N<sub>2</sub> (black circles), bubbling with N<sub>2</sub> (light blue-triangles) and mixing Urea in precursor (red down-triangles).

On the other hand, the absorption of N-doped TiO<sub>2</sub> films obtained by adding Urea in TiO<sub>2</sub> precursor shows no change of the peak position; it indicates that this doping method is not effectively achieved. One possible reason is that Urea is decomposed relatively fast during the spray pyrolysis process deposited at a temperature as high as 450 °C, and the decomposition products evaporate immediately without doping in TiO<sub>2</sub> film. For further research, a slow calcined process like sol-gel method could improve this doping method by adding Urea.

However, an additional absorption peak shows in all four absorption spectra around 400 nm can be attributed to the interference of the incident and reflected light [145]. As discussed in section 2.3.3, the responding wavelength of interference effect on the absorption spectra is determined by both of the refractive index and the thickness of the film. Since their positions are slightly different on the absorption spectra, it indicates that either the TiO<sub>2</sub> films thicknesses are not the same, or the refractive index of TiO<sub>2</sub> films are changed by doping. The differences of film thickness might be caused by the slight uncontrollable change during depositions, and it could also induce the slight different nanocrystalline size of the TiO<sub>2</sub> films. This grain-size

difference can possibly lead to the variation on light scattering because of the different films' surface, and the UV cut-off position of TiO<sub>2</sub> on the absorption spectra as well [146]. All of these effects might be the reasons for the shift of the absorption peaks.

The observable change of absorption is a fast way to detect the changes in the fundamental structure of TiO<sub>2</sub> films. However, the absorption measurement cannot give a more accurate depiction of the film structure or the material components. To determine whether the TiO<sub>2</sub> was successfully doped or not, it can be coupled with an alternative characterization technique such as XPS, where one can clearly see the substitution of oxygen for nitrogen, or XRD, where there should be a slight shift in the peaks as observed by Jagadale et al. [146].

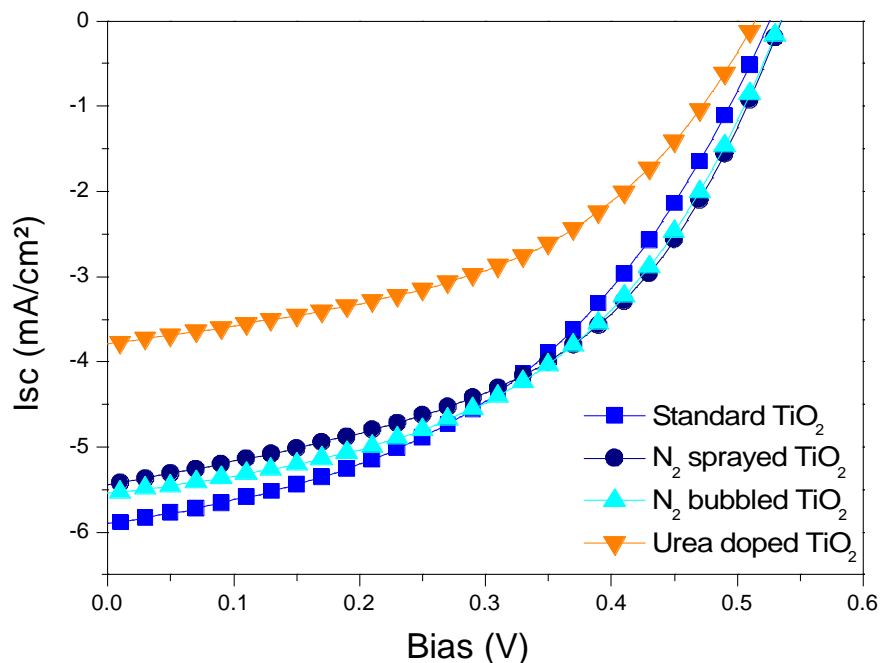


**Figure 3.6 I-V characterizations of TiO<sub>2</sub> films doped by different Nitrogen source.** I-V characteristics under illumination with simulated AM 1.5G solar light (100 mW/cm<sup>2</sup>). Without doping (blue squares), spraying with pressurized N<sub>2</sub> (black circles), bubbling with N<sub>2</sub> (light blue-triangles) and mixing Urea in precursor (red down-triangles).

Figure 3.6 shows the I-V measurement results for the devices based on four different TiO<sub>2</sub> films without and with different doping methods. Both of the N-doping by bubbling the gas in the precursor and by using pressurized nitrogen during spray pyrolysis present slight positive

effects on the performance of devices, especially on the  $V_{OC}$ , due to the enlarged bandgap by N-doping. However an unexpected slight reduce on  $I_{SC}$  is observed, which is supposed to be induced by the increasing light absorption of  $TiO_2$  layer. This can be explained by the filter effect of blocking layers discussed in Chapter 4, briefly described as follows: light absorption of  $TiO_2$  does not attribute to exciton photogeneration, but reduces the light intensity reaching the photoactive layer, resulting in a decreasing photocurrent. In comparison with the standard cell, the efficiencies of these two types of N-doped device are slightly enhanced from 1.74% to 1.86% and 1.90%, respectively. Although these results exhibit the average values calculated from six difference pixels of cells, the differences between these efficiencies are still unable to be clearly distinguished since the standard deviations are 0.5%.

On the other hand, the addition of Urea as a doping agent causes the device performance a significant decreasing, with the efficiency dropping down to 1.24 %. Corresponding to the absorption results, it indicates that the fast decomposition of Urea leaves defects in the  $TiO_2$  films rather than doping into the lattice, and then it reduces the performance of the complete device.

Despite the absorption measurement suggesting that both of bubbling  $N_2$  gas in the precursor solution and pressurized nitrogen for spray pyrolysis are promising methods to dope the blocking layer, the overall cell performance did not improve significantly compared to that of a standard reference cell without any doping. Further research is required to confirm the doping and to improve the efficiency of devices.

### **3.1.3 Mg-doped ZnO to enhance the $V_{OC}$**

One notable limitation on organic solar cells efficiency is the  $V_{OC}$  determined by the electronic bandgap of the donor-acceptor system [147]. It is given by the difference between the thermalized potential energies of the electron in the LUMO in the acceptor and the hole in the HOMO of the donor. However the  $V_{OC}$  in a real device is limited by several factors, such as the injected (dark) current, carrier recombination in bulk, or incomplete splitting of the quasi-Fermi levels determined by the incident light intensity [148, 149]. On the other hand, the  $V_{OC}$  and efficiency of devices could be increased by adding interface dipoles at the donor-acceptor interface in polymer-polymer devices [150], or optimizing the band offset of the donor-acceptor. This has been previously demonstrated in ZnO-P3HT hybrid solar cells, that substitution of Mg into ZnO to form  $ZnMgO_2$  alloy leads to a prominently reduced band offset

and an increased  $V_{OC}$  values in hybrid devices [151].

The  $ZnMgO_2$  film is produced by sol-gel method. For the sol-gel solution, zinc acetate-2-hydrate and magnesium acetate-4-hydrate (both from Sigma Aldrich, 99+ %) with a molar ratio of 4:1 are dissolved in a mixture of ethanol amine and 2-methoxyethanol with the weight ratio of 4:96, and the total concentration of metal acetate was 0.5 M. These solutions were spin-coated onto the ITO substrates and the gel films are thermal annealed zinc acetate film for 5 min at 375 °C in air. Following the description in section 2.2.2.2, standard ZnO film without doping is fabricated as a reference to compare the doping effect on devices performance. Then both ZnO films with and without Mg-doped films are rinsed with ethanol and dried with flowing  $N_2$  gas. 150 nm P3HT:PCBM blend layers are spin coated on top of these films. After  $WO_3$  and Ag being deposited by thermal evaporation, devices are annealed at 140 °C for 10 min.

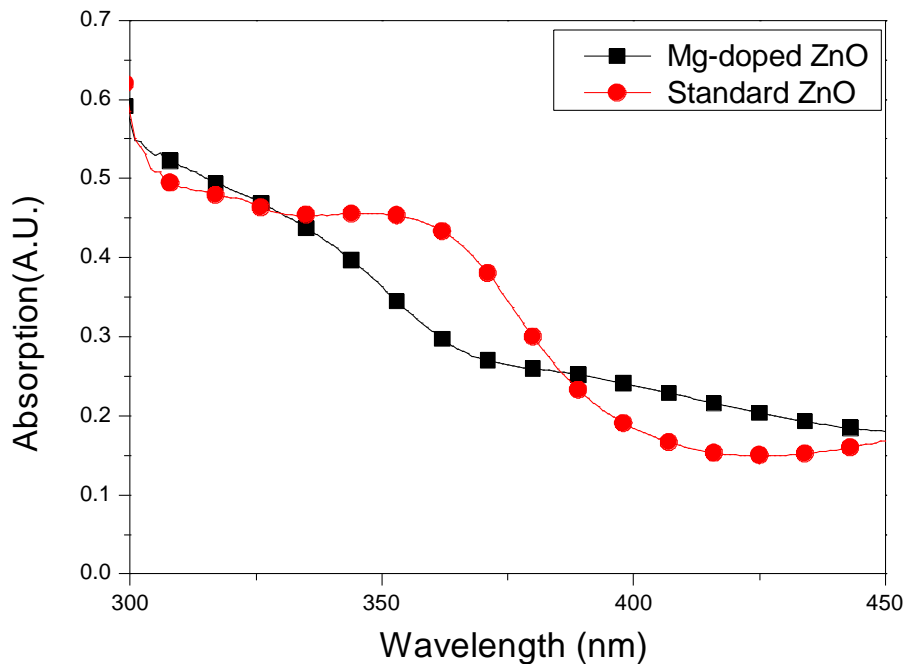
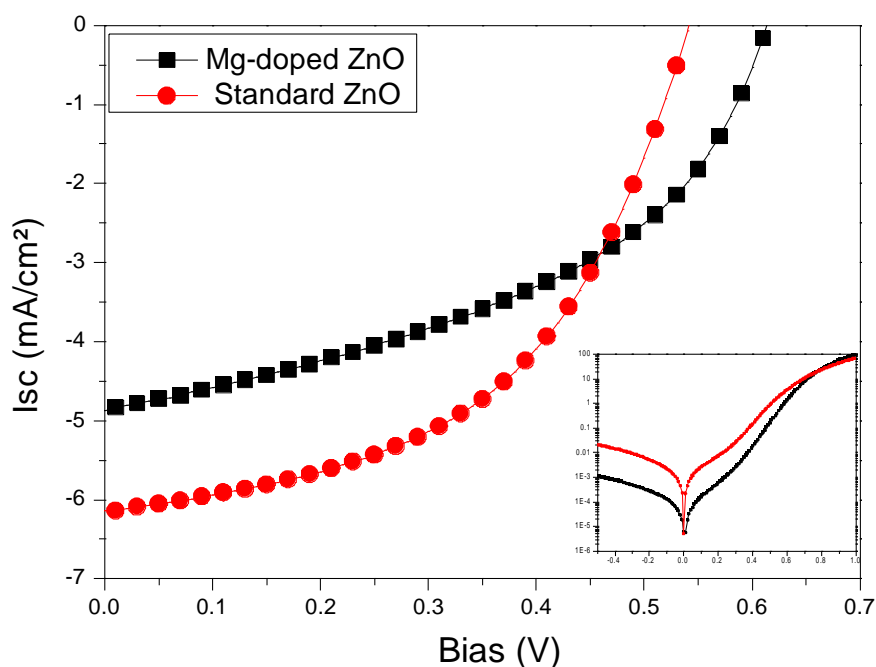


Figure 3.7 Absorption of ZnO films with (black squares) and without Mg-doping (red circles).

As the absorption spectra of ZnO films shown in Figure 3.7, an observable blue-shift appears on the ZnO band by Mg-doping. For the  $ZnMgO_2$  film, the absorption peak of metal oxide

shows at 350nm, and a second lower peak last until 400 nm. On the other hand, for the pure ZnO film, the absorption peak locals at 375nm, which is significantly sharper than the doped one. This indicates that the bandgap of ZnO is increased by Mg-doping as a result of the shift in its conduction-band energy closer to vacuum. It corresponds to a decrease in the donor-acceptor band offset, as reported in P3HT-ZnMgO<sub>2</sub> devices [151]. Further characterizations, such as XRD and XPS are required to confirm the doping state, and Kelvin probe measurements to clarify the work function shifts are favorable for device performance.

From I-V characterization presented in Figure 3.8, a significant improvement is observed on the  $V_{OC}$  of the solar cell based on Mg-doped ZnO layer, with a value increased from 0.54 to 0.62. The increasing of  $V_{OC}$  is attributed to the enhanced bandgap of ZnO by Mg-doping, which is corresponding to the absorption results. However, the decreasing  $I_{SC}$  observed for Mg-doped device is possibly attributed to the less efficient charge injection from PCBM into blocking layer, due to the up-shifted conduction band of ZnO-Mg. Another possibility is caused by the defects during the decomposition of ZnO sol gel leading to an increased recombination. These two problems can be resolved by optimizing the doping rate of Mg in ZnO film and the annealing process of the gel films.



**Figure 3.8:** I-V curves of ZnO films with (black squares) and without Mg doping (red circles). Measurements are carried out in dark and under illumination with simulated AM 1.5G solar light (100 mW/cm<sup>2</sup>).



### 3.1.4 TiO<sub>2</sub>-ZnO co-blocking layer

Both TiO<sub>2</sub> and ZnO work efficiently as hole blocking layers in organic inverted solar cells, and their influences on the devices performances will be discussed in Chapter 4. These two semiconductor materials have different advantages and drawbacks respectively. With the remarkable blocking effect for TiO<sub>2</sub>, it is difficult to modify the bandgap by doping, as shown in section 3.3.1. In addition, the commonly used methods during the fabrication of nanostructured TiO<sub>2</sub>, such as anodization is relatively environment unfriendly and not so easy to control, compared to ZnO nanowires grown by the hydrothermal method.

On the other hand, those disadvantages of TiO<sub>2</sub> are exactly the aspects for ZnO exhibiting the advantages of easy doping and controllable structuring. Another advantage of ZnO is the hydrophobic surface that could far improve the filling of polymer into the ordered nanostructure for hybrid solar cells, while the poor filling is a big challenge for the P3HT/TiO<sub>2</sub> devices [76, 152]. However the performance of solar cells based on ZnO in generally is not as efficient as TiO<sub>2</sub> devices. One important reason is that the high mobility and conductivity of ZnO films could increase the recombination in devices. Therefore a TiO<sub>2</sub>/ZnO co-blocking layer used for inverted solar cells is very promising to reduce the recombination of the device, as well as to optimize the bandgap and the morphology of the films.

The fabrication technique of standard TiO<sub>2</sub> films are described in section 2.2.1, which is prepared by spray TiO<sub>2</sub> precursor on ITO glass substrates at 450 °C. The ZnO film is produced by spin coating ZnO sol-gel solution on ITO and thermal annealing of the film at 375 °C in air (see section 2.2.2). For the TiO<sub>2</sub>/ZnO co-blocking layer fabrication, it is carried out in two steps: the first layer of TiO<sub>2</sub> film is deposited via spray pyrolysis. After cooling down to room temperature, the second layer of ZnO film is deposited on top of the first layer via sol-gel method. Absorption spectra of the three films of TiO<sub>2</sub>, ZnO and TiO<sub>2</sub>/ZnO are measured and shown in Figure 3.9. The inverted bulk-heterojunction solar cells based on the three types of blocking layers are assembled and characterized, and the devices performances are presented in Figure 3.10.

An obvious shift shows in the absorption spectra of the TiO<sub>2</sub>/ZnO co-blocking layer compared to TiO<sub>2</sub> film without the additional ZnO film coating. It indicates that the energy level of the combined layer slightly moves to a higher position due to the enlarged bandgap. This is corresponding to the improvement of V<sub>OC</sub> shown in the I-V curve of Figure 3.10. On the other hand, the FF of device based on the TiO<sub>2</sub>/ZnO co-blocking layer gives a value of 53%, which is

slightly increased from 49% given by ZnO solar cell. This should be attributed to the reduced recombination, which is induced by the efficient charge carrier blocking properties of TiO<sub>2</sub> films.

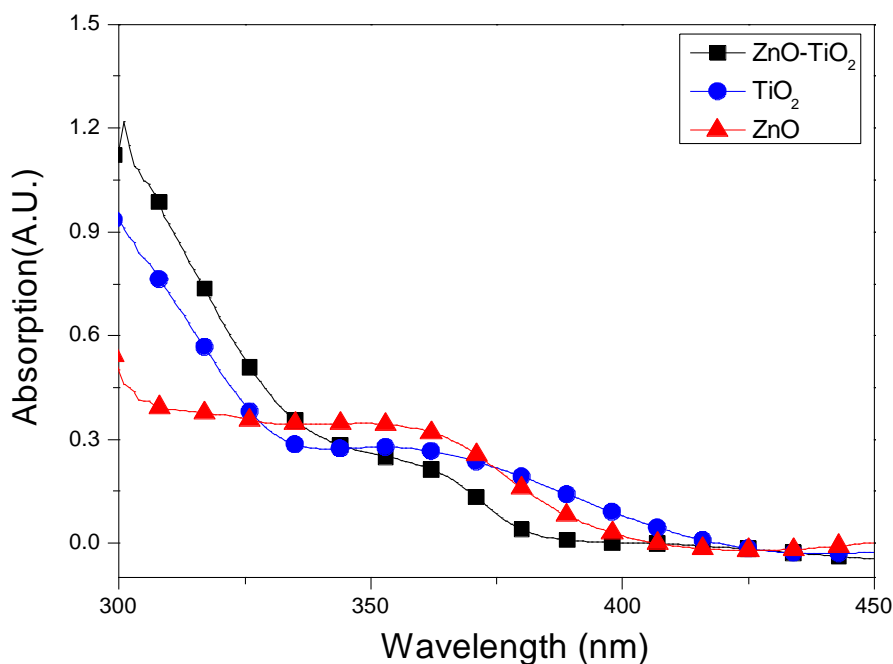


**Figure 3.9** Absorption of three blocking layers. TiO<sub>2</sub> (light blue-triangles), ZnO (red circles) and ZnO-TiO<sub>2</sub> layers (black squares).

In addition, TiO<sub>2</sub>/ZnO film co-blocking layers in solar cells devices could not only improve the performance, but also leaving more chance for further optimization of the devices in future research, such as modifying the bandgap to increase the  $V_{OC}$  by doping with Mg in ZnO film, and to grow the ZnO nanowires on the surface of TiO<sub>2</sub>/ZnO films via hydrothermal method. Initial results show that the devices based on ZnO NW grown on TiO<sub>2</sub>/ZnO films perform much better than the ones based on bared TiO<sub>2</sub>. This improvement of the device performance is supposed may be benefited by the reduced recombination due to efficient hole-blocking property of the TiO<sub>2</sub> layer.

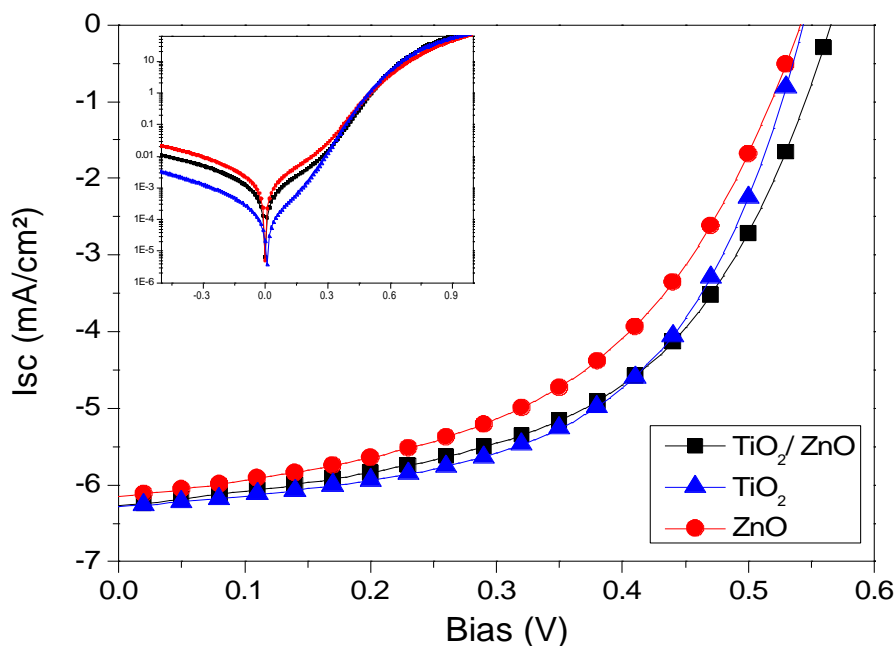


**Figure 3.10** I-V curves of devices based on three blocking layers.  $\text{TiO}_2$  (light blue-triangles), ZnO (red circles) and ZnO- $\text{TiO}_2$  layers (black squares). Measurements are under illumination with simulated AM 1.5G solar light ( $100 \text{ mW/cm}^2$ ).

### 3.2 P3HT:PCBM layer improvement

Among the geometries for organic photovoltaic devices investigated to date, polymer-fullerene based devices are mostly attractive due to their easy production technology. The advantage of the bulk-heterojunction concept has already been described in Chapter 1. In this respect, the P3HT:PCBM blend represents an optimized intermixture of the conjugated polymer as donor and the fullerene as acceptor. Many studies have shown that P3HT offers the added advantage of a tendency to self-organize, which allows the morphology of the blend to be controlled by varying the processing conditions [153, 154]. In this section, experiments are carried out to optimize the P3HT:PCBM layer by changing the parameters of the solution process, film thickness and post treatments.

### 3.2.1 P3HT:PCBM blend solutions

Initially, it has been demonstrated that the performance of a blend solar cell can be determined by the solvent used to dissolve the organic semiconductor. In detail, the selection of a proper solvent for a P3HT:PCBM bulk-heterojunction solar cell seems to be between chloroform (CF) and chlorobenzene (CBZ). The concentrations of photoactive materials are kept the same in the two solvents, 30 mg/ml for P3HT and 24 mg/ml for PCBM. Then they are mixed for blend solutions respectively with a ratio of 1:1. After spin coating the two blend solutions on TiO<sub>2</sub> coated ITO substrates, absorption measurements are carried out. Solar cells are finished by evaporating WO<sub>3</sub> and Ag on top of the two blend layers and their performances are recorded by EQE and I-V characterization.

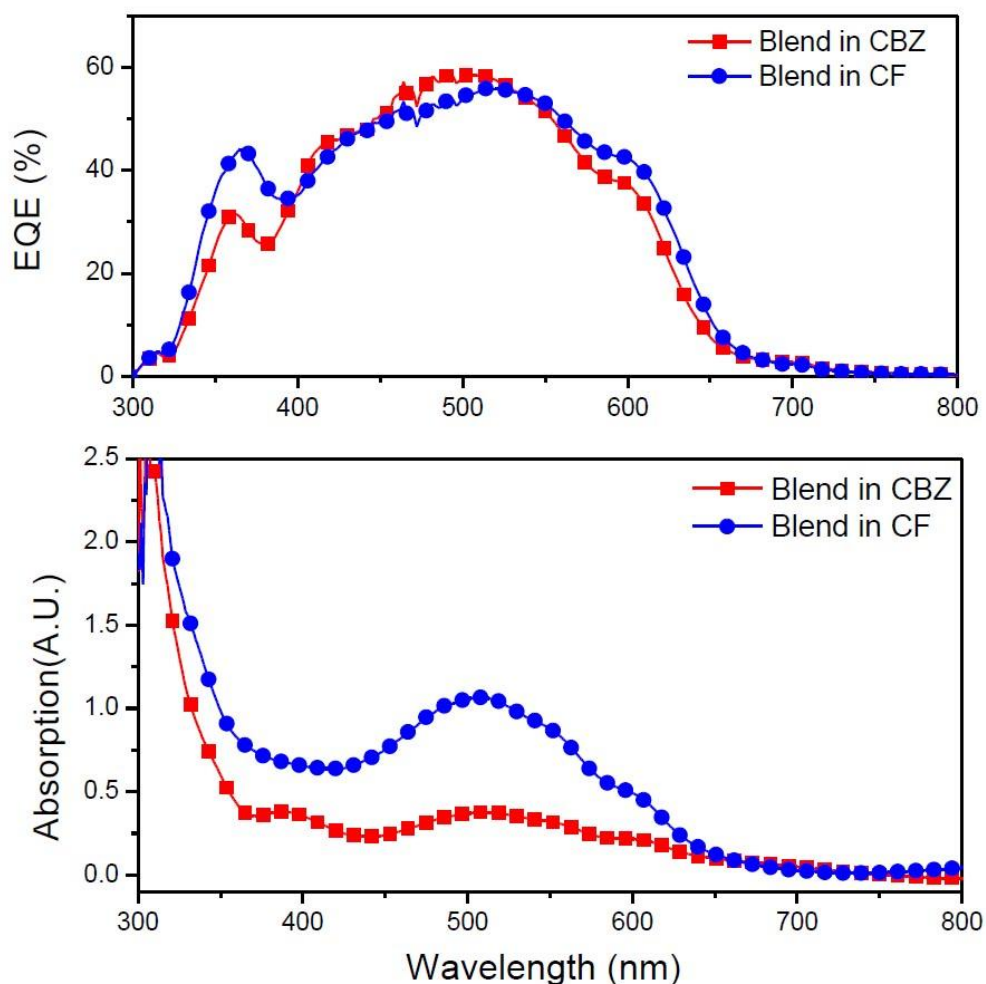
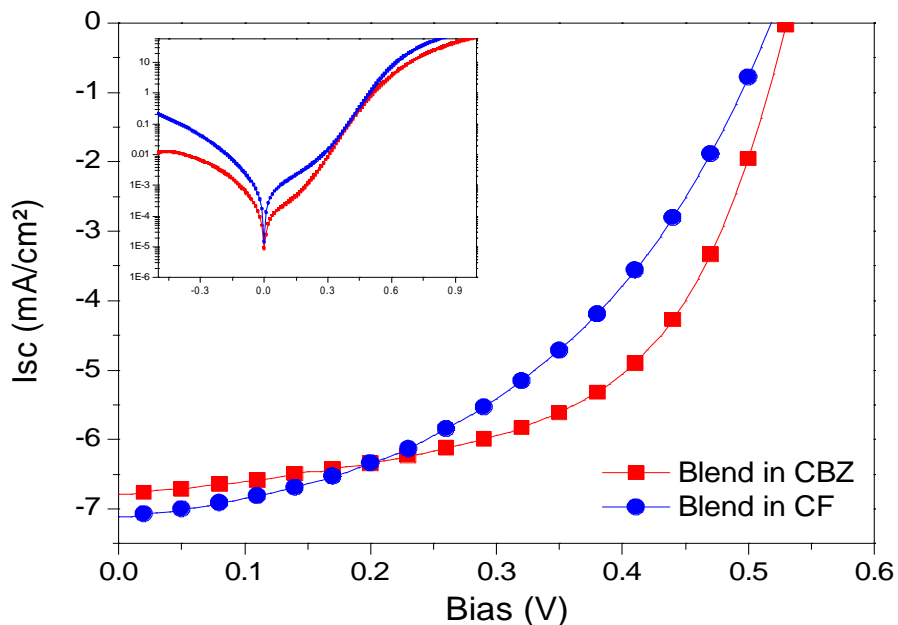


Figure 3.11: EQE and Absorption measurements of P3HT:PCBM blend dissolved in different solutions.

Chlorobenzene (red squares) and Chloroform (blue dots).

It is explicitly demonstrated in the EQE spectra shown in Figure 3.11 that the CBZ-based devices exhibit quite similar efficiency of converting photons to electrons as the device produced with CF. However, the absorption results show that the CF-based blend layer absorb significantly stronger than that based on CBZ. The high absorption peak can be attributed to a much thicker blend film, benefited from the quick evaporation of CF during spin coating. Therefore the CBZ-based devices show much higher internal conversion efficiency (IPCE). I-V characterizations confirm this by showing increased FF and  $V_{OC}$  for the devices fabricated with CBZ, leading to an approaching 20% improvement on efficiency with a value of 2.3%.

However a decreased short-circuit current density is observed in the I-V results of CBZ-based device due to the lower absorption of thin blend layer thickness. During spin coating process, blend film thickness could be increased due to the fast evaporation of CF solvent with a low boiling temperature. As a result, a higher absorption shows on the CF-based blend layer, leading to a higher value of  $I_{SC}$ . On the other hand, the fast evaporation of the solvent tends to induce segregation of the PCBM molecules into clusters [155], and then reduce the interface area in bulk-heterojunction layer for charge separation, resulting in a low FF. Morphology measurements such as AFM or SEM images of blend layer are required to verify this assumption.



**Figure 3.12: I-V characterization of blend solar cells produced in different solutions: Chlorobenzene (red squares) and Chloroform (blue dots)**

After mixing the P3HT and PCBM CBZ-based solutions, the stirring time of blend solution is investigated for its influence on the performance of solar cells. Before the I-V characterization, devices are produced by spin coating four different blend solutions stirred for incrementing times from 12 hours to 96 hours, while the concentrations of P3HT and PCBM are kept the same at 30 mg/ml and 24 mg/ml, respectively. Followed by the  $\text{WO}_3$  and Ag evaporation, devices are assembled for the performance characterization under 1.5 AM solar light illumination. The results presented in Table 3.1 show no clear difference on the efficiencies of the devices depending on the stirring time for the blend solutions. It is indicated that the blend solution is relatively stable after being mixed, and a stirring time of 12 hours is enough for a homogeneous mixture of P3HT and PCBM for the device production.

Stirring time (min)	PCE (%)	$V_{OC}$ (V)	$I_{SC}$ (mA/cm <sup>2</sup> )	FF (%)	$R_{Sh}$ ( $\Omega$ cm <sup>2</sup> )	$R_s$ ( $\Omega$ cm <sup>2</sup> )
12h	2.04	0.59	7.44	45	954	12.3
24h	2.06	0.58	7.38	45.4	965	11.2
48h	1.98	0.58	7.15	45.5	778	12.4
96h	2.01	0.57	7.26	44.6	622	13.6

**Table 3.1 Performances of blend solar cells produced in solutions stirred for different times.** Characterization carried out under 100W/cm<sup>2</sup> simulated solar illumination. Average values are given from calculation of 6 pixels of solar cells.

### 3.2.2 P3HT:PCBM ratios

Further consideration has to be given on the mixing ratio of blend solutions. As reported before, a P3HT:PCBM weight ratio of 1:0.8 could give the highest PCE for the normal structure solar cells [156]. However, this value may be slightly different for the inverted solar cells. Experiments have been carried out to optimize the ratio of P3HT:PCBM in blend solution used in the  $\text{TiO}_2$  based solar cells to improve the devices performance.

In this experiment, blend solutions with six different ratios are spin coated on  $\text{TiO}_2$  substrates.

While the concentrations of P3HT and PCBM in CBZ are kept constant as 30 mg/ml and 24 mg/ml respectively, the volume ratio of the two solutions changes from 1:0.6 to 1:1.4 for blend mixtures. Devices with six different ratios are assembled and characterized.

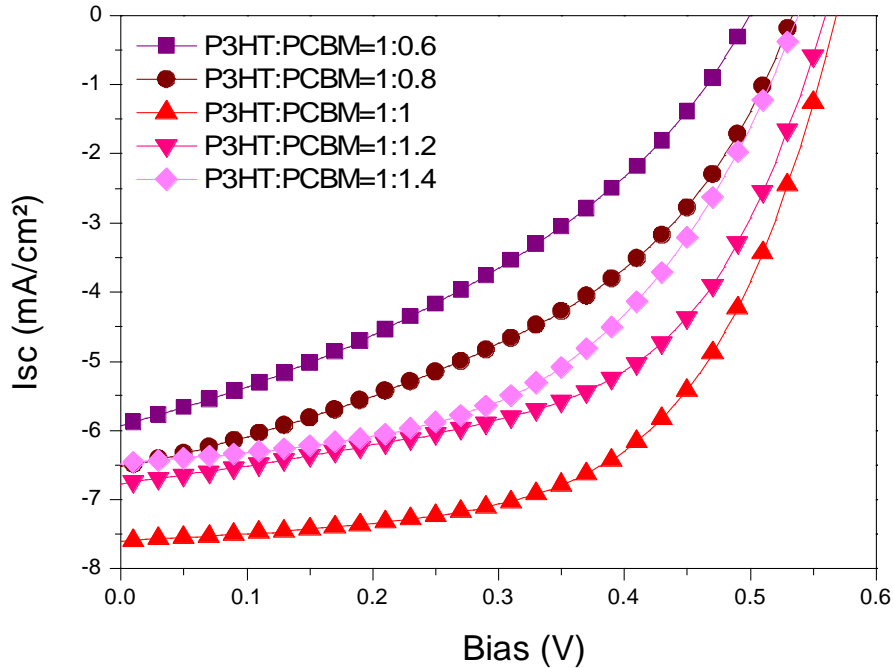


**Figure 3.13: I-V curves of devices with different ratios of P3HT and PCBM from 1:0.6 to 1:1.4.** Data taken under illumination with simulated AM 1.5G solar light ( $100 \text{ mW/cm}^2$ ).

As shown in Figure 3.13, significant improvements show in the I-V characterization results of solar cells, especially on  $I_{SC}$ ,  $V_{OC}$  and FF. While volume ratio of P3HT and PCBM solutions changing from 1:0.6 to 1:1, the absolute value of  $I_{SC}$  increases from  $5.95 \text{ mA/cm}^2$  to  $7.48 \text{ mA/cm}^2$ , however further increasing of the PCBM content leads to the decreasing of  $I_{SC}$ . Similar trends are shown in  $V_{OC}$  and FF as well: the 1: 1 volume ratio composition for blend solution gives the highest  $V_{OC}$  and FF, while a blend ratio reduces both of them. As a result, the maximum values of efficiency as high as 2.25% is obtained for the inverted structure solar cell, using the optimized blend volume ratio of 1:1. Calculated from the concentrations of P3HT and PCBM solutions, the optimized weight ratio for blend is 1:0.8, which is the same as for the normal structure devices.

Evidences have been given in an early report to explain the influences of blend ratio on the device performance that the surface morphology was slightly coarser for the weight ratio of 1:0.8 compositions of P3HT and PCBM [156]. For the blend material system, it has been established that a fairly homogenous blend is obtained for PCBM contents up to 50% by weight, and that at higher PCBM content, PCBM rich domains begin to segregate [157]. Due to the high electron mobility in PCBM, the PCBM rich domains may assist charge collection in blends, which induce the improvement on device performance. However further increased PCBM content induces a decreasing on the charge carrier collection because of the recombination in the over enlarged PCBM rich domains.

### **3.2.3 P3HT:PCBM layer thickness**

In organic solar cells, 60 % of the light intensity could be absorbed by a 100 nm P3HT:PCBM blend layer at the absorption peak of 500-650 nm [158]. After photon absorption and exciton dissociation, free charge carriers have to be collected and transfer to the electrodes before recombination. Due to the short exciton diffusion length, the possibility of charge extraction is much higher in thin a layer, which is attributed to a low recombination rate during the charge transport. On the other hand, a thicker photoactive layer can absorb more light, according to the Lambert-Beer's law. Additionally, the charge carrier selection property of TiO<sub>2</sub> films in inverted solar cells could efficiently improve the forward charge transfer and reduce back recombination at the interface of blocking layer and active layer [159]. Therefore performance of solar cell based on TiO<sub>2</sub> films can be further improved by optimizing the thickness of the active layer for a compromised absorption and charge collection.

Blend films with five different thicknesses are spin coated on a thin layer of TiO<sub>2</sub> deposited on ITO substrates. The thickness of blend layer is controlled by the blend solution: a gradually enhanced concentration of P3HT solution is used from 10 mg/ml to 50 mg/ml, mixed with an equal volume of PCBM solution, while the weight ratio of P3HT:PCBM keeps constant at 1:0.8. The blend layers thicknesses are measured with Dektak, absorption of the films are carried out by an UV-vis spectrometer, and device performances are characterized through I-V measurements.

As shown in Figure 3.14, the absorption of solar cells has been influenced significantly by the thickness of blend layers, and it increases with the thickness of blend layer increasing from 50 nm to 250 nm. The absorption peak shown at the wavelength from 500 nm to 650 nm is mainly



attributed to the P3HT absorption [184]. This dependence on the thickness of blend layer follows the Lambert-Beer's law, which is defined as the absorption of light to the proportion of the material through which the light is travelling [160].

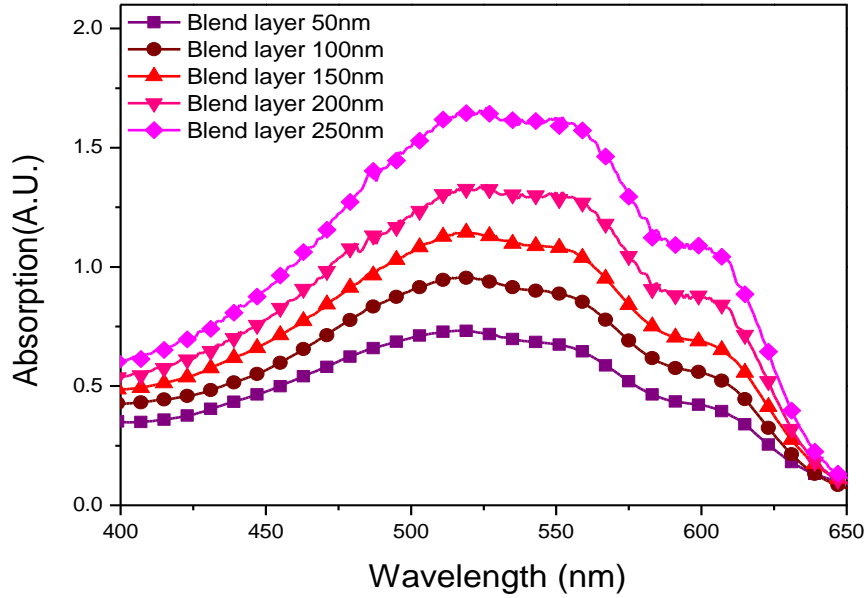


Figure 3.14: Absorption measurement of blend layers with five different thicknesses from 50nm to 250nm.

Blend layer thickness (nm)	PCE (%)	$V_{OC}$ (V)	$I_{SC}$ (mA/cm <sup>2</sup> )	FF (%)	$R_{Sh}$ ( $\Omega$ cm <sup>2</sup> )	$R_s$ ( $\Omega$ cm <sup>2</sup> )
50	1.3	0.59	3.69	45.1	1455	4.28
100	1.89	0.58	5.59	48.4	1061	7.72
150	2.25	0.58	7.44	49.5	989	6.07
200	2.01	0.57	7.38	49.6	1205	9.23
250	1.95	0.57	6.72	49.2	1322	8.65

Table 3.2: current-voltage measurement of devices with thicknesses of blend layers varies from 50 to 250nm.

Characterizations are carried out under 100W/cm<sup>2</sup> simulated solar illumination. Average values are given from calculation of 6 pixels of solar cells.

The averaged values of the parameters representing the solar cells performance are depicted in Table 3.2. It is indicated that the blend layer thickness significantly influences on the device performance. The efficiency and  $I_{SC}$  increase with the increasing layer thickness, and their maximum values of 2.44% and 7.44 mA/cm<sup>2</sup>, respectively, are shown for the devices with a 150 nm blend layer. However, while the blend layer thickness further increases, both the efficiency and  $I_{SC}$  reduce. Since  $V_{OC}$  is mainly correlated to energy levels of the donor: acceptor material, this value remains constant for all the devices. The variations of  $R_S$  and  $R_{Sh}$  do not depend on the blend layer thickness.

Initially, the increasing thickness of blend films is considered to be responsible for the significantly improvement on efficiency and  $I_{SC}$  due to the enhanced photon absorption and consecutively photogenerated charge carrier rate. While the blend layer thickness further increases from 150 nm to 250 nm, it results in a slight decreasing performance of device. This could be explained by the reduced charge extraction due to the thickness of blend layer that far beyond the charge diffusion length, leading to an increased recombination in the photoactive layer. As a summary of the results discussed above, the optimized thickness for blend layer is 150 nm, which exhibits the best efficiency for the TiO<sub>2</sub> based inverted device.

### **3.2.4 Post-deposition treatment process on blend layer**

Recently studies have shown that the morphology of the blend film could be controlled by the post-deposition procedures, such as drying process [8, 156, 161], melting of bilayers [162], thermal annealing of blends [6, 163]. These different treatments promote the formation of phase separated morphology with crystalline P3HT and PCBM domains and in all cases lead to an improved photovoltaic device performance [155]. In this section, two steps of post-deposition treatments: a slow dry process and an annealing process are applied on the blend layers. The device performances are characterized via I-V measurement, in order to optimize the fabrication process.

#### **Spin and dry process**

The blend films are all spin coated at a speed of 600 rpm for 1 min, followed by the drying processes that carried out in three different ways. The fast dry process is immediately carried

out after the slow spin coating with a high spin speed of 3000 rpm immediately applied. The second dry method is via exploring the samples in air after being taken out of spin coater. During the slow dry process, samples are covered with petri dish for 30min after taking out of spin coater. After top contact deposition, all three types of devices are assembled and characterized.

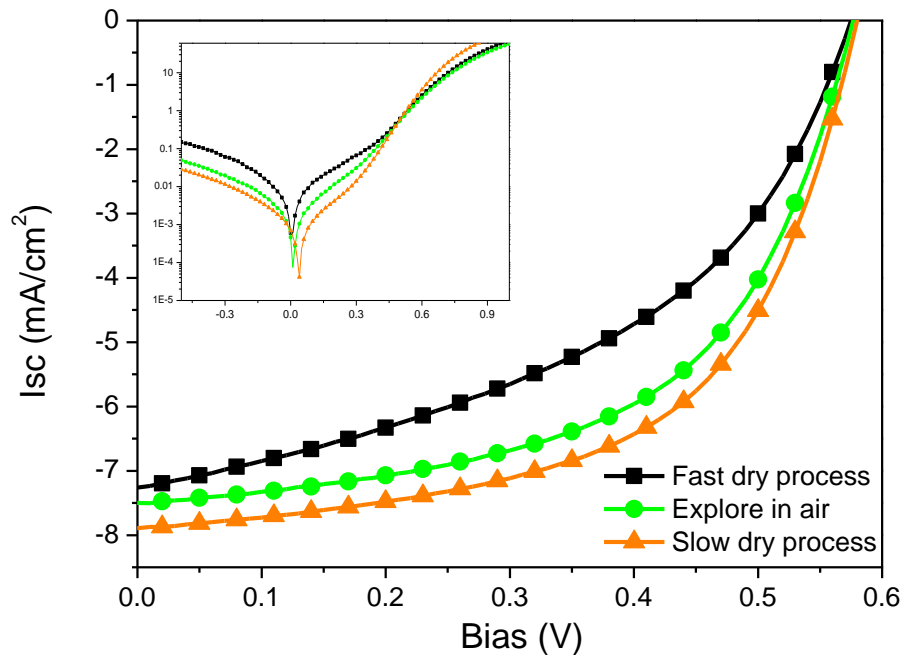


**Figure 3.15: I-V characteristics of devices with blend layers dried by: Fast dry process (black squares), explore in air (green circles) and Slow dry process (red triangles).** Data is obtained for under illumination with simulated AM 1.5G solar light ( $100 \text{ mW}/\text{cm}^2$ ).

Among the parameters of devices performances shown in Figure 3.15, FF and  $I_{sc}$  are observed to increase when devices are dried for longer time. When blend layers are dried via a fast process, the device performs badly with a FF as low as 42%. After the dry process carried out within 30 min, the performance of solar cell is significantly improved, exhibiting a remarkable high FF of 57.3% and a PCE of 2.40%. This improvement can be attributed to the enlarged donor-accepter interface area induced by the slow-grown P3HT:PCBM layer via the self-organization process, which in turn enhances ordered structure formation in the thin film [155].

### Thermal annealing process

After a slow dry process, the devices are applied for two different annealing processes. A pre-annealing process is carried out before the deposition of  $\text{WO}_3$  and Ag top contact at  $105\text{ }^\circ\text{C}$  for 5 min. And a post-annealing process is applied on the devices after top contact deposition at  $140\text{ }^\circ\text{C}$  for 10 min. Moreover, a non-annealed device is presented as a reference.

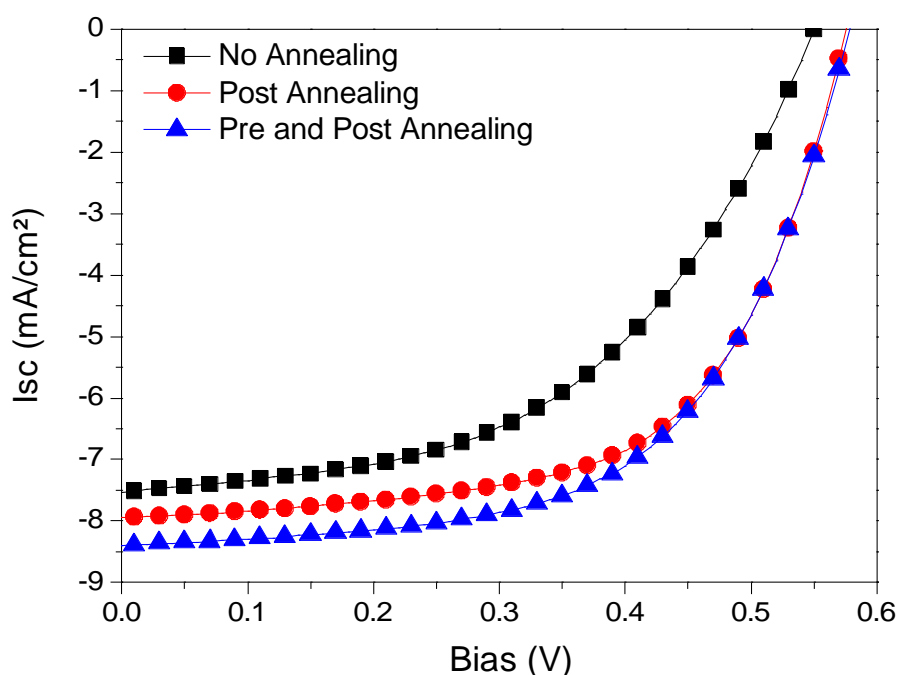


**Figure 3.16: I-V curves of devices with blend layer by different annealing processes:** No annealing (black squares), Post annealing (red circles) and Pre-Post annealing (blue triangles). Samples are characterized under illumination with simulated AM 1.5G solar light ( $100\text{ mW/cm}^2$ ).

The I-V curves for all the devices shown in Figure 3.16 indicate that both the pre-annealing and post-annealing can improve the performances of solar cells. By applying the two processes on devices, a significant enhancement shows on the device efficiency with a value as high as 2.40%, almost 20% increasing compared to the no annealing devices. Thermal annealing of P3HT films has been shown to enhance crystallization and to increase the carrier mobility in photovoltaic solar cells [164]. Annealing the slow-grown films might mainly help to remove the residue solvent and to reduce the number of trapping sites for a better carrier transport and extraction. Another positive potential of the annealing process is an obtained smooth surface

morphology of photoactive layers that can improve organic/cathode contact [155].

Further characterizations like morphology of blend layer are necessary to confirm the assumptions of the influence of annealing steps on devices performance. Since the optimized processes for P3HT and PCBM blend layer could improve the solar cells, they are taken for the inverted device fabrication and described as below:

P3HT and PCBM are dissolved in chlorobenzene with concentrations of 30 mg/ml and 24 mg/ml, respectively; After being mixed with a volume ratio of 1:1, blend solution is stirred in dark for 12 hours; then blend layers are obtained via spin coating the blend solution on a cleaned thin TiO<sub>2</sub> layers at a slow spin speed of 600 rpm for 1 min; a following slow dry process are carried out by covering the as-deposited samples with a petri dish for 30min; a pre-annealing process at 105 °C for 5 min and a post-annealing process at 140 °C for 10 min, are implement on the devices respectively before and after the deposition of WO<sub>3</sub> and Ag top contact.

### **3.3 Spray-deposited PEDOT: PSS for air stable inverted organic solar cells**

This section is based on the publication by J. Weickert, H. Sun et al., 2010, published in Solar Energy Materials & Solar Cells. Device fabrication and characterization are carried out by J. Weickert and the author of thesis, the manuscript has been written by J. Weickert.

#### **3.3.1 Background**

PEDOT:PSS is a conductive polymer with the potential to substitute metal contacts in the future. As an interface between active layer and top electrode that is alternative to WO<sub>3</sub>, it allows low-cost production, roll-to-roll processing and the fabrication of large area solar panels [165-167]. PEDOT:PSS exhibits a constant work function of -5.0 eV and is commonly used in non-inverted organic solar cells to enhance the hole collecting behavior of the bottom electrode. The use of PEDOT:PSS is also reported in inverted solar cells were the layer is mostly spin coated at 5000-6000 rpm [168, 169]. However, PEDOT:PSS has to be applied on top of the active layer and the wetting of the organic material is often insufficient due to the hydrophilic

character of the PEDOT:PSS suspension in aqueous solution.

Here we report on efficient inverted P3HT:PCBM solar cells with lifetimes exceeding 100 days for storage under ambient conditions in the dark. Cell fabrication is performed completely without the use of a nitrogen glovebox. We study the influence of a PEDOT:PSS interlayer on device performance and device time evolution. A novel deposition method is presented which allows the controlled deposition of a thin homogenous PEDOT:PSS film onto organic materials.

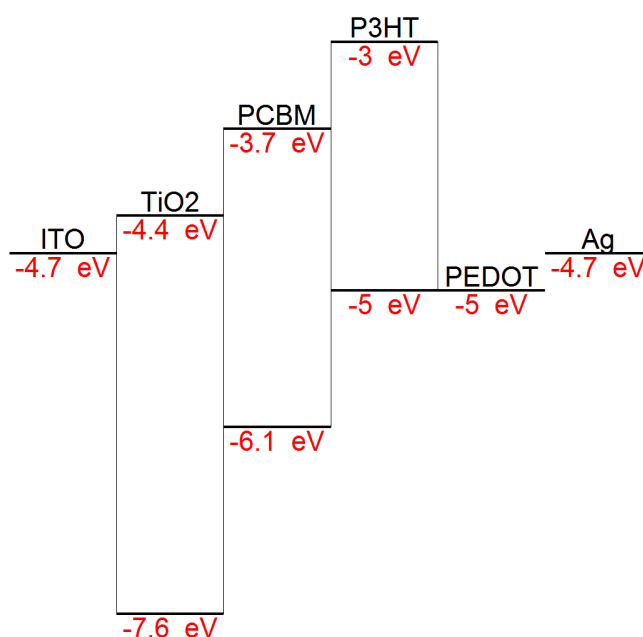


**Figure 3.17** Energy levels for an inverted P3HT:PCBM solar cell. Electrons are collected at the TiO<sub>2</sub> bottom electrode, holes at the Ag top contact. The work function of the PEDOT:PSS interlayer matches the HOMO level of the P3HT.

Figure 3.17 gives an overview over the energy levels in an inverted P3HT:PCBM solar cell. The hole blocking TiO<sub>2</sub> collects electrons from the acceptor PCBM whereas holes are transported through the P3HT towards the PEDOT:PSS. The work function of the PEDOT:PSS and the TiO<sub>2</sub> are close to the HOMO of PCBM and the LUMO of P3HT, respectively. This allows efficient electron injection into the TiO<sub>2</sub> whereas holes are collected at the PEDOT:PSS.

### 3.3.2 PEDOT:PSS layer deposition

For the PEDOT:PSS (H.C. Starck 1.2-1.4% in H<sub>2</sub>O) deposition the sample is mounted on a spin coater and abundantly sprayed with a 1:10 solution of PEDOT:PSS in 2-propanol using a glass nozzle. Immediately after wetting the sample is spin coated at 600 rpm to yield a homogenous layer of PEDOT:PSS. The thickness of the PEDOT:PSS can be easily varied using different spin speeds. Depositing the PEDOT:PSS via spray-coating before spinning is necessary to yield homogenous films [170], since other methods like drop-casting lead to insufficient wetting. To examine the influence of a PEDOT:PSS interlayer between the polymer-fullerene blend and the top contact solar cells are fabricated with and without spray deposited PEDOT:PSS of approximately 40 nm thickness. Additionally, two different methods are used to apply the metal top contact, namely thermal evaporation and sputtering.

### 3.3.3 Device performance

Current voltage curves acquired under simulated solar illumination (100 mW/cm<sup>2</sup>) for the different top contacts are shown in Figure. 3.18 Calculated characteristics are summarized in Table 3.3. The FF is defined as

$$FF = I_{MPP} \cdot V_{MPP} / I_{SC} \cdot V_{OC}$$

where  $I_{SC}$  denotes the short cut current,  $V_{OC}$  the open circuit voltage and  $I_{MPP}$  and  $V_{MPP}$  the current and voltage at the maximum power point, respectively.  $R_{Sh}$  and  $R_s$  are obtained following the generalized Shockley diode model and calculated from linear fits to the I-V curves at small reverse bias and moderate forward bias, respectively.

Both devices without PEDOT:PSS exhibit reasonable photocurrents but low FF around 35 %, low  $V_{OC}$  of about 400 mV and overall PCE below 1 %. In contrast, the devices utilizing PEDOT:PSS provide PCE values of 1.96 % and 2.44 % and FF above 50 % and 55 % for evaporated and sputtered Ag, respectively. Additionally, the  $V_{OC}$  is enhanced to almost 0.6 V for both metal contacts due to introduction of a PEDOT:PSS interlayer (Table 3.3).

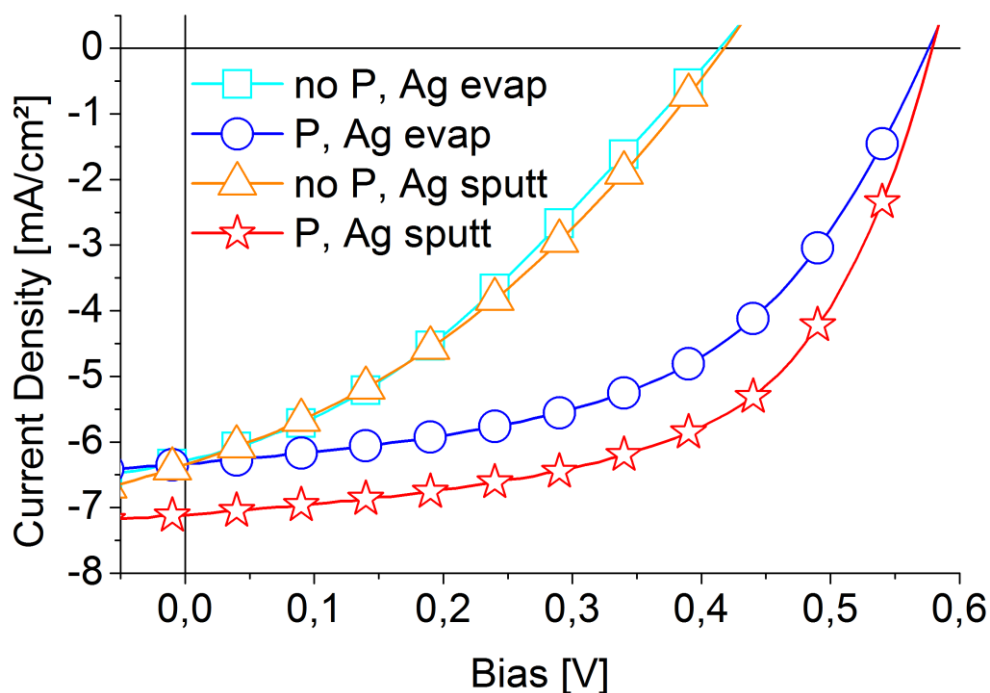


**Figure 3.18** I-V characteristics under illumination with simulated AM 1.5G solar light ( $100 \text{ mW/cm}^2$ ). Data is shown for devices with PEDOT:PSS (circles: thermally evaporated Ag, stars: sputtered Ag) and without PEDOT:PSS (squares: thermally evaporated Ag, triangles: sputtered Ag). Devices with PEDOT:PSS exhibit higher  $V_{OC}$  and FF.

The significantly better performance with PEDOT:PSS is attributed to two different effects. Ideally, the donor's HOMO and the acceptor's LUMO match the work functions of the hole and electron collecting electrodes, respectively. Ohmic contacts between the active materials and the external electrodes allow high photocurrents due to good charge extraction and high  $V_{OC}$  [171]. PEDOT:PSS exhibits a work function of  $-5.0 \text{ eV}$  matching the HOMO of P3HT better than the bare silver contact which has a work function between  $-4.5 \text{ eV}$  and  $-4.7 \text{ eV}$  [172] (compare Figure 3.17). Besides, PEDOT:PSS is known to accept holes from various donor materials even if the respective HOMO level doesn't fit its work function [173]. The improved energy level matching is also reflected in relatively lower  $R_s$  values for the devices with PEDOT:PSS.

The second effect caused by the PEDOT:PSS might be the protection of the P3HT:PCBM layer during the top contact deposition. Sputtered Ag-atoms are assumed to have higher energy when hitting the organic film (deposition rate about  $1.0 \text{ \AA/s}$ ). Additionally, when sputtering Ag clusters of different size are deposited next to single atoms [174]. Therefore, silver might



penetrate into the active layer especially in case of the sputtering [175]. This is also reflected in low  $R_{Sh}$  indicating leakage currents that are limiting the device performance and reducing the FF.  $R_{Sh}$  is only  $231 \Omega \cdot \text{cm}^2$  for the evaporated Ag and even lower ( $154 \Omega \cdot \text{cm}^2$ ) for the sputtered Ag, probably due to the deeper penetration into the organic layer during the sputtering. Leakage currents are known to also affect the  $V_{OC}$  if  $R_{Sh}$  is reduced to a certain point [176] which also might partly explain the observed low  $V_{OC}$  values for the devices without PEDOT:PSS. However, we attribute the lower  $V_{OC}$  mainly to a non-ideal work function of the fresh prepared Ag top contact as discussed later.

	PCE [%]	$V_{OC}$ [V]	$I_{SC}$ [mA/cm <sup>2</sup> ]	FF [%]	$R_{Sh}$ [ $\Omega \cdot \text{cm}^2$ ]	$R_S$ [ $\Omega \cdot \text{cm}^2$ ]
no PEDOT, Ag evap	0.92	0.41	6.29	34.1	231	26.9
PEDOT, Ag evap	1.96	0.58	6.32	51.7	638	17.6
no PEDOT, Ag sput	0.96	0.42	6.34	34.7	154	14.7
PEDOT, Ag sput	2.44	0.58	7.11	56.9	1019	2.62

**Table 3.3** Calculated characteristics from current-voltage data acquired under simulated solar illumination.

Values are given for solar cells with and without PEDOT:PSS and with thermally evaporated and sputtered Ag top contact.

The higher photocurrent observed for the sputtered compared to the evaporated top contacts with PEDOT:PSS is attributed to a better contact between the silver and the PEDOT:PSS. Very likely sputtered Ag penetrates deeper into the PEDOT:PSS than slowly evaporated Ag allowing for an unhampered hole injection into the silver electrode. This is also reflected in lower  $R_S$  values for the sputtered top contacts for both solar cell types, with and without PEDOT:PSS. The reduced  $R_S$  is also the main reason for the high FF of the device with PEDOT:PSS and sputtered Ag.

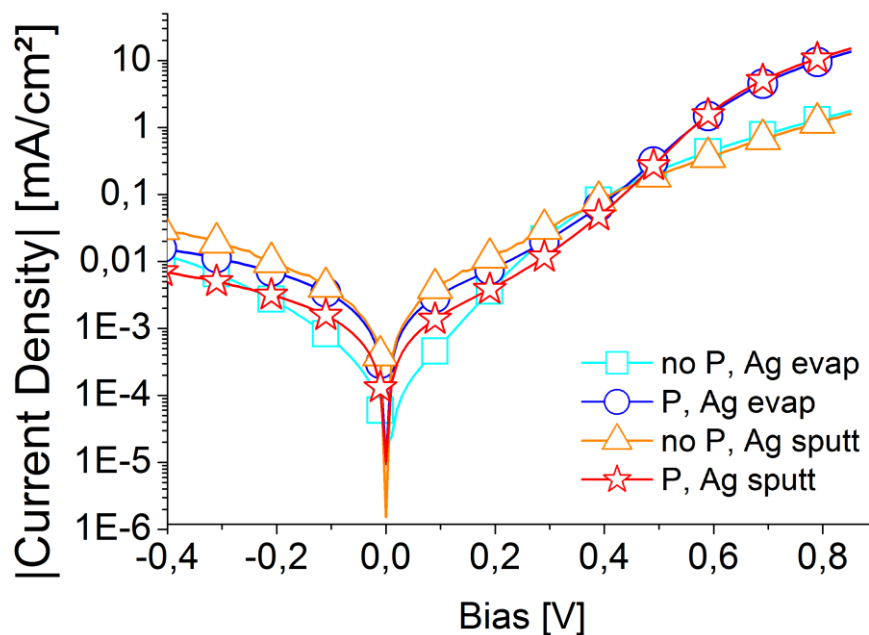


**Figure 3.19 Dark I-V curves.** Devices with PEDOT:PSS (circles: thermally evaporated Ag, stars: sputtered Ag) show higher currents in forward direction a shape indicating no space charge limits. Cells without PEDOT:PSS (squares: thermally evaporated Ag, triangles: sputtered Ag) seem to be space charge limited and allow only significantly lower forward currents.

Further hints for better hole collection with PEDOT:PSS are provided by the dark I-V curves in Figure 3.19. The devices with PEDOT:PSS allow a much higher current in forward direction and an enhanced rectifying behavior. Moreover, the differences in shape of the I-V curves with and without PEDOT:PSS at moderate forward bias indicate space charge limits in the devices without PEDOT:PSS [177, 178]. Since the electron collection in the  $\text{TiO}_2$  should be similar with and without PEDOT:PSS and P3HT:PCBM solar cells are known to be space charge limited mainly due to slow hole transport [32] we attribute this to space charge forming at the organic-silver interface if no PEDOT:PSS is used. In contrast, if the PEDOT:PSS interlayer ensures an ohmic contact between the P3HT and the top electrode holes can exit the device unhamperedly.

The observed variations of the reverse current in the dark I-V curves also correspond to the deeper penetration of the sputter Ag into organic layers. The device without PEDOT:PSS and the sputtered Ag exhibits the highest current at reverse bias, i.e. the highest leakage whereas the reverse current is significantly reduced if PEDOT:PSS protects the organic layer during the

sputtering.

The overall relatively low performance of about 2.5 % compared to record values of 5-6 % is attributed to two facts. First, our fabrication does not include any processing steps in an inert nitrogen atmosphere. Both spin coating and annealing are performed in ambient air. Secondly, the substrates used are suffering at the elevated temperatures used for spray pyrolysis of the  $\text{TiO}_2$  layers. This increases series resistances caused by the ITO which loses conductivity at the high temperatures during the  $\text{TiO}_2$  spray pyrolysis. Additionally, our active area of  $0.125 \text{ cm}^2$  is relatively large.

### 3.3.4 Time evolution of the $V_{\text{OC}}$

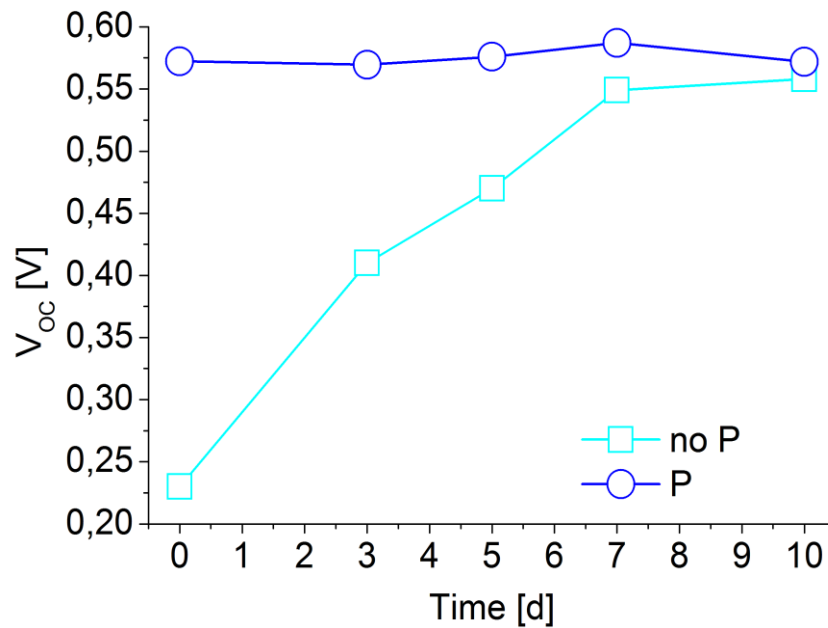


**Figure 3.20:** Time evolution of the  $V_{\text{OC}}$  for device with (circles) and without (squares) PEDOT:PSS. Devices are fabricated with a thermally evaporated Ag top contact.

To investigate the influence of PEDOT:PSS on the time evolution of the device performance a second experiment is carried out. Cells with evaporated Ag top contacts are fabricated and I-V characteristics are tested frequently under simulated solar light. Between the measurements

cells are kept in dark in ambient air. Figure 3.20 shows changes of the  $V_{OC}$  with time for representative devices with and without a PEDOT:PSS interlayer. The device with PEDOT:PSS exhibits a  $V_{OC}$  of 0.57 V immediately after production which stays stable during the period of ten days. Contrarily, the cell without PEDOT:PSS shows a low  $V_{OC}$  of around 0.25 V on the first day. During the following days the  $V_{OC}$  increases significantly but still remains below 0.5 V after five days. Around seven days after production the  $V_{OC}$  finally reaches 0.55 V to 0.6 V. This is attributed to slow oxidation reactions of the Ag which should decrease the top contact's work function yielding better matching of the P3HT HOMO level.

Both cell types with and without PEDOT:PSS are long term stable if stored in air. No significant changes in performance are observed after 80 days although the devices were not encapsulated or kept in a controlled atmosphere but stored in ambient atmosphere. Despite PEDOT:PSS is known to cause quick degradation in non-inverted [37] solar cells this is not confirmed for our inverted devices with and without PEDOT:PSS. Thus, for the inverted structure PEDOT:PSS helps to gain full performance immediately after fabrication but has no detrimental effect on device stability.

### 3.3.5 Summary

A spray-deposition technique for the application of aqueous solutions of PEDOT:PSS on hydrophobic surfaces is presented. This technique allows the fabrication of homogenous PEDOT:PSS layers on top of P3HT:PCBM which is beneficial for inverted solar cells. Devices with PEDOT:PSS exhibit full performance immediately after the fabrication with a slightly higher  $I_{SC}$ . The PEDOT:PSS allows efficient hole collection and protects the organic material during the top contact deposition. Both cells with and without PEDOT:PSS show long term stability and do not significantly decrease after 80 days storage in air. The techniques presented are a further step towards easy and cheap roll-to-roll fabrication. P3HT:PCBM and PEDOT:PSS are solution processed and no inert nitrogen atmosphere is needed.

---

### 3.4 Conclusion

In this chapter, the fabrication process of hybrid solar cells has been optimized on the blocking layers, blend layer and interface layer respectively. Significant increases of device performance have been observed due to these optimizations.

At the start of the discussion, the blocking layers are modified by surface cleaning and doping, as considered to optimize the device architectures. Both mechanical cleaning and ultrasonic cleaning could significantly enhance devices efficiency by the achievement of a smooth and defects free surface. However an O<sub>2</sub> plasma cleaning step reduced the solar cell performance possibly due to the reduced charge transport ability of O-rich TiO<sub>2</sub> surface, an effect that decreases with storage time. For the doping of blocking layers, N-doped TiO<sub>2</sub> layers via spraying and bubbling with N<sub>2</sub> show slightly influence on the absorption and I-V characterization results; while Mg-doped ZnO films exhibits obvious increased V<sub>OC</sub>, but the decreased I<sub>SC</sub> is possibly induced by the decomposition remain in the films, leading to a higher recombination. To use both of the advantages shown in TiO<sub>2</sub> and ZnO, a co-blocking layer combined with the two films is prepared for inverted solar cells. The devices improvement is not only due to the enlarged bandgap benefited from the wider absorption of ZnO layer, but also the reduced recombination due to the efficient hole blocking ability of TiO<sub>2</sub>. In additional the TiO<sub>2</sub>-ZnO indicates the possibility to further improve the inverted devices via the application of doping process and the fabrication of controllable nanostructure.

Then the organic material P3HT and PCBM dissolved in chlorobenzene, which can result in a better mixture than in CF due to the slower evaporation. 12 hours string time is long enough for a homogenously mixed blend solution, which is relatively stable when kept in dark. Then the optimized blend solution is spin coated on TiO<sub>2</sub> covered ITO substrates for the inverted solar cells.

A 150 nm thick blend layer, obtained from 30 mg/ml P3HT and 24 mg/ml PCBM mixed solution, demonstrates maximum efficacy for the devices. Furthermore, the best blend ratio, with a volume ratio of 1:1, is acquainted via a series of experiments. In addition, significant improvements of the devices are achieved by the implementation of three post treatment processes, which describe as follows: a slow dry step by covering as prepared blend layer with

petri dish for 30min, pre-annealing process at 105 °C for 5 min and post-annealing process at 140 °C for 10 min.

The last section of this chapter exhibits a homogenous PEDOT:PSS layer which is accomplished by spray-deposition technique as an interface layer between blend layer and top contact. It is beneficial for inverted solar cells giving higher  $I_{SC}$  and immediately exhibited full performance. It is able to efficiently collect hole, as well as to protect the organic material during the top contact deposition. Both cells with and without PEDOT:PSS are stable in air, no obvious degradation observed even after being stored for 80 days. This PEDOT:PSS deposition process could further reduce device cost by fabrication without nitrogen atmosphere.

## 4 Effects of Blocking Layer

In this chapter two types of inverted organic solar cells, using TiO<sub>2</sub> and ZnO films as respective hole-blocking layer have been investigated. The discussion of TiO<sub>2</sub> blocking layer is based on the publication of 'Photoinduce and UV light protection of TiO<sub>2</sub> blocking layers for inverted organic solar cells', in *Solar Energy Materials & Solar Cells*. 2011, Vol. 95, 3450.

### 4.1 Introduction

OPVs have been significantly improved during the last few years, and the power conversion efficiency as high as 8.3% has been reported [29, 179-181]. Even though OPVs hold the promise of low mass production costs when compared to conventional Si-based photovoltaics, much work has to be done to enhance the lifetime of OPVs [42]. The most commonly used geometry of OPVs is non-noble metals like Al and Ca as top contacts, which quickly oxidize in air. As a consequence, the performance of OPVs decreases rapidly if cells are operated in ambient air without elaborate encapsulation. OPVs with a so-called inverted structure with a TiO<sub>2</sub> layer or ZnO layer as hole blocking materials [183], allow the use of noble metals as top electrodes, thus increasing air stability [184]. As both a photoactive and an interfacial layer [179], metal oxide layers play an important role on the performance of OPVs. However, the inverted devices generally present a lower PCE than the normal structured devices. Additionally, the charge transport mechanism in inverted devices is still not clear in many fields, such as the recombination process in the metal oxide layer, and the limitation of the excitation rate.

In this chapter, the inverted devices based on TiO<sub>2</sub> and ZnO with different thicknesses are investigated for their performances, as well as the charge transport process. Initially the different properties of TiO<sub>2</sub> and ZnO films are investigated by XRD, Hall Effect measurements and AFM, for their crystallinity, conductivities and surface morphology. I-V characterizations depend more strongly on the thickness of the TiO<sub>2</sub> layer than the ZnO layer, which is caused by the light intensity loss due to the different absorption of these two types of devices. The absorption is determined by the trap states in the metal oxides, which results in a photo-doping effect. Device mobility measured via photo-CELIV method shows that the charge transport in hole-blocking layer does not limit the performance of inverted solar cells, and the mobility of organic layer has to be increased to achieve the improvement. The ZnO layers provide an inefficient UV protection for the organic layer, leading to the faster degradation. This can explain the lower recorded performance of ZnO solar cell than TiO<sub>2</sub> device; another reason is attributed to the larger recombination rate due to the higher conductivity of ZnO films. Both of these two types of solar cells show high air stability, providing more potential to further reduce the cost of production.

## 4.2 Device structure and experimental

Inverted solar cells are fabricated with the structure of ITO/ TiO<sub>2</sub> (ZnO)/ P3HT:PCBM/ PEDOT: PSS/Ag. For this two types of devices, the same thickness of polymer layer (150 nm), Ag top contact (100 nm) and PEDOT: PSS (about 10 nm) are deposited. Variations of the devices are only on the thickness of the metal oxides layers. Figure 4.1 shows the structure of solar cells based on TiO<sub>2</sub> and ZnO as hole-blocking layers.

The architectures of inverted devices are described in chapter 2. Both of TiO<sub>2</sub> and ZnO layers are deposited on cleaned ITO substrates via spray pyrolysis (see details in section 2.2.2). The cleaning steps for the metal oxides layers, as well as the deposition of blend layer and PEDOT:PSS layer are carried out via optimized processes described in chapter 3, followed by proper post- treatments to improve the performance of devices.



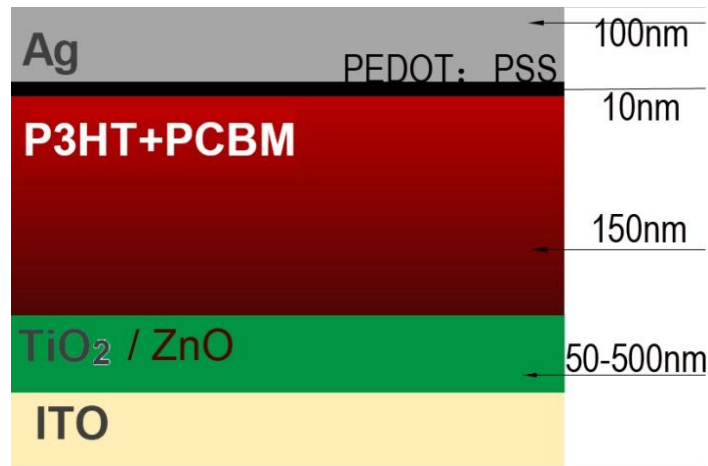


Figure 4.1: Inverted solar cells structure with different metal oxide layers.

A brief summary for the whole fabrication process is described as follows: for TiO<sub>2</sub> films a 1:10 solution of di-isopropoxytitanium bis (acetylacetonate) in ethanol is sprayed at 450 °C on ITO substrates, while ZnO films are prepared using Zinc acetate solution spray deposited on ITO at 375 °C. TiO<sub>2</sub> and ZnO layers thicknesses are controlled by the spraying times. After cooling down to room temperature, all the films are cleaned in acetone via ultrasonication for 5 min, rinsed with ethanol and dried in a nitrogen stream. The blend layers are deposited via spin coating at 600 rpm for 1 min and dried with a slow process. Then PEDOT:PSS layers is sprayed coated on top, followed by a pre-annealing step at 105 °C for 1 min. Devices are finished by the Ag deposition by thermal evaporation.

### 4.3 Properties of TiO<sub>2</sub> and ZnO layers

#### 4.3.1 Crystallinity

The XRD pattern of the TiO<sub>2</sub> and ZnO films are presented in Figure 4.2. A diffraction peak at 44.6 ° shown in both of the two patterns belongs to the ITO substrate. The diffraction peaks of pattern (a) are identified as the TiO<sub>2</sub> anatase phase, for the reflection of (101), (111) and (220). All the diffraction of (002), (101) and (103) from pattern (b) belong to ZnO wurtzite phase.

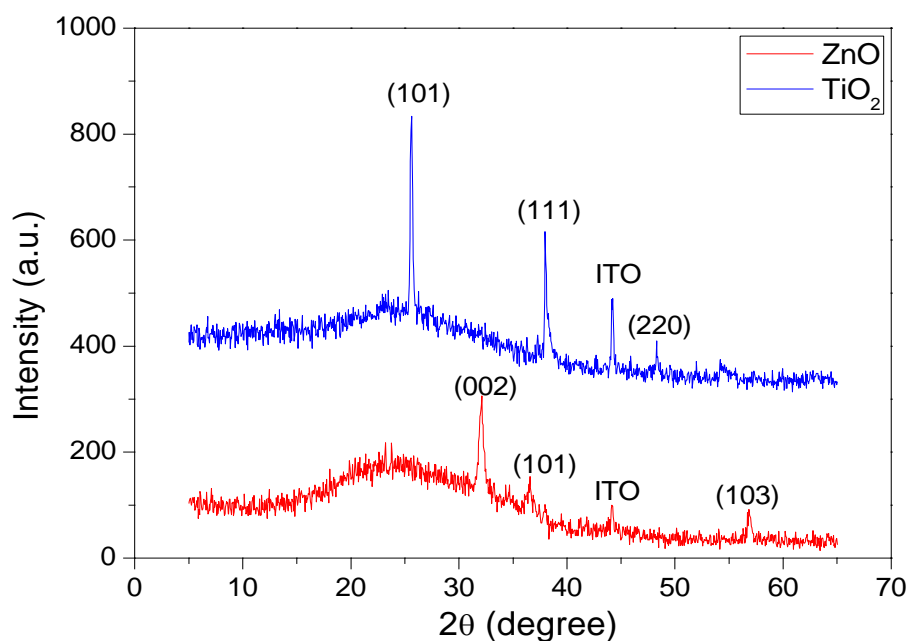


Figure 4.2: XRD for TiO<sub>2</sub> (blue) and ZnO (red) films fabricated by spray pyrolysis.

### 4.3.2 Conductivity and mobility

For the solar cells, two practical parameters to determine the charge transport abilities of the materials are known as electrical conductivity ( $\sigma$ ) and the mobility ( $\mu$ ). Electrical conductivity can be obtained by Van der Pauw method, while the mobility is a product of the conductivity and the charge carrier density ( $n_c$ ), which can be characterized by Hall Effect measurement (details described in Section 2.3). These two parameters are strongly interrelated with each other with a relation given as follows:

$$\sigma = q \times n_c \times \mu \quad (4.1)$$

Where  $\sigma$  is the conductivity (S/m),  $n_c$  is the charge carrier density,  $\mu$  is the charge mobility ( $\text{m}^2\text{V}^{-1}\text{s}^{-1}$ ),  $q$  is the elementary charge ( $1.6 \times 10^{-19}$  C).

Table 4.2 shows the electrical properties of TiO<sub>2</sub> layer and ZnO layer. Data is obtained via Van der Pauw method and Hall Effect measurement. The TiO<sub>2</sub> layer exhibits a conductivity of  $3.8 \times 10^{-7} \text{ Sm}^{-1}$  and a charge carrier density in the range of  $2 \times 10^6 \text{ m}^{-3}$ . The ZnO layer, on the other hand, shows a nearly 3 times higher conductivity and a charge carrier density as high as

$2.3 \times 10^6 \text{ m}^{-3}$ , almost 2 orders of magnitude over the TiO<sub>2</sub> layer. As results, the mobility of these two metal oxides shows a significant difference, that the mobility of TiO<sub>2</sub> layer is more than 30 times higher than that of ZnO.

	Conductivity ( $\text{Sm}^{-1}$ )	Charge carrier density ( $\text{m}^{-3}$ )	Mobility ( $\text{m}^2\text{V}^{-1}\text{s}^{-1}$ )
TiO <sub>2</sub>	$3.8 \times 10^{-7}$	$2.4 \times 10^6$	$9.9 \times 10^5$
ZnO	$1.1 \times 10^{-6}$	$2.3 \times 10^8$	$3.0 \times 10^4$

**Table 4.1: Charge carrier density and conductivity of TiO<sub>2</sub> and ZnO layers characterized by Hall Effect measurement and Van der Pauw method.**

The different mobilities of TiO<sub>2</sub> and ZnO might influence the charge transport of the assembled devices respectively. Further investigation of their influence on the device performance by charge transport will be discussed in section 4.4. Convincing evidences show that it is not the mobility of metal oxide, but the mobility of organic materials that determines the charge carrier transfer in the device; however the different conductivities of the two metal oxides can influence the device performance respectively with the different recombination rates.

### 4.3.3 Surface morphology

As shown in Figure 4.3, the AFM images present the surface morphologies of the TiO<sub>2</sub> and ZnO films with four different thicknesses. The TiO<sub>2</sub> films (see Figure 4.3 left) shows an average grain size around 20-50 nm for all four films, and the surface morphology of TiO<sub>2</sub> layers is independent on their thicknesses. When sprayed on the substrate heated at 450 °C, the droplets of precursor decompose immediately. And the TiO<sub>2</sub> as a main product, is highly polycrystalline and independent of the film thickness. Therefore the surface morphology of TiO<sub>2</sub> films is homogeneously formed during pyrolytic process.

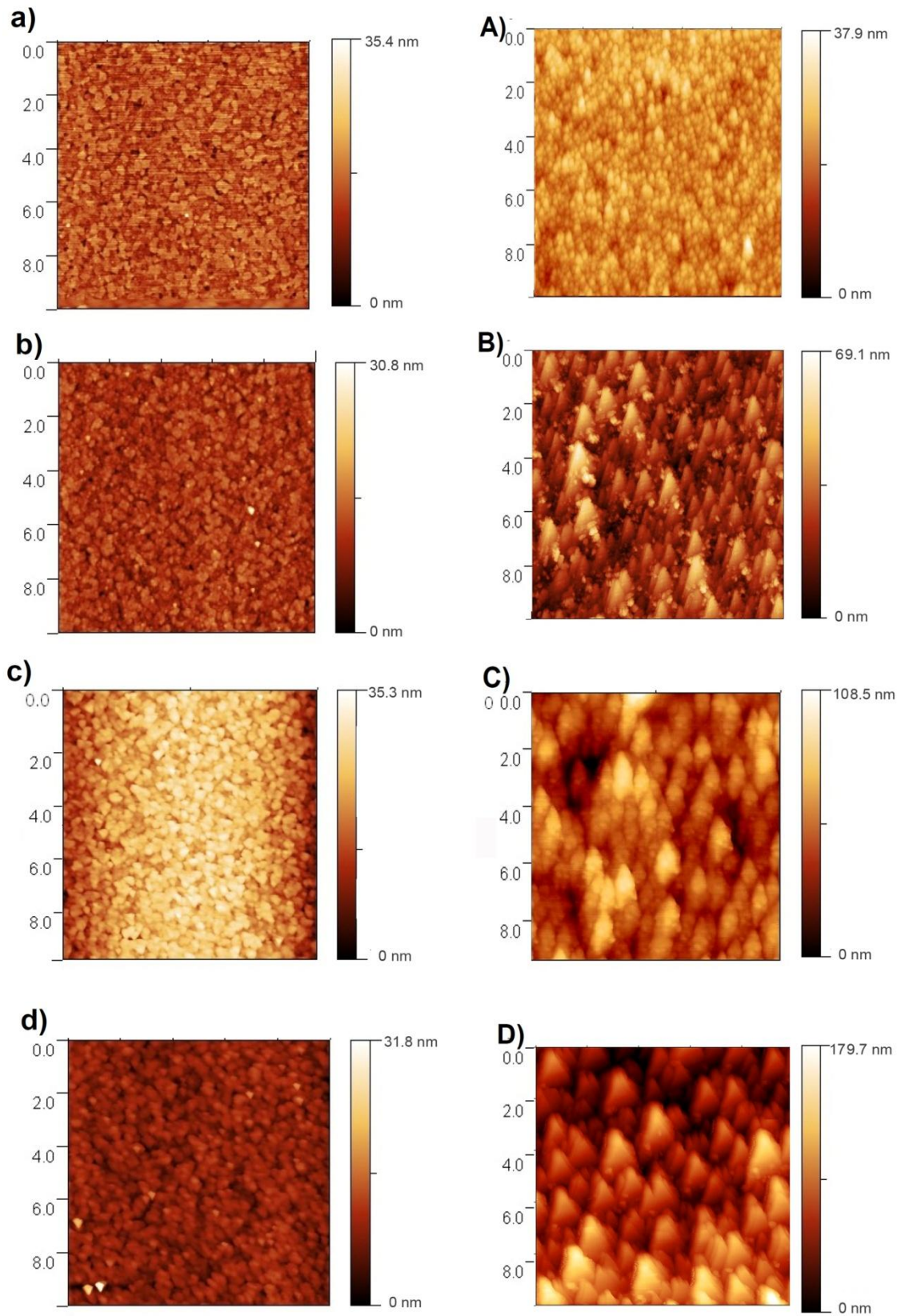


Figure 4.3: AFM of images of TiO<sub>2</sub> (left) and ZnO (right) films deposited on ITO with four different thicknesses: (a, A: 50 nm, b, B: 100 nm, c, C: 200 nm, d, D: 500 nm.)

On the other hand, the surface morphology of the ZnO layers shows a strong dependence on the thicknesses. As observed in Figure 4.3 (right), the ZnO nanocrystalline size significantly increases with an increasing layer thickness. The grain size is various from 20 to 30 nm for the 50 nm ZnO layer, while for the 500 nm ZnO film it is much wider distributed with values of 50-200 nm.

This growing grain size suggests that the morphology of layer-by-layer deposited ZnO is seriously influenced by the deposition times. The increasing size of nanocrystallite may be interpreted in the terms of a columnar grain growth in the structure, which may be attributed to the formation of new smaller crystallites on the larger grains [185]. As a result, the size of ZnO nanocrystalline is getting larger, leading to a broadened distribution.

As a potential advantage for the increasing grain size, the surface area of ZnO film could be enlarged. This is confirmed by the data read from AFM roughness analysis, which is obtained via a software of Gwyddion. According to the calculation, the surface area of ZnO films is enlarged by 20% when the film thickness increases from 50 nm to 500 nm. While the surface area of different TiO<sub>2</sub> films keeps nearly constant. In addition, by comparing the two metal oxides films both with a thickness of 100 nm, the surface area of ZnO is 10% larger than that of TiO<sub>2</sub>. This larger surface area of the hole-blocking layer can provide a larger interface between electron conducting layer and organic layer, which shows great potential to be beneficial for the charge separation leading to a better performance.

#### 4.3.4 Absorption

The TiO<sub>2</sub> layers showing a light yellow to brown color with the increasing thickness that suggests their ability to absorb light in the visible region. Neither of the interference effect nor the scattering effects should be considered as the main reason for this absorption spectra shift. As discussed in section 2.3.3, the interference effect should be only responses to a specific wavelength instead of overall spectra, since the refractive index of all the TiO<sub>2</sub> films fabricated via the same process supposed be identical. In addition, the similar surface morphology of on all the films indicates that the influence of scattering effect should be nearly the same, regardless the film thickness [186].

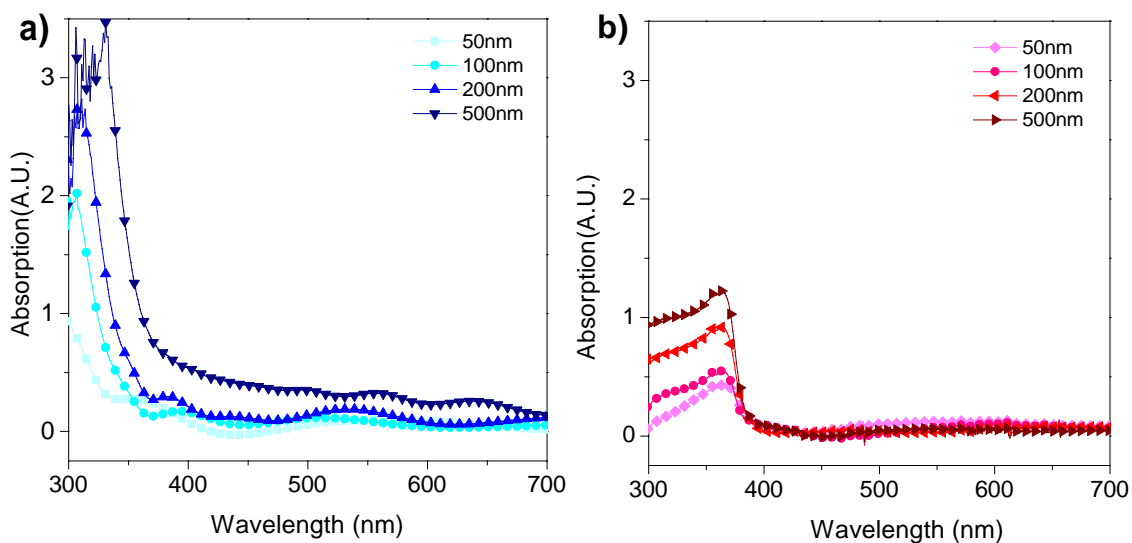


**Figure 4.4: Absorption spectra of different thickness of TiO<sub>2</sub> (left) and ZnO (right) films.** Both the absorption peaks of the two blocking layers show proportional increasing with thickness.

As shown in Figure 4.4 (left), the absorption peak of TiO<sub>2</sub> layer at 335nm increases proportionally to the layer thickness. A slight red-shift towards visible region absorption suggests that the bandgap in the TiO<sub>2</sub> is reduced probably due to the impurities [187]. Compared to the pure TiO<sub>2</sub> that has transitions from the valence band to the conduction band, the TiO<sub>2</sub> introduced with defects and traps exhibits additional extrinsic electronic levels, which can be located in its energy bandgap. As the TiO<sub>2</sub> layers are fabricated via spray pyrolysis method in air, they are quite possible N-doped [188], and on the barriers of TiO<sub>2</sub> crystallites, trap states cannot be avoided to form [189].

The ZnO layers are more transparent than the TiO<sub>2</sub> layers, and no visible color changes are observed depending on the layer thickness. As shown in Figure 4.4 (right), the ZnO absorption spectra are constant in the visible region, but significantly weaker than those of TiO<sub>2</sub> layers. This may be induced by the reform process of the ZnO nanocrystalline. As shown in AFM images (see Figure 4.3 right), that the growing size of grains may possibly reduce the defects in ZnO layers. Limited trap states of ZnO layers can dramatically reduce its influence on the absorption. The transparency of blocking layer thickness is important to guarantee a proper light intensity reaching the organic photoactive layer in the device for a high photogenerated excitation.

The ZnO absorption peak shown at 350 nm increases with the increasing layer thickness,

exhibiting the same trend as shown in TiO<sub>2</sub> layers. However the ZnO absorption peak is much wider and lower than that of TiO<sub>2</sub> layer with same thickness. It demonstrates that energy bandgap of ZnO fabricated by spray pyrolysis is slightly narrower than TiO<sub>2</sub>; on the other hand, the UV light absorption ability of ZnO is weaker than that of TiO<sub>2</sub>, which could induce a negative influence on the illumination stability of devices caused by the degradation of organic layer under UV light.

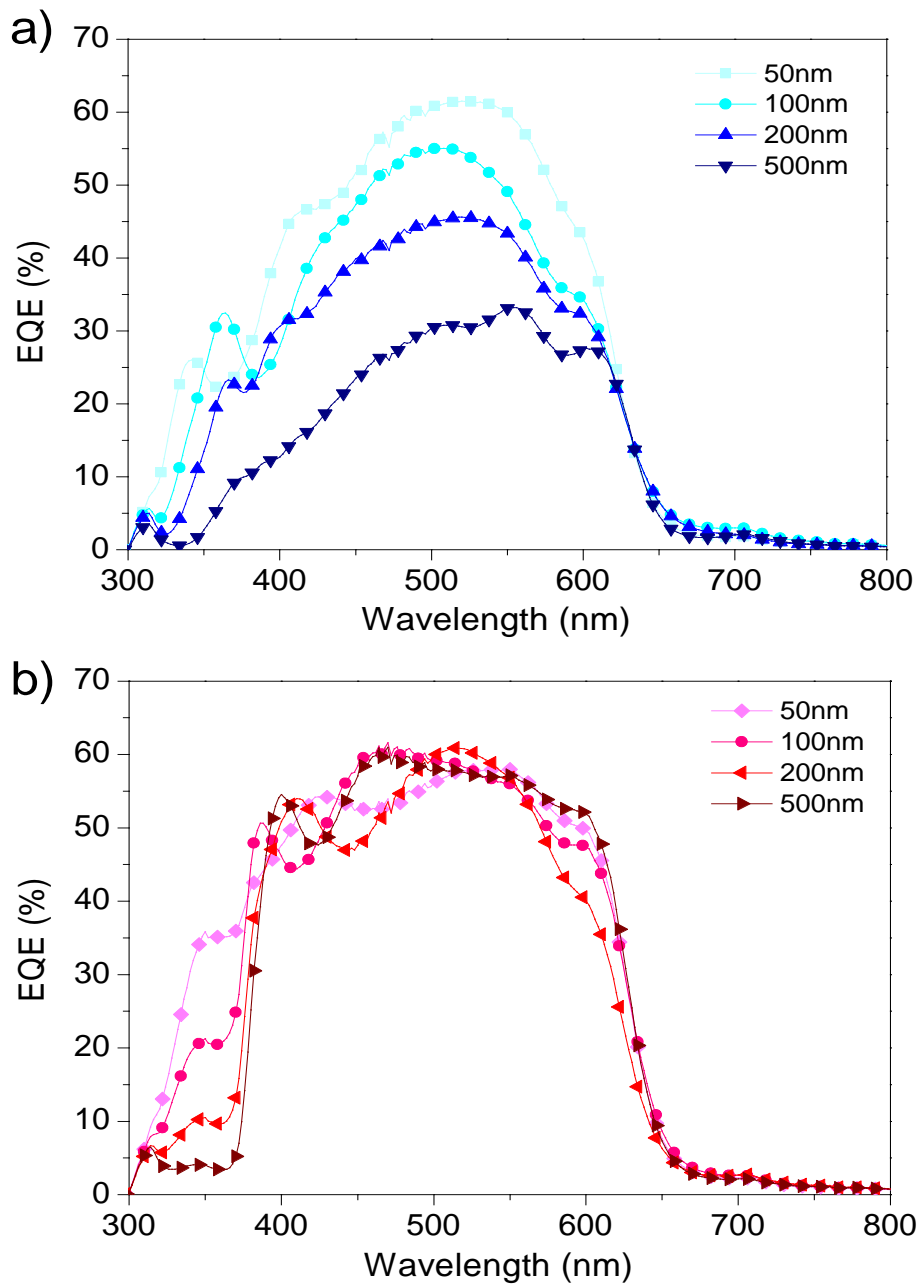
#### 4.3.5 Summary

In this section, the advantages of ZnO layers compared to the TiO<sub>2</sub> layers are discussed as follows: The higher conductivity could induce lower  $R_s$  and fast electron charge transport. The larger surface area could provide a larger interface for the charge separation. The less light intensity loss could guarantee a higher photon injection for the exciton generation. On the other hand, the ZnO layers exhibit a much lower mobility, which could possibly limit the charge transport in the device.

These two metal oxide layers with different properties can influence on the performance of the devices based on them. Further investigation about their effects on solar cells is presented in the following sections.

#### 4.4 Performances of inverted devices based on TiO<sub>2</sub> and ZnO

The performance of solar cells based on TiO<sub>2</sub> and ZnO layers, with four thicknesses of 50, 100, 200 and 500 nm, are studied respectively. The metal oxide layers effect differently on the device performance obtained via EQE and I-V characterization. Comparison between these two types of devices, especially on the charge transport in TiO<sub>2</sub> and ZnO layers, are discussed in this section.

4.4.1 EQE characterization of TiO<sub>2</sub> and ZnO devices

**Figure 4.5: EQE characteristics for devices with different thicknesses of TiO<sub>2</sub> (up) and ZnO (down).** EQE results of TiO<sub>2</sub> devices significantly decrease depend on the blocking layer thickness. EQE results of ZnO devices present similar trend at 350nm, the absorption band of ZnO; but no clear differences observed at wavelength of 500-600nm

As shown in Figure 4.5, the EQE results of TiO<sub>2</sub> solar cells clearly decrease with the



increasing film thickness. This decreasing trend observed in both UV region and visible region is opposite to their absorption results discussed above. For the EQE of ZnO solar cells, on the other hand, the differences depending on the blocking layer thickness only appear in UV region, corresponding to the constant ZnO absorption spectra in the visible region.

This phenomena can be explained as follows: when illuminated on the devices, solar light is first absorbed by TiO<sub>2</sub> or ZnO films. After passing through the blocking layers, light intensity is reduced due to the absorption of those layers. Since the EQE is mainly attributed to the charge collection efficiency of organic photoactive layer, the decreasing EQE is induced by the reduced light intensity reaching to this layer, with an inverted proportion to the thicknesses of blocking layers.

For the TiO<sub>2</sub> layers, a significantly light intensity loss is induced by the absorption of the blocking layers, and it is strongly depending on the TiO<sub>2</sub> layer thickness. As a result, the exciton generation rate will be reduced due to the limited photon injection, therefore a clearly decrease on the EQE is observed. For the ZnO devices, since the blocking layers are fairly transparent, much less visible light intensity loss occurs during light traveling through these layers, leading to the undistinguished EQE results in the visible region.

Further evidences supporting this assumption will be presented in details in section 4.5, which exhibits the different device performances responding to the back and in front paths for solar light illumination.

#### **4.4.2 I-V characterization of TiO<sub>2</sub> and ZnO devices**

I-V curves for devices on four different thicknesses of TiO<sub>2</sub> and ZnO layers are acquired under simulated illumination of AM 1.5G solar light (100mW/cm<sup>2</sup>) as shown in Figure 4.6. Their photovoltaic parameters from current-voltage data are given in Table 4.2 and Table 4.3. Values are obtained from solar cells with different thicknesses of TiO<sub>2</sub>. Data is extracted for the six individual pixels of each cell set and the respective standard deviations are calculated.

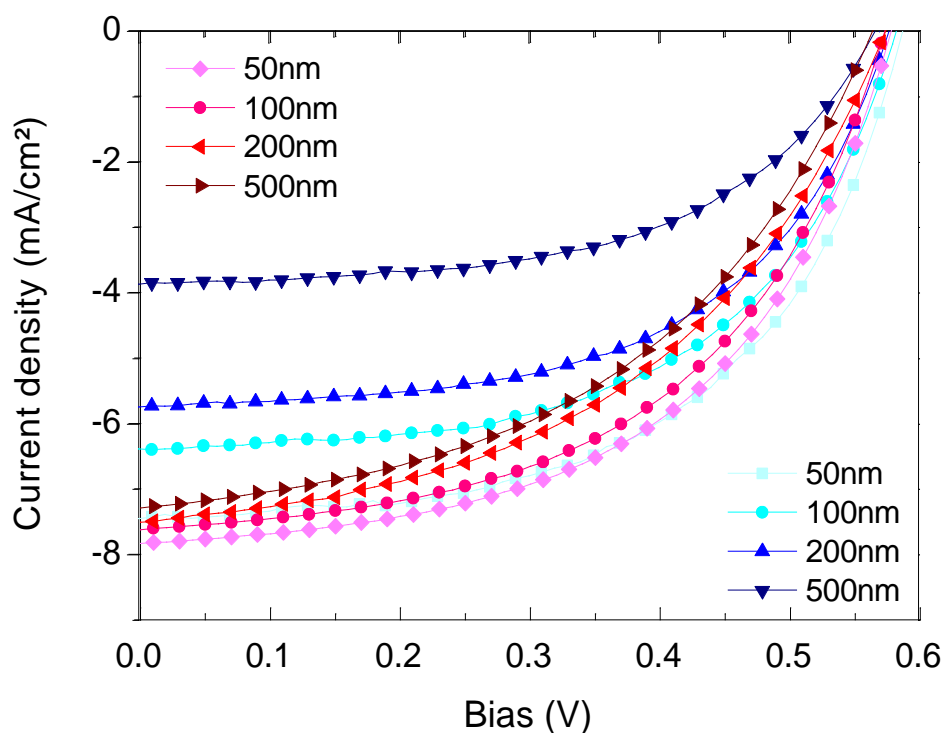


**Figure 4.6:** I-V characterization for devices with 4 different thicknesses of TiO<sub>2</sub> (blue) and ZnO (red), (Dark-blue squares: 500 nm; blue circles: 200 nm; cyan up-triangles: 100 nm; light-cyan down-triangles: 50 nm) (Dark-red diamond: 500 nm; red hexagon: 200 nm; pink right-triangles: 100 nm; light-pink left-triangles: 50 nm)

Thickness (nm)	PCE (%)	V <sub>OC</sub> (V)	I <sub>SC</sub> (mA/cm <sup>2</sup> )	FF (%)	R <sub>Sh</sub> (Ω/cm <sup>2</sup> )	R <sub>S</sub> (Ω/cm <sup>2</sup> )
50	2.41	0.59	7.44	55	5546	2.18
100	2.06	0.58	6.38	55.4	2961	2.27
200	1.84	0.58	5.74	55.5	1967	2.01
500	1.19	0.57	3.86	54.6	1622	6.62

**Table 4.2** Photovoltaic parameters of the solar cells based on TiO<sub>2</sub> layers with four different thicknesses.

For the TiO<sub>2</sub>-based devices with four different thicknesses of TiO<sub>2</sub> layers, best performance is

shown on the one with thinnest TiO<sub>2</sub> layer of only 50 nm. With the increasing thickness of TiO<sub>2</sub> layer, both efficiency and I<sub>SC</sub> linearly decrease, while the V<sub>OC</sub> and FF keep almost constant. The sample with 50 nm TiO<sub>2</sub> gives 2.4 % PCE, while the 500 nm device shows a PCE below 1.2%. This more than 50 % loss in efficiency is mainly caused by the reduced I<sub>SC</sub>.

The series resistances (R<sub>S</sub>) for all solar cells are relatively small and constant, which well corresponds to the high conductivity for all TiO<sub>2</sub> layers with different thicknesses (see Table 4.1). Since the FF is independent from TiO<sub>2</sub> layer thickness as well, it can be inferred that the I<sub>SC</sub> of the solar cells should not be limited by the resistance (or conductivity) of the TiO<sub>2</sub> layer. A possible reason for the decreasing current density might be the light absorbed in the TiO<sub>2</sub>, which can reduce the light intensity reaching to the photoactive organic layer.

Thickness (nm)	PCE (%)	V <sub>OC</sub> (V)	I <sub>SC</sub> (mA/cm <sup>2</sup> )	FF (%)	R <sub>Sh</sub> (Ω/cm <sup>2</sup> )	R <sub>S</sub> (Ω/cm <sup>2</sup> )
50	2.27	0.58	7.38	52.3	769.5	1.87
100	2.18	0.57	7.26	50.8	749.2	1.93
200	1.91	0.56	6.85	48.6	689.3	2.64
500	1.77	0.55	6.29	46.3	474.5	2.14

**Table 4.3 Photovoltaic parameters of the solar cells based on ZnO layers with four different thicknesses.**

The performance of devices based on ZnO layers with four different thicknesses are shown in Table 4.3. The best efficiency is obtained by the solar cell produced on the thinnest ZnO layer as well. Layer-thickness dependence shows in all the photovoltaic parameters of ZnO solar cells, which is similar to the TiO<sub>2</sub> solar cells. However this dependence is much weaker for ZnO cells. There is only 20 % loss in efficiency caused by the ZnO layer thickness increasing from 50 nm to 500 nm, while 60 % loss is observed in TiO<sub>2</sub> solar cells. Corresponding to the EQE results, the weaker dependence of ZnO devices indicates that the transparency of the hole-blocking layer is a premise for an efficient inverted device. Less absorption of the blocking layers can significantly limit the light intensity loss and provide enough photon injected in the organic material for the exciton photogeneration, leading to relatively high

power conversion efficiency.

The properties of ZnO layers, in comparison with the TiO<sub>2</sub> layers as discussed in section 4.3, show remarkable advantages of the higher conductivity, the larger surface area, and the less light intensity loss, all of which are supposed to result in a better device performance. However, a distinguished worse performance is observed for the 50 nm ZnO solar cells compared to the TiO<sub>2</sub> device with the same layer thicknesses. Regardless the smaller  $R_s$  of ZnO solar cells, which possibly caused by the much higher conductivity of ZnO layer, the FF and PCE are significantly lower than TiO<sub>2</sub> device.

One possible reason for the worse performance of ZnO solar cells could be the lower mobility of ZnO layers, with a value of nearly 30 times lower than that of TiO<sub>2</sub> layers, as the data presented in Table 4.1. To find out the influences of the metal oxide mobility on the performance of device, the charge carrier transport of the two types of solar cells are investigated and discussed in the following sections.

#### 4.4.3 Charge carrier mobility of TiO<sub>2</sub> and ZnO devices

Table 4.4 shows the Photo-CELIV measurement results for the TiO<sub>2</sub> and ZnO devices with 50 nm thickness. The details of measurement and data analysis are described in section 2.3.8. The mobilities of two types of solar cells are quite close,  $2.78 \times 10^{-6} \text{ m}^2 \text{ V}^{-1} \text{ s}^{-1}$  for TiO<sub>2</sub> solar cell and  $2.75 \times 10^{-6} \text{ m}^2 \text{ V}^{-1} \text{ s}^{-1}$  for ZnO solar cell, with an order of magnitude close to the mobility of organic material ( $\sim 10^{-7} \text{ m}^2 \text{ V}^{-1} \text{ s}^{-1}$ ).

	TiO <sub>2</sub> device	ZnO device
$t_{\text{max}}$ (s)	$7.91 \times 10^{-6}$	$6.92 \times 10^{-6}$
Mobility ( $\text{m}^2 \text{ V}^{-1} \text{ s}^{-1}$ )	$2.78 \times 10^{-6}$	$2.75 \times 10^{-6}$

**Table 4.4: Photo-CELIV measurements for solar cells with 50 nm blocking layers of TiO<sub>2</sub> and ZnO.**

However, the Hall Effect measurements for the mobilities of these two metal oxides materials (see Table 4.1) give much higher values of about  $9.9 \times 10^5 \text{ m}^2 \text{ V}^{-1} \text{ s}^{-1}$  and  $3.0 \times 10^4 \text{ m}^2 \text{ V}^{-1} \text{ s}^{-1}$  for

TiO<sub>2</sub> and ZnO, respectively, comparing to the device mobilities characterized via Photo-CELIV measurement.

The mobilities of devices based on the TiO<sub>2</sub> and ZnO are similar, even though the TiO<sub>2</sub> layers have 30 times higher mobility than ZnO. In addition, the difference on PCE between the two types of devices is fairly small as well, with a value of less than 10%. Considering all the facts given above, it can be stated that the charge transport in the inverted solar cells is mainly limited by the mobility of organic photoactive layer, instead of the metal oxide layer.

#### 4.4.4 Charge recombination of TiO<sub>2</sub> and ZnO devices

As the only disadvantage of ZnO device, the low mobility of hole blocking layer is not the factor to determine the device performance, according to the conclusion given in the last section. Regarding all the potentials of ZnO to improve the device performance, the reason for the opposite result has to be investigated in a different direction.

IS measurement is implemented to study the charge transfer processes of the two types of inverted solar cells. Since the TiO<sub>2</sub> and ZnO based solar cells are fabricated with the same structures and processes, their different performances should be induced by the charge transfer of metal oxide layers, as well as the respective interfaces between them and the photoactive layer coated on top.

Since the energy conversion of solar cells is the combination of carrier generation and collection [190], a solar cell can be simplified to a two-level system formed by an absorber material and two selective contacts [191]. As shown in Figure 4.7a, a typical device consists of a light absorber, a hole selective contact, and an electron selective contacts. In the case of the inverted devices, they are the P3HT:PCBM blend layer, the PEDOT:PSS and Ag electrode, and the ITO electrode coated with metal oxide layer, respectively. In the absorber, photon absorption can excite electronic charge carriers from a low energy  $E_v$  to a high energy  $E_c$  state (process 1). Excitation causes a separation of the quasi-Fermi levels of electrons  $E_{Fn}$  and holes  $E_{Fp}$  that is limited by recombination of the carriers (process 2). The reversible selective contacts to each kind of carrier allow their extraction (process 3) [192].

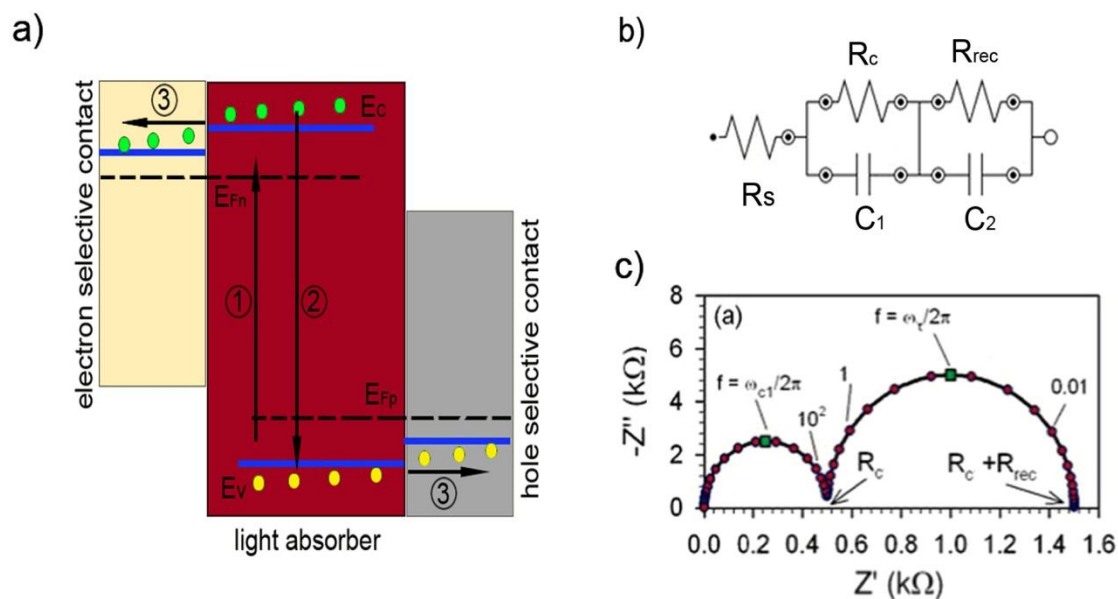


**Figure 4.7: Model of IS measurements.** a) Basic scheme of a solar cell. b) The ac equivalent circuit of scheme c including basic elements resistance and capacitance at the selective contact. c) Representation of the impedance in the complex plane plot and real part of the capacitance vs frequency for solar cell impedance [192].

A generally used ideal model for this system is shown in Figure 4.7b. It contains only the basic processes for the energy conversion, mainly focusing on the charge transport and recombination. In this model, it will not evolve either the irreversible losses associated with the extraction process, or the recombination of excess carriers in the absorber. Both of them are unavoidable because of the microscopic reversibility of the excitation process [193]. Since this model simplifies the solar cells as a structure of  $\text{TiO}_2$  ( $\text{ZnO}$ ) electrode/ Absorber/ Hole selective contact, the elements of this basic model can be distinguished as: capacity  $C_1$  is attributed to the interface of metal top contact and the organic materials, while capacity  $C_2$  represents the interface between blend layer and metal oxide layer. The resistances of this model are consisted by a  $R_s$  for all the layers contained in the device, a recombination resistance ( $R_{\text{rec}}$ ), and a transport resistance ( $R_c$ ), respectively (see Figure 4.7c).

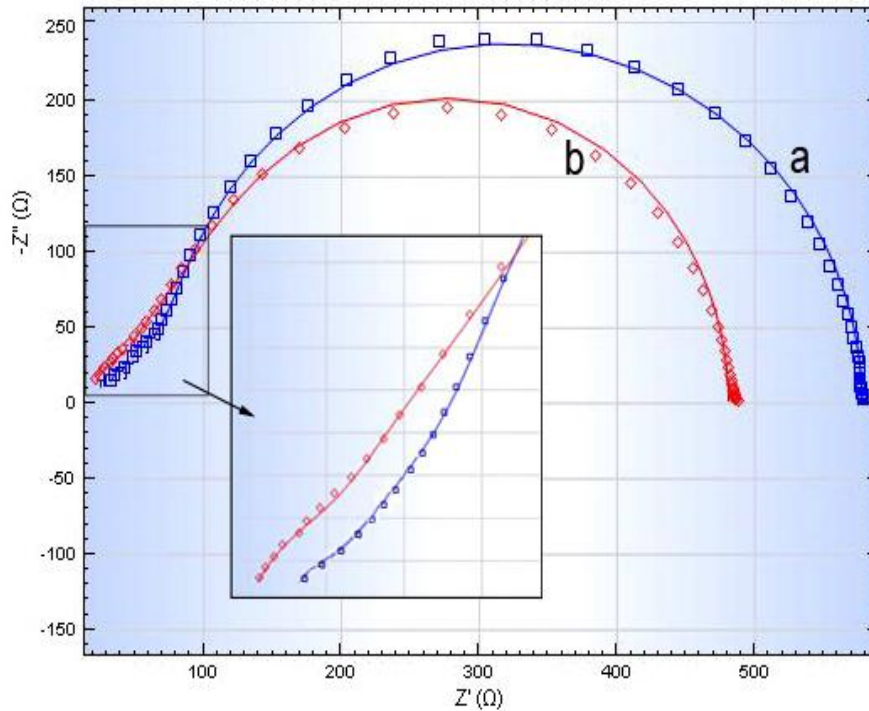


**Figure 4.8:** IS measurement data for solar cells with 50 nm blocking layer of TiO<sub>2</sub> (a) and ZnO (b). The simulated data fit the experimental data (symbols) well indicating a valid model (solid lines).

	TiO <sub>2</sub>	ZnO
R <sub>S</sub> (Ω)	48.2	20.8
R <sub>C</sub> (Ω)	34.6	46.1
R <sub>rec</sub> (Ω)	456.4	364.9
C <sub>1</sub> (nF)	58.5	47.7
C <sub>2</sub> (nF)	58.4	15.2

**Table 4.5:** Parameters calculated from IS measurement for solar cells with 100 nm blocking layer of TiO<sub>2</sub> and ZnO.

Then, this model is used to simulate the results of IS measurements. As presented in Figure 4.8, the IS data is fitted well to this model, and the values for every element obtained from this simulation are listed in Table 4.4. It is indicated that the recombination resistance of the TiO<sub>2</sub> solar cell has a value of 456.4 Ω, while for the ZnO solar cell, it is only 364.9 Ω. Since the recombination rate is inversely proportional to the recombination resistance, this higher

recombination in ZnO device can convincingly explain the worse device performance compared to TiO<sub>2</sub> devices.

However the reasons for the higher recombination in ZnO device are still under investigation. One possible explanation is given as follows: according to the Langevin bimolecular recombination in OPVs as mentioned in Chapter 1, the injection current at the metal oxide–organic interface is related to the charge density and electron mobility, which can be expressed as [194]:

$$J_{\text{rec}} = 16\pi\epsilon\epsilon_0(kT)^2\mu n_0/q^2 \quad (4.2)$$

where  $n_0$  is the charge density,  $\mu$  is the electron mobility,  $\epsilon_0$  is the permittivity of free space,  $\epsilon$  is the dielectric constant of the medium,  $k$  is the Boltzmann constant,  $T$  is the temperature,  $q$  is the elementary charge. Since the conductivity ( $\sigma$ ) is strongly interrelated with the mobility ( $\mu$ ), as referred in equation 4.1, it can be inferred that the  $J_{\text{rec}}$  is proportional to the conductivity of metal oxide. Therefore the higher conductivity of ZnO layer than TiO<sub>2</sub> layer results in a higher recombination and a lower efficiency for the device based on it.

On the other hand, the ZnO device has a much lower series resistance ( $R_s$ ) than the TiO<sub>2</sub> device, corresponding to the  $R_s$  calculated from I-V measurement results. It should be also induced by the higher conductivity of ZnO film, leading to lower resistances of this layer, and the whole devices.

Since those deposition of the blend layer, the PEDOT:PSS layer and the Ag top contact are kept the same, the interface of the absorber and hole selective contact should be identical, leading to a close  $C_1$  value for TiO<sub>2</sub> and ZnO solar cells. On the other hand, the results of  $C_2$  are significantly different between these two devices. As the surface morphology of TiO<sub>2</sub> and ZnO layer are quite similar (see Figure 4.3 A and a), this difference on  $C_2$  should be attributed to the different dielectric constants of these two metal oxides. Although further investigation is necessary to support these conclusions, the main reason for a low efficiency of ZnO device is clearly attributed to the high conductivity of hole-blocking layer, which leads to a negative influence on solar cells, regardless the advantages of large surface area and high transparency.

However, the higher conductivity and carrier mobility of ZnO layer is only one possibility for the worse performance of ZnO solar cells compared to TiO<sub>2</sub> solar cells. Another possibility is the limited illumination stability for ZnO solar cells. It is caused less UV protection provide by the ZnO layer for the organic layer, that will discussed in details in section 4.6.1.



## 4.5 Effects of trap states in blocking layers

### 4.5.1 Trap filling of photoinduced TiO<sub>2</sub> and ZnO

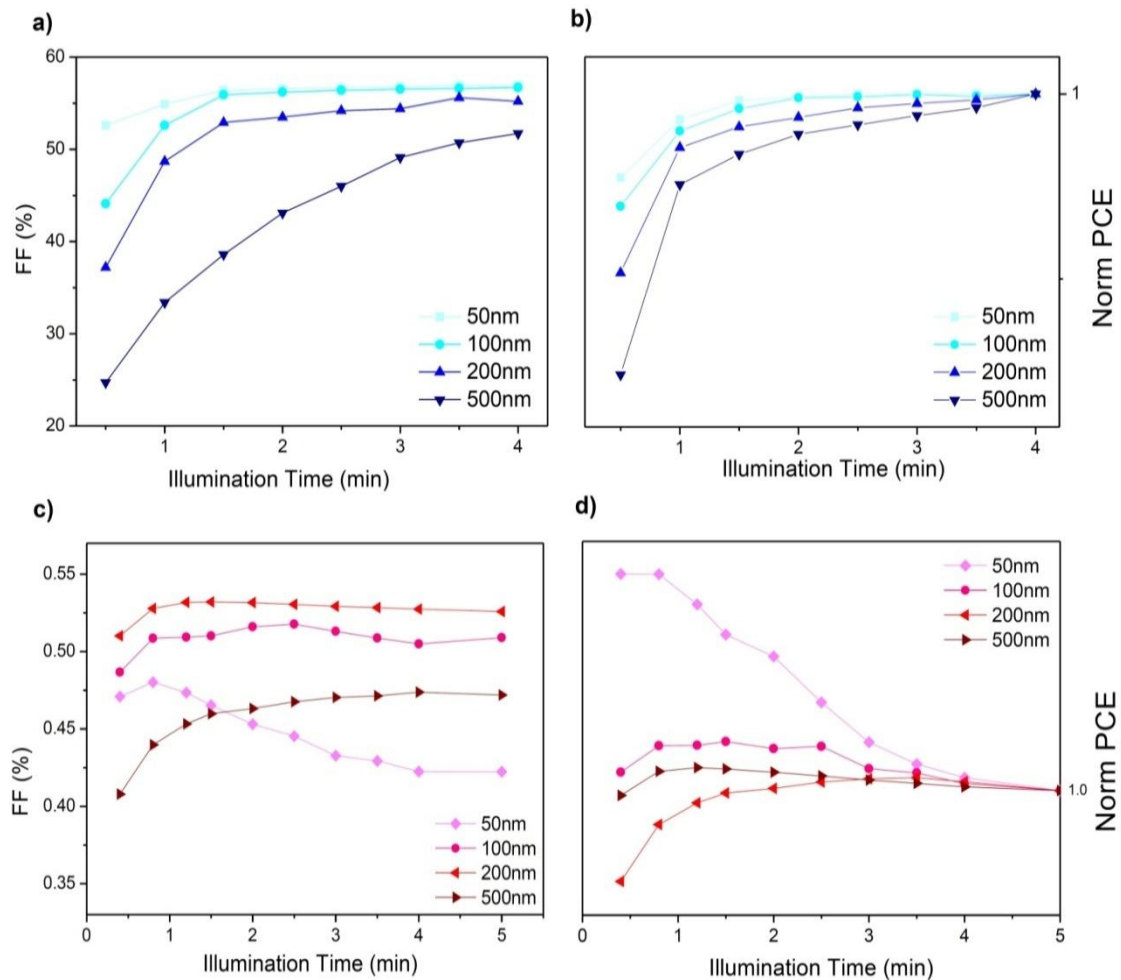


**Figure 4.9:** Trap filling of photoinduced TiO<sub>2</sub> (top) and ZnO (bottom) effect. Data is present for the time dependence of FF (a, c) and PCE (b,d) under a simulated AM 1.5G solar light (100 mW/cm<sup>2</sup>).

During the I-V measurements for all the samples, a trap filling effect is found in photoinduced TiO<sub>2</sub> and ZnO layers, influenced by the layer thickness. Figure 4.9 summarizes the dependence of FF and PCE for TiO<sub>2</sub> and ZnO solar cells on illumination time. These two parameters show significant changes among all the solar cell performances. Upon the first measurement under illumination, every device shows an obvious S-shape on the I-V curve,

with quite low FF and PCE. After being illuminated long enough, the performances of all solar cells are improved, and can reach their maximum points within a certain time, which is proportional to the thickness of TiO<sub>2</sub> and ZnO layers.

Devices with thicker metal oxide layers take longer to reach their best performances. Comparing to the TiO<sub>2</sub> solar cells with the same thickness, ZnO devices need less time for the photoinduced process. However, the solar cell based on the thinnest ZnO layer reaches its maximum point of performance within 1 min, and then the PCE begins to degrade after 3 min illumination.

As Weidmann reported, defects in TiO<sub>2</sub> layers can reduce the electron drift mobility [195]. It can be inferred that the trap states limit electron transport in TiO<sub>2</sub>, due to the barriers between TiO<sub>2</sub> crystallites. It is already observed that the absorption of TiO<sub>2</sub> shift to the visible light, caused by the trap states in TiO<sub>2</sub> layer, so the trap filling effect of solar cell could be explained as follows:

Photoexcited electrons and holes in TiO<sub>2</sub> are first obtained to fill the traps close to the conduction bands [196], and the trap becomes inactivated for further electron capture. This causes the low FF and efficiency on the first I-V curve of illuminated devices, and even a drop on I<sub>SC</sub> of solar cell with thickest TiO<sub>2</sub> layer, which probably contains the highest number of traps that limited the charge transport. As light induced filling of electron traps can cause an increase of the electron drift mobility, assist electron transport through TiO<sub>2</sub>, and improve the quantum yield of carriers at higher light intensities [198]. The performances of solar cell are improving with constant illumination in solar spectrum. Solar cells with thicker TiO<sub>2</sub> layers contain more traps, and thus it takes longer time to be filled and to reach the best charge transport state.

ZnO solar cells show a similar photoinduced effect as the TiO<sub>2</sub> solar cells, but it takes less time than TiO<sub>2</sub> solar cells. This fast response of the trap filling process indicates that less traps contained in ZnO layers, which is supported by a weak visible light absorption as shown in Figure 4.4 b. This is corresponding to the assumption made from AFM image for the surface morphology that a reform process occurs during the spray pyrolysis, leading to the decreasing space between the ZnO grains, and reduced defects in the ZnO films. The limited trap states in ZnO layers can not only provide an immediate photoinduce response, but also guarantee the photogeneration of exciton by the high transparency.

#### 4.5.2 Filter effect of TiO<sub>2</sub> and ZnO

A group of semitransparent solar cells based on TiO<sub>2</sub> and ZnO is fabricated by sputtering a 20 nm thin Ag as the top contact. As a result, these devices can be illuminated not only from the in front side, but also from the backside, with a light path through Ag/ PEDOT: PSS/ polymer/ TiO<sub>2</sub> (ZnO)/ ITO. Without the metal oxide absorption, it can be confirm that the light intensities inside the photoactive layers are identical for the two types of devices. Therefore the photogenerated excitons are supposed to be independent on the thickness of TiO<sub>2</sub> and ZnO.

As shown in Figure 4.10 a and b, when the TiO<sub>2</sub>-based solar cells are illuminated from the front side (through TiO<sub>2</sub> layer first), the EQE results of devices are inversely proportional to the TiO<sub>2</sub> thickness. This phenomenon is found on PCE of devices as well. While the TiO<sub>2</sub>-based devices illuminated from the back side, both the I-V and EQE results behave independently on the thickness of the TiO<sub>2</sub> layer. From this reverted illumination, it can be stated that the dependence of power conversion on the TiO<sub>2</sub> thickness is caused by a filter effect of the TiO<sub>2</sub> layer. Due to the absorption of TiO<sub>2</sub> layers, the light intensity is reduced when solar illumination passing through the TiO<sub>2</sub> layer before the organic layer. Thicker TiO<sub>2</sub> layers absorb more light including the visible region; accordingly, more light intensity is lost before reaching the organic photoactive layer, leading to less photogenerated excitons and a low efficiency in solar cells.

As the PCE of solar cells are independent on TiO<sub>2</sub> thickness when illuminated from back side, an important conclusion drawn out from this investigation of reverted illumination is that the TiO<sub>2</sub> layer does not limit the charge transport in polymer solar cell even with a thickness of 500 nm. This statement is also available for ZnO devices, which have much lower series resistances due to the 3 times higher conductivity (see Table 4.1)

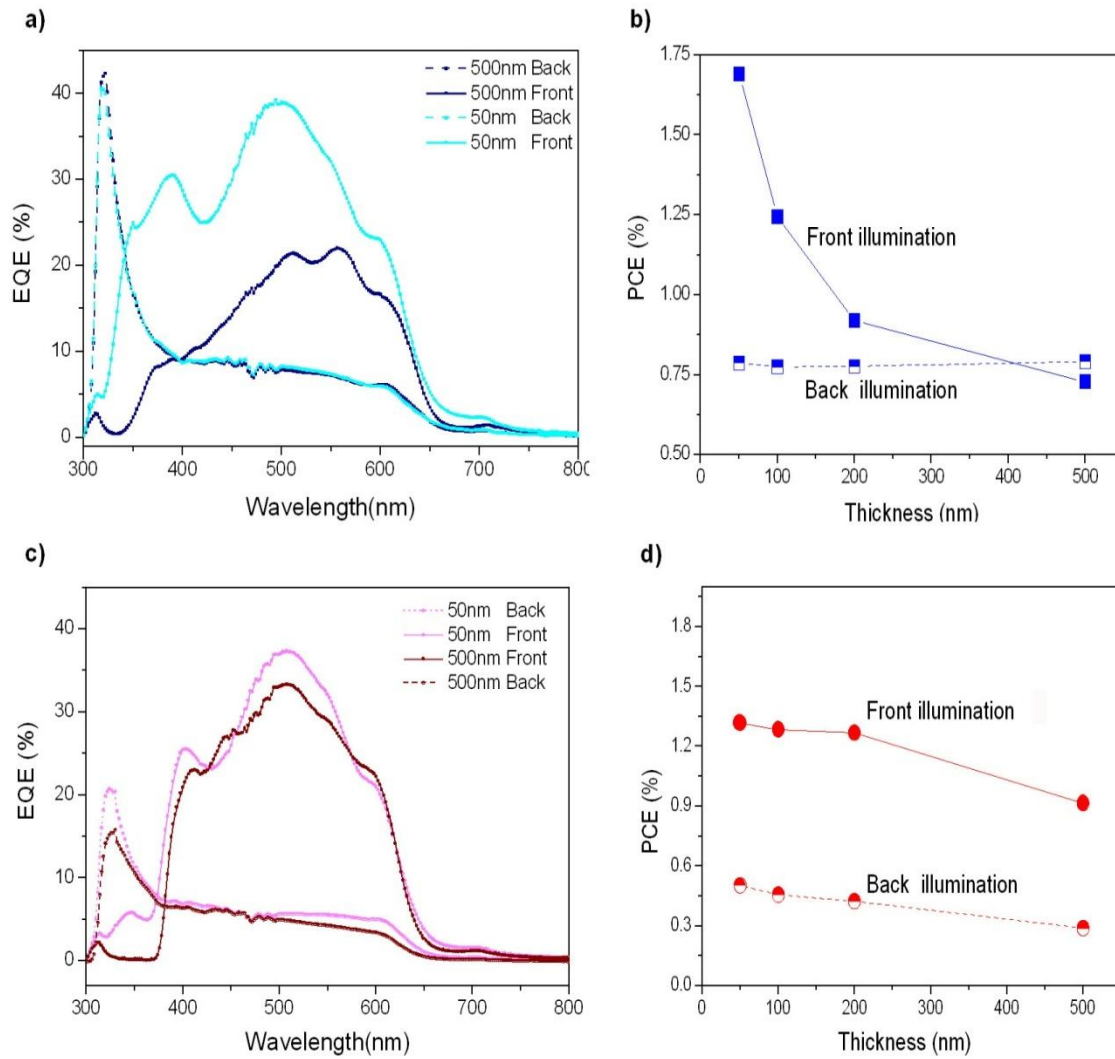


**Figure 4.10: Filter effect of TiO<sub>2</sub> (top) and ZnO (bottom).** EQE (a,c) and PCE(b,d) of devices illuminated from the front (solid) and back (dash) depending on the blocking layer thicknesses

As shown in Figure 4.10 c and d, the EQE and PCE results are obtained by illuminating the solar cells based on ZnO with different layer thicknesses from the front and back side. When illuminated from the front side, a slight inverse proportion to ZnO thickness shows on both EQE and PCE results, but it is much weaker than that of TiO<sub>2</sub> solar cells. While illuminated from the back side, these two parameters show a slight decreasing trend as well. This could confirm the filter effect also exists in the ZnO layers. Comparing the devices performances under the two illumination paths, their difference showing in ZnO devices is not as strong as that of observed in TiO<sub>2</sub> solar cells. Together with the less strong layer-thickness dependence, it can be attributed to the high transparency of the ZnO layers. Since the absorption of ZnO

layer in the visible region is almost independent from the thickness, leading to a relatively constant and low light intensity loss, the performances of ZnO solar cells show similar results for both illumination paths regardless layer thickness. The filter effect of ZnO devices confirms the assumption of less traps states in ZnO.

## 4.6 Stability of the inverted devices based on TiO<sub>2</sub> and ZnO

### 4.6.1 Illumination stability

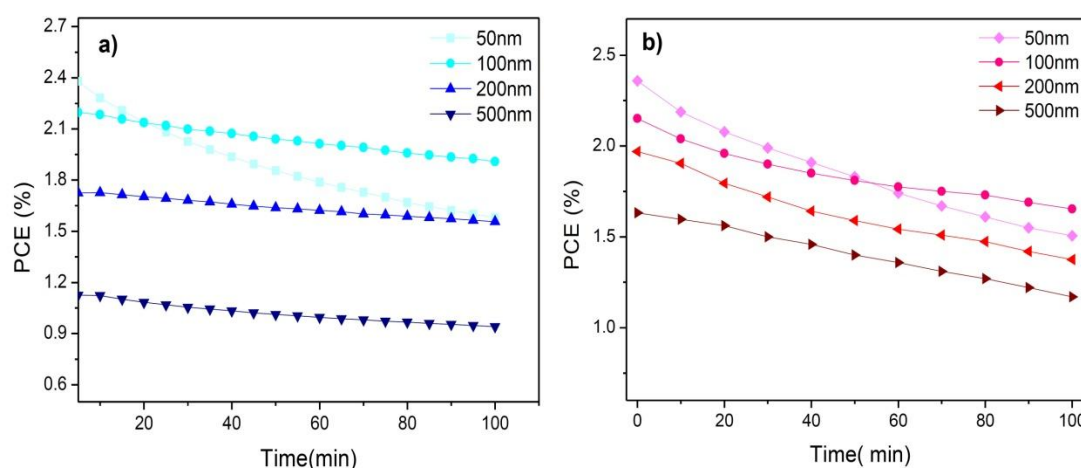


**Figure 4.11: Illumination stability for the solar cells with different TiO<sub>2</sub> (a) and ZnO (b) layers.**

(Dark-blue squares: 500 nm; blue circles: 200 nm; cyan up-triangles: 100 nm; light-cyan down-triangles: 50 nm)

(Dark-red diamond: 500 nm; red Hexagon: 200 nm; pink right-triangles: 100 nm; light-pink left-triangles: 50 nm)

Data is under illumination with simulated AM 1.5G solar light (100 mW/cm<sup>2</sup>).

Figure 4.11 shows the illumination stability investigated for the solar cells with different TiO<sub>2</sub> and ZnO thicknesses. In ambient condition within 100 min solar illumination, the solar cell with 50 nm TiO<sub>2</sub> layer exhibits a 33.5% degradation of PCE, while the thicker ones are much more stable, 13% for 100 nm TiO<sub>2</sub>, 10% and 16% for 200 nm and 500 nm TiO<sub>2</sub> respectively. The degradation for ZnO solar cells under solar illumination is generally larger than that of TiO<sub>2</sub> solar cells. 50 nm ZnO cell is also the most unstable one, showing a 38% degradation of

PCE. For the solar cells with thicker ZnO have the degradation 20% for 100 nm ZnO, 22% and 25% for 200 nm and 500 nm ZnO respectively.

The degradation of hybrid solar cells has many reasons, and the commonly accepted one is that oxygen is readily activated by UV illumination on the interface between metal oxides and the organics. If the TiO<sub>2</sub> or ZnO layer is not thick enough to filter out all the UV light, the super-oxide or hydrogen peroxide formed will then aggressively attack the organic compounds [37]. Besides UV light, thicker metal oxide layers also absorb part of the visible light thus reducing the I<sub>SC</sub> and PCE. However, filtering of UV light results in more stable solar cells, and makes devices with thicker hole-blocking layer more durable to solar irradiation. For TiO<sub>2</sub>-based devices, the competition between these two layer-thickness depending performances gets in balance at 100 nm, which has a reasonable slow degradation and high efficiency. Although the PCE of ZnO solar cells is much less influenced by the ZnO layer thickness, the dependence still shows on the I<sub>SC</sub>, PCE and illumination stability. As results of all the effects, the optimized thickness for ZnO solar cells is 100 nm, the same as TiO<sub>2</sub> devices.

As shown in absorption results of the two metal oxide layers, ZnO layers apparently absorbed less UV light than TiO<sub>2</sub> layer with the same thickness. It results in a generally stronger degradation for ZnO solar cells, which is induced by the less UV protection provided by the ZnO layers than the TiO<sub>2</sub> layers. Since their absorption bands are different (see Figure 4.4), it is difficult to find a thickness for these two materials with a similar absorption ability. However the absorption peak of 500 nm ZnO film is almost as strong as 50 nm TiO<sub>2</sub> film, and its illumination stability is close to the latter one as well. This could provide further confirmation to the conclusion that the illumination stability is related to the protection of metal oxide layers due to their UV filter effect.

Furthermore, the low illumination stability of ZnO devices could be potentially induces the low device performance. Comparing to TiO<sub>2</sub> solar cells, the faster degradation of ZnO solar cells can result in a slight decreasing performance within the I-V measurement time, which normally takes 0.5-1.5 min depending on applied voltage range. Therefore the measured I-V results for ZnO devices may have reduced already, exhibiting a slight lower performance than it should be, while the TiO<sub>2</sub> solar cells perform relatively constantly due to the high illumination stability. This could be another reason for the different performances observed from the two types of devices.

### 4.6.2 Air stability

For inverted solar cells, air stability is considered as one of the most significant advantages, comparing to the normal structured device. Without the influence from environment, the inverted device could dramatically reduce the cost of production. Therefore the difference between TiO<sub>2</sub> and ZnO solar cells on air stability is an important reference to value the two types of devices.

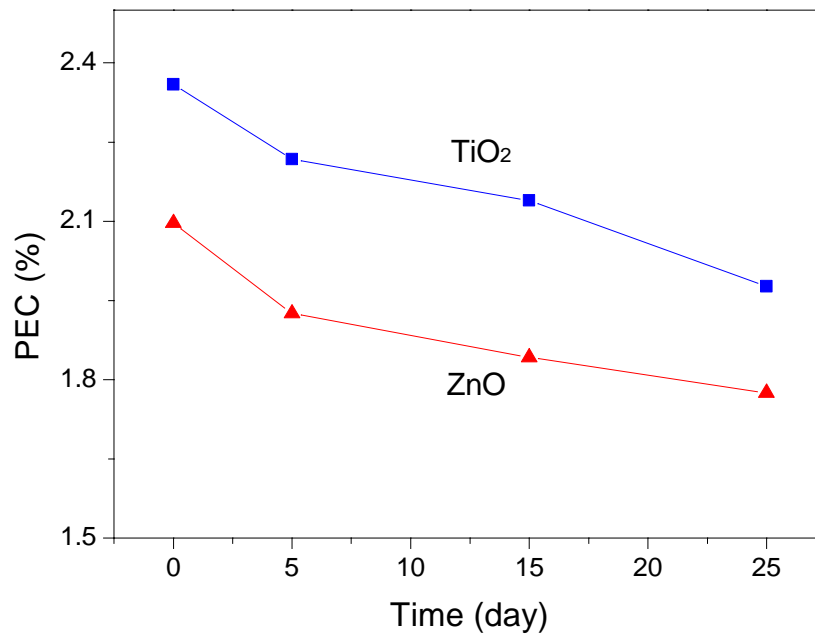


**Figure 4.12:** Air stability for solar cells with 100 nm blocking layers of TiO<sub>2</sub> (blue) and ZnO (red) films. TiO<sub>2</sub> device shows a 16.6% decrease on PCE after 25 days, while ZnO device has a 20.5% decrease. Solar cells stored in air and dark after every time measured with illumination of AM 1.5G solar light (100 mW/cm<sup>2</sup>)

The air stability of the devices with 100 nm TiO<sub>2</sub> and ZnO layers are compared in Figure 4.12. It presents almost the same decreasing rate depending on the storage time. TiO<sub>2</sub> device shows 16.6% degradation on PCE after 25 days, while ZnO device has a slight higher value of 19.5%. From the early report, it is commonly agreed that ZnO is reactive and unstable in oxidizing environments [199, 200], because of O<sub>2</sub> adsorption on the ZnO polar surfaces leading to electrical instability in an ambient environment [201, 202]. After being coated with polymer layer, the chance for exposing the ZnO layer to air is much lower, then the influence

of oxidizing is significantly reduced by this sealing process. As observed in Figure 4.12, it could be stated that the two metal oxide layers contribute almost the same to improve the air stability of inverted solar cells.

## 4.7 Conclusion

Compared to the  $\text{TiO}_2$  layers, the ZnO films has the advantage of higher conductivity and larger surface area, both of which could be beneficial for the solar cell performance by providing faster pathways for electron transfer, and a higher exciton dissociation rate, respectively. However the results of devices performances are opposite to the expectation, with a same layer thickness, ZnO-based device gives worse performance. This is caused by a higher recombination in ZnO solar cells than that of  $\text{TiO}_2$ -based devices and is confirmed via IS measurement. Convincing evidences obtained via Photo-CELIV characterizations indicate that the charge transport in inverted solar cells is mainly limited by the mobility of organic photoactive layer, instead of hole-blocking layer. These findings are important not only for polymer/oxide solar cells, but also for hybrid organic solar cells, which have a layer of semiconductor oxides.

Significantly different optical behavior between the  $\text{TiO}_2$  and ZnO films are induced by the trap states, leading to different performances on the photo-doping effect, filter effect and the illumination stability. Those performances are influenced by the blocking layer thickness, which can be easily controlled during the spray pyrolysis deposition. The  $\text{TiO}_2$ -based solar cells with a thicker layer of  $\text{TiO}_2$  show lower  $I_{\text{SC}}$  and PCE, but higher stability. The dependence of performance on  $\text{TiO}_2$  thickness is caused by the light intensity loss due to the absorption of  $\text{TiO}_2$  film, rather than its electron transport ability. The ZnO solar cells, on the other hand, neither the light absorption nor the trap filling shows any dependence on the thickness of the blocking layers, benefiting from the less traps formed during the spray pyrolysis. This allows a much thicker ZnO layer built in solar cell without influencing on the performance.

The stability of these two types of devices are studied and compared. The illumination stability shows strong dependence on the thickness of metal oxide layer, due to the UV-filter effect, providing a protection for the organic materials from degradation. In competition between the



decreasing performance and increasing of illumination stability with the metal oxide layer thickness, 100 nm turned out to be the optimized thickness for both the TiO<sub>2</sub> and ZnO layers to obtain stable well performing devices. While the air stabilities of these two types of devices exhibit similar behavior. The devices still have an over 80% performance left after storing for 25 days in air in dark, compared to the original device. This high stability shows a promising foreground for widely application and further reduced cost for OPVs.



---

## 5 ZnO Nanowires Electrodes

This chapter provides experimental findings for a set of hybrid solar cells based on ZnO nanowires (NW) fabricated by a hydrothermal (HT) method.

Initially, the growing conditions of ZnO NW are investigated to control the morphology of NW. A set of NW with different lengths are obtained by growing for various times. P3HT:PCBM blend solar cells are prepared based on these substrates, and their performances are characterized to study the influences of the NW length.

Compared to flat layer devices, the PCE improvement shown in ZnO NW solar cells is benefited from the increased blend layer thickness, the enlarged surface area and the reduced recombination at the interface of the NW and organic materials. Since the ZnO NW provide ultra-fast pathways in the devices for the electron transfer, it allows to reduce the PCBM content in blend layer that can be replaced by ZnO NW for the charge transport. Therefore the ratio of P3HT:PCBM for the blend-ZnO NW system is optimized to improve the device performance.

In addition, the ZnO NW surface is modified by a thin layer of N-doped ZnO deposited via AALD method, in order to further improve the device performance, especially the  $V_{OC}$ , by reducing charge recombination.

## 5.1 Introduction

The bulk hetero-junction OPVs have opened new opportunities for the development of a future generation of solar cells to overcome the current hurdles toward low-cost photovoltaic devices. However, polymer-based organic photovoltaic devices are presently limited in their power efficiency by un-optimized properties and device designs.

In order to absorb enough light for charge separation, organic solar cells must be a certain thickness. Normally the absorber layer is 150 nm, which is far beyond the exciton diffusion length [16]. This will enhance the chance for excitons to recombine, before they can be transferred to the electrodes. As a result, the photocurrent and performance of solar cells will be reduced. By carefully controlling the morphology of donor-acceptor interface, all generated excitons could be efficiently dissociated, and the charge carriers transported out of the device [203]. Morphology of blend devices can be controlled through solvent selection and annealing process [155]. However the disordered mixed structure of donor-acceptor blends can increase the charge recombination, reduce the carrier mobility and decrease the power efficiencies of devices.

One-dimensional nanostructured inorganic semiconductors can provide a direct path for created electrons to be transport toward the negative electrode in solar cells. This fast photoinduced charge transfer has been shown recently, between a conjugated polymer and a metal oxide semiconductor such as TiO<sub>2</sub>, SnO<sub>2</sub> or ZnO [204]. In addition, metal oxides are currently lower in cost than fullerenes, and could reduce material costs in device fabrication. Another advantage for inverted solar cells as discussed in Chapter 4 is the significantly enhanced lifetime. Using metal oxides as an exciton selective layer in hybrid solar cells allows the use of more stable high work function counter electrodes, therefore the air stability can be dramatically improved compared to a traditional blend device.

Due to their catalytic, electrical, optoelectronic and piezoelectric properties [89], ZnO NW are used for a variety of applications such as sensors, photovoltaics, energy harvesting nano-generators, and field emitters. Among all these attractive properties of ZnO NW, the high mobility allows them to work as ultra-fast pathways for photoinduced charge transfer. Compared to other metal oxide nanotechnologies, the hydrothermal method to grow ZnO NW is more attractive due to its simplicity and environmentally-friendly growth conditions. HT method synthesis is carried out in aqueous solution, and the growth temperatures are less than

the boiling point of water [101].

During the HT process, the morphology of ZnO NW is significantly influenced by the growth conditions, such as starting materials, solution concentration, temperature and time. By growing within different times, NW with controllable lengths could be obtained. Then a set of solar cells is prepared by coating a P3HT:PCBM layer on the ZnO NW with different lengths, and the influence of their lengths on device performance is investigated. In the blend-ZnO NW system, part of the PCBM could be replaced by NW for charge transfer, therefore the ratio of P3HT:PCBM is optimized for the best solar cell performance.

Using ZnO NW as the electron collection material for ZnO:P3HT hybrid solar cells have been performed by several groups [55, 205, 206]. However, the performance of the ZnO NW based hybrid solar cells are still limited by many problems. A non-optimized interface between the organic photoactive layer and ZnO NW, for instance, leads to a low  $V_{OC}$  around 0.2–0.44 V [94, 207]. To modify the surface of ZnO NW, a thin layer of N-doped ZnO is coated by an AALD method. Significant improvement in solar cell performance is observed, especially an increased  $V_{OC}$ , as a result of the reduced charge recombination.

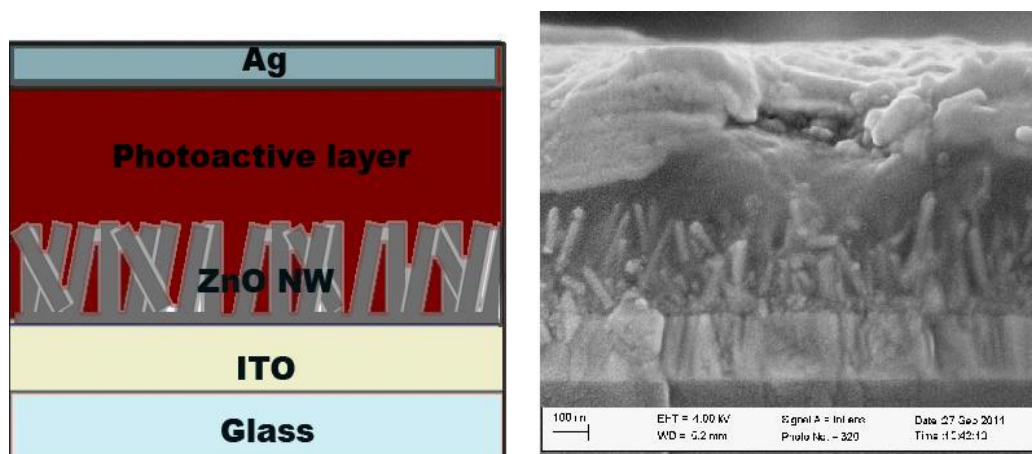


**Figure 5.1** Hybrid solar cells based on ZnO NW. Left: hybrid device structure. Right: SEM cross-section image of a hybrid device.

## 5.2 Device fabrication and optimization

### 5.2.1 Devices fabrication

The hydrothermal method for ZnO NW fabrication is required a ZnO seed layer, which is coated on the ITO substrates via sol-gel method (see section 2.2.3.2). Then the substrates with seed layers are dipped in a solution composed of zinc nitrate hexahydrate and hexamethylenetetramine (HMT) from Sigma-Aldrich. Experiments are carried out to select the proper starting material and concentration of solution. The temperature for NW growth is chosen from 50 °C to 95 °C, and the growing time is controlled from 10 min to 60 min. These HT growing conditions significantly influence on the morphology of ZnO NW, and the details are investigated in section 5.3.

Then the P3HT:PCBM blend solar cells are fabricated using ZnO NW with different lengths as electrodes. The fabrication process are described as follows: after the HT growth, a blend of P3HT and PCBM mixed solution is spin coated on top of the ZnO NW. The preparation of blend solution and spin coating process has been described in Chapter 2.1. To avoid short circuits, a relatively thick blend layer is required to cover all the ZnO NW with different lengths. It can be obtained by using high concentration solutions, with 42 mg/ml of P3HT and 36 mg/ml of PCBM in CBZ.

To optimize the performance of blend-ZnO NW devices, various P3HT:PCBM mixed ratios are used by reducing the fraction of PCBM solution in the blend from 1:1 to 1:0.25, while the concentration of the solutions is kept the same at 42 mg/ml and 36 mg/ml, respectively. A slow-dry process and a pre-annealing process of 10 min at 105 °C are carried out after spin coating the blend layer, followed by the spray coating of PEDOT:PSS and the evaporation of a 100 nm Ag layer. Then the devices are annealed at 140 °C for 10 min in air before measurements.

To investigate the charge transport properties of ZnO NW, the P3HT-ZnO hybrid devices are fabricated based on ZnO NW with different lengths. And then a thin layer of ZnO is coated on the ZnO NW via AALD deposition, with expectation of modifying the surface to reduce charge recombination. P3HT is dissolved in CBZ with a concentration of 36 mg/ml, and then spin coated on ZnO NW with a speed of 800 rpm for 1 min. The drying processes and top electrode deposition for the P3HT solar cells is the same as used for the blend devices. Then

P3HT-ZnO NW devices are finished by post-annealing at 140 °C for 10 min in air.

Device structure and SEM cross-section images are shown in Figure 5.1. Solar cells are assembled to directly acquire characteristics like PCE,  $V_{OC}$ ,  $I_{SC}$ , FF and the equivalent circuit resistances  $R_s$  and  $R_{sh}$  from I-V curves (see section 2.3.1). The absorption measurements of ZnO NW, P3HT and blend films, together with EQE characterization are carried out to analyze the material's potential under solar illumination. Additionally, light intensity measurements are conducted to get insight into charge carrier recombination and collection processes in the cells.

### 5.2.1 Hydrothermal method

Compared to the other synthesis methods for ZnO NW, such as chemical vapor deposition [98], vapor-liquid-solid growth [99], and solution chemistry [100], hydrothermal method draws great attention for its convenient fabrication conditions of low cost, low temperature, easy control, and non-toxic. It has been successfully used for the fabrication of large scale arrays of vertical ZnO NW on glass, ITO, Si wafers[208], and even on plastic substrates [209].

The mechanism of the hydrothermal process is discussed in the early report [101]. Typical ZnO NW grown by the HT method is hexagonal wurtzite, the most common polar surface is the basal plane (001), with lattice parameters  $a = 0.3296$  and  $c = 0.52065$  nm; and the other two most commonly observed facets for ZnO are (211) and (010), which are non-polar and have lower energy than the (001) facets [101]. 1-D ZnO nano-structures tend to maximize the area of the lower energy facets during the HT growth process.

All the ZnO NW samples grown by hydrothermal process have been synthesized in an autoclave (see Figure 5.2). This equipment contains two parts: a metal cover designed for thermal conductivity, and a plastic container that is deformable under high pressure and temperature, which was used to seal the solution.

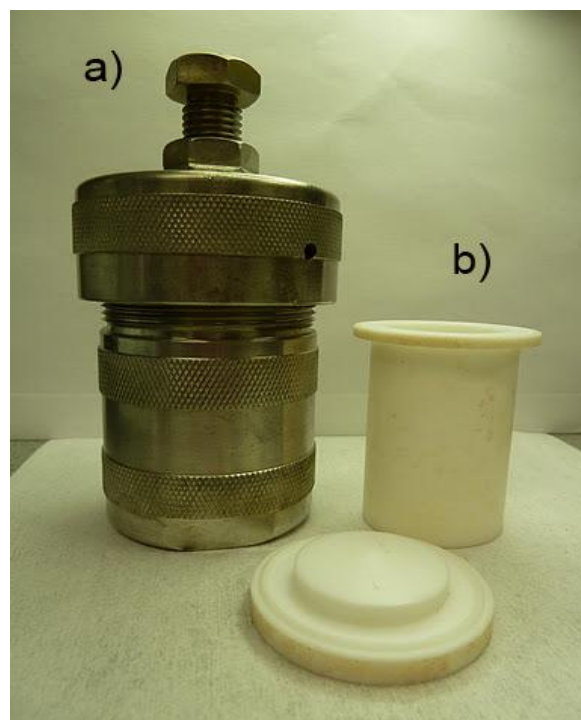


**Figure.5.2: Autoclave.** Custom-designed equipment for HT growth. a) Metal cover, b) High-temperature plastic container

$\text{Zn}(\text{NO}_3)_2$  is dissolved in water as the source of  $\text{Zn}^{2+}$  ions, and the solution concentration can significantly affect the morphology of ZnO NW. Two concentrations of 0.025 M and 0.05 M  $\text{Zn}(\text{NO}_3)_2$  aqueous solution are used for NW growth, and their influences on the surface ZnO NW are discussed in section 5.3.3. The starting material as a growing template also plays an important role in determining the morphology of the ZnO NW, and it is selected from the hexamethylenetetramine (HTM) and ethylenetetramine by comparing their resulting samples (see section 5.3.2). Experiments are carried out to further optimize the morphology of NW by growing at the temperatures from 50 °C to 95 °C, and for the growing time from 10 min to 60 min in section 5.3.2 and 5.3.5 respectively.

After growth, ZnO NW substrates are removed from the solution and rinsed with deionized water, followed by a 3 min ultra-sonic cleaning step in ethanol, then dried with nitrogen gas. The resulting samples are shown in Figure 5.3.



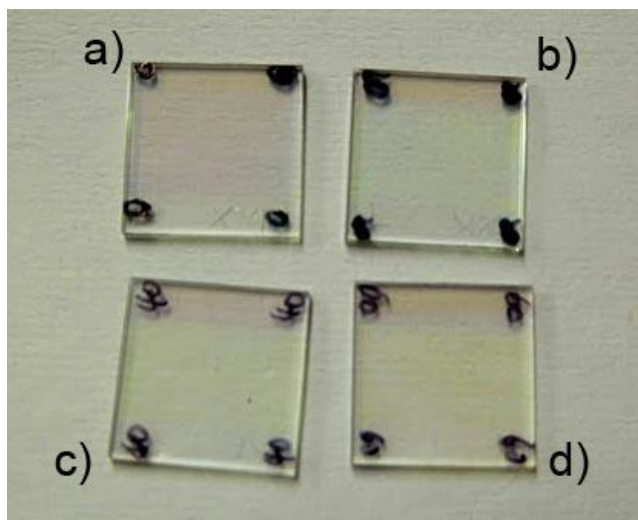


**Figure 5.3: ZnO seed layer a) and ZnO NW grown on ITO for different times: b) 20 min, c) 40 min, d) 60min.** The color of the substrates is slightly changed from light pink to light green or yellow depending on the ZnO films coating on top.

### 5.2.2 ZnO seed layers optimization

For the ZnO NW grown by HT, a flat ZnO layer is required as a seed layer to grow the NW on top [210]. Among all the fabrication methods for flat ZnO layers, the sol-gel method has gained a lot of popularity since it offers controlled consolidation, shape modulation and patterning of the nanostructures [101]. Therefore it is a competitive candidate for the preparation of the ZnO seed layer, as well as spray pyrolysis, which has been well studied in Chapter 4. As the SEM images of ZnO films show in Figure 5.4, a sample fabricated by the sol-gel method is observed to be much smoother compared to the one prepared by ZnO spray pyrolysis. The roughness of the seed layer could directly influence the orientation of NW grown on top [59]. From the morphology of ZnO NW on these two seed layers, it is obvious that NW grown on the ZnO flat layer fabricated by sol-gel is much more homogeneously distributed and vertically oriented than those grown on the ZnO film obtained by spray pyrolysis. Therefore the sol-gel method is chosen as the seed layer fabrication method for HT growth of ZnO NW. The fabrication process is optimized via a series of experiments, and their influence on the device performance is exhibited in Table 5.1.

Sol-gel processes	PCE (%)	V <sub>OC</sub> (V)	I <sub>SC</sub> (mA/ cm <sup>2</sup> )	FF (%)	R <sub>Sh</sub> ( $\Omega$ / cm <sup>2</sup> )	R <sub>s</sub> ( $\Omega$ / cm <sup>2</sup> )
Spin speed 1000 rpm	1.04	0.42	6.05	38.3	220	28
Spin speed 1500 rpm	1.22	0.45	6.81	40.3	258	17
Spin speed 2000 rpm	0.81	0.37	6.10	35.8	157	18
Annealing time 5 min	1.58	0.54	6.48	45.4	348	7
Annealing time 10 min	0.94	0.45	5.34	37.5	217	15
Annealing time 30 min	0.56	0.20	5.06	35.4	125	18

**Table 5.1: The performances of blend solar cells based on ZnO films fabricated by sol-gel method with different spin coating speeds and post-annealing times.** I-V characteristic data acquired under simulated solar illumination. Values are given for solar cells with different thicknesses of TiO<sub>2</sub>. Data is extracted for the six individual pixels of each cell set and the respective standard deviations are calculated.

The fabrication process sol-gel method for ZnO films are given in details in Section 2.2.3.2. It can be briefly described as follows: the ZnO sol-gel is prepared by Zn(CH<sub>3</sub>COO)<sub>2</sub>•2H<sub>2</sub>O dissolved in 2-methoxyethanol and ethanolamine with a concentration of 0.5 mol/L; then gel films are fabricated by spin coating the solution on ITO substrates with a speed of 1500 rpm; after being calcined the gel films at 375 °C for 10 min, ZnO seed layers are obtained.

Furthermore, the air stability of ZnO seed layers is investigated by storing the ZnO layers in air for 3 days, 7 days and 14 days. Then solar cells are prepared based on those aged ZnO seed layers and a device based on as-prepared ZnO is built for reference. Their performances are recorded by I-V measurements, and results are shown in Table 5.2. A clear degradation of solar cell performance with aging time is observed. It means that the ZnO film is not stable and a fresh ZnO seed layer is required for optimal ZnO NW and solar cell fabrication.

ZnO film Type	PCE (%)	V <sub>OC</sub> (V)	I <sub>SC</sub> (mA/ cm <sup>2</sup> )	FF (%)	R <sub>Sh</sub> (Ω/ cm <sup>2</sup> )	R <sub>s</sub> (Ω/ cm <sup>2</sup> )
As prepared	1.58	0.54	6.48	45.4	348	7
After 3 days	1.20	0.45	5.68	40.3	158	10
After 7 days	0.89	0.46	5.10	35.6	147	13
After 14 days	0.74	0.45	4.75	32.9	121	15

**Table 5.2: I-V measurements of blend solar cells based on ZnO films stored for different periods.** Data is record under illumination with simulated AM 1.5G solar light (100 mW/cm<sup>2</sup>). Values are extracted for the six individual pixels of each cell set and the respective standard deviations are calculated.

### 5.3 Morphology of ZnO NW

The morphology of the ZnO NW is required to be homogeneous for solar cell fabrication. The vertically aligned NW can provide solar cells with a conducting path towards the external contact to enhance electron collection. However, the parameters of the ZnO NW, such as density, diameter and length, are still difficult to control. In this section, HT growth conditions are studied through experiments to modify the morphology of ZnO NW. Briefly, the orientation and alignment of ZnO NW are determined by the ZnO seed layer, their density and diameter could be controlled by the template and concentration of solution, and the length depends on temperature and growing time.

#### 5.3.1 Influence of ZnO seed layer on morphology

ZnO NW array growth is influenced strongly by the underlying seed layer [211]. The alignment of the ZnO seed layer can directly determine the orientation of NW grown on top. Figure 5.4 shows SEM images of ZnO films fabricated by the two different methods. It is obvious that the ZnO layer fabricated by the sol-gel method is much smoother than the one fabricated by spray pyrolysis. The morphology of ZnO NW grown on the two seed layers is

compared in Figure 5.4 as well.

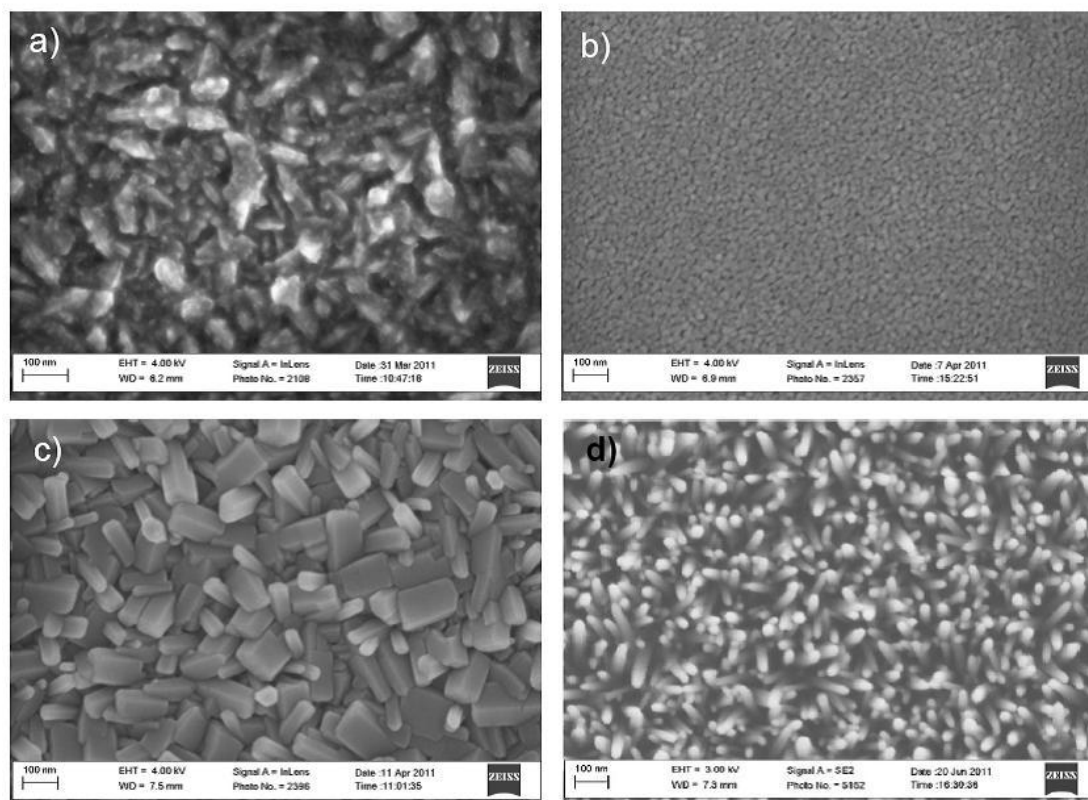


**Figure 5.4:** SEM images of ZnO seed layers (up) fabricated by a) spray pyrolysis, b) sol-gel method, and ZnO NW (down) grown on the seed layer by c) spray pyrolysis, d) sol-gel method. ZnO seed layer via sol-gel method can obtain NW with smaller diameters and more homogeneous orientation.

As SEM images shown in Figure 5.4, the ZnO seed layer fabricated by the sol-gel method gives much smaller ZnO NW with a narrower diameter distribution, as compared to the one fabricated by spray pyrolysis. The diameter, length and density of NW determine the surface area of ZnO electrodes. A large surface area can be beneficial to the charge separation occurring on the interface between the photoactive layer and the conducting electrodes. ZnO NW on the seed layer fabricated by sol-gel method are narrow and dense, which indicates a significantly larger surface on this substrate, with the potential to improve the performance of solar cell devices. In addition, the orientation of the ZnO NW on the sol-gel seed layer is more vertical than the ones on the sprayed layer. This alignment offers a fast pathway for charge transfer to the electrode, and supposes to speed the polymer filling into the nanostructures. Considering all the facts above, the sol-gel method is chosen as the ZnO seed layer preparation technique for HT growth of NW.

### 5.3.2 Influence of HT solution on morphology

#### The influence of starting materials

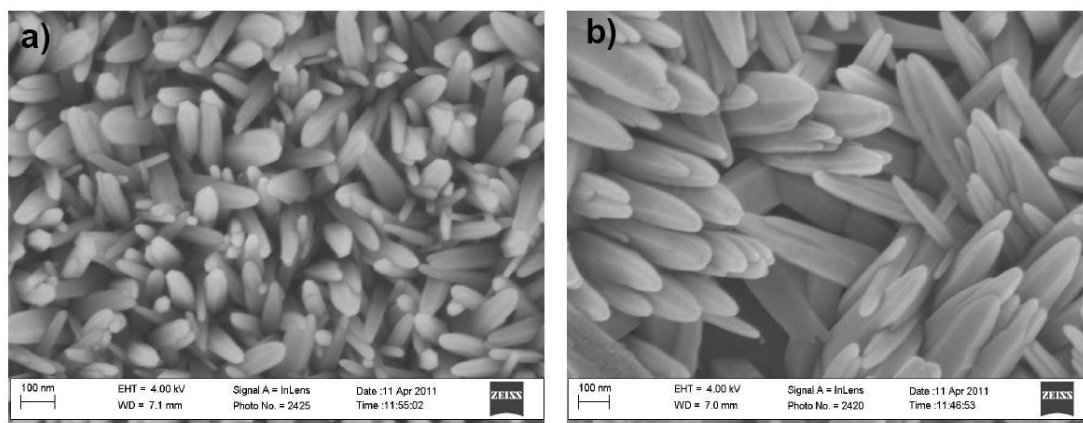


**Figure 5.5: SEM images of the morphology of ZnO NW grown by using different starting materials.**

**a) Hexamethylenetetramine (HTM) (left), b) Ethylenetetramine (right).** The HTM solution can obtain NW with smaller diameters and more vertical alignment.

The starting materials play important roles in supplying the hydroxyl ions to react with  $\text{Zn}^{2+}$  ions form ZnO during the HT growth process [210]. It is generally accepted that the hydroxyl ions drive the precipitation reaction [212]. Therefore the starting materials, which work as templates for the HT growth, could determine the morphology of the ZnO NW.

From the SEM images of Figure 5.5, it is observed that the diameters of ZnO NW grown in HMT are much smaller than those grown in ethylenetetramine. Their distribution and orientation are more homogeneous, and the alignment of the NW is more vertical as well. For the same reason as discussed above, HMT is more suitable than ethylenetetramine as the template to grow ZnO NW for solar cell devices.

#### The influence of solution concentration

$\text{Zn}(\text{NO}_3)_2$  solution supplies the source of  $\text{Zn}^{2+}$  ions for HT growth, and its concentration in aqueous solution could certainly influence the morphology of the ZnO NW. An experiment is

carried out by growing ZnO NW in two different  $\text{Zn}(\text{NO}_3)_2$  solutions, with concentrations of 0.05 M and 0.025 M, respectively. Their morphologies are compared in Figure 5.6.

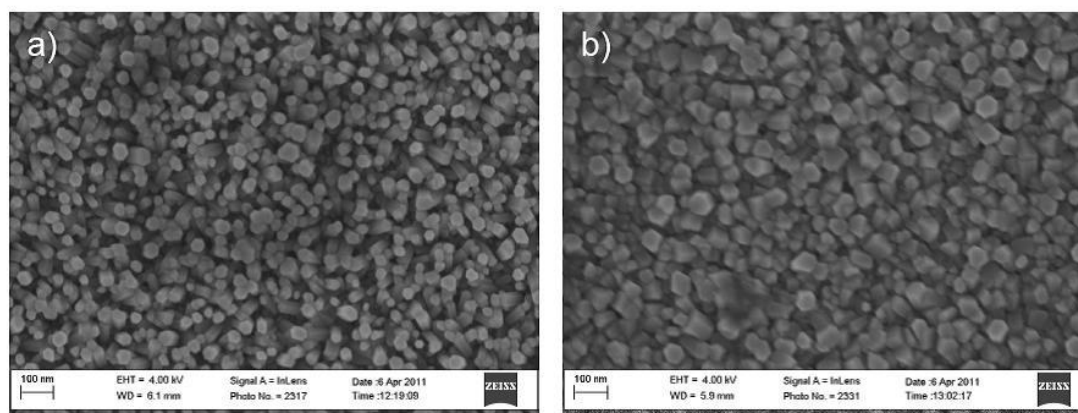


**Figure 5.6: SEM images of ZnO NW grown in solutions with different  $\text{Zn}(\text{NO}_3)_2$  concentration: a) 0.025 mol/L (left), b) 0.05 mol/L (right).** The 0.025 mol/L solution can obtain NW with much smaller diameters.

SEM images show that the diameter of ZnO NW grown in 0.025 M  $\text{Zn}(\text{NO}_3)_2$  solution is much smaller than the ones grown in the high concentration solution, and the distance between the nanowires is larger than the latter. Based on this, it could be assumed that controllable NW spacing can be simply achieved by adjusting the concentration of solution. When the NW spacing is reduced close to exciton diffusion length, it can be highly favorable for exciton dissociation, and then improvement of solar cell performance is expected.

### 5.3.3 Influence of temperature on morphology

The SEM images in Figure 5.7 show the morphology of ZnO NW grown at different temperatures chosen from 50 °C to 105 °C. Meanwhile, all the other growing conditions are the same: the ZnO seed layer is fabricated by the sol-gel method, the ZnO NW are grown in an aqueous solution of equimolar HMT and  $\text{Zn}(\text{NO}_3)_2$  with a concentration of 0.025 M, and growth time is kept at 60 min.

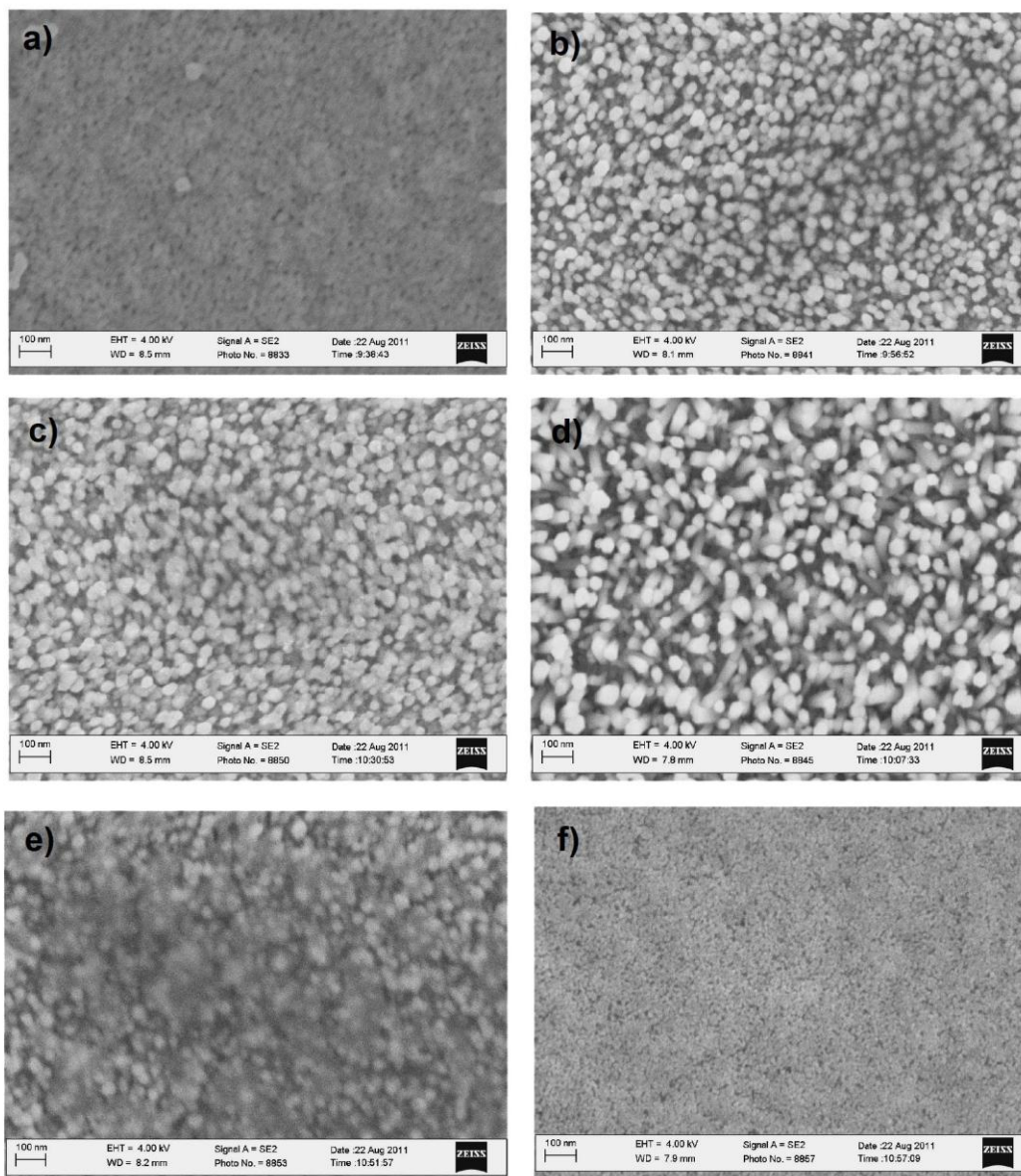


**Figure 5.7:** SEM images of ZnO NW grown at different temperatures: a) 50 °C, b) 70 °C, c) 90 °C, d) 95 °C, e) 100 °C, f) 105 °C. Initially the length of ZnO NW increases with the rising temperature. NW grown at 95 °C exhibits the longest length. While the temperature is higher, the ZnO NW start to shrink.

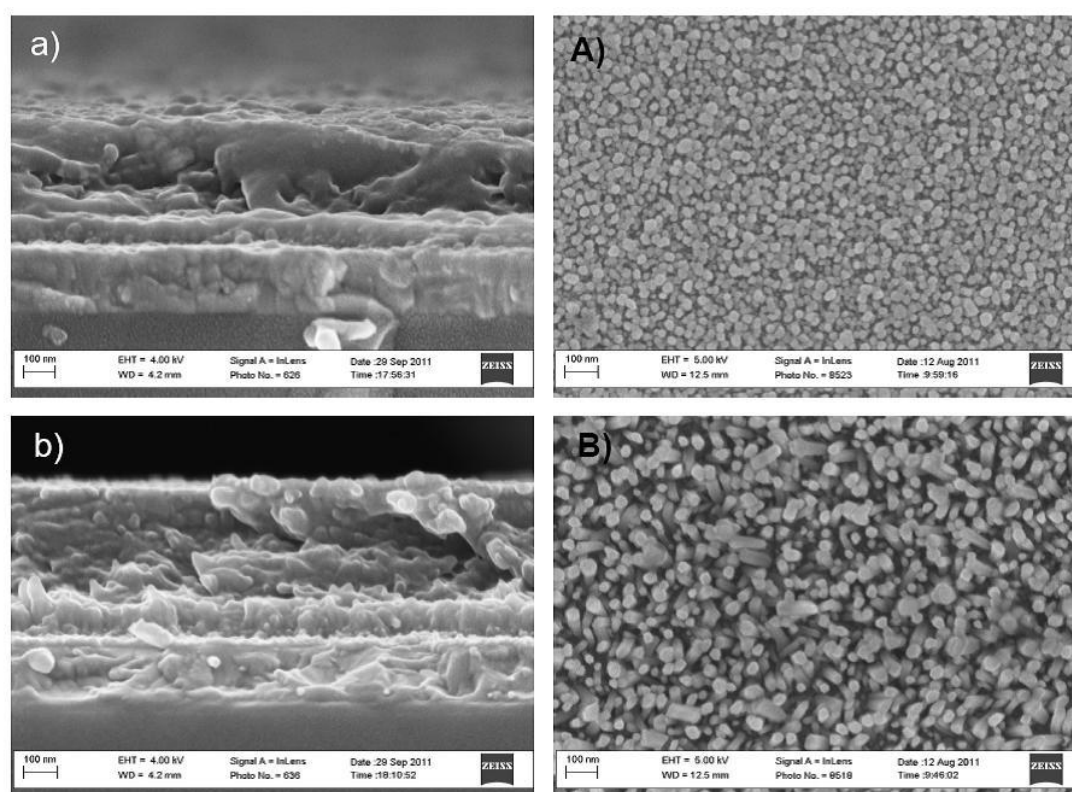
When growing at 50 °C, nanocrystalline conformation starts, while the length of ZnO NW increases with the rising temperature. ZnO NW grown at 95 °C exhibit the longest length. When the hydrothermal temperature is higher, the ZnO NW start to shrink, and probably dissolve into the solution. Finally the nanostructure disappears when the temperature increase to 105 °C. As a summary, 95 °C is the best temperature for ZnO NW growth.

### 5.3.4 Influence of time on morphology

Figure 5.8 shows SEM images of ZnO NW grown at 95 °C for six different times, in the same solution and concentration as used in section 5.3.3. The length of the ZnO NW depends nearly linearly on the growth time, which increases from 10 min to 60 min.

From cross-sections of ZnO NW shown on the left, the dependence of NW length on the growth time is observed: 50 nm for 10 min, 80 nm for 20 min, 100 nm for 30 min, 150 nm for 40 min, 200 nm for 50 min, and 250 nm for 60 min.

On the other hand, the top views of the ZnO NW shown on the right side of Figure 5.8 indicate that the diameters of the ZnO NW barely change with growth time. This one-dimensional growth of ZnO NW makes the controlling of NW length available by simply setting the growth time.





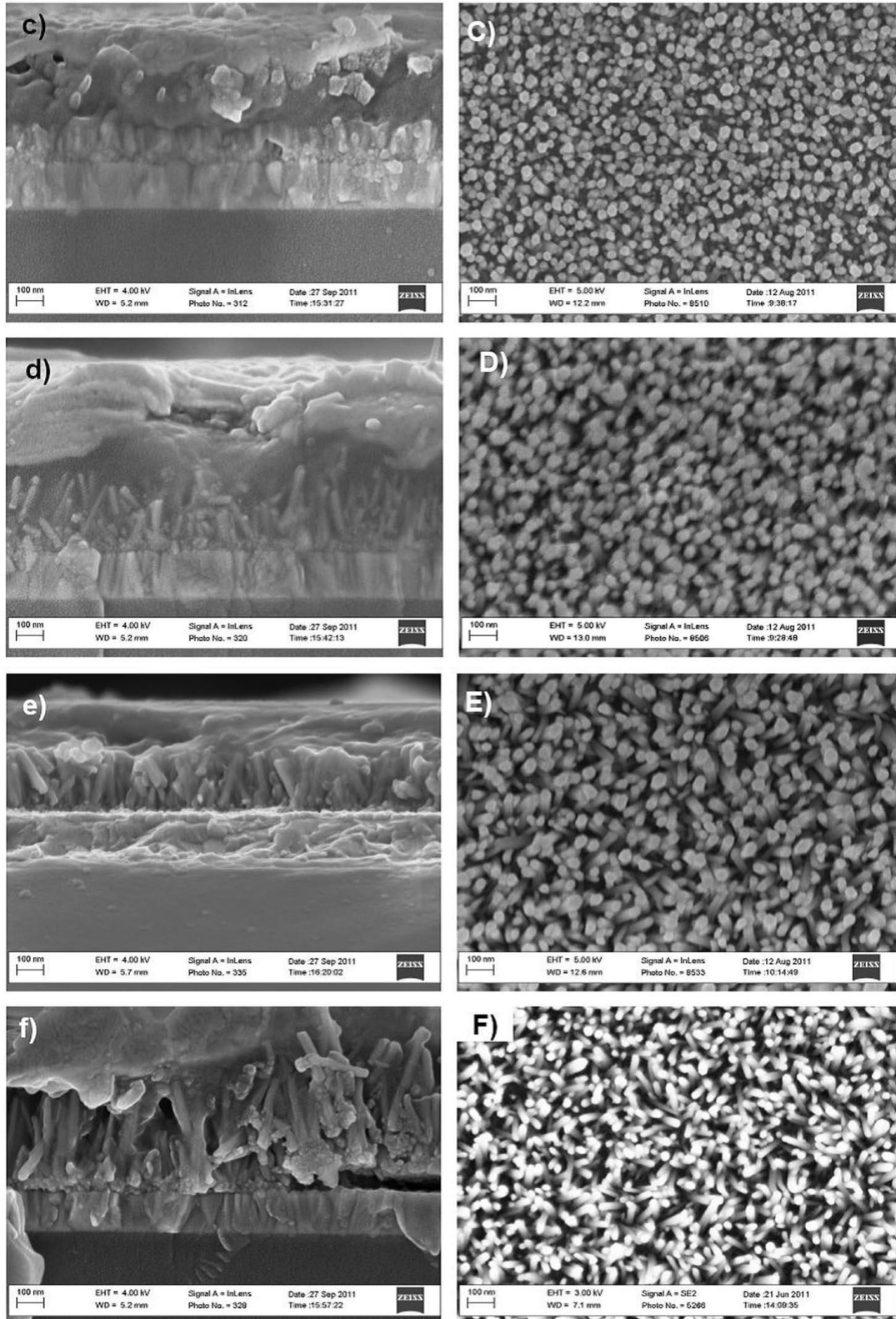


**Figure 5.8: SEM of ZnO NW grown on ITO for different times: a), A) 10 min, b), B) 20 min, c), C) 30 min, d), D) 40 min, e), E) 50 min, f), F) 60 min. Lower case letters (left): cross-section of ZnO NW covered with blend layer in solar cells; capital (right): top-view of bared ZnO NW.**

### 5.3.5 Summary

A series of experiments have been carried out to optimize the ZnO NW HT growth conditions. The optimized growth process is as follows:

A flat dense ZnO film fabricated by a sol-gel method is used as a seed layer. It is dipped into an aqueous solution composed of equal molar  $\text{Zn}(\text{NO}_3)_2$  and HTM, with a concentration of 0.025 M. The temperature is kept at 95 °C, and the growth time is controlled from 10 min to 60 min. A set of ZnO NW with length from 50 nm to 250 nm could be obtained.

## 5.4 P3HT:PCBM solar cells based on ZnO NW

ZnO NW used as the electron collection electrodes for hybrid solar cells has been reported in previous research [55, 205, 206]; however, the performances of the ZnO NW-polymer solar cells are limited mainly by exciton collection efficiency. In order to dissociate more photogenerated excitons and to increase the photocurrent of the device [54], a blend of P3HT and PCBM is intercalated into the ZnO NW. The performance of the ITO/ ZnO NW/ P3HT:PCBM/ PEDOT: PSS/ Ag devices is investigated and optimized in this section.

### 5.4.1 Dependence of solar cell performance on the ZnO NW length

The P3HT:PCBM devices based on ZnO NW with six different lengths (fabrication process described in 5.2) are investigated for the performance as a function of the NW length. The flat ZnO layer obtained via sol-gel method is used for the reference device, in comparison with ZnO NW devices. It is also used in all the ZnO NW devices as a seed layer for the HT growth.

### SEM cross-section characterization of the devices

SEM cross-section images of all the devices are shown in Figure 5.9. It is obvious that the P3HT:PCBM blend is filled completely into the spaces between the nanowires with length

from 50 nm to 150 nm. However, the SEM image suggests that the device on 200 nm ZnO NW may have space in the bottom of the array that is not filled. The 250 nm ZnO NW film is not included in this comparison because they have peeled off from the substrate as observed in Figure 5.8f. Both of these two devices are assumed to perform worse than normal, because the charge transport may be interrupted at the interfaces of the blend and the NW by the poor filling, or on the ITO contact due to the peeling off of ZnO NW.

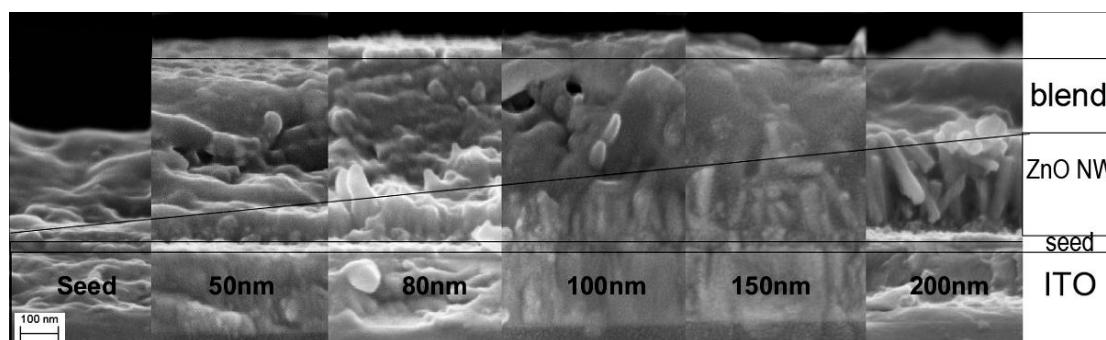


**Figure 5.9:** SEM cross-section images of blend solar cells based on ZnO seed layer and ZnO NW with different lengths from 50 nm-250 nm. Blend layer coated on the ZnO NW are much thicker than that on the seed layer; the ZnO NW devices thickness is almost constant, regardless of the particular ZnO NW length.

It is observed that the blend layers coated on the ZnO NW are much thicker than that on the seed layer, despite their spin coating processes being the same. It indicated that the rough surface of NW may assist to obtain more organic material during the spin coating process. However, the thickness of the entire devices based on ZnO NW is almost constant, about 400 nm for all the solar cells, regardless of the particular ZnO NW length. Therefore, the thickness of the blend layers covered on top of the ZnO NW decreases with the increasing length of NW.

### Absorption measurements

Since the exciton generation is induced by the photo injection into the organic conjugated material, the part of solar light absorbed by the ZnO NW does not participate in the excitation. In this case, the absorption of the ZnO NW has to be subtracted from the absorption spectra measured for the whole devices, in order to investigate the influence of light absorption on the

performance of blend-ZnO NW solar cells.

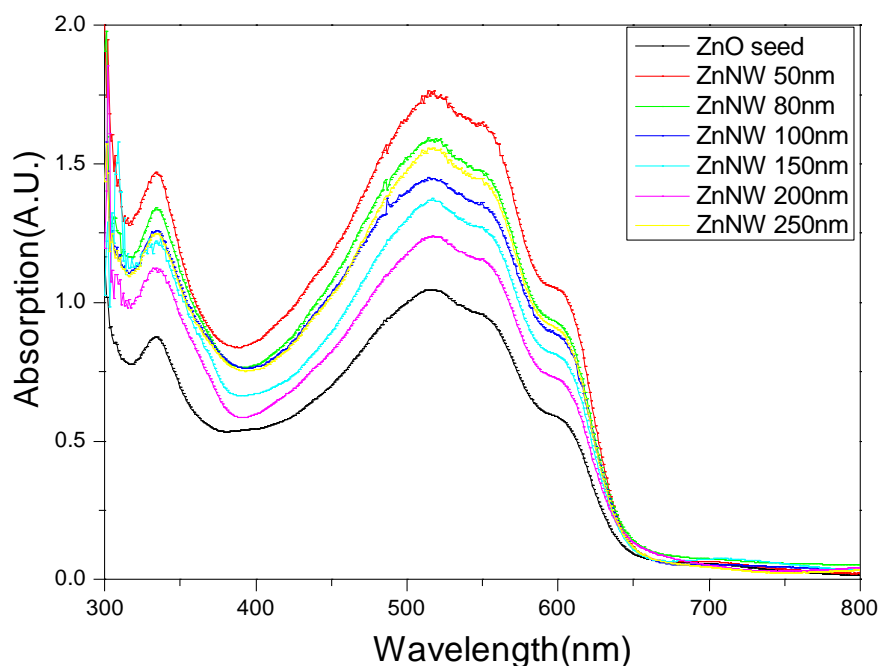


**Figure 5.10: Absorption of blend layers only coated on ZnO seed layer (black) and ZnO NW with different lengths: 50 nm (red), 80 nm (green), 100 nm (blue), 150 nm (cyan), 200 nm (magenta), 250 nm (yellow).** The absorption of blend layer coated on the 50 nm ZnO NW is much higher than that on the seed layer; while it decreases with the length of ZnO NW increasing from 50 nm to 200 nm.

Figure 5.10 shows the absorption results of P3HT:PCBM layers coated on different lengths of ZnO NW. Absorption peaks around 500 nm belong to P3HT, and ones at the 600 nm are induced by PCBM. The peaks shown at 335 nm are attributed to UV light filtered by the ZnO NW with different lengths.

Compared to the blend layer coated on a seed layer only, the one coated on 50 nm ZnO NW shows a significantly improved absorption, which is also the highest absorption among all the blend layers recorded on different ZnO substrates. With the length of ZnO NW increasing from 50 nm to 200 nm, a clear decreasing trend is observed for the absorption of the blend layer coated on those substrates. A possible explanation is given as follows: since the space between the nanowires is relatively small, the blend materials intercalated inside are much

less than the part covered on top of ZnO NW. Therefore, the absorption of the blend layer is mainly attributed to the latter part, which has a thickness that decreases strongly depending on the length of the ZnO NW underneath (see Figure 5.9). Thus a reduction in the blend layer absorption follows for longer NW.

However, the device with 250 nm ZnO NW is out of this trend, because the peeling and disordering of its NW (as seen in SEM cross-section images) could seriously influence its absorption and the resulting solar cell performance. Therefore, it should be considered independently from the other ZnO NW devices.

### EQE characterizations

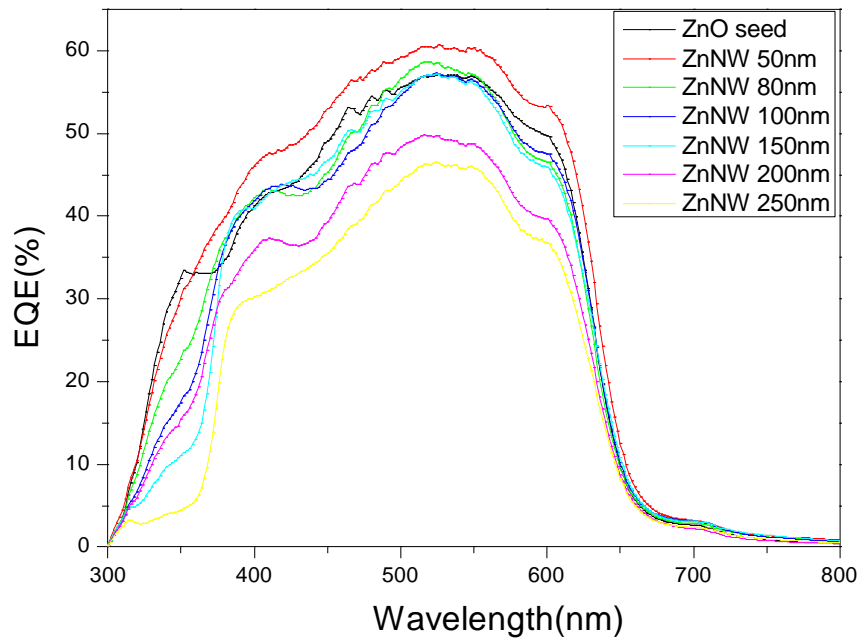


**Figure 5.11: EQE results of blend solar cells based on ZnO seed layer (black) and ZnO NW with different lengths: 50 nm (red), 80 nm (green), 100 nm (blue), 150 nm (cyan), 200 nm (magenta), 250 nm (yellow).** The EQE at 350 nm clearly decreases with the increasing ZnO NW length, while the part at 520 nm decreases with the length of ZnO NW increasing from 50 nm to 200 nm.

To investigate the working mechanisms of the photovoltaic devices under solar illumination, the spectrally resolved current generation is analyzed by EQE measurements. Figure 5.11 shows the EQE characterization results for the blend solar cells on ZnO NW with lengths from 50 nm to 250 nm. The EQE around the wavelength of 350 nm clearly decreases with the increasing ZnO NW length. It is attributed to the filter effect from the absorption of ZnO layers (see section 4.3.5) that can be briefly described as follows: longer ZnO NW can absorb more UV light, but this part of light is filtered out rather than involved in photogeneration. A maximum EQE around 500-600 nm attributed to the absorption of P3HT and PCBM, is observed in all devices. It has a similar dependence on NW length as shown in the absorption results, which decreases with the length of ZnO NW increasing from 50 nm to 200 nm.

### Internal quantum efficiency

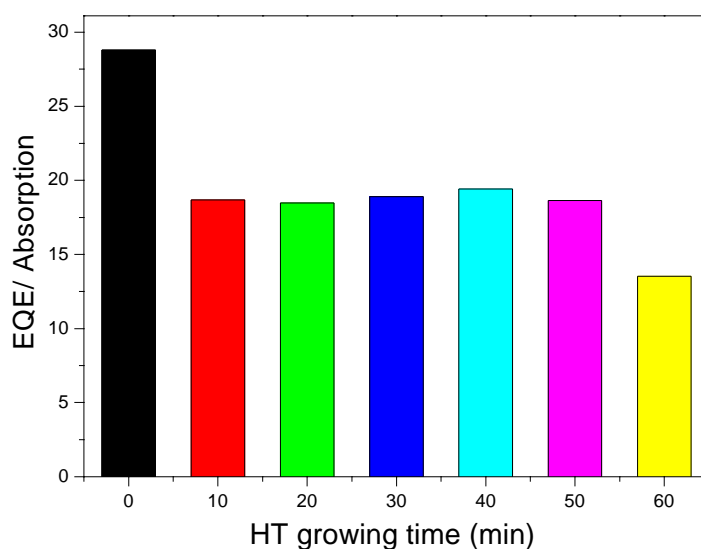


**Figure 5.12: Internal quantum efficiency of solar cells obtained by dividing EQE by absorption of blend layers that coated on ZnO seed layer (black) and ZnO NW with different lengths: 50 nm (red), 80 nm (green), 100 nm (blue), 150 nm (cyan), 200 nm (magenta), 250 nm (yellow).**

To further investigate the dependence of device performance on the ZnO NW length, the influence of differing light absorption caused by the device thickness has to be removed. The

internal quantum efficiency (IQE) of devices is obtained by dividing the EQE results by the absorption spectra (Abs) of the blend layers [213]:

$$\text{IQE}(\lambda) = \text{EQE}(\lambda) / \text{Abs}(\lambda) \quad (5.1)$$

As shown in Figure 5.12, the IQE results of devices slightly increase while the NW length increases from 50 nm to 150 nm. It indicates that the exciton collection efficiency might be enhanced by the ZnO NW intercalating the blend system. For the 200 nm and 250 nm NW devices, the opposite trend in the charge transfer could be caused by poor filling of the organic material or nanostructure peeling problems. On the other hand, the significant difference between the devices based on the seed layer and the 50 nm NW indicates that these two layers perform differently in blend-ZnO system for the electron collection. The obviously low IQE of the device based on 50 nm ZnO NW indicates that the high absorption seems to be the main reason for its improved EQE.

As discussed in section 1.2.1, the optical-to-electrical conversion process is the result from:

$$\eta_{\text{EQE}} = \eta_{\text{Abs}} \cdot \eta_{\text{ED}} \cdot \eta_{\text{CT}} \cdot \eta_{\text{CC}} \quad (5.2)$$

where  $\eta_{\text{Abs}}$  is the absorption efficiency,  $\eta_{\text{ED}}$  is the exciton diffusion efficiency,  $\eta_{\text{CT}}$  is the charge transfer efficiency, and  $\eta_{\text{CC}}$  is the charge collection efficiency.

Using the equation of 5.1, the IQE is determined by the  $\eta_{\text{ED}}$ ,  $\eta_{\text{CT}}$  and  $\eta_{\text{CC}}$ . The  $\eta_{\text{CT}}$  could be negatively influenced by the increasing blend layer thickness, due to the random mixture of donor and acceptor [31];  $\eta_{\text{CC}}$ , on the other hand, might be improved by the large surface and long pathways for directly electron transport, provided by the NW. The variation of  $\eta_{\text{ED}}$  is not clear: since the exciton diffusion occurs on the interface of P3HT and PCBM, the blend morphology between the NW and seed layer based devices is expected to be different, resulting in different  $\eta_{\text{ED}}$ ; on the other hand it might be also effect by the blend layer thickness due to the light intensity loss during the photo injection through this layer [160].

Although the absorption seems to affect most on the result of EQE, the charge transport and collection induced by the NW may influence on the device performance as well. Additionally, the IQE or EQE is not identical to photovoltaic energy conversion; therefore, further investigations on the performance of devices depending on NW length have to be given by I-V characterization.

## I-V characterizations

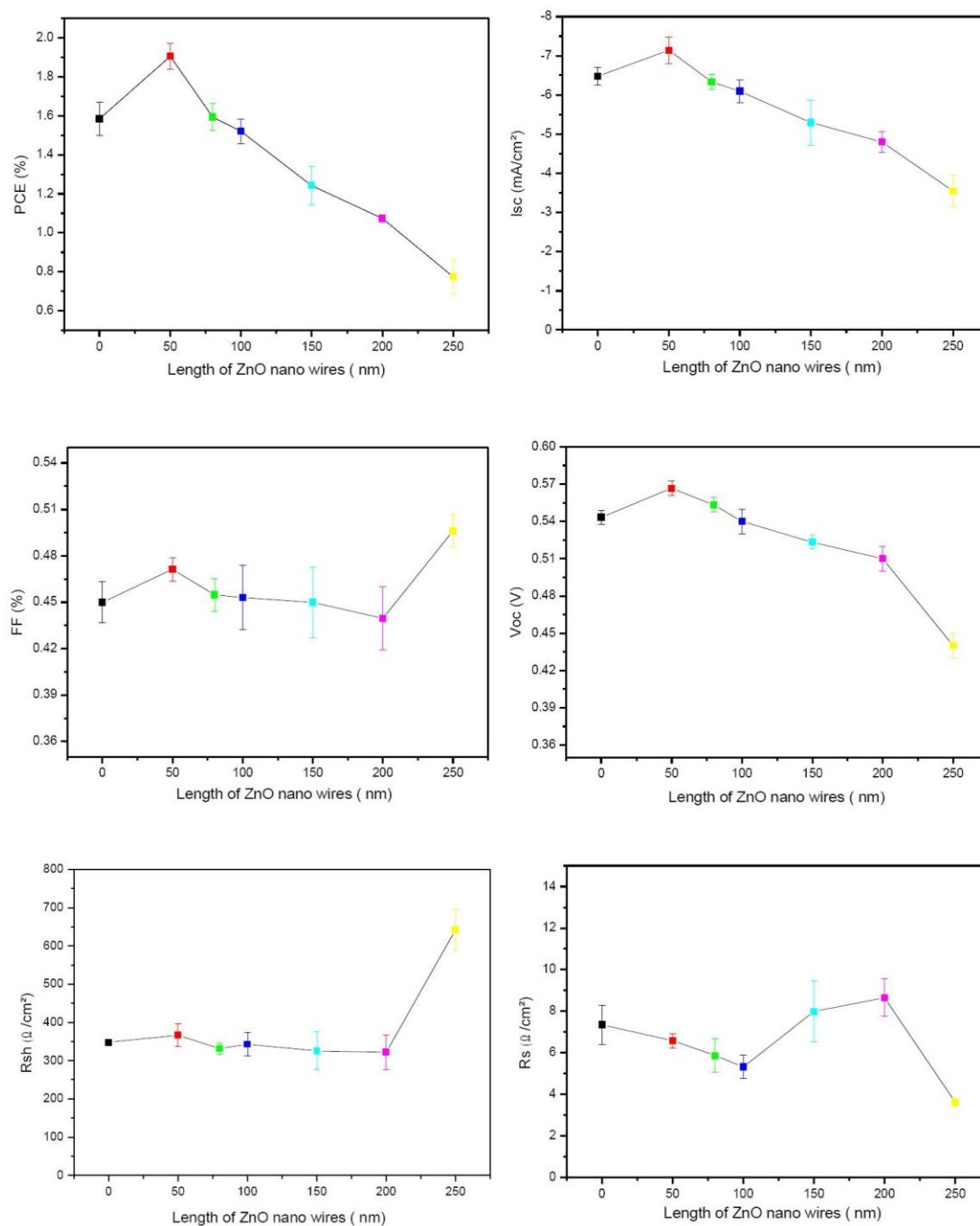


**Figure 5.13: Parameters of device performance depending on the length of ZnO NW. (0 nm stands for the ZnO seed layers)** I-V results carried out for blend solar cells based on ZnO seed layer (black) and ZnO NW with different lengths: 50 nm (red), 80 nm (green), 100 nm (blue), 150 nm (cyan), 200 nm (magenta), 250 nm (yellow).

Figure 5.13 and Table 5.3 show the I-V measurements results of the devices based on ZnO



seed layer and ZnO NW with different lengths. Data is acquired under simulated solar illumination and extracted for the six individual pixels of each cell set and the respective standard deviations are calculated. Values are given for solar cells with different thicknesses of ZnO.

ZnO substrates Type	PCE (%)	$V_{OC}$ (V)	$I_{SC}$ (mA/cm <sup>2</sup> )	FF (%)	$R_{Sh}$ ( $\Omega$ /cm <sup>2</sup> )	$R_s$ ( $\Omega$ /cm <sup>2</sup> )
Seed layer	1.58	0.54	6.48	45.4	348	7.3
ZnO NW 50 nm	1.91	0.57	7.13	47.3	366	6.5
ZnO NW 80 nm	1.62	0.55	6.39	45.5	331	5.8
ZnO NW 100 nm	1.54	0.56	6.31	45.3	343	5.3
ZnO NW 150 nm	1.24	0.52	5.29	45.2	325	7.9
ZnO NW 200 nm	1.07	0.51	4.78	44.1	321	8.5
ZnO NW 250 nm	0.77	0.44	3.55	49.0	642	3.6

**Table 5.3: I-V Characteristics results of blend solar cells based on ZnO seed layer and ZnO NW with different lengths from 50 nm-250 nm.**

Among all the solar cells with different ZnO layers, the best performance is given by the device with 50 nm ZnO NW, demonstrating values for the  $V_{OC}$ ,  $I_{SC}$ , FF and PCE of 0.57 V, 7.13 mA/cm<sup>2</sup>, 0.47, and 1.91 %, respectively. Compared with the solar cell based on a ZnO seed layer, a nearly 20 % improvement in the PCE is shown in 50 nm ZnO NW devices, as a result of increased FF,  $V_{OC}$  and  $I_{SC}$ . With the length of ZnO NW increasing from 50 nm to 200 nm, both  $I_{SC}$  and  $V_{OC}$  decrease, but FF,  $R_s$  and  $R_{Sh}$  show slightly variations with unclear trends. Furthermore, the 250 nm NW device behaves much differently from the other ones as expected and discussed before.

Corresponding to the discussion about EQE and IQE results, the PCE of devices is mainly attributed to the absorption of blend layers, since it presents a similar NW length dependence

as shown in SEM images and absorption results of blend layers (see Figure 5.9 and 5.10). However, the influences of NW length are not only shown in photocurrent, which is responding to the absorption efficiency, but also present in FF and  $V_{OC}$ . It indicates that the NW can influence on the charge transfer of devices as well. This is investigated by comparing the 50 nm ZnO-based device with the flat ZnO solar cell on the I-V curves, giving more information of the charge transport in the devices.

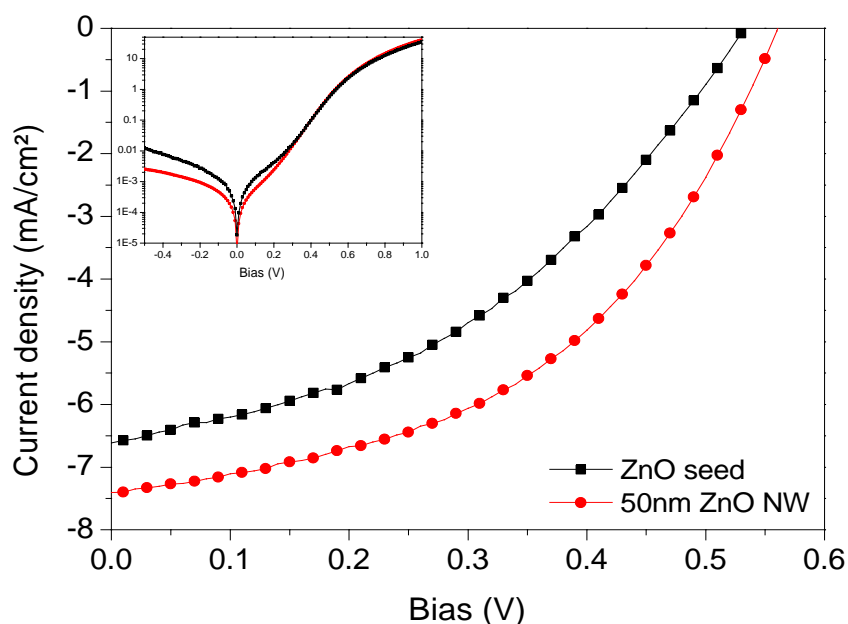


**Figure 5.14: I-V curves of blend solar cells based on: a) ZnO seed layer (black square), b) 50 nm ZnO NW (red circle).** Data is acquired under illumination with simulated AM 1.5G solar light ( $100 \text{ mW/cm}^2$ ).

Figure 5.14 shows the I-V curves of devices based on a ZnO seed layer only and 50 nm ZnO NW. The light I-V curve of the 50 nm ZnO NW solar cell presents a better FF and a steeper slope near the  $V_{OC}$  than the seed layer cell, which suggests a lower  $R_S$  and a higher  $R_{Sh}$ , as confirmed in Table 5.3. As shown on the dark I-V curves, the device based on 50 nm ZnO NW exhibits a much lower current in back direction compared with the ZnO seed layer device, which may indicate a lower charge carrier recombination rate in the NW cell. All these facts discussed above indicate that the charge transport ability of ZnO NW device is improved, together with the enhanced photocurrent, leading to a better device performance.

These improvements may be benefited from the participation of ZnO NW that offer ultra-fast

pathways for the electrons transport when they intercalate into the organic materials; on the other hand, the additional layer of NW grown on flat ZnO films may also provide better hole blocking properties for the device. The reasons for the improved charge transport have to be given by further study, like the light intensity measurements.

### Light intensity measurements

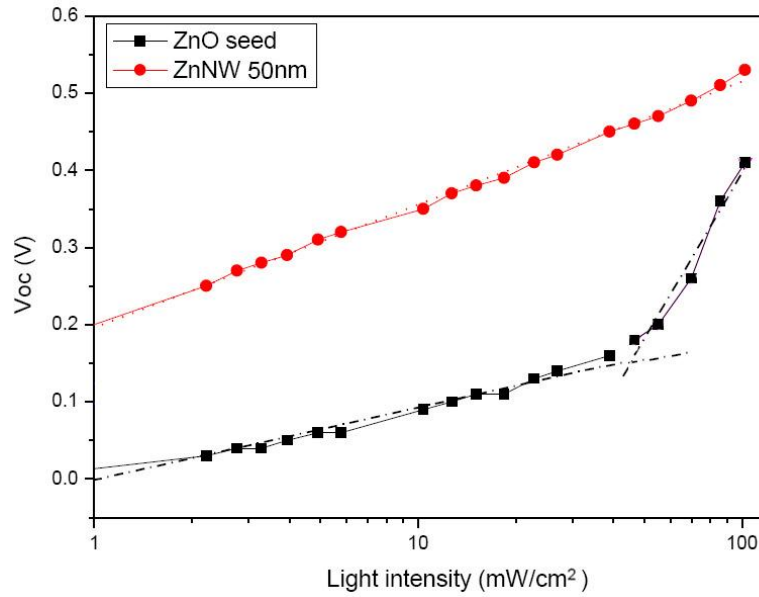


Figure 5.15: Light intensity measurement of blend solar cells based on: a) ZnO seed layer (black square), b) 50 nm ZnO NW (red circle).

Figure 5.15 shows the light intensity results of solar cells on a ZnO seed layer only substrate and a 50 nm ZnO NW substrate. It is observed that the  $V_{OC}$  of the device on the 50 nm ZnO NW depends linearly on the logarithm of light intensity, which fits the theory of Langevin recombination shown in the equation below [214]:

$$V_{OC} = \frac{E_{gap}}{q} - \frac{kT}{q} \ln \left[ \frac{(1-P)\gamma N_c^2}{PG} \right] \quad (5.3)$$

This formula predicts the right slope  $S$  of  $V_{OC}$  versus light intensity. The variables in the equation are defined as:  $E_{gap}$  is the energy bandgap denoting the energy difference between the

HOMO and LUMO levels,  $q$  is the elementary charge,  $k$  is Boltzmann's constant,  $T$  is temperature,  $\gamma$  is the Langevin recombination constant,  $N_c$  is the effective density of states  $P$  is the dissociation probability of a bound electron-hole pair into free charge carriers,  $G$  is the generation rate of bound electron-hole pairs, The generation rate of free charge carriers is then represented by  $PG$ , both of which do not depend on intensity [215].

On the other hand, the  $V_{OC}$ -light intensity curve for the device on the ZnO seed layer can be fit by two straight lines with different slopes. It indicates that other recombination should be considered in this situation. As discussed in the paper reported by Rappaport et al, [216], the light intensity dependence of the  $V_{OC}$  could also be influence by another recombination mechanism, Shockley–Read–Hall (SRH) recombination, which is a trap assisted recombination mechanism [217]. Since the SRH has a different dependence on carrier density than the Langevin recombination [29], it indicates that the significantly increased recombination responding at higher light intensities ( $>30 \text{ mW/cm}^2$ ) may be the result of these two recombination mechanisms.

The additional trap-assisted recombination is only one reasonable explanation for the low performance of the device based on ZnO seed layer. Other reasons like mobility, structure, and surface properties, as results of the different fabrication methods for the ZnO layers, might also influence on the charge transport of these two types of ZnO devices. However, since this system is complicatedly affected by both the thickness of blend layers and the morphology of ZnO layers, it is difficult to confirm the reason for the different charge transport in ZnO NW-based device compared to the solar cell based on ZnO seed layer.

Despite the unclear charge transport and recombination mechanisms that can be further investigated in the future, it is clear that the ZnO NW can improve the device performance with great potential to further enhance the efficiency.

#### **5.4.2 P3HT:PCBM ratio vs different ZnO NW lengths**

As discussed above, the ZnO NW is able to penetrate into the blend solar cells, acting as an acceptor like PCBM for charge transfer. Therefore, less PCBM in the blend layer is needed in the ZnO NW-based devices, comparing to that normally used for a flat ZnO-based device. To

fully utilize the charge transport ability of the ZnO NW, the ratio of PCBM has to be reduced in the P3HT:PCBM blend system.

Experiments are carried out to optimize the mixing ratio of PCBM:P3HT from 1:1 to 0.25:1, for the best performance of ZnO NW-blend solar cells. Figure 5.16 shows that the performance of solar cells with different lengths of ZnO NW depends on the volume ratio of PCBM:P3HT. The PCE of devices based on a ZnO seed layer significantly decreases with the decreasing ratio of PCBM in the blend, which is limited by the low exciton dissociation efficiency [218].

A mixed blend volume ratio of 1:1 is required for optimal charge transfer in a flat blocking layer solar cell. For the devices on ZnO NW, both the PCE and  $I_{SC}$  give maximum values when PCBM ratio is 0.75, and then decrease when the ratio becomes lower. Meanwhile, it is observed that longer ZnO NW solar cells need less PCBM to generate the same amount of photocurrent and reach the best PCE. When the PCBM:P3HT is mixed at a volume ratio of 0.75:1, the solar cell based on 50 nm ZnO NW gives the best performance among all the devices.

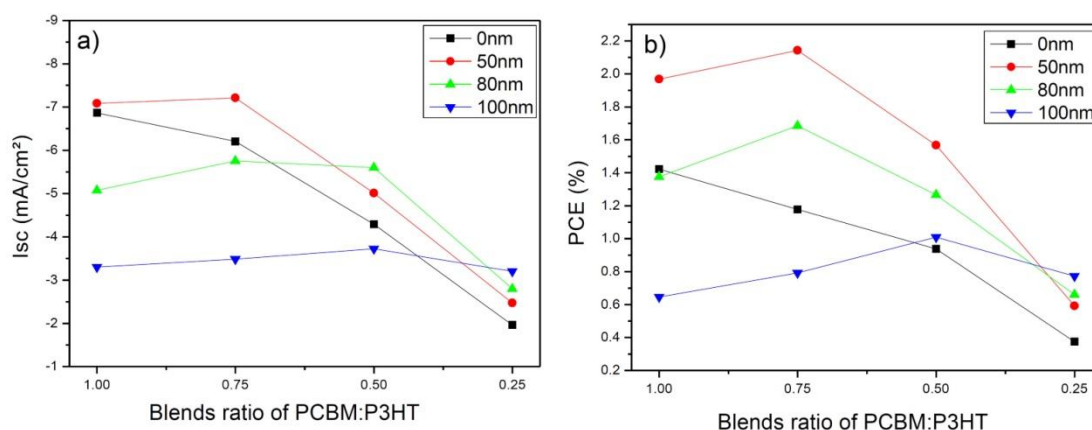


**Figure 5.16: I-V measurements of blend solar cells with different PCBM:P3HT volume ratios coated on ZnO seed layer and ZnO NW with different lengths from 50 nm to 100 nm.**

When ZnO NW penetrate into the blend system to act as an acceptor together with PCBM, it is necessary to reduce the PCBM ratio for balanced charge transport. Otherwise the excessive electron collection materials will act as recombination centers instead of transferring charge

carriers, leading to a reduced performance of devices [219].

To determine the best ratio of PCBM in the blend solution, smaller variations are applied between 1 and 0.5. Figure 5.17 shows the PCE of blend solar cells with different PCBM:P3HT volume ratios on 50 nm ZnO NW. It is obvious that PCBM:P3HT mixed at a volume ratio of 0.8:1 gives the best solar cell performance with a maximum PCE value of 2.23%.

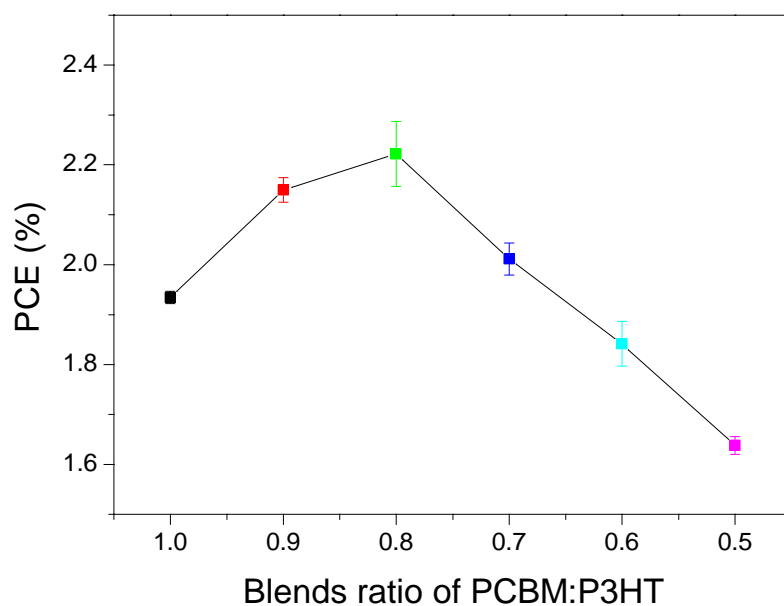


**Figure 5.17** PCE of blend solar cells coated on 50 nm ZnO NW with different PCBM:P3HT volume ratios. PCBM:P3HT mixed at 0.8:1 gives the best efficiency of 2.23%.

### 5.5 ZnO NW surface modified by AALD N-doped ZnO

ZnO NW-polymer solar cells have a number of device and material parameters to be optimized for improvement of the device performance. A low measured  $V_{OC}$  is one of the most common limitations, which is far below the effective bandgap of P3HT-ZnO of approximately 0.9 eV. Possible explanations are given as: the presence of mid-gap states on

the surface of the ZnO that pin the Fermi level; or the high electron mobility of the ZnO NW which results in increased carrier recombination at the ZnO/P3HT interface and in a reduced  $V_{OC}$  [54]. Therefore the surface modification of ZnO NW is necessary and promising for improving the device performance by reducing carrier recombination.

In this section, ZnO NW are coated with a thin layer of ZnO by an AALD method, in order to enhance the  $V_{OC}$  and recombination of the devices. This project is in cooperation with Dr. Kevin Musselman and Dr. David Muñoz-Rojas. ZnO NW and solar cells are fabricated in Prof. Lukas Schmidt-Mende's group in Munich, and AALD deposition is carried out in Prof. Judith Driscoll's group in Cambridge.

### 5.5.1 Solar cells preparation

Solar cells with a structure of ITO /ZnO NW /P3HT /PEDOT: PSS /Ag are designed as shown in Figure 5.18. Three types of devices are based on different ZnO substrates: bare ZnO NW and ZnO NW coated -with a thin layer of ZnO with and without N-doping.

All devices are based on a set of ZnO NW with six different lengths from 50 nm to 150 nm, and the HT NW growth process is discussed in section 5.3.5. Thin ZnO layers are deposited on the NW surface by the AALD method (see section 2.2.3.4) with a thickness of approximately 10 nm. The N-doped ZnO layer is produced by using a 30% ammonia solution as oxidizing precursor to the oxidizing water. Then P3HT is coated on those substrates (process described in section 5.2), and solar cells are assembled and characterized to investigate the surface modification mechanism.

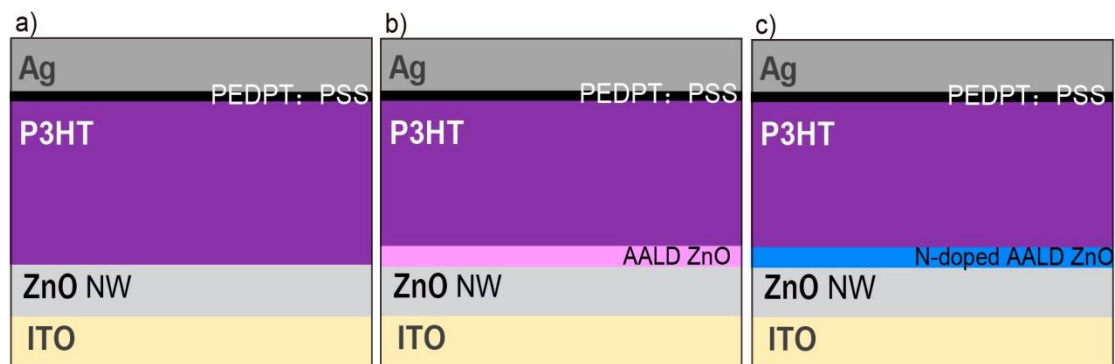


**Figure 5.18:** Device structures of solar cells with: a) bare ZnO NW (black), b) AALD coated ZnO NW (red), c) AALD coated N-doped ZnO NW (blue)

### 5.5.2 Stability of ZnO NW

The process of device fabrication takes a relatively long time (about a week) since the fabrication steps are carried out in different places. The storage of the ZnO NW substrates is a huge challenge during the transfer, as ZnO is well known for its oxygen sensitivity [220, 221]. Sealing the samples in  $N_2$  is assumed to be able to reduce the degradation of the ZnO NW. The stability of the ZnO NW in  $N_2$  is studied by building devices on ZnO NW immediately after NW growth and after storing the NW in  $N_2$  for 7 days. Their performances are presented in Figure 5.19.

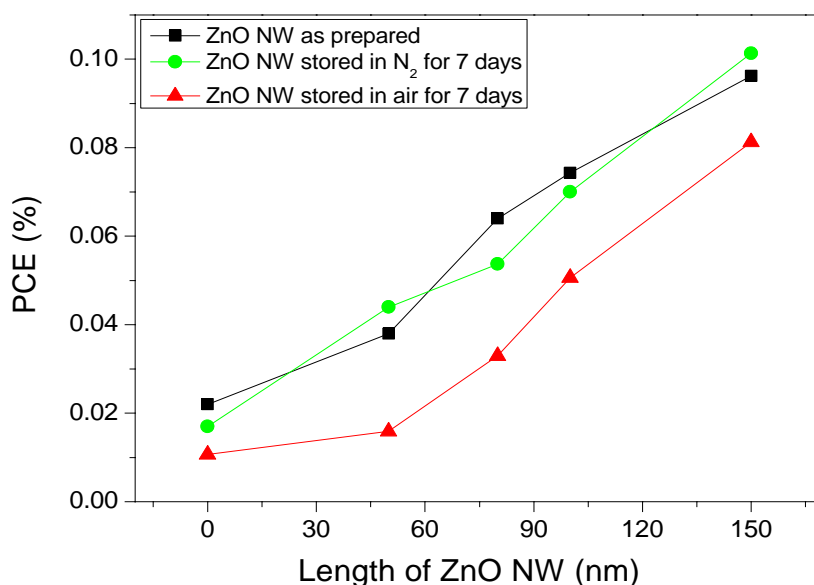


**Figure 5.19: PCE of solar cells based on ZnO seed layer and ZnO NW with different lengths.** ZnO substrates have been aging for various times after fabrication: a) as prepared (black), b) stored in  $N_2$  for 7 days (black), c) stored in air for 7 days (red).

A significant degradation of PCE is observed in the devices based on ZnO NW stored in air for 7 days, which may be induced by the surface properties effected by the oxygen and humidity [222]. However, there is no clear difference observed in the performances of solar



cells using ZnO NW stored in  $N_2$ . It can be stated that a  $N_2$  environment can efficiently reduce the degradation of ZnO NW.

### 5.5.3 Absorption measurements

#### Absorption of ZnO NW

Figure 5.20 shows the optical absorption spectrum of different ZnO substrates, including a ZnO seed layer and four ZnO NW substrates with NW lengths from 50 nm to 150 nm. The UV spectra for the ZnO layers display excitonic absorption peaks at 370 nm, which suggests that both the surface of ZnO seed layer and the ZnO NW have relatively small diameters of ZnO nanocrystalline [223]. The bandgap of ZnO NW calculated from the UV cut-off is found to be 3.40 eV, which is blue shifted compared to the bulk zinc oxide value of 3.37 eV [224]. A clear NW length-dependence is observed in the ZnO NW absorption peaks. More UV light is absorbed by the longer ZnO NW. However the UV cut-off is not influenced by NW length, which suggests a constant diameter for all nanowire lengths. The lack of visible light absorption is consistent with the photo images of transparent NW substrates shown in Figure 5.3.

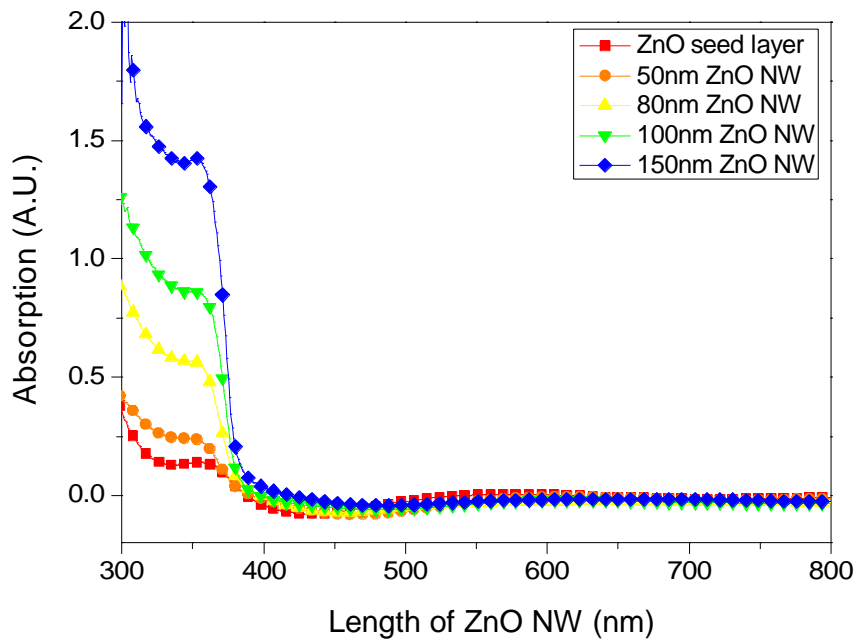
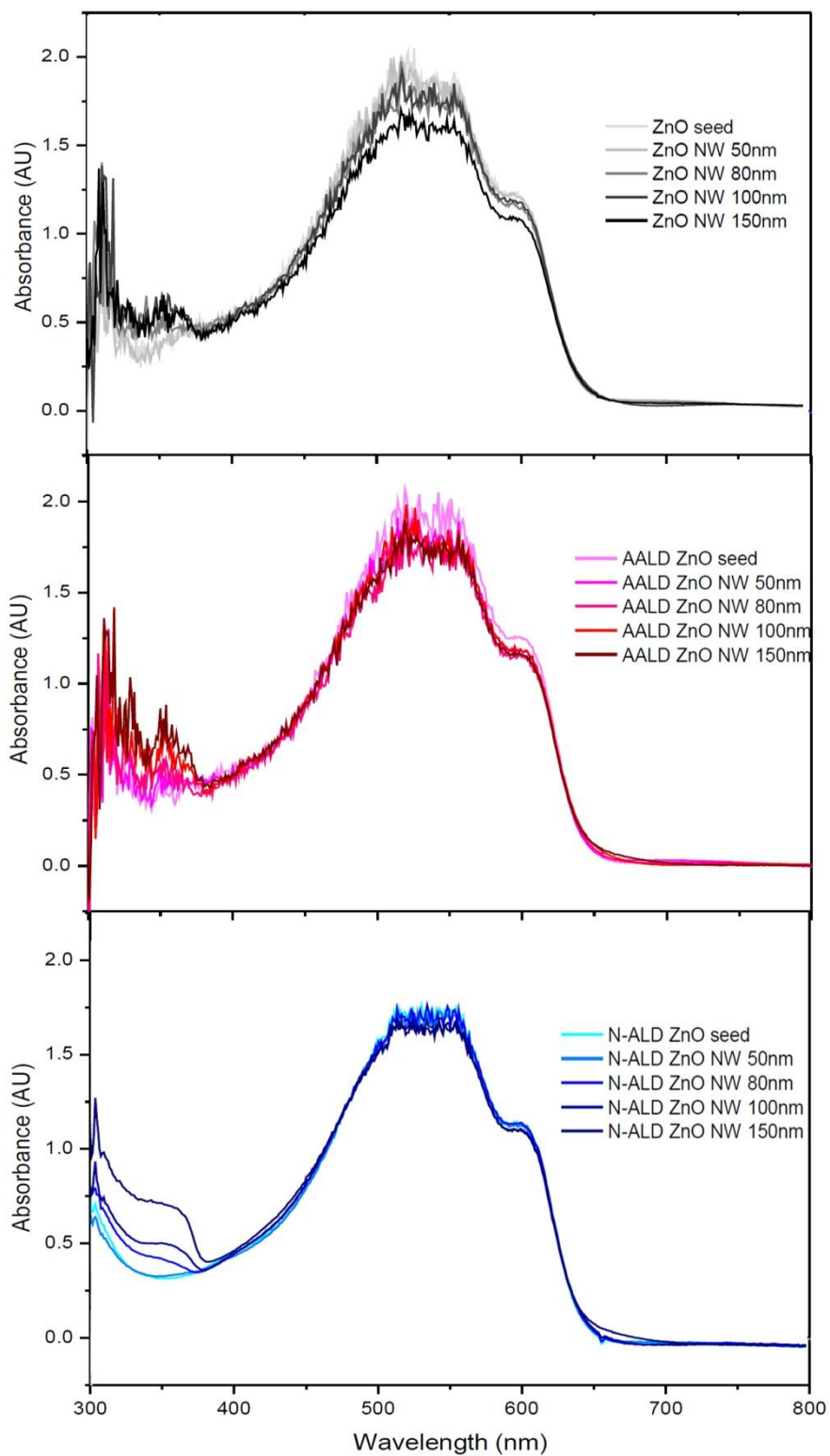


Figure 5.20: Absorption results of ZnO seed layer (red square) and ZnO NW with different lengths: 50 nm (orange circle), 80 nm (yellow up-triangle), 100 nm (green down-triangle) and 150 nm (blue

diamond).

### Absorption of P3HT layers



**Figure 5.21: Absorption results of P3HT solar cells on 50-150 nm ZnO NW, with different surface modification: a) bared ZnO NW (black), b) AALD coated ZnO (red), c) AALD coated N-doped ZnO (blue)**

As shown in Figure 5.21, three types of solar cells with different surface modifications exhibit P3HT absorption peaks of a similar magnitude, which is much stronger than the absorption peaks of the NW. There is no clear difference in P3HT absorption depending on the length of the ZnO NW. It indicates that the active layer thicknesses are nearly the same for all the devices, since no visible light absorption is contributed from ZnO NW.

#### 5.5.4 EQE measurements

In Figure 5.22, all three types of devices show a large EQE band with a maximum at 525 nm, which represents the P3HT's contribution to the photocurrent. EQE spectra of all devices are shown as a function of the ZnO NW length. More charge extraction is observed in the solar cells with longer ZnO NW, which can be attributed to the larger surface area for increased charge separation.

The EQE results of the AALD-coated samples are enhanced compared to the devices based on bare ZnO NW. It indicates that the thin ZnO layer at the interface between the NW and P3HT improves charge carrier collection, possibly by reducing the charge recombination in the device.

Compared to the devices on bare ZnO NW, an obvious drop in the EQE band is seen for the surface modified solar cells at 370 nm, where charge collection is due to absorption in the ZnO and the hole injection into the P3HT [54]. The reduced EQE band indicates that AALD coated thin ZnO limits the amount of photogenerated charges collected from the ZnO, because the additional interface can up-shift the conduction band, therefore less efficient charge injects from P3HT into ZnO NW. However, UV intensity in the solar spectrum is fairly small, compared to the influence of P3HT absorption in the visible, which is the main contribution to the photocurrent.

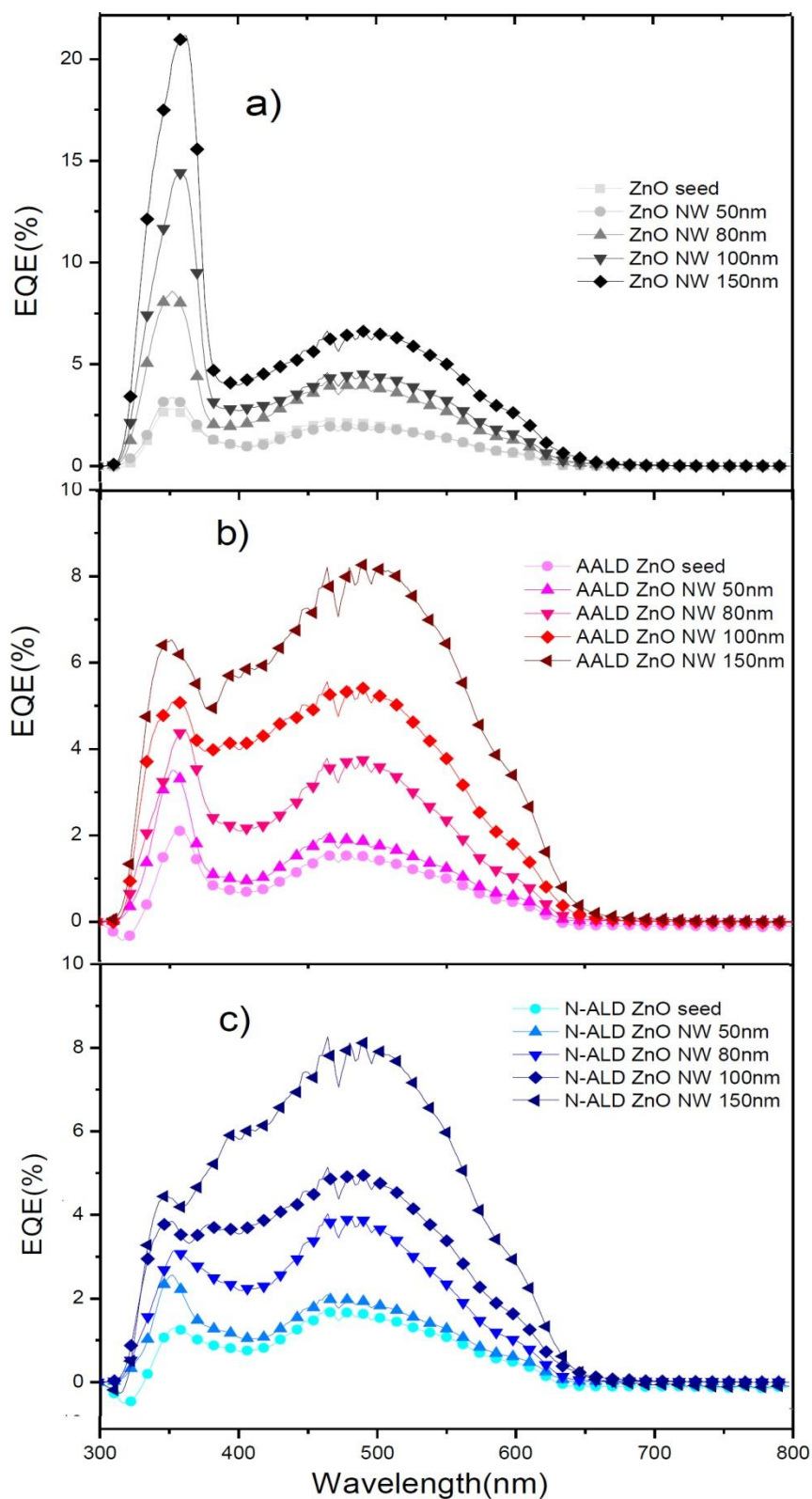
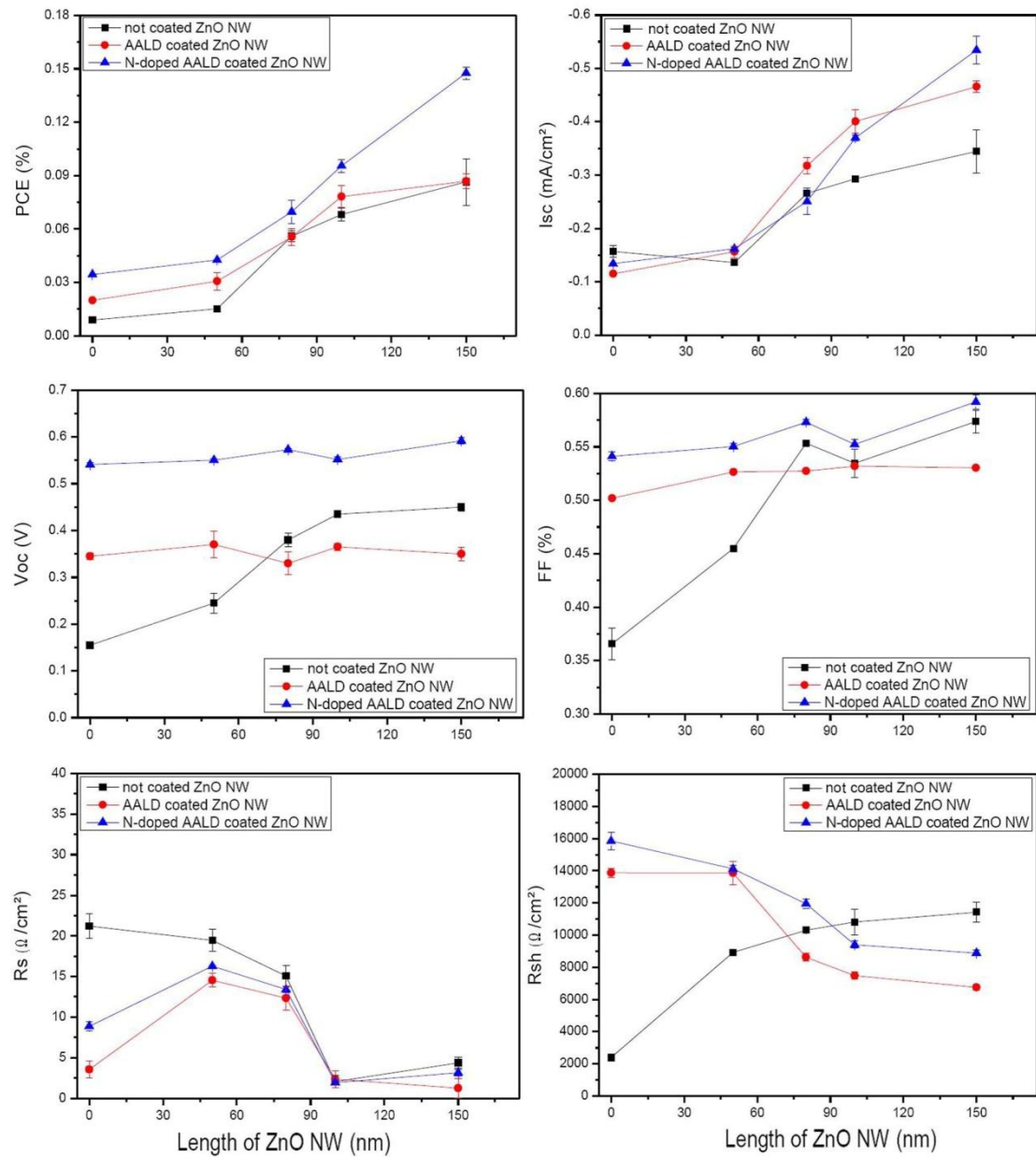


Figure 5.22: EQE measurements of P3HT devices based on ZnO seed layer and 50-150 nm ZnO NW, with different surface modifications: a) bare ZnO NW (black), b) AALD coated ZnO (red), c) AALD coated N-doped ZnO (blue)

## 5.5.6 I-V measurements



**Figure 5.23: I-V measurement results of P3HT solar cells based on ZnO seed layer (presented as 0 nm NW) and 50-150 nm ZnO NW. Three different types of surface modification are applied on these substrates: a) bare ZnO NW (black), b) AALD coated ZnO (red), c) AALD coated N-doped ZnO (blue).**

As shown in Figure 5.23, the performance of all three types of devices depends strongly on the length of the ZnO NW. An increasing trend in  $I_{SC}$  with NW length indicates that more charge carriers are collected due to the enlarged interface area, in agreement with the EQE

spectra. As a result, the PCE of devices increases with the increasing NW length as well. However, there is no clear difference in PCE between the cells on bare ZnO NW and the devices with AALD coated undoped ZnO on NW. Besides of the enhanced  $I_{SC}$ , all three types of devices exhibit general increasing  $V_{OC}$  and FF, as well as decreasing  $R_S$  and  $R_{Sh}$ , with the increasing length of NW. More investigation is currently undertaken to understand the mechanism of the devices performance depending on the length of ZnO NW.

As shown in Figure 5.24, the solar cells based on 150 nm ZnO NW with N-doped ZnO coatings gives a PCE twice as much as the not-coated devices, due to the surface modification of the NW. As expected, the  $V_{OC}$  of N-doped device is significantly enhanced from 0.42-0.44 up to 0.54, compared to the not coated and undoped devices. This might be attributed to the charge transfer of devices, especially the charge carrier recombination that is influenced by the surface modification. Further study is carried out by the light intensity measurements.

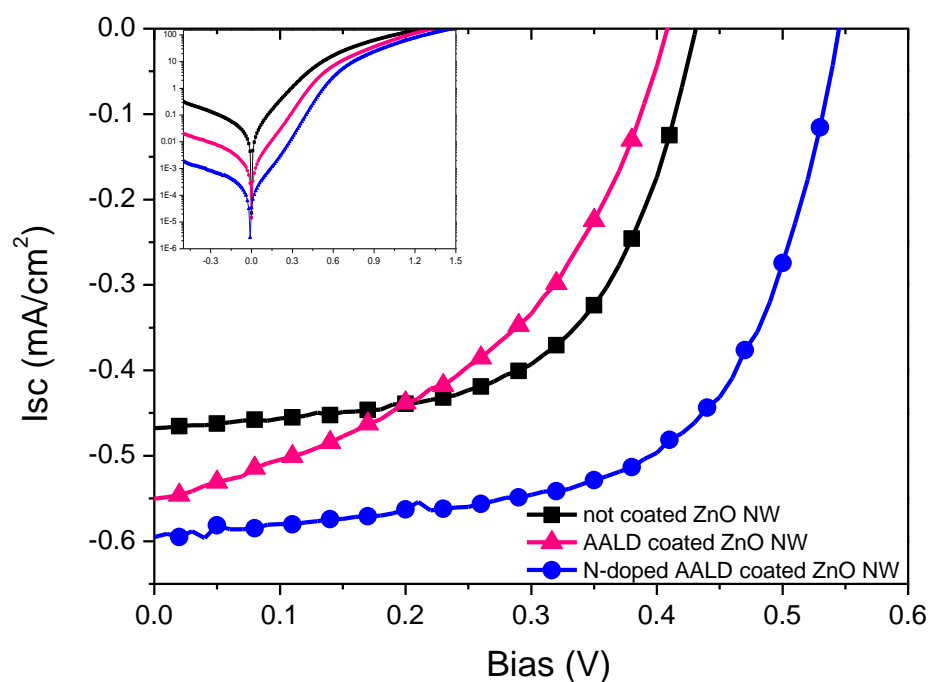
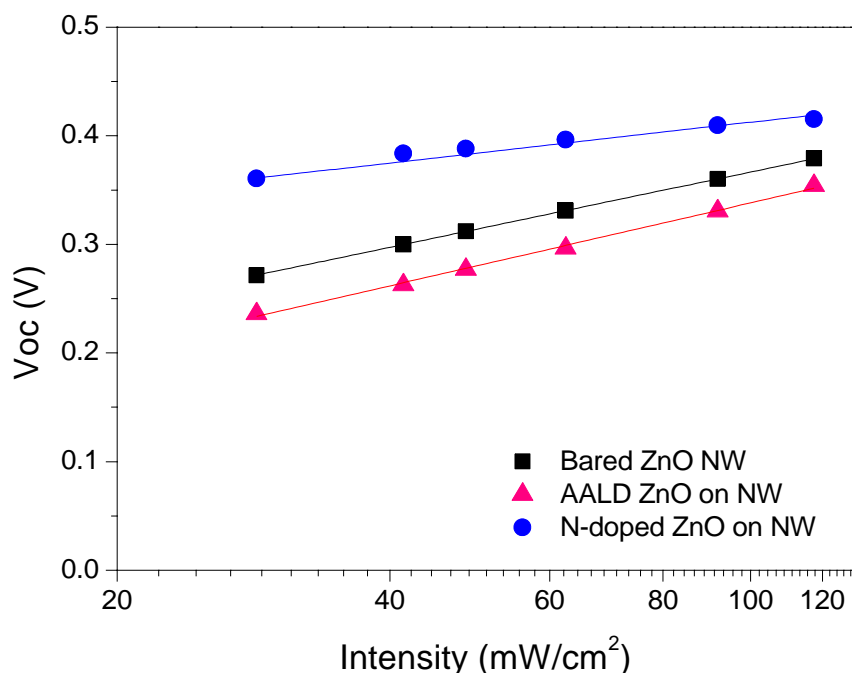


Figure 5.24: I-V curves of P3HT solar cells based on 150 nm ZnO NW, with different surface modifications:

a) bare ZnO (black), b) AALD coated ZnO (red), c) AALD coated N-doped ZnO (blue)

## 5.5.7 Light intensity measurements



**Figure 5.25:** Light-intensity measurement of P3HT solar cells based on 150 nm ZnO NW, with different surface modifications: a) bare ZnO (black), b) AALD coated ZnO (red), c) AALD coated N-doped ZnO (blue)

Light-intensity measurements are shown in Figure 5.25, which were carried out and analyzed by Dr. Kevin Musselman. The  $V_{OC}$  of all three types of devices shows a logarithmic dependence on light intensity as expected [215]. The slopes for the devices on bare ZnO NW and AALD ZnO-coated NW are similar, corresponding to the similar performances shown in the I-V measurements. However the slope for device based on N-doped ZnO coated NW is smaller than the other two. This indicates an ideality factor closer to 1 for the heterojunctions with the N-doped ZnO coating [225], which suggests less recombination may occur in these devices, consistent with the larger  $V_{OC}$  observed. It could be attributed to an additional junction created by the doped ZnO coating between the thin doped-ZnO layer and ZnO NW, which inhibits recombination in these cells and further study is required to verify this.

### 5.5.8 Improvement of the performance

As shown in Table 5.4, significant improvement is observed in the performances of all three types of devices with 150 nm ZnO NW after storing in air for 30 days. For the device on bare ZnO NW, the PCE increases from 0.09% to 0.15%. The two types of surface modified devices with and without N-doping are increased to 0.22% and 0.32%, respectively. Both are enhanced by a factor of about 2 compared to the PCE measured for the as prepared cells. It indicates that a stabilization period is required for the device to reach its maximum performance, as reported by early research from other groups [116]. This enhanced efficiency depends on oxygen exposure time in a complicated way. Possible reasons for the improvement caused by aging in air could be that doubly ionized interstitial oxygen diffuses through the ZnO structure [226], as well as the oxidation of Ag electrodes [227].

	Bared ZnO NW (%)	AALD coated ZnO NW (%)	N-doped ZnO coated ZnO NW (%)
As prepared	0.09	0.09	0.15
After stored for 30 days	0.15	0.22	0.32

**Table 5.4: PCE of P3HT solar cells based on 150 nm ZnO NW with different surface modification**

## 5.6 Conclusion

The morphology of ZnO NW fabricated by the hydrothermal method can be controlled by growing in different conditions. The optimized growing conditions are determined by experiments and described as follows: a flat dense ZnO seed layer is fabricated by a sol-gel method; zinc nitrate hexahydrate and hexamethylenetetramine are chosen as the starting



materials in an aqueous solution with an equimolar concentration of 0.025 M. The growth temperature is set at 95 °C, and growth time is controlled from 10 min to 60 min for ZnO NW with lengths from 50 nm to 250 nm.

P3HT:PCBM blend solar cells based on ZnO NW are prepared and characterized to study the influence of the NW length on device performance. Among all the solar cells with different ZnO layers, the best performance is given by the 50 nm ZnO NW device, demonstrating values for the  $V_{OC}$ ,  $I_{SC}$ , FF and PCE of 0.57 V, 7.13 mA/cm<sup>2</sup>, 0.47, and 1.91%, respectively. Compared with a solar cell based on a ZnO seed layer only, a nearly 20% improvement in PCE is shown in the 50 nm ZnO NW device. This variation of the devices performance is mainly attributed to the thickness of blend layer, which is found from the absorption and EQE results with the same blend-layer-thickness dependence as the I-V characterizations.

Despite the influence of absorption, ZnO NW can slightly enhance the charge carrier collection due to the lower recombination, indicated from the light intensity measurements in devices based on 50 nm ZnO NW layers. Although the reason for the improved charge transport is still under investigation, ZnO NW can penetrate into blend acting as electron conductors in the same manner as PCBM. Therefore, the performance of ZnO NW-blend solar cells can be further improved with a maximum PCE value of 2.23%, by the reducing the ratio of P3HT:PCBM from 1:1 to 1:0.8.

ZnO NW-P3HT hybrid solar cells based on different lengths of NW are examined and optimized by an N-doped ZnO layer through AALD coated on the ZnO NW surface. A significant improvement in device performance is observed after the surface modification, especially in the  $V_{OC}$ , which is attributed to an additional junction created by the doped ZnO coating between the thin N-doped ZnO layer and the ZnO NW. Light-intensity measurement indicates a lower recombination rate for the N-doped device. Both of them verify that the N-doped ZnO layer could inhibit the recombination in ZnO NW-P3HT devices. Furthermore, an obvious improvement is observed in the performance of all devices with 150 nm ZnO NW after storing in air for 30 days (compared to the as prepared cell) with about a two-fold increase in the PCE.

## 6 Conclusion and Outlook

In this thesis, both the flat TiO<sub>2</sub> and ZnO films as well as ZnO nanowires (NW) layers are used in organic solar cells, as the hole blocking layer and the electron transport layer. The effects of the metal oxides layers on performances of the devices are investigated in details.

### 6.1 Flat TiO<sub>2</sub>/ZnO-blend solar cells

Initially, the fabrication process of devices based on flat TiO<sub>2</sub> and ZnO layers has been optimized, and significant increases of device performance have been observed. The TiO<sub>2</sub> blocking layers are modified by surface cleaning and N-doping, to avoid short circuit and to increase the absorption of TiO<sub>2</sub> films. Mg-doped ZnO films obtained by sol-gel method exhibits significantly increased open circle voltage. The device based on TiO<sub>2</sub>-ZnO co-blocking layer shows improved efficiency, benefiting from the large bandgap of ZnO and the efficient hole blocking ability of TiO<sub>2</sub>. In addition, the blend layer in hybrid devices is optimized by several processes of choosing proper solvent, optimizing solution concentration and film thickness, implementing post-treatment, all of which bring remarkable improvements on the performances of devices. Moreover, an interface layer of PEDOT:PSS between blend layer and top contact is fabricated by spray-deposition technique, and is beneficial for the device, giving higher photocurrent by efficient hole collection and exhibiting protection of the organic material during the top contact deposition. All of these optimization processes exhibit great potential to significantly enhance the efficiency of the devices.

Additionally, the TiO<sub>2</sub> and ZnO layers fabricated by spray pyrolysis are investigated for their respective influences on the devices performances. Despite the advantage of the ZnO films

with higher conductivity and larger surface area compared to the TiO<sub>2</sub> layers, which supposed to be beneficial for the device performance by providing a higher exciton dissociation rate and faster pathways for electron transfer, ZnO-based device gives worse performance than TiO<sub>2</sub> cell. This is caused by a higher recombination rate in ZnO solar cells than in TiO<sub>2</sub>-based devices. Furthermore, it is indicated that the charge transport in hybrid device is mainly limited by the mobility of the charge carriers in the organic photoactive layer, instead of hole blocking layer.

Significantly different optical behaviors of TiO<sub>2</sub> and ZnO films are induced by their respective trap states, leading to the different performances of photo-doping effect, filter effect and the illumination stability. Those performances are influenced by the metal oxides thickness, which can be easily controlled during the spray pyrolysis deposition. The TiO<sub>2</sub>-based devices with thicker layers of TiO<sub>2</sub> show lower photocurrent and efficiency, but better stability. This thickness dependent performance of TiO<sub>2</sub>-based devices is caused by the light intensity loss due to the absorption of TiO<sub>2</sub> film. In the ZnO solar cells, on the other hand, neither the light absorption, nor the trap filling shows strong dependence on the thickness of ZnO films, because of fewer traps formed during the spray pyrolysis. This allows a much thicker ZnO layer to be built in a solar cell without negatively influencing the performance.

The illumination stability shows a strong thickness dependence on the metal oxide layer due to the UV-filter effect, providing a protection for the organic materials from degradation. In competition between the decreasing performance and increasing of illumination stability with the metal oxide layer thickness, 100 nm turns out to be the optimized thickness for both the TiO<sub>2</sub> and ZnO layers to obtain stable well performing devices. The air stabilities for these two types of devices exhibit similar behavior, both of which retain over 80% of their initial efficiency after storage for 25 days in air in the dark. This high stability shows a promising foreground for wide range application and further reduced cost for solar cells.

## 6.2 ZnO NW-blend/P3HT solar cells

The morphology of ZnO NW can be controlled by the optimized growth conditions of the hydrothermal method. By using a flat dense ZnO obtained via sol-gel method as a seed layer, choosing zinc nitrate hexahydrate and hexamethylenetetramine as the starting materials with

an equimolar concentration of 0.025 M, setting growth temperature at 95 °C and time from 10 min to 60 min, a series of ZnO NW with lengths from 50 nm to 250 nm can be obtained.

Initially, the ZnO NW-P3HT:PCBM devices are fabricated to investigate the length of ZnO NW on device performance. The thickness of blend layer is found to decrease with the increasing ZnO NW length, which is responsible for the reducing device performance. Besides the influence of absorption, ZnO NW can slightly enhance the charge carrier collection as well. Compared to flat ZnO layers, the 50 nm ZnO NW device gives a much better efficiency, mainly attributed to the higher absorption caused by the thicker blend layer. Meanwhile, the reduced recombination is observed for the further improvement on device performance. In these ZnO NW-blend devices, NW are penetrating into blend and acting as electron conductors in the same manner as PCBM, therefore the volume ratio of P3HT:PCBM has to rise up to 1:0.8 for the best performance.

To optimize the charge transport ability of ZnO NW, the ZnO NW-P3HT hybrid solar cells are fabricated, showing increasing efficiency correlated with an increase in length of NW. Remarkable improvement of device performance has been achieved by modifying the NW surface by depositing an N-doped ZnO layer via AALD method, especially for the  $V_{OC}$ . The N-doped ZnO provided an additional junction between the P3HT layer and the ZnO NW that can lower the recombination rate. This is confirmed by light-intensity measurements. Furthermore, a significant improvement is observed in the efficiency of ZnO NW devices after storing in air for 30 days.

As a conclusion, the metal oxides based organic solar cells, with the advantages of controllable morphology, high transparency and low recombination, efficient charge separation and transport ability, as well as remarkable air stability, can significantly enhance the device performance and reduce the manufacture cost, leading to high efficiency, low price and stable photovoltaic devices.

### **6.3 Outlook**

Metal oxides working principles in organic solar cells have been investigated in this thesis. The research results strongly motivate the application of TiO<sub>2</sub> and ZnO layers in devices as

hole blocking and electron transport layers, which shows great potential to further improve the exciton dissociation, charge transport, and the stability. A few promising fields for the further research to approach a high efficiency hybrid solar cell are discussed as follows:

### **The fabrication of TiO<sub>2</sub> layer**

TiO<sub>2</sub> layer can be fabricated via other methods described in section 2.2.1, such as sol-gel method and sputtering techniques, with expectation to produce fewer trap states during the preparation process. An ideal trap free TiO<sub>2</sub> film can provide device with enough UV-perfection for the illumination stability, without any filter effect in visible regain that can limit the light intensity and reduce the photocurrent.

Beside of that, both of sol-gel method and sputtering deposition can offer much easier ways to dope TiO<sub>2</sub> with nitrogen. For the sol-gel method, chemical band can be formed during the slow annealing process [146, 228], while during the sputter process, a N<sub>2</sub> contained atmosphere can directly offer the N source for doping [229, 230]. The bandgap of TiO<sub>2</sub> can be decreased by N-doping to obtain a higher V<sub>OC</sub> in solar cells.

### **Surface modification for ZnO layer**

Since the recombination in ZnO solar cells is the primary limitation of the device performance, a proper surface modification is necessary for the ZnO layer, as well as for the ZnO NW. A promising method is using dye sensitization to modify the surface [231], with the expectation of further reduce the recombination and improve charge selection ability of ZnO.

### **Morphology of the ZnO NW**

To further improve the efficiency of ZnO NW-P3HT solar cells, the morphology of NW has to be optimized by producing longer nanowires and smaller spacing between the wires. The longer NW can provide larger interface for charge separation and longer continuous pathways for charge transport, while the smaller spacing approaching the diffusion length can enhance

the exciton dissociation rate. Such controllable morphology can be achieved by modifying the surface of ZnO seed layer, which can directly determine the orientation of NW growth on top [231], or optimizing the concentration or composition of starting materials (see section 5.3.2).

### **Transparent devices**

One of the important limitations of hybrid solar cells is the light absorption efficiency. Since this type of devices is normally illuminated from the metal oxide side, part of the solar spectra will be filtered by this layer that would be otherwise absorbed by organic photoactive layer for the exciton generation. The transparent devices (see section 2.2.5) can be illuminated from both sides and offer large region of light spectrum to increase the light absorption efficiency of the device.

However, attention should be paid on the thickness of organic layer, as well as on the illumination stability of devices. Both of them can bring negative side-effects on device performance, leading to limited exciton dissociation and reduced lifetime respectively.

### **Air stable flexible solar cell**

Since the AALD deposition offers an important tool for the metal oxides deposition at the temperature below the glass temperature of flexible ITO substrates, it allows the fabrication of the flexible solar cell as described in section 2.2.6. This type of device has a wide range of applications due to the air stability, low cost, and the promising high efficiency, owing to doping and nanostructuring of the metal oxides layers. Experiments on these projects are currently underway and will be continued after this thesis.

## Bibliography

1. Abbott, D., *Keeping the energy debate clean: How do we supply the world's energy needs?* Proceedings of the IEEE. **98**(1): p. 42-66.
2. Council, W.E., *Survey of energy resources 2007*. Retrieved January20, 2009.
3. [http://en.wikipedia.org/wiki/Organic\\_solar\\_cell](http://en.wikipedia.org/wiki/Organic_solar_cell).
4. Scully, S.R. and M.D. McGehee, *Physics and Materials Issues of Organic Photovoltaics*. Flexible Electronics, 2009: p. 329-371.
5. Luce, B., *Cost Comparison of Ridge Line Wind and Solar Power*.
6. Brabec, C.J., *Organic photovoltaics: technology and market*. Solar energy materials and solar cells, 2004. **83**(2): p. 273-292.
7. Hoppe, H. and N. Sariciftci, *Polymer solar cells*. Photoresponsive Polymers II, 2008: p. 1-86.
8. Sariciftci, N.S., et al., *Photoinduced electron transfer from a conducting polymer to buckminsterfullerene*. Science, 1992. **258**(5087): p. 1474-1476.
9. Wong, L.Y., et al., *Interplay of Processing, Morphological Order, and Charge-Carrier Mobility in Polythiophene Thin Films Deposited by Different Methods: Comparison of Spin-Cast, Drop-Cast, and Inkjet-Printed Films*. Langmuir, 2010.
10. Hoppe, H., S. Shokhovets, and G. Gobsch, *Inverse relation between photocurrent and absorption layer thickness in polymer solar cells*. physica status solidi (RRL)-Rapid Research Letters, 2007. **1**(1): p. R40-R42.
11. Payne, M.M., S.R. Parkin, and J.E. Anthony, *Functionalized higher acenes: Hexacene and heptacene*. Journal of the American Chemical Society, 2005. **127**(22): p. 8028-8029.
12. Winder, C. and N.S. Sariciftci, *Low bandgap polymers for photon harvesting in bulk heterojunction solar cells*. J. Mater. Chem., 2004. **14**(7): p. 1077-1086.
13. Mühlbacher, D., et al., *High photovoltaic performance of a low - bandgap polymer*. Advanced Materials, 2006. **18**(21): p. 2884-2889.
14. Barbour, L.W., et al., *Excitation transport and charge separation in an organic photovoltaic material: Watching excitations diffuse to interfaces*. The Journal of Physical Chemistry C, 2008. **112**(10): p. 3926-3934.
15. Forrest, S.R., *The limits to organic photovoltaic cell efficiency*. MRS bulletin, 2005. **30**(01): p. 28-32.
16. Günes, S., H. Neugebauer, and N.S. Sariciftci, *Conjugated polymer-based organic solar cells*. Chemical Reviews, 2007. **107**(4): p. 1324-1338.
17. Shaw, P.E., A. Ruseckas, and I.D.W. Samuel, *Exciton diffusion measurements in poly (3 - hexylthiophene)*. Advanced Materials, 2008. **20**(18): p. 3516-3520.
18. Yu, G., et al., *Polymer photovoltaic cells: enhanced efficiencies via a network of internal donor-acceptor heterojunctions*. Science, 1995. **270**(5243): p. 1789-1791.
19. Archer, M.D. and R. Hill, *Clean electricity from photovoltaics (Series on Photoconversion of Solar Energy vol. 1)*2001: Imperial College Press, London.

20. Mihaietchi, V., et al., *Photocurrent generation in polymer-fullerene bulk heterojunctions*. Physical review letters, 2004. **93**(21): p. 216601.
21. Mozer, A.J. and N.S. Sariciftci, *Negative electric field dependence of charge carrier drift mobility in conjugated, semiconducting polymers*. Chemical physics letters, 2004. **389**(4): p. 438-442.
22. Tumbleston, J.R., et al., *Analyzing local exciton generation profiles as a means to extract transport lengths in organic solar cells*. Physical Review B, 2010. **82**(20): p. 205325.
23. Liu, J., Y. Shi, and Y. Yang, *Solvation-induced morphology effects on the performance of polymer-based photovoltaic devices*. Advanced Functional Materials, 2001. **11**(6): p. 420.
24. Chamberlain, G., *Organic solar cells: a review*. Solar Cells, 1983. **8**(1): p. 47-83.
25. Hoppea, H. and N.S. Sariciftci, *Organic solar cells: An overview*. J. Mater. Res, 2004. **19**(7): p. 1925.
26. Pandey, A.K., S. Dabos-Seignon, and J.M. Nunzi, *Pentacene: PTCDI-CH molecular blends efficiently harvest light for solar cell applications*. Applied Physics Letters, 2006. **89**: p. 113506.
27. Tang, C., *Two -layer organic photovoltaic cell*. Applied Physics Letters, 1986. **48**(2): p. 183-185.
28. Grätzel, M., *Photoelectrochemical cells*. 2001.
29. Dennler, G., M.C. Scharber, and C.J. Brabec, *Polymer - Fullerene Bulk - Heterojunction Solar Cells*. Advanced Materials, 2009. **21**(13): p. 1323-1338.
30. Mor, G.K., et al., *High efficiency double heterojunction polymer photovoltaic cells using highly ordered TiO<sub>2</sub> nanotube arrays*. Applied Physics Letters, 2007. **91**(15): p. 152111-152111-3.
31. Wong, W.S. and A. Salleo, *Flexible electronics: materials and applications* 2009: Springer Verlag.
32. Mihaietchi, V.D., et al., *Charge transport and photocurrent generation in poly (3 - hexylthiophene): methanofullerene bulk - heterojunction solar cells*. Advanced Functional Materials, 2006. **16**(5): p. 699-708.
33. Charton, C., et al., *Development of high barrier films on flexible polymer substrates*. Thin Solid Films, 2006. **502**(1): p. 99-103.
34. Yializis, A., G.L. Powers, and D. Shaw, *A new high temperature multilayer capacitor with acrylate dielectrics*. Components, Hybrids, and Manufacturing Technology, IEEE Transactions on, 1990. **13**(4): p. 611-616.
35. Leterrier, Y., *Durability of nanosized oxygen-barrier coatings on polymers*. Progress in Materials Science, 2003. **48**(1): p. 1-55.
36. Brabec, C.J., et al., *Production aspects of organic photovoltaics and their impact on the commercialization of devices*. MRS bulletin, 2005. **30**(01): p. 50-52.
37. Jørgensen, M., K. Norrman, and F.C. Krebs, *Stability/degradation of polymer solar cells*. Solar energy materials and solar cells, 2008. **92**(7): p. 686-714.
38. Cai, W., X. Gong, and Y. Cao, *Polymer solar cells: Recent development and possible routes for improvement in the performance*. Solar energy materials and solar cells, 2010. **94**(2): p. 114-127.
39. Dibb, G.F.A., et al., *Analysis of the Relationship between Linearity of Corrected Photocurrent and the Order of Recombination in Organic Solar Cells*. The Journal of Physical Chemistry



- Letters, 2011.
40. Hochbaum, A.I. and P. Yang, *Semiconductor nanowires for energy conversion*. Chemical Reviews, 2010. **110**(1): p. 527.
  41. Bozano, L., et al., *Temperature-and field-dependent electron and hole mobilities in polymer light-emitting diodes*. Applied Physics Letters, 1999. **74**: p. 1132.
  42. Huynh, W.U., J.J. Dittmer, and A.P. Alivisatos, *Hybrid nanorod-polymer solar cells*. Science, 2002. **295**(5564): p. 2425-2427.
  43. Norrman, K., N. Larsen, and F.C. Krebs, *Lifetimes of organic photovoltaics: combining chemical and physical characterisation techniques to study degradation mechanisms*. Solar energy materials and solar cells, 2006. **90**(17): p. 2793-2814.
  44. Norrman, K. and F.C. Krebs. *Chemical degradation mechanisms of organic photovoltaics studied by TOF-SIMS and isotopic labeling*. 2005.
  45. Krebs, F.C. and K. Norrman, *Analysis of the failure mechanism for a stable organic photovoltaic during 10 000 h of testing*. Progress in Photovoltaics: Research and Applications, 2007. **15**(8): p. 697-712.
  46. Glatthaar, M., et al., *Efficiency limiting factors of organic bulk heterojunction solar cells identified by electrical impedance spectroscopy*. Solar energy materials and solar cells, 2007. **91**(5): p. 390-393.
  47. Xiao-e, L., et al., *Light-driven oxygen scavenging by titania/polymer nanocomposite films*. Journal of Photochemistry and Photobiology A: Chemistry, 2004. **162**(2): p. 253-259.
  48. Peiró A.M., et al., *Freestanding Polymer -Metal Oxide Nanocomposite Films for Light - Driven Oxygen Scavenging*. Advanced Materials, 2005. **17**(19): p. 2365-2368.
  49. Peiró A.M., et al., *Photochemical reduction of oxygen adsorbed to nanocrystalline TiO<sub>2</sub> films: A transient absorption and oxygen scavenging study of different TiO<sub>2</sub> preparations*. The Journal of Physical Chemistry B, 2006. **110**(46): p. 23255-23263.
  50. Beek, W.J.E., et al., *Hybrid zinc oxide conjugated polymer bulk heterojunction solar cells*. The Journal of Physical Chemistry B, 2005. **109**(19): p. 9505-9516.
  51. Krebs, F.C. and H. Spanggaard, *Significant improvement of polymer solar cell stability*. Chemistry of materials, 2005. **17**(21): p. 5235-5237.
  52. Lira-Cantu, M. and F.C. Krebs, *Hybrid solar cells based on MEH-PPV and thin film semiconductor oxides (TiO<sub>2</sub>, Nb<sub>2</sub>O<sub>5</sub>, ZnO, CeO<sub>2</sub> and CeO<sub>2</sub>-TiO<sub>2</sub>): Performance improvement during long-time irradiation*. Solar energy materials and solar cells, 2006. **90**(14): p. 2076-2086.
  53. Lira-Cantu, M., et al., *Oxygen release and exchange in niobium oxide MEHPPV hybrid solar cells*. Chemistry of materials, 2006. **18**(24): p. 5684-5690.
  54. Olson, D.C., et al., *Hybrid photovoltaic devices of polymer and ZnO nanofiber composites*. Thin Solid Films, 2006. **496**(1): p. 26-29.
  55. Beek, W.J.E., M.M. Wienk, and R.A.J. Janssen, *Hybrid solar cells from regioregular polythiophene and ZnO nanoparticles*. Advanced Functional Materials, 2006. **16**(8): p. 1112-1116.
  56. Brabec, C.J., V. Dyakonov, and U. Scherf, *Organic Photovoltaics: Materials, Device Physics, and Manufacturing Technologies* 2008: Vch Verlagsgesellschaft Mbh.
  57. Huynh, W.U., et al., *Controlling the morphology of nanocrystal-polymer composites for solar cells*. Advanced Functional Materials, 2003. **13**(1): p. 73-79.

58. Sun, B. and N.C. Greenham, *Improved efficiency of photovoltaics based on CdSe nanorods and poly (3-hexylthiophene) nanofibers*. Phys. Chem. Chem. Phys., 2006. **8**(30): p. 3557-3560.
59. Greene, L.E., et al., *General route to vertical ZnO nanowire arrays using textured ZnO seeds*. Nano Letters, 2005. **5**(7): p. 1231-1236.
60. Greene, L.E., et al., *ZnO-TiO<sub>2</sub> core-shell nanorod/P3HT solar cells*. The Journal of Physical Chemistry C, 2007. **111**(50): p. 18451-18456.
61. Ferry, V.E., et al., *Plasmonic nanostructure design for efficient light coupling into solar cells*. Nano Letters, 2008. **8**(12): p. 4391-4397.
62. Kim, J.Y., et al., *New Architecture for High - Efficiency Polymer Photovoltaic Cells Using Solution - Based Titanium Oxide as an Optical Spacer*. Advanced Materials, 2006. **18**(5): p. 572-576.
63. Gains, R.E., *Outlook Brightens for Plastic Solar Cells*.
64. Mayer, A.C., et al., *Polymer-based solar cells*. Materials today, 2007. **10**(11): p. 28-33.
65. O'Regan, B. and M. Gratzel, *A low-cost, high-efficiency solar cell based on dye-sensitized colloidal TiO<sub>2</sub> films*. nature, 1991. **353**(6346): p. 737-740.
66. Grätzel, M., *Dye-sensitized solar cells*. Journal of Photochemistry and Photobiology C: Photochemistry Reviews, 2003. **4**(2): p. 145-153.
67. Nazeeruddin, M.K., et al., *Engineering of efficient panchromatic sensitizers for nanocrystalline TiO<sub>2</sub>-based solar cells*. Journal of the American Chemical Society, 2001. **123**(8): p. 1613-1624.
68. Sinke, W.C. and M.M. Wienk, *Solid-state organic solar cells*. nature, 1998. **395**(6702): p. 544-5.
69. Li, B., et al., *Review of recent progress in solid-state dye-sensitized solar cells*. Solar energy materials and solar cells, 2006. **90**(5): p. 549-573.
70. Shankar, K., et al., *Highly-ordered TiO<sub>2</sub> nanotube arrays up to 220 μm in length: use in water photoelectrolysis and dye-sensitized solar cells*. Nanotechnology, 2007. **18**: p. 065707.
71. Snaith, H.J. and L. Schmidt - Mende, *Advances in Liquid - Electrolyte and Solid - State Dye - Sensitized Solar Cells*. Advanced Materials, 2007. **19**(20): p. 3187-3200.
72. Lin, Y.Y., et al., *Nanostructured metal oxide/conjugated polymer hybrid solar cells by low temperature solution processes*. J. Mater. Chem., 2007. **17**(43): p. 4571-4576.
73. Weller, H., *Quantized semiconductor particles: a novel state of matter for materials science*. Advanced Materials, 1993. **5**(2): p. 88-95.
74. Shim, J.B., H. Chang, and S.O. Kim, *Rapid hydrothermal synthesis of zinc oxide nanowires by annealing methods on seed layers*. Journal of Nanomaterials, 2011. **2011**: p. 25.
75. Arango, A., S. Carter, and P. Brock, *Charge transfer in photovoltaics consisting of interpenetrating networks of conjugated polymer and TiO nanoparticles*. Applied Physics Letters, 1999. **74**: p. 1698.
76. Coakley, K.M. and M.D. McGehee, *Photovoltaic cells made from conjugated polymers infiltrated into mesoporous titania*. Applied Physics Letters, 2003. **83**(16): p. 3380-3382.
77. Huisman, C.L., A. Goossens, and J. Schoonman, *Aerosol synthesis of anatase titanium dioxide nanoparticles for hybrid solar cells*. Chemistry of materials, 2003. **15**(24): p. 4617-4624.
78. Kröger, M., et al., *P-type doping of organic wide band gap materials by transition metal oxides: A case-study on Molybdenum trioxide*. Organic Electronics, 2009. **10**(5): p. 932-938.

79. Ramakrishna, S. and S. Peng, *Electrospun Metal Oxides for Energy Applications*. Zero-Carbon Energy Kyoto 2011, 2012: p. 97-108.
80. Lloyd, M.T., et al., *Impact of contact evolution on the shelf life of organic solar cells*. J. Mater. Chem., 2009. **19**(41): p. 7638-7642.
81. Baeten, L., et al., *Towards Efficient Hybrid Solar Cells Based on Fully Polymer Infiltrated ZnO Nanorod Arrays*. Advanced Materials, 2011.
82. Tachikawa, T., M. Fujitsuka, and T. Majima, *Mechanistic insight into the TiO<sub>2</sub> photocatalytic reactions: design of new photocatalysts*. The Journal of Physical Chemistry C, 2007. **111**(14): p. 5259-5275.
83. Schmidt, H., et al., *Efficient semitransparent inverted organic solar cells with indium tin oxide top electrode*. Applied Physics Letters, 2009. **94**(24): p. 243302-243302-3.
84. Yella, A., et al., *Porphyrin-Sensitized Solar Cells with Cobalt (II/III)-Based Redox Electrolyte Exceed 12 Percent Efficiency*. Science, 2011. **334**(6056): p. 629-634.
85. Chen, X. and S.S. Mao, *Titanium dioxide nanomaterials: synthesis, properties, modifications, and applications*. ChemInform, 2007. **38**(41): p. no-no.
86. Dagan, G. and M. Tomkiewicz, *Titanium dioxide aerogels for photocatalytic decontamination of aquatic environments*. The Journal of Physical Chemistry, 1993. **97**(49): p. 12651-12655.
87. Bavykin, D.V., J.M. Friedrich, and F.C. Walsh, *Protonated titanates and TiO<sub>2</sub> nanostructured materials: synthesis, properties, and applications*. Advanced Materials, 2006. **18**(21): p. 2807-2824.
88. Li, Y., et al., *One-Dimensional Metal Oxide Nanotubes, Nanowires, Nanoribbons, and Nanorods: Synthesis, Characterizations, Properties and Applications*. Critical Reviews in Solid State and Materials Sciences, 2012. **37**(1): p. 1-74.
89. Westwater, J., et al., *Growth of silicon nanowires via gold/silane vapor-liquid-solid reaction*. Journal of Vacuum Science & Technology B: Microelectronics and Nanometer Structures, 1997. **15**(3): p. 554-557.
90. Wang, Z.L., *Zinc oxide nanostructures: growth, properties and applications*. Journal of Physics: Condensed Matter, 2004. **16**: p. R829.
91. Su, Y. and W. Lu, *Effects of different thermal annealing on the performance of DB-PPV based PLED*, 2005, Thesis for Master of Science degrees in National Cheng Kung University, Taiwan, ROC.
92. Ishikawa, T. and E. Matijevic, *Preparation and properties of uniform colloidal metal phosphates\* I,\* 2:: III. Cobalt (II) Phosphate*. Journal of colloid and interface science, 1988. **123**(1): p. 122-128.
93. Li, Z. and W. Gao, *Growth of zinc oxide thin films and nanostructures by wet oxidation*. Thin Solid Films, 2007. **515**(7): p. 3323-3329.
94. Gonzalez-Valls, I. and M. Lira-Cantu, *Vertically-aligned nanostructures of ZnO for excitonic solar cells: a review*. Energy Environ. Sci., 2008. **2**(1): p. 19-34.
95. Cozzoli, P.D., M.L. Curri, and A. Agostiano, *Efficient charge storage in photoexcited TiO<sub>2</sub> nanorod-noble metal nanoparticle composite systems*. Chemical communications, 2005(25): p. 3186-3188.
96. Lee, S., C. Jeon, and Y. Park, *Fabrication of TiO<sub>2</sub> tubules by template synthesis and hydrolysis with water vapor*. Chemistry of materials, 2004. **16**(22): p. 4292-4295.
97. Kang, T.S., et al., *Fabrication of highly-ordered TiO<sub>2</sub> nanotube arrays and their use in*

- dye-sensitized solar cells*. Nano Letters, 2009. **9**(2): p. 601-606.
98. Dalal, S., et al., *Controllable growth of vertically aligned zinc oxide nanowires using vapour deposition*. Nanotechnology, 2006. **17**: p. 4811.
99. Satoh, Y., S. Ohshio, and H. Saitoh, *Photoluminescence spectroscopy of highly oriented Y<sub>2</sub>O<sub>3</sub>: Tb crystalline whiskers*. Science and Technology of Advanced Materials, 2005. **6**(2): p. 215-218.
100. Yasuda, T. and Y. Segawa, *Zinc oxide thin films synthesized by metal organic chemical reactions*. physica status solidi (b), 2004. **241**(3): p. 676-679.
101. Baruah, S. and J. Dutta, *Hydrothermal growth of ZnO nanostructures*. Science and Technology of Advanced Materials, 2009. **10**: p. 013001.
102. Spanhel, L., *Colloidal ZnO nanostructures and functional coatings: A survey*. Journal of sol-gel science and technology, 2006. **39**(1): p. 7-24.
103. Krunks, M. and E. Mellikov, *Zinc oxide thin films by the spray pyrolysis method*. Thin Solid Films, 1995. **270**(1-2): p. 33-36.
104. Hara, K., et al., *Highly efficient photon-to-electron conversion with mercurochrome-sensitized nanoporous oxide semiconductor solar cells*. Solar energy materials and solar cells, 2000. **64**(2): p. 115-134.
105. Yu, J., X. Zhao, and Q. Zhao, *Effect of surface structure on photocatalytic activity of TiO<sub>2</sub> thin films prepared by sol-gel method*. Thin Solid Films, 2000. **379**(1): p. 7-14.
106. Takeda, S., et al., *Photocatalytic TiO<sub>2</sub> thin film deposited onto glass by DC magnetron sputtering*. Thin Solid Films, 2001. **392**(2): p. 338-344.
107. Pore, V., et al., *Atomic layer deposition of photocatalytic TiO<sub>2</sub> thin films from titanium tetramethoxide and water*. Chemical Vapor Deposition, 2004. **10**(3): p. 143-148.
108. Suda, Y., et al., *Preparation of high quality nitrogen doped TiO<sub>2</sub> thin film as a photocatalyst using a pulsed laser deposition method*. Thin Solid Films, 2004. **453**: p. 162-166.
109. Weickert, J., et al., *Spray-deposited PEDOT:PSS for inverted organic solar cells* Solar Energy Materials & Solar Cells 2010. **94**: p. 2371-2374
110. Abou-Helal, M. and W. Seeber, *Preparation of TiO<sub>2</sub> thin films by spray pyrolysis to be used as a photocatalyst*. Applied surface science, 2002. **195**(1-4): p. 53-62.
111. Mills, A., et al., *Novel TiO<sub>2</sub> CVD films for semiconductor photocatalysis*. Journal of Photochemistry and Photobiology A: Chemistry, 2002. **151**(1-3): p. 171-179.
112. Paronyan, T.M., A. Kechiantz, and M. Lin, *Highly active nanocrystalline TiO<sub>2</sub> photoelectrodes*. Nanotechnology, 2008. **19**: p. 115201.
113. Poodt, P., et al., *Spatial atomic layer deposition: A route towards further industrialization of atomic layer deposition*. Journal of Vacuum Science & Technology A: Vacuum, Surfaces, and Films, 2012. **30**(1): p. 010802-010802-11.
114. Martinez, M., J. Herrero, and M. Gutierrez, *Deposition of transparent and conductive Al-doped ZnO thin films for photovoltaic solar cells*. Solar energy materials and solar cells, 1997. **45**(1): p. 75-86.
115. Zhao, J., et al., *High-quality ZnO thin films prepared by low temperature oxidation of metallic Zn*. Applied surface science, 2004. **229**(1): p. 311-315.
116. Levy, D.H., et al., *Stable ZnO thin film transistors by fast open air atomic layer deposition*. Applied Physics Letters, 2008. **92**: p. 192101.

117. Schuler, T. and M.A. Aegerter, *Optical, electrical and structural properties of sol gel ZnO: Al coatings*. Thin Solid Films, 1999. **351**(1): p. 125-131.
118. Marotti, R., et al., *Bandgap energy tuning of electrochemically grown ZnO thin films by thickness and electrodeposition potential*. Solar energy materials and solar cells, 2004. **82**(1): p. 85-103.
119. Paraguay D, F., et al., *Growth, structure and optical characterization of high quality ZnO thin films obtained by spray pyrolysis*. Thin Solid Films, 1999. **350**(1): p. 192-202.
120. Miki-Yoshida, M. and E. Andrade, *Growth and structure of tin dioxide thin films obtained by an improved spray pyrohydrolysis technique*. Thin Solid Films, 1993. **224**(1): p. 87-96.
121. Brabec, C.J., et al., *Effect of LiF/metal electrodes on the performance of plastic solar cells*. Applied Physics Letters, 2002. **80**: p. 1288.
122. Grozea, D., et al., *Chemical structure of Al/LiF/Alq interfaces in organic light-emitting diodes*. Applied Physics Letters, 2002. **81**: p. 3173.
123. Tao, C., et al., *Role of tungsten oxide in inverted polymer solar cells*. Applied Physics Letters, 2009. **94**: p. 043311.
124. Lovinger, A.J. and L.J. Rothberg, *Electrically active organic and polymeric materials for thin-film-transistor technologies*. Journal of materials research, 1996. **11**(06): p. 1581-1592.
125. Connolly, J.R., *Introduction to X-Ray Powder Diffraction*. Published Spring, 2007.
126. Cowan, S.R., A. Roy, and A.J. Heeger, *Recombination in polymer-fullerene bulk heterojunction solar cells*. Arxiv preprint arXiv:1010.5021, 2010.
127. Dennler, G., et al., *Charge carrier mobility and lifetime versus composition of conjugated polymer/fullerene bulk-heterojunction solar cells*. Organic Electronics, 2006. **7**(4): p. 229-234.
128. Mozer, A., et al., *Charge transport and recombination in bulk heterojunction solar cells studied by the photoinduced charge extraction in linearly increasing voltage technique*. Applied Physics Letters, 2005. **86**(11): p. 112104-112104-3.
129. Mozer, A., et al., *Time-dependent mobility and recombination of the photoinduced charge carriers in conjugated polymer/fullerene bulk heterojunction solar cells*. Physical Review B, 2005. **72**(3): p. 035217.
130. Chiba, Y., K. Kashiwagi, and H. Kokai, *Plasma surface treatment effect of TiO<sub>2</sub> thin film*. Vacuum, 2004. **74**(3-4): p. 643-646.
131. Sung, Y.M. and H.J. Kim, *Sputter deposition and surface treatment of TiO<sub>2</sub> films for dye-sensitized solar cells using reactive RF plasma*. Thin Solid Films, 2007. **515**(12): p. 4996-4999.
132. Mills, A., et al., *Demonstration of a novel, flexible, photocatalytic oxygen-scavenging polymer film*. Journal of Photochemistry and Photobiology A: Chemistry, 2006. **177**(2): p. 328-331.
133. Yamada, K., et al., *Preparation of N-doped TiO<sub>2</sub> particles by plasma surface modification*. Comptes Rendus Chimie, 2006. **9**(5): p. 788-793.
134. Wilcoxon, J.P., *Catalytic photooxidation of pentachlorophenol using semiconductor nanoclusters*. The Journal of Physical Chemistry B, 2000. **104**(31): p. 7334-7343.
135. Serpone, N., *Photocatalysis*1989: Wiley Online Library.
136. Schiavello, M., *Photoelectrochemistry, photocatalysis, and photoreactors: fundamentals and developments*1985: Springer.
137. Ihara, T., et al., *Visible-light-active titanium oxide photocatalyst realized by an oxygen-deficient structure and by nitrogen doping*. Applied Catalysis B: Environmental, 2003.

- 42**(4): p. 403-409.
138. Irie, H., Y. Watanabe, and K. Hashimoto, *Nitrogen-concentration dependence on photocatalytic activity of TiO<sub>2-x</sub>N<sub>x</sub> powders*. The Journal of Physical Chemistry B, 2003. **107**(23): p. 5483-5486.
139. Miao, L., et al., *The improvement of optical reactivity for TiO<sub>2</sub> thin films by N<sub>2</sub>-H<sub>2</sub> plasma surface-treatment*. Journal of Crystal Growth, 2004. **260**(1): p. 118-124.
140. Ma, T., et al., *High-efficiency dye-sensitized solar cell based on a nitrogen-doped nanostructured titania electrode*. Nano Letters, 2005. **5**(12): p. 2543-2547.
141. Asahi, R., et al., *Visible-light photocatalysis in nitrogen-doped titanium oxides*. Science, 2001. **293**(5528): p. 269-271.
142. Nakamura, I., et al., *Shinichi Sugihara c, Koji Takeuchi*. Journal of Molecular Catalysis A: Chemical, 2000. **161**: p. 205-212.
143. Mrowetz, M., et al., *Oxidative power of nitrogen-doped TiO<sub>2</sub> photocatalysts under visible illumination*. The Journal of Physical Chemistry B, 2004. **108**(45): p. 17269-17273.
144. Nakamura, R., T. Tanaka, and Y. Nakato, *Mechanism for visible light responses in anodic photocurrents at N-doped TiO<sub>2</sub> film electrodes*. The Journal of Physical Chemistry B, 2004. **108**(30): p. 10617-10620.
145. Stathatos, E., et al., *Photocatalytically deposited silver nanoparticles on mesoporous TiO<sub>2</sub> films*. Langmuir, 2000. **16**(5): p. 2398-2400.
146. Jagadale, T.C., et al., *N-Doped TiO<sub>2</sub> Nanoparticle Based Visible Light Photocatalyst by Modified Peroxide Sol–Gel Method*. The Journal of Physical Chemistry C, 2008. **112**(37): p. 14595-14602.
147. Gregg, B.A., *The photoconversion mechanism of excitonic solar cells*. MRS bulletin, 2005. **30**(01): p. 20-22.
148. Brabec, C.J., et al., *Origin of the open circuit voltage of plastic solar cells*. Advanced Functional Materials, 2001. **11**(5): p. 374-380.
149. Gregg, B.A. and M.C. Hanna, *Comparing organic to inorganic photovoltaic cells: Theory, experiment, and simulation*. Journal of Applied Physics, 2003. **93**: p. 3605.
150. Ramsdale, C., et al., *The origin of the open-circuit voltage in polyfluorene-based photovoltaic devices*. Journal of Applied Physics, 2002. **92**: p. 4266.
151. Olson, D.C., et al., *Band - Offset Engineering for Enhanced Open - Circuit Voltage in Polymer - Oxide Hybrid Solar Cells*. Advanced Functional Materials, 2007. **17**(2): p. 264-269.
152. Wang, H., et al., *Titania bicontinuous network structures for solar cell applications*. Applied Physics Letters, 2005. **87**(2): p. 023507-023507-3.
153. Campoy-Quiles, M., et al., *Morphology evolution via self-organization and lateral and vertical diffusion in polymer: fullerene solar cell blends*. Nature materials, 2008. **7**(2): p. 158-164.
154. Zhao, N., et al., *Microscopic studies on liquid crystal poly (3, 3''-dialkylquaterthiophene) semiconductor*. Macromolecules, 2004. **37**(22): p. 8307-8312.
155. Li, G., et al., *High-efficiency solution processable polymer photovoltaic cells by self-organization of polymer blends*. Nature materials, 2005. **4**(11): p. 864-868.
156. Chirvase, D., et al., *Influence of nanomorphology on the photovoltaic action of polymer–fullerene composites*. Nanotechnology, 2004. **15**: p. 1317.

157. Kim, Y., et al., *Composition and annealing effects in polythiophene/fullerene solar cells*. Journal of materials science, 2005. **40**(6): p. 1371-1376.
158. Scientists, C.F.N.F., et al., *Nanostructured organic photodiodes*.
159. Hau, S.K., et al., *Interfacial modification to improve inverted polymer solar cells*. J. Mater. Chem., 2008. **18**(42): p. 5113-5119.
160. Botev, I., *A new conception of Bouguer-Lambert-Beer's law*. Fresenius' Journal of Analytical Chemistry, 1979. **297**(5): p. 419-419.
161. Yang, F., M. Shtein, and S.R. Forrest, *Controlled growth of a molecular bulk heterojunction photovoltaic cell*. Nature materials, 2004. **4**(1): p. 37-41.
162. Shrotriya, V., et al., *Absorption spectra modification in poly (3-hexylthiophene): methanofullerene blend thin films*. Chemical physics letters, 2005. **411**(1): p. 138-143.
163. Grévin, B., et al., *Multi-scale scanning tunneling microscopy imaging of self-organized regioregular poly (3-hexylthiophene) films*. The Journal of chemical physics, 2003. **118**: p. 7097.
164. Padinger, F., R.S. Rittberger, and N.S. Sariciftci, *Effects of postproduction treatment on plastic solar cells*. Advanced Functional Materials, 2003. **13**(1): p. 85-88.
165. Medford, A.J., et al., *Grid-connected polymer solar panels: initial considerations of cost, lifetime, and practicality*. Optics Express, 2010. **18**(103): p. A272-A285.
166. Krebs, F.C., S.A. Gevorgyan, and J. Alstrup, *A roll-to-roll process to flexible polymer solar cells: model studies, manufacture and operational stability studies*. J. Mater. Chem., 2009. **19**(30): p. 5442-5451.
167. Krebs, F.C., T. Tromholt, and M. Jørgensen, *Upscaling of polymer solar cell fabrication using full roll-to-roll processing*. Nanoscale, 2010. **2**(6): p. 873-886.
168. Hesse, H.C., et al., *Discotic materials for organic solar cells: Effects of chemical structure on assembly and performance*. Solar energy materials and solar cells, 2010. **94**(3): p. 560-567.
169. Kuwabara, T., et al., *Inverted type bulk-heterojunction organic solar cell using electrodeposited titanium oxide thin films as electron collector electrode*. Thin Solid Films, 2009. **517**(13): p. 3766-3769.
170. Lim, Y.F., et al., *Spray-deposited poly (3, 4-ethylenedioxythiophene): poly (styrenesulfonate) top electrode for organic solar cells*. Applied Physics Letters, 2008. **93**: p. 193301.
171. de Boer, B., et al., *Tuning of Metal Work Functions with Self - Assembled Monolayers*. Advanced Materials, 2005. **17**(5): p. 621-625.
172. Weast, R.C., M.J. Astle, and W.H. Beyer, *CRC handbook of chemistry and physics*. Vol. 69. 1988: CRC press Boca Raton, FL.
173. Scharber, M.C., et al., *Design rules for donors in bulk - heterojunction solar cells—Towards 10% energy - conversion efficiency*. Advanced Materials, 2006. **18**(6): p. 789-794.
174. Willecke, R. and F. Faupel, *Diffusion of gold and silver in Bisphenol A polycarbonate*. Macromolecules, 1997. **30**(3): p. 567-573.
175. Dür, A.C., et al., *Morphology and thermal stability of metal contacts on crystalline organic thin films*. Advanced Materials, 2002. **14**(13-14): p. 961-963.
176. Nelson, J., *The physics of solar cells*. Vol. 57. 2003: Imperial College Press London.
177. Huynh, W.U., et al., *Charge transport in hybrid nanorod-polymer composite photovoltaic cells*. Physical Review B, 2003. **67**(11): p. 115326.
178. Dobbertin, T., et al., *Inverted hybrid organic light-emitting device with polyethylene*

- dioxythiophene-polystyrene sulfonate as an anode buffer layer*. Applied Physics Letters, 2003. **83**: p. 5071.
179. Kim, J.Y., et al., Science, 2007.
180. Mor, G.K., et al., Appl. Phys. Lett., 2007. **91**: p. 152111.
181. Steim, R., et al., Appl. Phys. Lett., 2008. **92**: p. 093303.
182. See Konarka press release 2010, [www.konarka.com](http://www.konarka.com).
183. Steim, R., F.R. Kogler, and C.J. Brabec, *Interface materials for organic solar cells*. Journal of Materials Chemistry, 2010. **20**: p. 2499–2512.
184. Lira-Cantu, M., et al., *Nb–TiO<sub>2</sub>/polymer hybrid solar cells with photovoltaic response under inert atmosphere conditions*. Solar Energy Materials & Solar Cells, 2010. **94**: p. 1227–1234.
185. Öztas, M. and M. Bedir, *Thickness dependence of structural, electrical and optical properties of sprayed ZnO: Cu films*. Thin Solid Films, 2008. **516**(8): p. 1703-1709.
186. Hecht, B., et al., *Local excitation, scattering, and interference of surface plasmons*. Physical review letters, 1996. **77**(9): p. 1889-1892.
187. Chen, X. and C. Burda, *The Electronic Origin of the Visible-Light Absorption Properties of C-, N- and S-Doped TiO<sub>2</sub> Nanomaterials* J. AM. CHEM. SOC. , 2008. **130**: p. 5018–5019.
188. Zaleska, A., *Doped-TiO<sub>2</sub>: A Review*. Recent Patents on Engineering 2008. **2**: p. 157-164.
189. Conde-Gallardo, A., et al., *TiO<sub>2</sub> anatase thin films deposited by spray pyrolysis of an aerosol of titanium diisopropoxide*. Thin Solid Films, 2005. **473**: p. 68– 73.
190. Bisquert, J., et al., *Physical chemical principles of photovoltaic conversion with nanoparticulate, mesoporous dye-sensitized solar cells*. The Journal of Physical Chemistry B, 2004. **108**(24): p. 8106-8118.
191. Bisquert, J., *Chemical capacitance of nanostructured semiconductors: its origin and significance for nanocomposite solar cells*. Physical Chemistry Chemical Physics, 2003. **5**(24): p. 5360-5364.
192. Mora-Sero, I., et al., *Implications of the negative capacitance observed at forward bias in nanocomposite and polycrystalline solar cells*. Nano Letters, 2006. **6**(4): p. 640-650.
193. Shockley, W. and H.J. Queisser, *Detailed balance limit of efficiency of p - n junction solar cells*. Journal of Applied Physics, 1961. **32**(3): p. 510-519.
194. Scott, J.C. and G.G. Malliaras, *Charge injection and recombination at the metal–organic interface*. Chemical physics letters, 1999. **299**(2): p. 115-119.
195. Weidmann, J., *Influence of oxygen and water related surface defects on the dye sensitized TiO<sub>2</sub> solar cell*. Solar Energy Materials and Solar Cells, 1999. **56**: p. 153-165.
196. Dittrich, T., et al., *Thermal activation of the electronic transport in porous titanium dioxides*. Mater. Sci. Eng. B, 2000. **489**: p. 69–70.
197. *Monitoring Hole Trapping in Photoexcited TiO<sub>2</sub>(110) Using a Surface Photoreaction*.
198. Kytin, V., A. Petrov, and V.Y. Timoshenko, *Photoassisted electrical transport in porous TiO<sub>2</sub>*. phys. stat. sol. (a), 2003. **197**(2): p. 487– 491.
199. Wang, D. and T. Zhang, *Study on the defects of ZnO nanowire*. Solid State Communications, 2009. **149**(43): p. 1947-1949.
200. Park, J.Y., J.J. Kim, and S.S. Kim, *Ambient air effects on electrical transport properties of ZnO nanorod transistors*. Journal of Nanoscience and Nanotechnology, 2008. **8**(11): p. 5929-5933.
201. Khranovskyy, V., et al., *Effect of oxygen exposure on the electrical conductivity and gas*



- sensitivity of nanostructured ZnO films*. Thin Solid Films, 2009. **517**(6): p. 2073-2078.
202. Liu, M. and H.K. Kim, *Ultraviolet detection with ultrathin ZnO epitaxial films treated with oxygen plasma*. Applied Physics Letters, 2004. **84**: p. 173.
203. Peet, J., et al., *Efficiency enhancement in low-bandgap polymer solar cells by processing with alkane dithiols*. Nature materials, 2007. **6**(7): p. 497-500.
204. van Hal, P.A., et al., *Photoinduced Electron Transfer and Photovoltaic Response of a MDMO - PPV: TiO<sub>2</sub> Bulk - Heterojunction*. Advanced Materials, 2003. **15**(2): p. 118-121.
205. Yin, Z., et al., *Electrochemical deposition of ZnO nanorods on transparent reduced graphene oxide electrodes for hybrid solar cells*. Small, 2010. **6**(2): p. 307-312.
206. Briseno, A.L., et al., *Oligo-and polythiophene/ZnO hybrid nanowire solar cells*. Nano Letters, 2009. **10**(1): p. 334-340.
207. Chen, L.M., et al., *Recent progress in polymer solar cells: manipulation of polymer: fullerene morphology and the formation of efficient inverted polymer solar cells*. Advanced Materials, 2009. **21**(14 - 15): p. 1434-1449.
208. Cui, Y., et al., *Diameter-controlled synthesis of single-crystal silicon nanowires*. Applied Physics Letters, 2001. **78**: p. 2214.
209. Kwon, S.S., et al., *Piezoelectric Effect on the Electronic Transport Characteristics of ZnO Nanowire Field - Effect Transistors on Bent Flexible Substrates*. Advanced Materials, 2008. **20**(23): p. 4557-4562.
210. Schmidt-Mende, L. and J.L. MacManus-Driscoll, *ZnO-nanostructures, defects, and devices*. Materials today, 2007. **10**(5): p. 40-48.
211. Mueller, U., et al., *Metal-organic frameworks—prospective industrial applications*. J. Mater. Chem., 2006. **16**(7): p. 626-636.
212. Ashfold, M.N.R., et al., *The kinetics of the hydrothermal growth of ZnO nanostructures*. Thin Solid Films, 2007. **515**(24): p. 8679-8683.
213. Azimi, H., et al., *Determining the internal quantum efficiency of organic Bulk Heterojunctions based on mono and bis-adduct fullerenes as acceptor*. Solar energy materials and solar cells, 2011.
214. Tzabari, L. and N. Tessler, *Shockley-Read-Hall recombination in P3HT: PCBM solar cells as observed under ultralow light intensities*. Journal of Applied Physics, 2011. **109**: p. 064501.
215. Koster, L., et al., *Light intensity dependence of open-circuit voltage of polymer: fullerene solar cells*. Applied Physics Letters, 2005. **86**: p. 123509.
216. Coakley, K.M. and M.D. McGehee, *Conjugated polymer photovoltaic cells*. Chemistry of materials, 2004. **16**(23): p. 4533-4542.
217. Kippelen, B. and J.L. Brédas, *Organic photovoltaics*. Energy Environ. Sci., 2009. **2**(3): p. 251-261.
218. Van Bavel, S.S., et al., *P3HT/PCBM Bulk Heterojunction Solar Cells: Impact of Blend Composition and 3D Morphology on Device Performance*. Advanced Functional Materials, 2010. **20**(9): p. 1458-1463.
219. Ma, W., et al., *Thermally stable, efficient polymer solar cells with nanoscale control of the interpenetrating network morphology*. Advanced Functional Materials, 2005. **15**(10): p. 1617-1622.
220. Chaabouni, F., M. Abaab, and B. Rezig, *Metrological characteristics of ZnO oxygen sensor at*

- room temperature. *Sensors and Actuators B: chemical*, 2004. **100**(1): p. 200-204.
221. Fan, Z., et al., *ZnO nanowire field-effect transistor and oxygen sensing property*. *Applied Physics Letters*, 2004. **85**(24): p. 5923-5925.
222. Chang, S.J., et al., *A ZnO nanowire vacuum pressure sensor*. *Nanotechnology*, 2008. **19**: p. 095505.
223. Basak, D., et al., *Photoconductive UV detectors on sol-gel-synthesized ZnO films*. *Journal of Crystal Growth*, 2003. **256**(1): p. 73-77.
224. Jagadish, C. and S.J. Pearton, *Zinc oxide bulk, thin films and nanostructures: processing, properties and applications* 2006: Elsevier Science.
225. Street, R., et al., *Interface state recombination in organic solar cells*. *Physical Review B*, 2010. **81**(20): p. 205307.
226. Soares Sabioni, A.C., *About the oxygen diffusion mechanism in ZnO*. *Solid state ionics*, 2004. **170**(1): p. 145-148.
227. He, C., et al., *Photoelectrochemical performance of Ag-TiO<sub>2</sub>/ITO film and photoelectrocatalytic activity towards the oxidation of organic pollutants*. *Journal of Photochemistry and Photobiology A: Chemistry*, 2003. **157**(1): p. 71-79.
228. Di Valentin, C., et al., *Characterization of paramagnetic species in N-doped TiO<sub>2</sub> powders by EPR spectroscopy and DFT calculations*. *The Journal of Physical Chemistry B*, 2005. **109**(23): p. 11414-11419.
229. Lindgren, T., et al., *Photoelectrochemical and optical properties of nitrogen doped titanium dioxide films prepared by reactive DC magnetron sputtering*. *The Journal of Physical Chemistry B*, 2003. **107**(24): p. 5709-5716.
230. Liu, B., L. Wen, and X. Zhao, *The structure and photocatalytic studies of N-doped TiO<sub>2</sub> films prepared by radio frequency reactive magnetron sputtering*. *Solar energy materials and solar cells*, 2008. **92**(1): p. 1-10.
231. Plank, N.O.V., et al., *Efficient ZnO Nanowire Solid-State Dye-Sensitized Solar Cells Using Organic Dyes and Core-shell Nanostructures*. *The Journal of Physical Chemistry C*, 2009. **113**(43): p. 18515-18522.

## Appendix: Publications and Presentations

H. Sun, J. Weickert, H.C. Hesse, L. Schmidt-Mende, “*UV light protection through TiO<sub>2</sub> blocking layers for inverted organic solar cells*” Sol. Cells and Sol. Energy Mat. doi: 10.1016/j.solmat.2011.08.004

J. Weickert, H. Sun, C. Palumbiny, H.C.Hesse, L.Schmidt-Mende: “*Spray-deposited PEDOT:PSS for air stable inverted organic solar cells*” Sol. Cells and Sol. Energy Mat.94 p. 2371

D. Muñoz-Rojas, H. Sun, et.al : “*Ultra fast and low temperature AALD deposition of high quality amorphous TiO<sub>2</sub> blocking layers for inverted bulk heterojunction solar cells*” in preparation.

H.C. Hesse, J. Weickert, H. Sun, M. Hussein, L. Dössel, X. Feng, K. Müllen, L. Schmidt-Mende: “*Discotic small molecules in organic solar cells: Influence of residues on structure and performance*” Sol. Cells and Sol. Energy Mat. 94 p.560

H. Sun et.al. “*Organic solar cell based on ZnO nanowires fabricated by a hydrothermal method*”. Optoelectronics workshop, Riezlern, Austria (oral presentation).

H. Sun et.al. “*Investgation of TiO<sub>2</sub> layers in Oragnic solar cells*”, CeNS workshop 2011, Venice, Italy (poster).

## Curriculum Vitae

### Haiyan Sun

Born in 1982, China.

LMU, Department für Physik,

Amalienstr. 54, 80799 München

Phone: 017682054090

Email: sun.haiyan@physik.uni-muenchen.de



### EDUCATION

2008– Doctorate in Physics

Ludwig-Maximilians University, Munich, Germany.

Thesis Title: Metal oxides in hybrid solar cells

Developing novel nanostructured metal oxides with various techniques, and the physical characteristics in hybrid solar cells.

2005–2008 M.S. in Physics, Shandong University, China.

Thesis Title: Dielectric property of macroporous  $\text{Al}_2\text{O}_3$

Preparation and Characteristics of bulk macroporous metal oxides by hydrothermal method.

2001–2005 B.S. in Physics, Shandong University, China.

### PROFESSION

- Assembly and characterization of organic solar cells.
- Metal oxides deposition via spray pyrolysis, sol-gel, solution, sputtering, atmospheric atomic layer deposition, and hydrothermal method.
- Surface characterization by scanning electron and atomic force microscopy.
- Charge carrier dynamics investigation by charge carrier decay measurements.
- Charge recombination analysis by Photoluminescence, Impedance spectroscopy, and Intensity-dependent device characterization techniques.
- Supervision of Master and Bachelor students.
- Clean room, Laser and chemistry laboratory experience.

**Research visits:**

- At the Professor Driscoll group, Cambridge University, UK. (short term)  
Funded by the “Royal Society International Join Project“
- At Departament de Física, Universitat Jaume, Spain (short term)  
“Charge transport process in solar cells analysis by Impedance spectroscopy”

**Collaborations:**

“Nanostructured ITO based solar cells ” with Dr. Y. Liu in Ludwig-Maximilians University  
“TiO<sub>2</sub> based flexible solar cells” with Dr. D. Muñoz-Rojas Cambridge University  
“N-doped ZnO hybrid solar cells”with Dr. K. Musselman Cambridge University

**HONORS AND AWARDS**

State Scholarship for doctoral study abroad, China, 2008–present.

Graduated Students Scholarship, Shandong University, 2005–2008

Physics Base Class Scholarship, Shandong University, 2004

National Scholarship, Shandong University, 2003

Excellent Students, Shandong University, 2002

**SKILLS:**

General skills: research project management and data analysis.

Computing Skills: MS-Office, Origin, Photoshop.

Language Skills: Chinese (native), English (Good), German (Basic).

Soft skills: Time Management, Communication, Team work, Organization.

## Acknowledgment

I would like to give my most sincere thanks to all the people who have helped me in last few years. First, I would like to thank the CSC scholarship program for the financial support, to offer me the chance to come here and finish my PhD study. I want to thank Professor Lukas Schmidt-Mende for providing the opportunity to work in this nice group, and for all the patience guidance and great suggestions when discuss with me about my projects. I'd like to thank Dr. Dina Fattakhova-Rohlfing, my second supervisor, for her nice advice for my research. I also want to thank Professor Alexander Högele for his kindness to be the second reviewer on my thesis.

I have to thank Dr. Kevin Musselman from Cambridge University for his warmly helps on both our collaborated research and the corrections for my writing. I also want to thank Dr. David Muñoz-Rojas, Diana Iza and Clare for the happy time we worked together in UK, special thanks to Professor Driscoll and Professor Schmidt-Mende for supporting this research visit. I truly appreciate Yan Li and Dr. Yujing Liu from Department of Chemistry of LMU, and all the other people in AK Bein, for their help on the measurements and discuss with me about the results. I strongly acknowledge all the nice group members in Feldmann group from LMU, for their friendly help and warm welcome to share not only the equipment but also happy spare times together. I would like to thank Jinhu Yang and Feng Gu from Shanghai China, for their generous offers of suggestions and experimental materials. I also have to thank Dr. James Dorman for his advices and corrections on this thesis.

Many thanks to the Hybrid Nanostructures Group, I can't image the lab work without you, and I appreciate you to share all the joys with me during work and free time. Claudia, Dominik, Sandra, Severin, and Wolfgang, I had a great time when worked with you. Special thanks to Andi, Julian and Thomas for kindly helping me with the measurements and computer programs, and opening the chemistry bottles. I have to give my deep thanks to Holger and Jacek, who patiently discussed with me about the results and teach me such a lot. My truly numerous thanks to Jonas, who can always save me from trouble, like a superman, and to Ricky, who can always made my hard time turned good, good time become better. I appreciate for all the helps from you all, to support and warm me for more than one thousand PhD days.

Last but not least, I want to thank my families and my friends. Their love, support and encouragement made me to go through all the challenging moments in my life abroad.